Single-Molecule Kinetic and Thermodynamic Studies of Cosolute-Influenced Nucleic Acid Conformational Transitions

by

Erik Dylan Holmstrom

B.A., Willamette University, 2008

A thesis submitted to the
Faculty of the Graduate School of the
University of Colorado in partial fulfillment
of the requirement for the degree of
Doctor of Philosophy
Biochemistry
2014

This thesis entitled:
Single-Molecule Kinetic and Thermodynamic Studies of Cosolute-Influenced Nucleic Acid Conformational Transitions
written by Erik Dylan Holmstrom
has been approved for the Department of Chemistry and Biochemistry

____
David J. Nesbitt

____
Robert T. Batey

Date_______________

The final copy of this thesis has been examined by the signatories, and we
Find that both the content and the form meet acceptable presentation standards
Of scholarly work in the above mentioned discipline.

Holmstrom, Erik Dylan (Ph.D., Biochemistry)

Single-Molecule Kinetic and Thermodynamic Studies of Cosolute-Influenced Nucleic Acid Conformational Transitions

Thesis directed by Professor David J. Nesbitt

Over the last 40 years the number of biochemical functionalities attributed to nucleic acids has increased tremendously. This diverse array of chemical functionality is intimately coupled to the spatial arrangement of atoms associated with these molecules. The three-dimensional structures and functions of nucleic acids are known to be dependent on the concentration and identity of solutes in solution. These nucleic acid cosolutes can be as simple and universal as atomic metal cations that favorably interact with the negatively charged phosphate backbone of nucleic acids and resulting in stabilization of electronegatively dense conformations. Alternatively, they may be complex organic molecules that are able to promote conformational transitions in certain RNA sequences responsible for regulating gene expression. Understanding the biophysical principles responsible for these cosolutes-influenced conformational transitions represents the primary objective of this work.

Single-molecule fluorescence resonance energy transfer (smFRET) is a technique that is well suited for this goal because it provides the ability to watch individual nucleic acids undergo cosolute-influenced conformational transitions in real-time. These experimental results provide direct access to rate and equilibrium constants for any nucleic acid of interest. The temperature-dependence of these smFRET experiments can be used to partition the free energy change associated with these conformational transitions into the enthalpic and entropic components. The kinetic and thermodynamic information acquired from these experiments, in conjunction with existing structural models, is used to describe the folding pathways and free energy landscapes associated with these nucleic acids.

The types of nucleic acid conformational transitions described in this thesis are as follows: the GAAA Tetraloop Receptor interaction, a 21 bp DNA duplex, and 8bp DNA duplex, a minimal version of the human Telomerase RNA pseudoknot, and a vitamin-B_{12} riboswitch. The cosolutes investigated for these nucleic acid constructs include: $MgCl_2$, KCl, NaCl, urea, trimethylamine oxide, and vitamin-B_{12}. Lastly, this thesis documents the development of an advanced heating technique used to conduct many of the temperature-dependent experiments associated with the aforementioned nucleic acids.

Acknowledgments

This thesis would not exist without never-ending support, encouragement, and inspiration from a number of individuals. The following is a brief, and almost certainly incomplete, list of people that deserve some acknowledgment for their role in getting me here to write this thesis.

First and foremost, I would like to thank my immediate family, especially my parents—Roy and Sue Holmstrom. Throughout my entire life they have remained positive and enthusiastic about all of my scientific interests. It is their parental guidance and financial assistance that has provided me the opportunity to attend graduate school. Lindsay Holmstrom has been a wonderful sister, and deserves credit for being patient with my long-winded answers to her chemical and biological questions. As a nurse, she has also continually fostered my interest in issues related to human health.

It was in elementary school where I remember my first prolonged exposure to the natural and physical sciences and for that I would like to thank my third grade teacher—Mrs. Walley. Early exposure to the sciences certainly played an important role in setting me on the path that led to this thesis. I am grateful for Mr. Micheletto, my seventh grade science teacher, who was always able to make science interesting and applicable to the real world. However, it was not until high school that I fully realized my devotion to the sciences in the classes of: Mr. Honzel (earth science), Mr. McMaster (anatomy and physiology), Mrs. Prather (biology), Ms. Smith (chemistry), and Mr. Govertson (physics). I must also acknowledge Mr. Little (calculus) and Mrs. Umba (statistics) for demonstrating how fundamental math is in describing the world on which we live.

This amazing collection of pre-collegiate experiences primed me for an enlightening tenure as an undergraduate student. I would like to extend my gratitude to the many mentors and advisors I had during those four years: (*i*) Myles Jackson—history and philosophy of science (Willamette University), (*ii*) Susan Kephart— biology (Willamette University), (iii) Sarah Kirk—chemistry (Willamette University), (*iv*) Kent Sugden and his wife Brooke Martin—summer research (University of Montana) and (*v*) David Johnson—summer internship (GlaxoSmithKline).

Myles is certainly the most memorable educator I have ever interacted with and only those who have had the opportunity to experience his wisdom would know why. Susan and Sarah continually encouraged me to actually apply my talents to my studies and encouraged me to consider the possibility of graduate school. Kent Sugden, Brooke Martin, and David Johnson gratefully opened up their laboratories, which allowed me to experience real scientific research. It was Kent who first piqued my interest in nucleic acids and, at the last minute, encouraged me to apply to the University of Colorado at Boulder for graduate school.

My first exposure to the fundamental ideas behind the work contained within this thesis was through my eventual graduate student mentor, Julie Fiore, at a poster session during the graduate student recruitment weekend in the spring of 2008. If I could only acknowledge one person for his or her contributions to this thesis it would be hard to say thanks to anyone other than Julie. She taught me exactly what I needed to know to prosper as a graduate student and provided a great source of scientific motivation and information. Thank you Julie! Tom Baker also deserves special mention for his omnicious presence in graduate school. It didn’t take long for me to understand why everyone in the department came to Tom for answers to their questions. The lab was never the same after he graduated. Both Tom and Julie were first class senior graduate students during my first few years in Boulder.

I would also like to thank all of the other lab mates I have had over the years for their memorable contributions to my graduate school experience: Nick Dupuis for Friday afternoon experiments, Kevin Early for listening to KEXP, Grant Buckingham for pushup contests, and Andy Gisler for being the lab general, Mike Ziemkiewicz for lunchtime volleyball, Mario Vieweger for the Top 40, Larry Fiegland for help with Lab Windows, Andrej Grubisic for being a great neighbor, Rob Roscioli for darts at the Sundown Saloon, Danny Bell for remaining incredibly calm during some contentious group presentations, Mia Zutz for the baked goods, Lora Nugent-Glandorf for showing me the TIRF microscope, Monika Gruetter for continually asking for company on coffee breaks (even though I don't drink coffee), Dan Nelson for wearing clogs in the lab, Mel Roberts for hockey games, Erin Sharp-Willams for the birthday cakes, Volker Schweikhard for the computer and workstation, Chih-Hsuan Chang for learning how to ice skate with the lab, and Fang Wang for continually talking about organizing group activities.

I would like to acknowledge the 2008 class of biochemistry graduate students, most of whom I consider friends rather than classmates. I would like to thank the many colleagues I have had the opportunity to work with over the years: Rob Batey, Andrew Garst, Jake Polaski, Jeremy Trausch, Joe Falke, Kene Piasta, Yun-xing Wang, and Yu Li. It is also worth noting a few of the people who have provided useful feedback during the many struggles and obstacles of graduate school: Laura Johnson, Dan Hickstein, Dan Adams, Kevin Dean, Allison Churnside, Thayne Dickey, Art Pardi, Jeff Swan, Mike Yarus, Tom Cech, Cara Florence, and Debbie Wutke.

My graduate school experience has been significantly enriched by the NIH/ University of Colorado Molecular Biophysics program, which is passionately run by Joe Falke with additional support provided by Lin Pharris. JILA—the jointly run set of research labs between the National Institutes of Standards and Technology (NIST) and the University of Colorado at Boulder—has been the home of my graduate research for the past 6 years. This building is not only populated by a number of Noble laureates and MacArthur fellows, but also by some of the best staff, and administration on campus. Specific mention is essential for Julie Philips and Brad Baxley from SRO, and J.R. Wraith, Philip Kao, Jim Mckown, Alan Dunwell, and Peter Ruprecht from Computing. The JILA electronics and instruments shops also need acknowledgement, notably: James Fung-a-Fat, Carl Sauer, Hans Green, Todd Asincar, and Kim Hagen. I would like to thank Jeffrey Sauter, Brian Lynch and Randall Holliness from the purchasing office for handing the unusually complex process associated with purchasing nucleic acids as well as a couple of helpful people from JILA administration—Maryly Dole and Agnieszka Lynch.

Thanks to my oral examination committee—Rob Batey, Art Pardi, and Amy Palmer—for ensuring that I had the necessary skills to advance to PhD candidacy. Thanks to my thesis Committee for their assistance and support while I was preparing to graduate: Norm Pace, Dick McIntosh, Joe Falke, Rob Batey, and, most importantly, my research Advisor—David Nesbitt.

David shares a diverse collection of qualities with many of the most influential people in my life. Like my parents did when I was a child, David has provided me with financial support. Like my seventh grade science teacher, David has shown me the importance of science in the real world. Like my high school math teachers, David has stressed the importance of math in describing scientific observations. Like my undergraduate chemistry and biology advisors, David has continually asked me to "raise the bar" and apply my talents to my research. As my graduate research advisor, David taught be to be a strong critic of my own work. His vast reservoir of scientific wisdom and intuition served as a great Litmus test for how well I understood my own research. Most importantly, he provided me with a graduate school experience unlike any other in the world and for that he deserves special acknowledgment.

Last, but certainly not least, I would like to thank the single most important person in my life—my partner and best friend—Jennifer McWilliams. She has been by my side for my entire graduate career, which inevitably involves listening to me talk about my research to myself late at night while staring at the computer. Her undying support and encouragement has allowed me to preserver though the trials and tribulations of graduate school. Jen’s warm compassionate heart and cheerful sense-of-humor have always been able to brings a smile to my face, no matter what was holding me down. Most importantly, she has provided a source of balance in my life like none other and for that I am forever grateful.

Table of Contents

Chapter 1:

Introduction.. 1

1.1 Nucleic Acids.. 1
1.2 Nucleic Acid Conformational Transitions.. 5
1.3 Cosolute-Influenced Nucleic Acid Conformational Transitions.. 7
1.4 Single-Molecule Fluorescence.. 11
1.5 References.. 16

Chapter 2:

Experimental Methods.. 19

2.1 Experimental Observation.. 19
  2.1.1 Molecular Fluorescence.. 19
  2.1.2 Forster Resonance Energy Transfer (FRET).. 22
2.2 Single-Molecule Confocal Microscope.. 25
  2.2.1 Excitation Path.. 25
  2.2.2 Microscope and Sample Stage.. 27
  2.2.3 Emission path.. 29
  2.2.4 TCSPC Detection.. 30
  2.2.5 Temperature Control.. 30
    2.2.5.1 Bulk Heating Methods.. 31
    2.2.5.2 Infrared-based Heating.. 33
2.3 Sample Preparation.. 34
  2.3.1 Sample Holder.. 34
  2.3.2 Sample of Interest.. 36
2.4 Data Collection and Analysis.. 38
  2.4.1 Single-Molecule Freely Diffusing.. 38
  2.4.2 Single-Molecule Surface Immobilized.. 41
2.5 Single-Molecule Construct Design.. 43
2.6 References.. 45

Chapter 3:

Real-Time IR Overtone Laser Control of Temperature in Picoliter H_2O Samples: “Nano-Bathtubs” for Single Molecule Microscopy.. 47

3.1 Introduction.. 47
3.2 Results and Discussion.. 49
3.3 Conclusions.. 56
3.4 Experimental Methods.. 57
3.5 References.. 58

Chapter 4:

Pulsed Infrared-Heating Studies of Single Molecule DNA Duplex Dissociation Kinetics and Thermodynamics **60**

4.1 Introduction 60
4.2 Overtone Infrared Laser Based Heating Technique 64
    4.2.1 *In Situ* Measurement and Dynamic Range of Accessible Temperatures .. 65
    4.2.2 High Resolution Spatial Control of Temperature 67
    4.2.3 Rapid Temperature Modulation 69
4.3 A Test Application: Single Molecule Kinetics of DNA Duplex Dissociation 73
    4.3.1 Laser Heating Induced Duplex DNA Dissociation Kinetics 74
4.4 Duplex Dissociation Model 81
4.5 Conclusions 85
4.6 Experimental Methods 86
    4.6.1 Fluorescent Oligonucleotides 86
    4.6.2 Sample Preparation 87
    4.6.3 Fluorescence Microscope 87
    4.6.4 Duplex Dissociation Experiments 87
4.7 References 89

Chapter 5:

Thermodynamic Origins of Monovalent-Facilitated RNA Folding **94**

5.1 Introduction 94
5.2 Molecular Model 96
5.3 Results 99
    5.3.1 Folding Kinetics and Standard State Free Energy of Folding 99
    5.3.2 Standard State Enthalpy and Entropy of Folding 101
    5.3.3 Transition State Thermodynamics 105
    5.3.4 Temperature Dependence of k_{fold} 107
5.4 Discussion 112
    5.4.1 Folding Pathways and Ion Atmospheres 112
    5.4.2 Folding in a Free Energy Neutral Monovalent Ion Atmosphere 113
    5.4.3 Folding in a “Free Energy Favorable” Monovalent Ion Atmosphere 115
    5.4.4 Dependence on Monovalent Cation Identity 120
5.5 Conclusion 121
5.6 Experimental Methods 124
    5.6.1 Experimental Apparatus 124
    5.6.2 Temperature Control 124
    5.6.3 RNA and Sample Preparation 125
5.7 Acknowledgment 125
5.8 References 126

Chapter 6:

Kinetic and Thermodynamic Origins of Osmolyte-Influenced Nucleic Acid Folding 131

6.1 Introduction 131
6.2 Results 134
  6.2.1 Folding in the Absence of Osmolytes 136
  6.2.2 Osmolyte-Dependent Folding Kinetics 137
  6.2.3 Osmolyte-Dependent Folding Free Energies (m-value analysis) 139
  6.2.4 Osmolyte-Dependent Thermodynamics for the 8 bp DNA Duplex 140
  6.2.5 Osmolyte-Dependent Thermodynamics for the TL-TLR 143
6.3 Discussion 144
  6.3.1 TMAO-Dependent Folding Free Energies 145
  6.3.2 Urea-Dependent Folding Free Energies 146
  6.3.3 Kinetic Origins of Osmolyte-Influenced Nucleic Acid Folding 146
  6.3.4 Osmolyte-Dependent Entropy Changes for the 8bp DNA Duplex 148
  6.3.5 Osmolyte-Dependent Entropy Changes for the TL-TLR 149
6.4 Conclusions 151
6.5 Experimental Methods 153
  6.5.1 Nucleic Acids 153
  6.5.2 Solution and Sample Preparation 154
  6.5.3 smFRET Microscope 155
6.6 References 157

Chapter 7:

Single Molecule FRET Studies of the Human Telomerase RNA Pseudoknot: Temperature/Urea Dependent Folding Kinetics and Thermodynamics 161

7.1 Introduction 161
7.2 Results 164
  7.2.1 Freely Diffusing Burst Measurements 164
  7.2.2 Surface Immobilized Images 168
  7.2.3 Surface Immobilized Time Trajectories 170
  7.2.4 van't Hoff Thermodynamics 174
7.3 Discussion 177
  7.3.1 Folding Free Energies 177
  7.3.2 Urea-dependent Free Energies and Rate Constants 180
  7.3.3 Urea-Dependent Entropies and Enthalpies 181
7.4 Conclusions 183
7.5 Experimental Methods 184
  7.5.1 Construct Design 184
  7.5.2 Single-molecule Microscope 186
  7.5.3 Freely Diffusing smFRET Experiments 187
  7.5.4 Surface Immobilized smFRET Experiments 189
  7.5.5 smFRET Temperature Control 190
  7.5.6 smFRET Buffer Conditions 190

7.6 References 191

Chapter 8:

Vitamin B12-facilitates formation of a regulatory RNA kissing loop 196

- 8.1 Introduction 196
- 8.2 Results 200
  - 8.2.1 KL docking equilibrium in the absence of ligand 201
  - 8.2.2 KL docking equilibrium in the presence of ligand 204
  - 8.2.3 Ligand binding properties 205
  - 8.2.4 CBL-dependence of the KL docking equilibrium 209
  - 8.2.5 KL docking kinetics in the absence of ligand 211
  - 8.2.6 KL docking kinetics in the presence of ligand 213
  - 8.2.7 Cell-based CBL-dependent expression of GFP 216
- 8.3 Discussion 218
  - 8.3.1 Kissing Loop docking dynamics 218
  - 8.3.2 KL docking in the *presence* of a macromolecular stabilizing agent 219
  - 8.3.3 Ligand Recognition 221
  - 8.3.4 Mechanism of regulation for the *env*8 hydroxocobalamin riboswitch .. 222
- 8.4 Conclusions 223
- 8.5 Experimental Methods 224
  - 8.5.1 Fluorescent Construct Design 224
  - 8.5.2 Freely-Diffusing smFRET 226
  - 8.5.3 Ensemble Fluorometry 226
  - 8.5.4 Surface-Immobilized smFRET 227
  - 8.5.5 *in vivo* Regulation of GFP Expression 227
- 8.6 References 229

Bibliography **233**

List of Tables

Table 2.1 .... **22**

Table of approximate photophysical properties associated with four fluorophores commonly used throughout this thesis. All reported values are for free dye molecules in buffered aqueous solutions, expect for Cy3-DNA*, where the conjugation to a nucleic acid significantly increases the quantum yield and fluorescence lifetime of the fluorophore.

Table 6.1 .... **142**

Values for the van't Hoff analysis of the osmolyte-influenced folding nucleic acids. Additional information about the methods of data analysis for the van't Hoff plots can be found in Section 6.3.4. See Figure 6.6 for experimental data.

Table 7.1 .... **173**

Rate and equilibrium constants for the **a)** wild-type and **b)** mutant forms of the human telomerase RNA pseudoknot under varying urea concentrations. For both RNA pseudoknot constructs, the rate constant for forming the pseudoknot from the hairpin conformation is largely insensitive to urea concentration.

Table 7.2 .... **176**

Thermodynamics parameters from the single-molecule van't Hoff analyses. **a)** Entropy and enthalpy changes for the wild-type human telomerase pseudoknot at various urea concentrations. $\Delta H°$ and $\Delta S°$ are (*i*) insensitive or (*ii*) linearly dependent on urea concentration, respectively. Together they predict folding thermodynamics under non-denaturing conditions. **b)** Enthalpy and entropy changes for the dyskeratosis congenita mutant form of the human telomerase RNA pseudoknot under non-denaturing conditions.

List of Figures

Chapter 1:

Figure 1.1 2

Structural components of a nucleic acid. **(a)** Hydrogen bonding pattern between pairs of guanine and cytosine nucleobases. **(b)** Hydrogen bonding pattern between pairs of adenine and thymine nucleobases in DNA. **(c)** Hydrogen bonding pattern between pairs of adenine and uracil nucleobases in RNA. **(d)** Schematic representation of the phosphate, sugar, and base constituents in the context of duplex deoxyribonucleic acid.

Figure 1.2 3

Central Dogma of Molecular Biology. Schematic representation of the linear transfer of genetic information in a cell. Pointed and blunted arrows represent some of the many ways that RNA can influence the processing of this genetic information.

Figure 1.3 5

Hierarchical folding of RNA. Example depicts the major structural transitions associated with the formation of a tRNA molecule. Colors correspond to base paired regions within the oligonucleotide.

Figure 1.4 6

Cartoon graphics depicting the numerous oligonucleotide conformation transitions discussed in the chapters of this thesis.

Figure 1.5 9

Chemical structures of two osmolytes known to significantly influence the conformational transitions of nucleic acids.

Figure 1.6 13

Fluorescence Resonance Energy Transfer (FRET). An excited donor fluorophore (green) can transfer energy to a nearby acceptor fluorophore (red) in a distance-dependent process. When the donor and acceptor are proximal, energy transfer is efficient; when they are distal, energy transfer is poor.

Chapter 2:

Figure 2.1 21

Jablonski energy level diagram depicting absorption (excitation) and emission (fluorescence) of photons. (http://www.microscopyu.com/articles/fluorescence/fret/fretintro.html)

Figure 2.2 24

Jablonski energy level diagram depicting Fluorescence Resonance Energy Transfer (FRET). (http://www.microscopyu.com/articles/fluorescence/fret/fretintro.html)

Figure 2.3 25

Distance dependence of FRET efficiency (E_{FRET}) for a fictitious biological molecule. Separation of the donor and acceptor fluorophores results in less efficient energy transfer.

Figure 2.4 .... **26**
Cartoon cut-away diagram of the single-molecule microscope system used to conduct the research associated with this thesis.

Figure 2.5 .... **28**
(left and middle) Visual depictions of the Airy disc associated with a diffraction-limited focus. (right) Graphical representation of the normalized radial intensity distribution (red solid line, *I(x)/Io)* and the relative encircled power (blue dotted line, *P(x)/Po)*. Note $x = kasin(\theta) = 2\pi rN.A./\lambda$, as used in Eq. 2.7. (http://en.wikipedia.org/wiki/Airy_disk).

Figure 2.6 .... **28**
Sample surface image of immobilized fluorescence molecules using the 3-D nano-positioning peizo-electric scanning stage (not shown).

Figure 2.7 .... **31**
Diagram of the original, bulk, heating capabilities established by Dr. Julie Fiore (stage not shown).

Figure 2.8 .... **33**
Cut-away cartoon of the infrared-based heating apparatus coupled to the existing inverted confocal fluorescence microscope.

Figure 2.9 .... **35**
Image of the three types of sample holders used for fluorescence studies. See Section 2.3.1 for details.

Figure 2.10 .... **38**
Schematic representation (not-to-scale) of the commonly used biotin- streptavidin surface immobilization technique. Approximately one out of ten BSA(blue ovals) molecules contains a biotin (black triangle) moiety. Streptavidin (purple rectangle) has four binding sites for biotin, which can be used to immobilize fluorescent nucleic acids to the glass coverslip.

Figure 2.11 .... **39**
Schematic for freely-diffusing single-molecule experiments.

Figure 2.12 .... **41**
Images of the scanning (top) and time trajectory (bottom) windows of the SPCImage.exe software used to acquire fluorescence data.

Figure 2.13 .... **42**
Image of the vffta64.exe software use to analyze the data acquired via the SPCImage.exe program.

Chapter 3:

Figure 3.1 49
Cutaway diagram of IR absorption based heating apparatus. Inset shows the absorption coefficient (α) of water in the $v_{OH} = 2 \leftarrow 0$ overtone band region near 1.45 μm.

Figure 3.2 52
Arrhenius analysis of the non-radiative component $k_{nrad}(T)$ for temperature- dependent rhodamine B fluorescence rates. By explicitly measuring $k_{fl} = k_{rad} + k_{nrad}(T)$ and modeling $k_{nrad}(T)$ as a thermally activated Arrhenius process, one can use TCSPC and the Arrhenius equation as a calibration curve for temperature.

Figure 3.3 52
Van't Hoff plot of $R\ln[K_{eq}]$ vs $1/T$ for single molecule FRET studies of RNA folding provides ΔH° and ΔS° for the GAAA tetraloop−receptor tertiary interaction. Note the excellent agreement between the laser-overtone and stage-based heating techniques.

Figure 3.4 54
Time scale for IR-absorption based heating. By monitoring rhodamine B fluorescence lifetimes, one can directly measure characteristic times associated with laser heating of the sample. The characteristic heating time is currently limited by the time binning resolution of the data (< 20 ms), which is slower than, but consistent with, predictions (see section 3.2 for details).

Chapter 4:

Figure 4.1 64
Schematic representation of the infrared heating apparatus illustrating the coaxially aligned foci of the infrared (red) and excitation (green) lasers within a standard sample holder (not to scale). The intensity plot depicts the experimentally measured radial intensity profile at the focus of the infrared laser ($\omega_o = 10.04(4)$ μm).

Figure 4.2 66
Fluorescence decay profile for Rhodamine B as a function of temperature. The linearity of the fluorescence decay over three orders of magnitude attests to the single-exponential behavior of Rhodamine B. The inset represents the Eyring analysis of the temperature-dependent non-radiative rate constant for Rhodamine B (see section 4.2.1 for details), which is used to determine the temperature rise in the diffraction-limited confocal volume of the sample.

Figure 4.3 68
Experimentally measured steady state temperature rise (ΔT) as a function of **(a)** incident laser power as well as **(b)** radial and **(c)** axial distances from the laser focal point. The solid red region in **(b)** represents the radial intensity profile of the infrared laser beam scaled to the maximum ΔT. Note the clear broadening of the temperature profile beyond the laser excitation region, which arises largely from thermal diffusion away from the heating axis.

Figure 4.4 71
Real time observation of the infrared heating and cooling behavior, as obtained by

time-correlated single-photon fluorescence measurements of Rhodamine B in the confocal excitation region. **(a)** Sample temperature trajectory (black ⊗'s) resulting from a 50 mW heating pulse with a duration of 500 ms. The solid lines represent multi-exponential fits used to calculate the half-maximal times for heating (solid red) and cooling (solid blue). **(b)** A linear-log plot demonstrating the dependence of cooling time constant on the heating duration, which suggests that the system achieves a steady state thermal distribution on the few second time scale.

Figure 4.5 .... **74**
(a) Diagram of the duplex DNA fluorescent construct used for the dissociation experiments. Green and red stars represent the Cy3 and Cy5 FRET pair used in the experiments. The solid cyan line corresponds to the PEG$_{18}$ internal linker within the construct to easily allow the construct to form the closed conformation. **(b)** ALEX surface image (10 µm × 10 µm) prior to and **(c)** after exposure to a pulse of infrared light. White circles represent the mask used to measure survival probability (see section 4.3.1 for details).

Figure 4.6 .... **76**
ALEX scanned image (80 µm × 80 µm) of the fluorescent DNA duplex constructs after heating the center of the image to 72.3(5) °C for 10 sec. Note the clear circular region of high FRET molecules (red), corresponding to duplex constructs that have undergone dissociation, while the surrounding low FRET species (green) remain in the duplex conformation.

Figure 4.7 .... **79**
(a) DNA duplex survival probability data, $S(\Delta t,T)$, as a function of heating duration, Δt, at four steady-state heating pulse temperatures. Dashed lines represent least squares fit to a consecutive first order reaction model, which yields n = 4.1(3) sequential reaction steps with an assumed identical rate constant. Notice the rapid increase in this rate constant with increasing temperature, which implies a large endothermic component the transition state barrier. **(b)** Eyring transition state analysis of the temperature-dependent rate constant, suggesting a highly endothermic ($\Delta H^{\ddagger}$ = 50(10) kcal/mol) and entropically rewarding ($\Delta S^{\ddagger}$ = 100(20 cal/mol/K) component of the free energy barrier for each of the fraying events.

Figure 4.8 .... **83**
Model depicting the "consecutive fraying at both ends" mechanism for duplex dissociation. The colored bars represent short segments of the 21 bp DNA duplex that are either associated (green) or dissociated (red). The transparent black numbers correspond to the relative abundance of each partially dissociated species as predicted by a binomial distribution. After four consecutive fraying events, the single remaining associated (green) segment of the duplex is sufficiently frayed to undergo a final rapid dissociation step (see section 4.4 for details).

Chapter 5:

Figure 5.1 .... **97**
Schematic of the three-piece donor/acceptor label RNA construct. The isolated GAAA

tetraloop–receptor serves as a model system to investigate the thermodynamics and kinetics of monovalent-facilitated formation of tertiary interactions in structured RNAs.

Figure 5.2 .... **98**
(a) Sample time trajectories for the model construct. A hidden Markov fit to the FRET trajectory is used to demonstrate the two-state behavior of folding process. **(b)** Cumulative distribution function (CDF) of the dwell times demonstrates single-exponential behavior and are used to extract unimolecular rate constants for folding and unfolding.

Figure 5.3 .... **100**
(a) Na^+-dependent kinetics for the formation of the GAAA tetraloop–receptor interaction. Increasing [Na^+] yields a significant enhancement of the folding rate constant (k_{fold}) and a subtle reduction in the rate constant for the unfolding process (k_{unfold}). **(b)** The dependence of the free energy on [Na^+] and **(c)** preferential interaction coefficient analysis for the formation of the tertiary interaction, which yields an ion pair uptake of $2\Delta\Gamma_{\pm} = 2.4(1)$ and no change in free energy at [Na^+] = 170(20) mM.

Figure 5.4 .... **102**
(a) van’t Hoff analysis of the tetraloop–receptor interaction at four [Na^+]. Increasing [Na^+] increases both the $\Delta H°$ (decreasing slope) and the $\Delta S°$ (increasing vertical intercept) for the formation of the tertiary interaction. **(b)** Table of thermodynamic parameters from the van’t Hoff analysis. **(c)** Bar graph to visually display the change in $\Delta H°$ and $\Delta S°$ as a function of ln[a_{Na+}].

Figure 5.5 .... **107**
(a) Transition state theory (TST) analysis of the rate constant associated with formation of the tetraloop–receptor interaction (k_{fold}) as a function of temperature. **(b)** Table of thermodynamics parameters from the TST analysis. **(c)** Bar graph depicting the change in $\Delta H^{\ddagger}_{fold}$ and $\Delta S^{\ddagger}_{fold}$ at four values of ln[$a_{\mathrm{Na+}}$].

Supplemental Figure S5.1 .... **110**
Schematic of the three-piece donor/acceptor label RNA construct. The poly-U_7 linker is used to determine the effect of the linker on the folding thermodynamics.

Supplemental Figure S5.2 .... **111**
(a) van’t Hoff analysis of tetraloop–receptor interaction at four [Na^+] with the poly-U_7 linker. Increasing [Na^+] increases both the $\Delta H°$ (decreasing slope) and the $\Delta S°$ (increasing vertical intercept) for the formation of the tertiary interaction. **(b)** Table of thermodynamic parameters from the van’t Hoff analysis. **(c)** Visual display of changes in $\Delta H°$ and $\Delta S°$ as a function of ln[Na^+].

Supplemental Figure S5.3 .... **111**
(a) Transition state theory (TST) analysis of the rate constant associated with formation of the tetraloop–receptor interaction (k_{fold}) as a function of temperature with the poly-U_7 linker based construct **(b)** Table of thermodynamics parameters from the

TST analysis **(c)** Bar graph depicting the change in $\Delta H^{\ddagger}_{fold}$ and $\Delta S^{\ddagger}_{fold}$ at four values of ln[Na^+].

Figure 5.6 .... **112**
Complete thermodynamics reaction coordinates for the formation of the GAAA tetraloop−receptor tertiary interaction. The three panels depict the: **(a)** enthalpy, **(b)** entropy, and **(c)** free energy along the reaction coordinate at 180 and 630 mM Na^+. The horizontal distance between states qualitatively represents how "early" or "late" they are along the reaction coordinate (see Section 5.4 for details).

Figure 5.7 .... **117**
Structural representation of the free and bound receptor domain. Bases that undergo significant structural rearrangement upon forming the tetraloop−receptor interaction are color-coded. Bases of the GAAA tetraloop are not shown to emphasize changes within the receptor domain (see Section 5.4.3 for details).

Figure 5.8 .... **121**
Monovalent-identity and folding kinetics for the formation of the GAAA tetraloop−receptor interaction. Increasing monovalent concentration provides a significant enhancement of the folding rate constant (k_{fold}) and a subtle reduction in the rate constant for the unfolding process (k_{unfold}). No significant difference is observed between Na^+ and K^+.

Figure 5.9 .... **122**
(a) van't Hoff analysis of tetraloop−receptor interaction comparing [Na^+] and [K^+]**(b)** Eyring analysis of tetraloop−receptor interaction comparing [Na^+] and [K^+]. **(c,d)** Table of thermodynamic parameters from the van't Hoff and Eyring analyses. As depicted, folding behavior is largely independent of monovalent cation identity.

Chapter 6:

Figure 6.1 .... **133**
Free energy diagram representing the effect of TMAO or urea on the stability of the unfolded (**U**) or folded (**F**) structures of a nucleic acid. TMAO has a *more unfavorable* interaction with the *unfolded* structure than the *folded* structure, which results in a net *decrease* in $\Delta G^{\circ}_{\text{fold}}$. Urea has a *more favorable* interaction with the *unfolded* conformation than *folded* conformation, which gives rise to a net *increase* in $\Delta G^{\circ}_{\text{fold}}$.

Figure 6.2 .... **135**
Cartoon representation of the two smFRET nucleic acid constructs used throughout the study. The DNA duplex construct (**a** and **b**) is intended to be a model system for nucleic acid secondary structure, where as the TL-TLR construct (**c** and **d**) serves as a model for tertiary interactions in structured RNAs. For both constructs, formation of the interaction (**b** and **d**), referred to as folding, results in an increase in E_{FRET} (**a** and **c**).

Figure 6.3 .... **137**
Representative donor (green) and acceptor (red) fluorescence trajectories for **(a)** the TL-TLR and **(b)** the DNA duplex. Fluorescence data is use to calculate the FRET

trajectories (black), which are then analyzed to measure the folding (k_{fold}) and unfolding (k_{unfold}) rate constants for each of the nucleic acid constructs.

Figure 6.4 .... **138**
Kinetic origin of osmolyte-influenced nucleic acid folding. The *stabilizing* osmolytes TMAO (blue box) *increases* **(a)** the folding rate constant (k_{fold}, red) and *decreases* the **(b)** unfolding rate constant (k_{unfold}, green) for both the GAAA tetraloop—receptor (triangle) and DNA duplex (circle) constructs. The *destabilizing* osmolyte, urea, *decreases* the **(c)** folding rate constant (k_{fold}, red) and *increases* the **(d)** unfolding rate constant (k_{unfold}, green) for both constructs.

Figure 6.5 .... **139**
Osmolyte-dependent folding free energy change for **(a)** the DNA duplex and **(b)** the TL-TLR constructs. For both constructs, addition of TMAO (blue stars) always *stabilizes* the folding transitions, where as addition of urea (orange squares) *destabilizes* the folding transitions as indicated by the dependence of ΔG° on the osmolyte concentration.

Figure 6.6 .... **141**
van't Hoff plots for the osmolyte-influenced folding of both **(a)** the DNA duplex and **(b)** the TL-TLR interaction. Solid lines in **(a)** correspond to a global fit with a common slope, as discussed in the text, to reduce parameter correlation between the three data sets: 1 M TMAO (blue stars), 0 M osmolyte (pink circles), and 1 M urea (orange squares). The solid lines for the TL-TLR interaction **(b)** are also the result of a global fit of the 0 M osmolyte and 1 M urea data sets in order to reduce parameter correlation, while the solid line for the 1M TMAO data set represents an independent fit of the data. See Table 6.1 for values of the fitted parameters.

Supplemental Figure S6.1 .... **142**
Temperature-dependent kinetic data for the **(a)** folding and **(b)** unfolding rate constants for the DNA duplex. The data are analyzed using transition state theory. Solid lines in correspond to a global fit with a common slope, as discussed in the text, to reduce parameter correlation. The large entropic offset in the temperature-dependence of the unfolding rate constants **(b)** suggests that most of the change in ΔS° arises from changes in the entropic barrier to unfolding ($\Delta S^{\ddagger}_{\mathrm{unfold}}$). The data table **(c)** contains values for the transition state theory analysis of the temperature-dependent kinetic data for the DNA duplex. Fitting methods are identical to those used in the van't Hoff analysis (Figure 6.6), which is discussed in section 6.3.4.

Supplemental Figure S6.2 .... **144**
Temperature-dependent kinetic data for the **(a)** folding and **(b)** unfolding rate constants for the TL-TLR. The data are analyzed using transition state theory. Solid lines for 1 M urea (orange squares) and 0 M osmolyte (pink circles) correspond to a global fit with a common slope, as discussed in the text, to reduce parameter correlation. The large entropic offset for 1 M urea in the temperature-dependence of the folding rate constant **(a)** suggests that most of the change in ΔS° arises from changes in the entropic barrier to folding ($\Delta S^{\ddagger}_{\mathrm{fold}}$). The distinct thermodynamic behavior of TMAO- facilitated

formation of the TL-TLR interaction is discussed in the text. The data table **(c)** contains values for the transition state theory analysis of the temperature-dependent kinetic data for the DNA duplex. Fitting methods are identical to those used in the van't Hoff analysis (Figure 6.6), which is discussed in section 6.3.4.

Figure 6.7 .... **155**

Schematic representation of the inverted confocal fluorescence microscope used to acquire smFRET trajectories. Individual molecules are immobilized to the glass coverslip using standard biotin-streptavidin chemistry. Excitation and emission is achieved using standard epifluorescence techniques. Fluorescent photons are focused through a confocal pinhole before being separated by color and polarization and directed onto 4 single photon avalanche photodiodes. Upon detection, the arrival times of individual photons are recorded and sent to a time-correlated single-photon counting (TCSPC) router where they are used to generate trajectories of donor and acceptor fluorescence.

Chapter 7:

Figure 7.1 .... **163**

Details of the human telomerase RNA pseudoknot **a)** Secondary structure diagrams of the minimal pseudoknot motif in a partially unfolded (hairpin) conformation and a folded (pseudoknot) conformation. The GC→AG mutation at the orange nucleotides in the psuedoknot region corresponds to the genetic disorder dyskeratosis congenita. Green (Cy3) and red (Cy5) stars indicate the location of two fluorophores, where size of the stars reflect FRET efficiency between the two dyes and the black vertical bar represents the ligation site. **b)** Model solution structure of the minimal pseudoknot motif, with the same color scheme as the secondary structure diagram. **c)** Schematic equilibrium between the pseudoknot and hairpin conformations.

Figure 7.2 .... **165**

Freely diffusing FRET histograms of **a)** the wild-type human telomerase RNA pseudoknot and **b)** the dyskeratosis congenita mutant of the human telomerase RNA pseudoknot. The urea titrations demonstrate strong shifts in the pseudoknot-hairpin equilibrium behavior for both constructs.

Supplemental Figure S7.1 .... **167**

a) Details of the alternative labeling scheme for the wild-type human telomerase RNA pseudoknot secondary structure. The minimal pseudoknot motif is in a partially unfolded (hairpin) conformation and a folded (pseudoknot) conformation. The green (Cy3) and red (Cy5) stars indicate the location of the two fluorophores, while the size of the stars represents the FRET efficiency between the two dyes. The grey vertical bar represents the location of the ligation site (see Section 7.5.1 for details) **b)** Freely diffusing FRET histograms of alternate wild-type human telomerase RNA pseudoknot. The nearly identical FRET values at high and low urea concentrations confirm that: (*i*) the P2 region of the pseudoknot remains intact under all experimental conditions and (*ii*) the dynamics associated with the conventional constructs results from formation/disruption of the P3 region of the pseudoknot.

Figure 7.3 .... **168**
Urea dependence of the free energy change for forming the pseudoknot from the hairpin conformation for the wild-type human telomerase RNA pseudoknot (grey) and the dyskeratosis congenita mutant (orange) of the human telomerase RNA pseudoknot. Linear extrapolation to 0 M urea yields the 4.5(3) kcal/mol differential folding free energy between the WT and mutant pseudoknot under non-denaturing conditions.

Figure 7.4 .... **169**
Images of surface immobilized molecules for the wild-type **a,b)** and dyskeratosis congenita **c,d)** pseudoknots. Each diffraction limited fluorescence spot represents the location of an individual dually labeled RNA molecule. The urea dependence of the images yields kinetic information about the two different pseudoknot constructs (see Section 7.2.2 for details).

Figure 7.5 .... **170**
Surface immobilized folding and unfolding kinetics for the **a)** wild-type pseudoknot and **c)** the mutant human telomerase RNA pseudoknots under denaturing and non-denaturing conditions, respectively. Rate constants are determined from exponential fits to cumulative distribution plots of dwell times for the **b)** wild-type and **d)** dyskeratosis congenita pseudoknots.

Figure 7.6 .... **172**
Log-linear plot of the urea-dependent folding and unfolding kinetics for the **a)** wild-type and **b)** dyskeratosis congenita pseudoknots. For both constructs, the unfolding rate constant is substantially more sensitive to addition of urea than the folding rate constant, which suggests that most of the change in base solvent accessible surface area (SASA) occurs after formation of the transition state. Lines indicate trends and are not actual fits to the data.

Figure 7.7 .... **175**
Single-molecule van't Hoff analyses. **a)** A plot of the temperature-dependence of the equilibrium constant of the wild-type human telomerase RNA pseudoknot at three urea concentrations. The identical slopes indicate a urea-*independent* folding enthalpy, while the constant vertical offset indicates a urea-*dependent* entropy. **b)** A plot of the urea-dependent entropy suggests a linear dependence of folding entropy on urea concentration. **c)** van't Hoff analysis of the mutant pseudoknot under non-denaturing conditions. All entropy and enthalpy changes can be found in Table 7.2.

Figure 7.8 .... **178**
Free energy landscape for formation of the pseudoknot from the hairpin conformation. Secondary structure diagrams for the wild-type human telomerase RNA pseudoknot are shown, including the predicted structure of the transition state where only a few nucleotides from the P3 region of the pseudoknot have formed (see Section 7.3.1 for details).

Figure 7.9 .... **186**
Single-molecule fluorescence microscope. Diagram of the experimental setup and data

collection (see Section 7.5.2 for details).

Figure 7.10 .... **188**
Freely diffusing experiments. **a)** Schematic representation of single-molecules freely diffusing in and around the overlapping excitation volumes of the red and green lasers (see Materials and Methods for details). **b)** Freely diffusing data of the human telomerase RNA pseudoknot obtained using ALEX methods, with the four possible outcomes for the fluorescent molecules. ALEX filtering permits events from dually labeled donor-acceptor molecules to be selectively considered for data analysis.

Chapter 8:

Figure 8.1 .... **198**
Schematic representation of the **a)** secondary and **b)** tertiary structure of the *env8*HyCbl riboswitch, complete with the Cy3 (green star), Cy5 (red star), and biotin (blue rectangle) synthetic moieties. The loops, L5 (red) and L13 (green) form a regulatory RNA kissing-loop (KL), which contains the purine-rich ribosome binding site (shadowed green nucleotides). Binding of hydroxocobalamin (bronze spheres, HyCbl) facilitates formation of the KL, which decreases the distance between the Cy3 (donor) and Cy5 (acceptor) fluorophores resulting in more efficient energy transfer (E_{FRET}).

Figure 8.2 .... **199**
Four-state kinetic model for the *env*8HyCbl riboswitch represented **a)** graphically and **b)** symbolically. The four macroscopic conformations are linked by three coupled equilibria: (*i*) KL docking in the absence of ligand, (*ii*) ligand binding in the undocked conformation, and (*iii*) KL docking in the presence of ligand. Formation of the KL decreases the inter-dye distance, resulting in more efficient fluorescence resonance energy transfer (E_{FRET}). Ligand binding quenches Cy3, which decreases the total fluorescence of Cy3 and Cy5 and can be monitored independent of KL docking/undocking.

Figure 8.3 .... **202**
Freely diffusing smFRET experiments depict the Mg^{2+}-dependence of the KL docking equilibrium in the a) *absence* and **b)** *presence* of 1000 nM HyCbl. **c)** The presence of HyCbl (bronze circles) decreases the concentration of divalent cations (i.e., $[Mg2+]_{1/2}$) required for *FD* = 0.5.

Supplemental Figure S8.1 .... **204**
Results of freely diffusing experiments conducted on the L5-mutant *env8*HyCbl construct. The L5-mutation (inset, underlined nucleotides) inhibits formation of the KL interaction, which prevents occlusion of the ribosome binding site (inset, shadowed nucleotides).

Figure 8.4 .... **206**
Time-dependent ensemble fluorometry. **a)** HyCbl binding quenches the fluorescence of Cy3 (Supplementary Figure S8.2). **b)** Elevated concentrations of ligand increases the rate constant for establishing equilibrium. **c)** A linear-fit to the [HyCbl]-dependence of

this rate constant is used to measure the apparent ligand binding ($^{app}k_{bind}$) and dissociation ($^{app}k_{diss}$) rate constants.

Supplemental Figure S8.2 .... **207**
The fluorescence lifetime (τ_{fluor}) of Cy 3 as determined from surface-immobilized riboswitches bound to (light green triangles) or free of (dark green circles) hydroxocobalamin (HyCbl).

Figure 8.5 .... **210**
Freely diffusing single-molecule burst titrations of hydroxocobalamin (HyCbl) at various concentrations of $MgCl_2$. **a)** At 0 mM Mg^{2+}, addition of ligand *does not* significantly influence distribution of FRET values associated with the L5-L13 regulatory switch. **b)** At intermediate concentrations of Mg^{2+}(e.g., 0.5, 1.0, and 2.5 mM), addition of HyCbl *does* significantly alter the FRET distributions. **c)** 20 mM Mg^{2+} is sufficient to completely form the L5-L13 KL interaction, irrespective of [HyCbl].

Figure 8.6 .... **211**
Experimental validation of the four-state kinetic model for the *env8*HyCbl riboswitch. The experimentally determined fractional occupancy of the docked conformation (FD, colored circles) is well described by the steady-state solution (dotted line) to the four-state model (Figure 8.2) over a wide range of Mg^{2+} and HyCbl concentrations.

Figure 8.7 .... **212**
Kissing-loop docking kinetics in the absence of bound ligand. Representative **a)** fluorescence and **b)** FRET time-trace from a surface immobilized *env8*HyCbl riboswitch. **c)** Rate constants are determined using both a dwell time analysis and a 2-state Bayesian maximum- likelihood model (orange line). **d)** Kinetic parameters are used to calculate the fractional occupancy of the docked conformation in the absence of HyCbl (FD_{free}), which reveals that the surface immobilized results are in accordance with the freely diffusing experiments.

Figure 8.7 .... **214**
Surface immobilized KL docking kinetics in the presence of hydroxocobalamin (HyCbl). **a)** Representative fluorescence trajectory from a surface immobilized molecule in the presence of 2.5 nM HyCbl. While in the undocked conformation, ligand binding (arrow) significantly diminishes the fluorescence intensity, which returns to normal after dissociation. **b)** When the ligand is not bound, the docking kinetics of the regulatory KL are experimentally indistinguishable from those in the absence of any HyCbl (Figure 8.7b). **c)** When the ligand is bound, a maximum-likelihood 2-state model (black line) is used to quantify the dwell times associated with the subtle fluctuations in acceptor fluorescence resulting from KL docking and undocking. A comparison between the two KL docking equilibria reveals that HyCbl binding significantly decreases the undocking rate constant (k_{undock}).

Supplemental Figure S8.3 .... **215**

Representative surface immobilized trajectories revealing the HyCbl-induced decrease in fluorescence intensity of both Cy3 (green squares) and Cy5 (pink circles). Inspection of trajectories reveals that HyCbl binding events (black arrows) can only occur when the RNA is in the *undocked* (low E_{FRET}) conformation. This is consistent with the assumptions of our 4-state kinetic model, whereby formation of the L5-L13 KL interactions prevents HyCbl binding/dissociation events. Only trajectories that exhibit clean fluctuations in acceptor fluorescence after a decrease in total fluorescence are considered for analysis. This constraint excludes molecules that have undergone other photophysical processes resulting in a decrease in fluorescence (e.g., blinking or bleaching).

Figure 8.9 .... **217**

Cell-based regulation of gene expression via the *env8*HyCbl riboswitch. **a)** Schematic diagram relating the four-state kinetic model to the regulation of gene expression *in vivo*. **b)** Histograms comparing the normalized fluorescence and relative GFPuv expression of cell cultures grown in the presence (bronze bars) or absence (grey bars) of 5000 nM HyCbl.

Chapter 1

Introduction

This chapter serves as a broad and general overview of the scientific experiments contained within this thesis. Chapter 2 provides a thorough and technical description of all of the experimental procedures required for each of the research topics contained herein. A more comprehensive and scientific summary of these projects can be found in their respective chapters (i.e., Chapter 3-8).

1.1 Nucleic Acids

Some of the most essential components of all living organisms are nucleic acids because of the fundamental role they play in the processes of life. Originally discovered in the 1860s (1), they are polymeric biomolecules comprised of chemically linked building blocks, called nucleotides (Figure 1.1). Each nucleotide consists of three components: (*i*) a cyclic 5-carbon sugar whose 5′ oxygen and 1′ carbon atoms are attached to (*ii*) a phosphate group and (*iii*) a nitrogenous base, respectively. These building blocks are linked together, forming a polymeric chain, by phosphodiester bonds between the sugar and phosphate moieties. One of the distinguishing characteristics among the various classes of nucleic acids is the type of sugar molecule. The presence or absence of a hydroxyl group (-OH) on the 2′ carbon of the ribose sugar differentiates between ribonucleotides and deoxyribonucleotides. Covalently linked together, these nucleotides form the two major types of nucleic acids—ribonucleic acid (RNA) and deoxyribonucleic acid (DNA). The vast majority of nucleic acids consist of sequentially linked nucleotides, each with one-of-four different nitrogenous bases—(*i*) Guanine (G), (*ii*) Cytosine, (*iii*) Adenine (A) and (*iv*) either Thymine (T) in DNA or Uracil (U) in RNA.

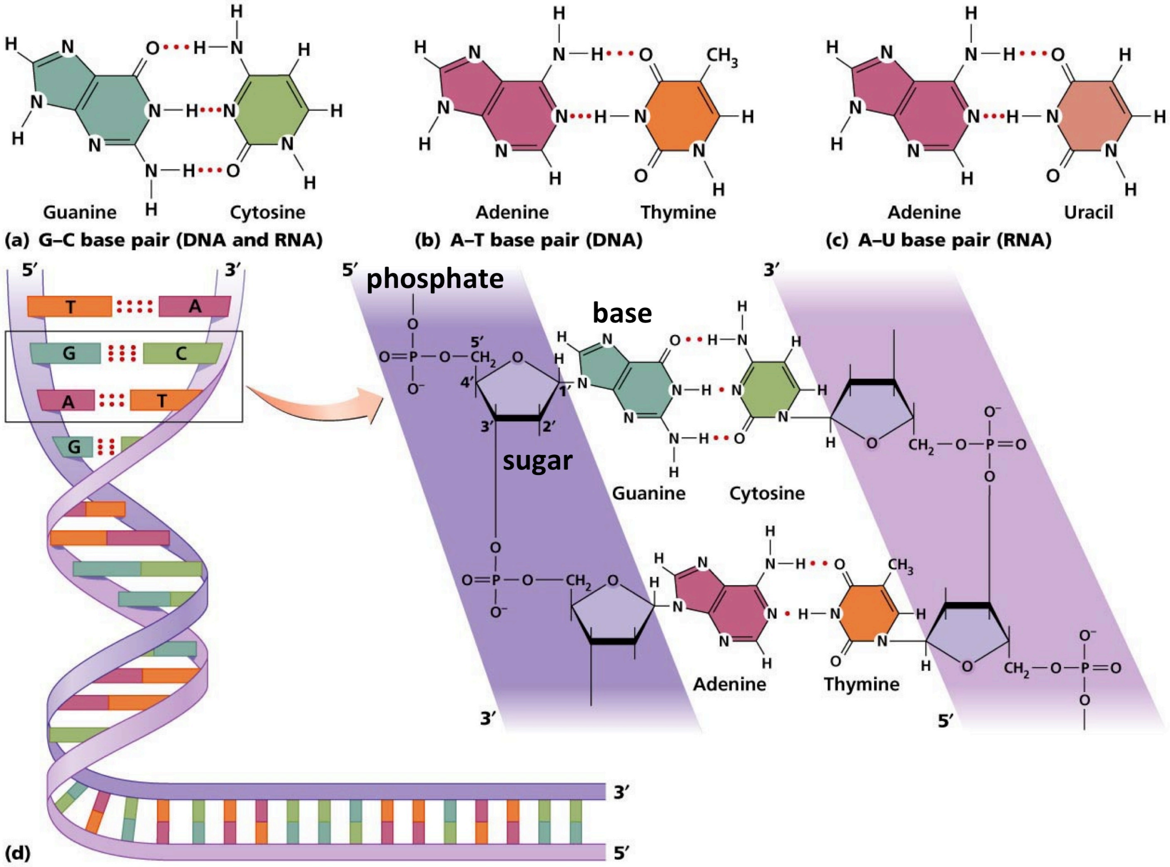

Figure 1.1 Structural components of a nucleic acid. **(a)** Hydrogen bonding pattern between pairs of guanine and cytosine nucleobases. **(b)** Hydrogen bonding pattern between pairs of adenine and thymine nucleobases in DNA. **(c)** Hydrogen bonding pattern between pairs of adenine and uracil nucleobases in RNA. **(d)** Schematic representation of the phosphate, sugar, and base constituents in the context of duplex deoxyribonucleic acid.

The specific sequential arrangement of nucleotides in DNA, typically written starting from the unlinked 5′ end of the polymer, constitutes the genetic code of all living organisms. The ability for DNA to compose the genetic code, or genome, is one of the most well known functions of nucleic acids(2). Living organisms are continually interpreting this warehouse of information in order to carry out the plethora of chemical tasks essential for life. Historically, it was thought that execution of a particular biological task is accomplished by creating an RNA-based copy (messenger RNA, mRNA) of a specific segment of the genome—a process called transcription(3). The function of this RNA molecule was to deliver the genetic message to a large biological machine, called the ribosome, which would construct the encoded protein—a process called translation. This linear transfer of genetic information is commonly referred to as the Central Dogma of Molecular Biology (Figure 1.2).

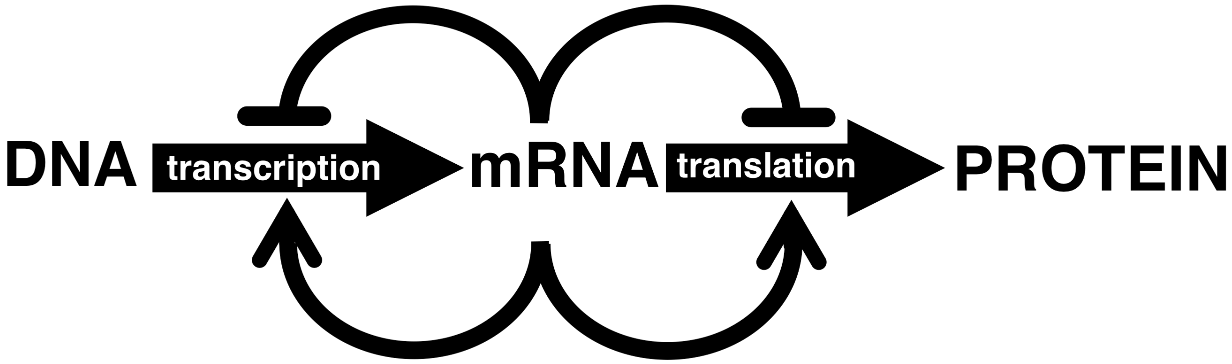

Figure 1.2 Central Dogma of Molecular Biology. Schematic representation of the linear transfer of genetic information in a cell. Pointed and blunted arrows represent some of the many ways that RNA can influence the processing of this genetic information.

For a number of years, it was thought that proteins were the molecular agents responsible for carrying out most biological tasks. However, over the past 60 years it has become increasingly apparent that this represents an oversimplified view of life. Nucleic acids, specifically RNAs, are capable of performing many biological processes(4).

As is commonly the case throughout all of biology, the function of a molecule is strongly influenced by its molecular structure, and nucleic acids are no exception. The functional diversity of nucleic acids arises almost completely from the diversity of nucleotide sequences, or primary (1°) structures available to nucleic acids. Nucleic acid secondary (2°) structure arises predominantly from intra- or intermolecular interactions among individual nucleotides. These 2° structural interactions are held together by favorable contacts between pairs of nucleotides.

Specifically, the nucleotides G and C are able to pair together in a precise orientation to form three favorable hydrogen-bonds, while the nucleotides A and T (or A and U in RNA) are able to pair and form two hydrogen-bonds (Figure 1.1). One of the results of base pairing is that two nucleic acids with complementary sequences, when oriented appropriately, are able to favorably interact with one another. This was beautifully demonstrated in 1953 with the discovery of the double helical structure of duplex (i.e., double stranded) DNA(5).

As opposed to the *intermolecular* 2° structure of duplex DNA (comprising all living genomes), the single stranded nature of RNA results in primarily *intramolecular* 2° structures. For any RNA molecule that is not perfectly self-complementary, intramolecular base pairing will result in structures that have regions of unpaired nucleotides that join together the double helical regions of paired nucleotides to form 2° structural elements like loops and junctions. One advantage of the unpaired junctions commonly found in RNAs is that they are more conformationally flexible than the paired regions. This allows formation of additional favorable intramolecular interactions (sometimes canonical base pairs) between individual 2° structural elements like loops. The interactions among elements of 2° structure result in the formation of tertiary (3°) structural elements (Figure 1.3). A single RNA polymer can simultaneously form many different 2° structural elements that can associate with each other in a complex network of 3°interactions. For an RNA of 130 nucleotides, there are $>10^{78}$ unique 1° structures (e.g., sequences). A single copy of each of the unique sequences would have a combined mass that is nearly identical to that of the observable universe (1.6×10^{55} g (6)). Some of these sequences would have the potential to form 2° and 3° interactions, each of which would result in a molecule with a slightly different molecular conformation. It is this diverse array of intricate three-dimensional structures that gives rise to localized, chemically diverse environments that have the potential to perform a myriad of useful biological functions.

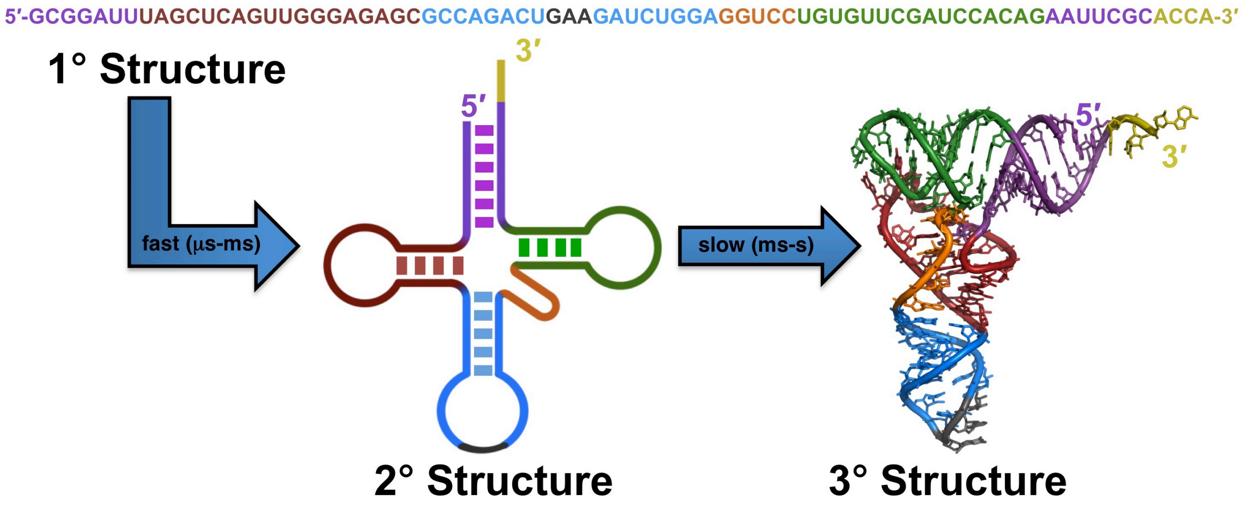

Figure 1.3 Hierarchical folding of RNA. Example depicts the major structural transitions associated with the formation of a tRNA molecule. Colors correspond to base paired regions within the oligonucleotide.

1.2 Nucleic Acid Conformational Transitions

It is important to mention that for all chemical reactions there is a characteristic time-scale associated with how long a particular species will exist before undergoing a chemical transformation. There are two general classes of nucleic acid chemical transformations, or conformational transitions, that are relevant to this thesis. The first is formation (or disruption) of 2° structures from 1°structures (Figure 1.3). Since these conformational transitions give rise to, or break apart, paired regions of nucleotides with a double helical structure, they are often referred to as duplex association/dissociation events. The second class of conformational transitions that pertain to this thesis is the formation (or disruption) of 3° structures from 2°structures (Figure 1.3). Because these types of transitions result from interactions between 2°structural elements (e.g., loops) they will be referred to as either loop docking/undocking events or sometimes more generally as folding/unfolding events. Of course, the time-scales associated with these structural transitions also influence the ability for the nucleic acid to have a useful biological function. Stated more explicitly, the biological function of a nucleic acid is influenced not only by its structure, but also by the dynamics of the relevant structure.

The five nucleic acid conformational transitions described in this thesis are as follows (Figure 1.4):

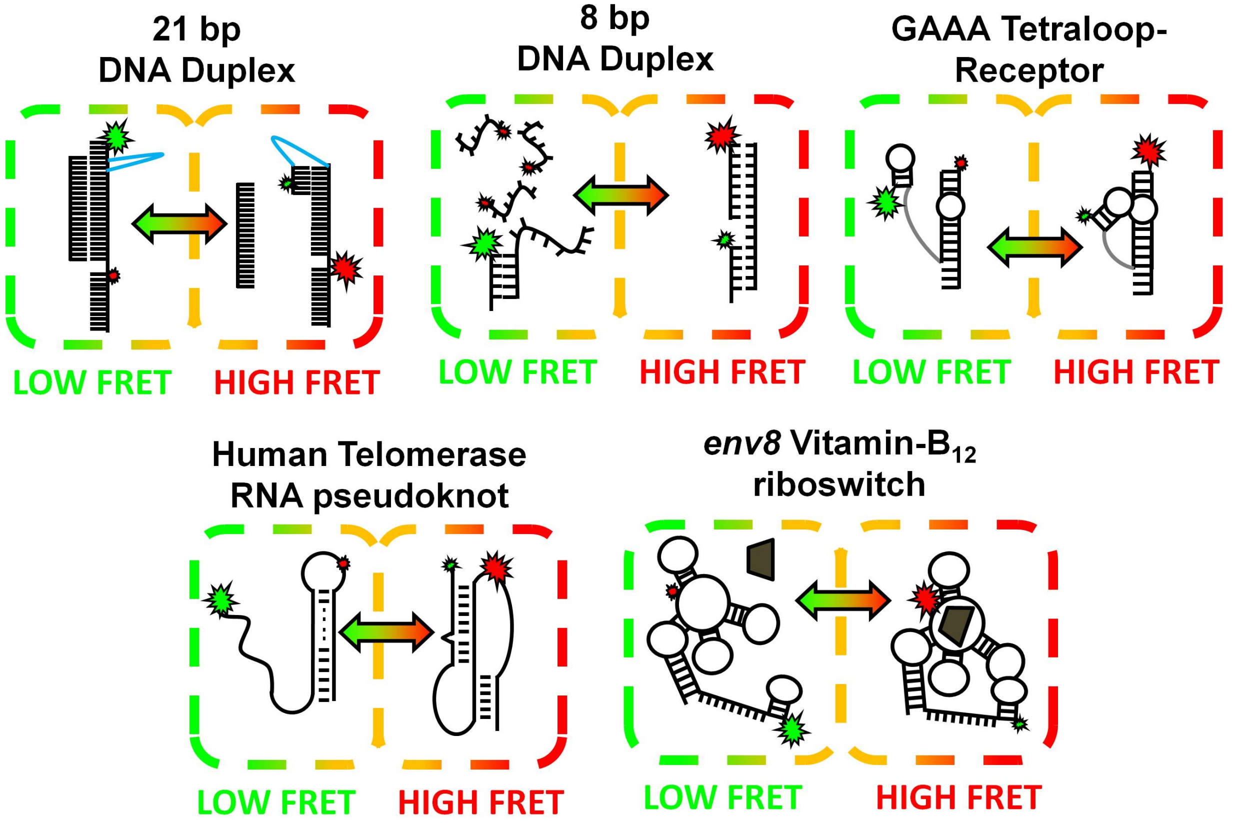

Figure 1.4 Cartoon graphics depicting the numerous oligonucleotide conformation transitions discussed in the chapters of this thesis.

(*i*) a 21 bp DNA duplex(7) that serves as a simple model system to understand the fundamentals of nucleic acid duplex association and dissociation, which has relevance in the field of microRNAs, (*ii*) an 8 bp DNA duplex inspired by the telomereic repeat sequence in the human genome which also serves as a model to better understand 2° structure formation(8) (*iii*) a ubiquitous 3° structural interaction from an RNA that aids in the maturation of pre-mRNAs—the

GAAA tetraloop-receptor from the *Tetrahymena* ribozyme(9), (*iv*) an isolated 3° structural element from an RNA that helps prevent damage from occurring at the ends of linear genomic DNA—the human telomerase RNA pseudoknot(10), and (*v*) an entirely functional element of some bacterial mRNAs with a 3° interaction that prevents translation by the ribosome—the *env8* vitamin-B_{12} riboswitch.

1.3 Cosolute-Influenced Nucleic Acid Conformational Transitions

One common feature of all nucleic acid conformational transitions, either *in vitro* or *in vivo*, is that the favorability (or stability) of the interactions and/or the time-scales associated with these structural changes are influenced by the presence of other cosolutes in solution(11). The most common cosolutes associated with nucleic acid conformational transitions are the biologically relevant alkali and alkaline earth salts of NaCl, KCl, $CaCl_2$ and $MgCl_2$. In aqueous solutions, these salts readily dissociate into their ionic components of either monovalent (i.e., K^+ or Na^+) or divalent (i.e., Ca^{2+} or Mg^{2+}) cations and monovalent anions (i.e., Cl^-). As cosolutes in a solution with dissolved ions, nucleic acids are able to interact with these charged species. Specifically, the negative charge associated with each phosphate in the backbone of a nucleic acid excludes proximal anions, which reduces the local concentration (12). The opposite is true for positively charged anions, which are accumulated near the nucleic acids, thus increasing the local concentration. This effectively neutralizes the high negative charge density of a nucleic acid. When nucleic acids undergo transitions to higher-order conformations, they tend to become more compact and as a result the molecule will have an increased negative charge density(13). Accordingly, additional cations or anions are accumulated or excluded from around the nucleic acid, respectively, so as to compensate for the increased negative charge density. Because of the greater positive charge density associated with higher valance cations (e.g., Mg^{2+} and Ca^{2+}), a smaller number of them need to be accumulated in order to accomplish the same degree of charge neutralization. This is partially responsible for lowering the cation concentrations required for half-maximal folding (i.e., $[M^{n+}]_{1/2}$) from ~ 100 mM for monovalent cations to ~ 1 mM for divalent cations and ~0.1 mM for trivalent cations(11). The influence of metal cations on nucleic acid conformational transitions is the topic of Chapter 5 in this thesis and covered extensively in an entire thesis from a former graduate student in the lab—Dr. Julie Fiore. Briefly, Chapter 5 describes how experiments were performed to obtain a better understanding of how monovalent cations facilitate formation of the GAAA tetraloop-receptor interaction from the *Tetrahymena* ribozyme(14).

Although metal cations are some of the most common cosolutes associated with nucleic acid conformational transitions, there are many others, including non-ionic organic molecules. The most commonly used cosolute to destabilize nucleic acid structures is the non-ionic organic osmolyte urea(15)(Figure 1.5). Osmolytes are highly soluble chemical compounds that can be used by cells to control osmotic pressure(16). High concentrations of urea are known to hinder formation of both 2° and 3° structures in both DNA and RNA(17). This is due to favorable dipole-driven base stacking and hydrogen bonding interactions between urea and the nucleobases (18) that can out compete the corresponding water-nucleobase interactions. Accordingly, urea tends to accumulate around the solvent accessible surface area (SASA) of these nitrogenous bases, which stabilizes any given nucleic acid structure. However, nucleic acid conformational transitions (e.g., duplex association) frequently decrease the amount of base SASA leading to the unfavorable expulsion of urea from the buried surfaces. This phenomenon results in a less effective stabilization of higher-order nucleic acid structures (i.e., 1° structure > 2° structure > 3°

structure). As a result, urea has a net *destabilizing* effect on more compact and folded conformations, relative to the more voluminous unfolded conformations.

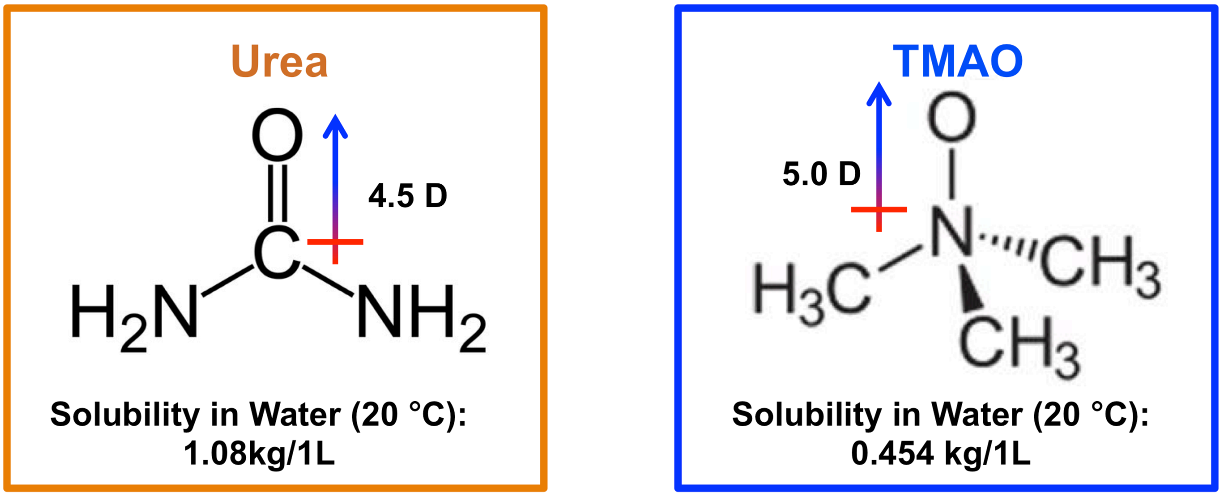

Figure 1.5 Chemical structures of two osmolytes known to significantly influence the conformational transitions of nucleic acids.

Surprisingly, there are other osmolytes, for example trimethylamine oxide (TMAO), that can *stabilize* nucleic acid conformational transitions (Figure 1.5). TMAO interacts unfavorably with the phosphate SASA of nucleic acids (19), and, although the details of this unfavorable interaction are not entirely understood, it is also likely related to the large dipole-moment of the molecule. However, unlike urea, the three methyl groups sterically impair dipole-driven interactions between TMAO and the phosphates, rendering this osmolyte as a less effective solvent than water. However, as mentioned earlier, conformational transitions responsible for the formation of 2° and 3° structures (e.g., loop docking) decrease the amount of SASA. Therefore, when an RNA becomes more compact, TMAO is ejected from the buried surfaces, which is energetically rewarding. As a result, TMAO is less detrimental to higher-order, more compact nucleic acid structures, leading to a net *stabilization*. The influence of both osmolytes—TMAO and urea—on nucleic acid conformational transitions represents the research topic of Chapter 6 in this thesis.

Additionally, the destabilizing ability of urea is used as a biochemical tool in Chapter 7 of this thesis to study how a two-nucleotide substitution mutation associated with a genetic disorder influences an RNA conformational transition required for proper biological activity of an enzyme—telomerase—that is highly associated with cancer(10). There are many other non-ionic organic molecules (e.g., molecular crowding agents like polyethelyne glycol and viscous agents like glycerol) that non-specifically influence nucleic acid conformational transitions. The reports of these investigations have been published in peer-reviewed journals in conjunction with another Nesbitt group member, Nick Dupuis, as first author and thus are not included in this thesis.

Contrary to the non-specific effects of all of the cosolutes described above, certain nucleic acid conformational transitions are known to be particularly sensitive to specific cosolutes. The specificity of the interaction is achieved by precise intermolecular contacts between discrete functional groups on the cosolute and nucleic acid. Because of the specificity associated with this class of cosolute-nucleic acid interactions, the cosolutes are often referred to as biochemical ligands, in that they are substances that complex with, or are bound by, biomolecules to produce a chemical response. Some nucleic acids that contain these cosolute-specific conformational transitions have been employed by nature to act as molecular switches capable of changing their biochemical function upon ligand binding. This switch of biochemical function is most frequently accomplished by ligand-induced conformational transitions. Some of the most well known examples of ligand-induced conformational transitions in nucleic acids are found in riboswitches(20, 21). Riboswitches are structural elements genetically encoded at the beginning of mRNAs that modulate expression of a downstream gene via ligand-dependent conformational changes. The modulation of gene expression can occur by prematurely terminating the transcription of the mRNA, or by an inability of the ribosome to initiate translation of the mRNA. Chapter 8 in this thesis describes the study of a translational riboswitch that, upon binding vitamin B_{12}, prevents expression of downstream genes.

This thesis covers a number of cosolute-influenced nucleic acid conformational transitions. These reports vary both in terms of the type of conformational transition investigated and the identity of the cosolutes. As a compilation of six scientific publications, this document provides a detailed review of the numerous ways in which these conformational transitions are influenced by the presence of aqueous cosolutes.

1.4 Single-Molecule Fluorescence

Because of the small size of molecules, most biochemical experiments are performed at the ensemble level by studying billions of molecules simultaneously. These types of experiments have been extremely useful for unveiling numerous details about a number of cosolute-influenced nucleic acid conformational transitions. For years, temperature-dependent ultraviolet/visible spectroscopy and circular dichroism have been used to investigate the stability of various nucleic acids in the presence of a diverse array of cosolutes. However, these experiments are unable to provide detailed information about the time-scales (i.e., kinetics) of the conformational transitions because the billions of molecules are all changing conformations at random times. In order for ensemble techniques to obtain useful kinetic information, the molecules must be synchronized so that all of the nucleic acids undergo conformational transitions at the same time. Molecular synchronization is most frequently accomplished by watching a sample return to equilibrium after rapid heating/cooling or in the case of cosolute-influenced conformational transitions, rapid mixing. These synchronized experiments often require various assumptions about which processes are fast, relative to others, in order to yield meaningful kinetic information. Another assumption that is intrinsic to ensemble experiments is that the billions of molecules in an experiment are identical, and thus statistically behave exactly the same. This set of constraints can be nullified by watching individual molecules undergo discrete chemical transformations—a concept frequently quoted as being "every chemist's dream."

The path towards realization of this dream started nearly a quarter-century ago with the observation of absorption(22, 23) and fluorescence(24) from single molecules in a cryogenic crystal. Over the past 25 years, single-molecule fluorescence techniques have greatly improved due to more powerful lasers, better microscope objectives, higher efficiency detectors, and brighter fluorophores. These advancements have made direct observation of single molecules much more attainable.

Of the many fluorescence methods that can be extended to the single-molecule level, this thesis exploits the power of Förster Resonance Energy Transfer (FRET)(25-27) to observe single nucleic acids undergo cosolute-influenced conformational transitions in real-time. In 1948, Theodore Förster was the first to correctly define the physics behind the process of FRET(28), which describes the transfer of energy between two molecular species that absorb light (i.e., chromophores). Most commonly, and of particular relevance to this thesis, these chromophores also emit light (i.e., fluorophores). After absorbing a photon of a specific color, the electronic arrangement of a ground state molecule is altered to a higher-energy excited configuration. In the *absence* of an acceptor fluorophore, the excited donor will relax back down to the ground state electronic configuration and, in the process, potentially give off a photon(29). However, in the *presence* of an acceptor fluorophore, the excited donor can, instead, transfer the excess energy associated with this excited electronic configuration to an acceptor via near-field nonradiative dipole-dipole coupling. After an energy transfer event, the newly-excited acceptor fluorophore will, just like the donor, relax back down to the ground state electronic arrangement and potentially emit a photon.

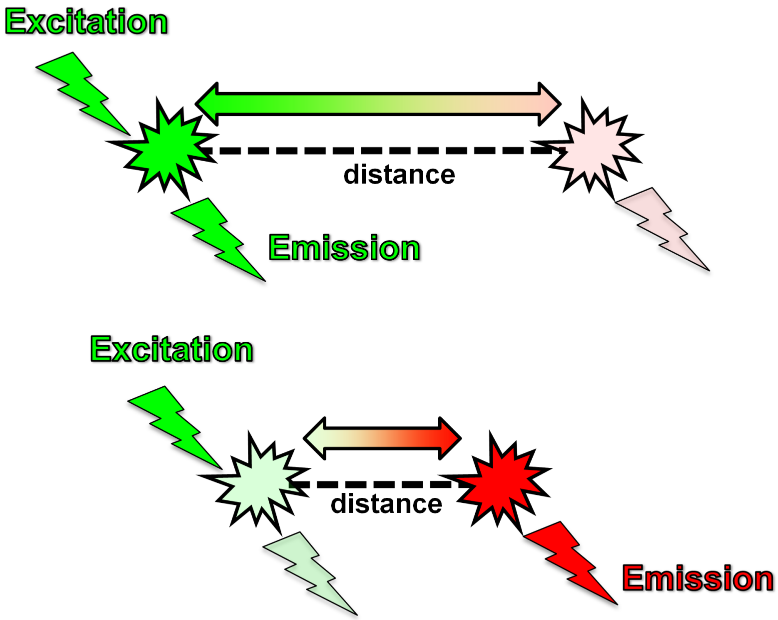

Figure 1.6 Fluorescence Resonance Energy Transfer (FRET). An excited donor fluorophore (green) can transfer energy to a nearby acceptor fluorophore (red) in a distance-dependent process. When the donor and acceptor are proximal, energy transfer is efficient; when they are distal, energy transfer is poor.

The efficiency of FRET (E_{FRET}) can readily be determined by observing the ratio of acceptor fluorescence to total fluorescence (i.e., donor plus acceptor). The physics of this energy transfer process dictate that the E_{FRET} is inversely related to the sixth-power of the distance between the donor and acceptor fluorophores. The effective distance scale for FRET depends on the spectral properties of the fluorophores and ranges between 10-100 Å(30). Conveniently, this is also the distance scale associated with the change in molecular dimensions for many nucleic acid conformational transitions. For any FRET fluorophore pair (i.e., donor-acceptor pair), conformational transitions that decrease the donor-acceptor distance result in an increase in E_{FRET} (Figure 1.6), as determined by a decrease in donor fluorescence and a corresponding increase in acceptor fluorescence.

My general strategy for all of the single-molecules studies described within this thesis can be summarized using the following three steps: (*i*) First, donor and acceptor fluorophores must cleverly and nonperturbatively attach to the nucleic acid of interest(31). (*ii*) Then, a single-molecule fluorescence microscope with a high numerical aperture objective can be used to excite and collect the fluorescence from single donor and acceptor labeled nucleic acid. When combined together, single-molecule fluorescence techniques and FRET (smFRET) make it possible to watch the donor-acceptor distance of individual nucleic acids change, as a result of conformation transitions, in real-time. (*iii*) Finally, cosolutes can easily be added into the experimental solutions to readily interrogate the influence of these species on the kinetics and dynamics of nucleic acid conformational transitions.

Although smFRET is a useful experimental technique to observe the kinetics of conformational transitions in nucleic acids, it can be even more informative when combined with the ability to precisely control the temperature at which experiments are performed(7, 14, 32-34). This provides the ability to understand various *thermodynamic* aspects of nucleic acid conformational transitions. This topic is the research topic of Chapter 3 in this thesis, which describes the development of a specialized heating technique using focused infrared laser light(34). Furthermore, Chapter 4 provides a detailed characterization of the aforementioned heating technique and demonstrates how it can be utilized to probe the dissociation of a 21 base pair DNA double helix(7).

In conclusion, this document describes a highly interdisciplinary collection of rigorous and quantitative physical chemistry experiments performed on a diverse array of nucleic acids. These single-molecule investigations explore the effects of various different aqueous cosolutes on the conformational transitions associated with these biomolecules. The results of these undertakings provide a more fundamental understanding of the numerous scientific concepts related to each of the six chapters. As a whole, the conclusions contain within this body of work provide the scientific community with a holistic foundation for understanding cosolute-influenced conformational transitions that can be expanded to include complex solutions such as those associated with living cells. One day, these fundaments idea might influence the way we address pressing societal issues, particularly those related to human health and wellbeing.

1.5 References

1. Dahm, R. Discovering DNA: Friedrich Miescher and the early years of nucleic acid research, *Hum. Genet.*, **2008,** *122*, 565-581.

2. Voet, D.; J. G. Voet (2011) *Biochemistry*, 4th ed., John Wiley & Sons, Hoboken, NJ.

3. Crick, F. Central dogma of molecular biology, *Nature*, **1970,** *227*, 561-563.

4. Silverman, S. K. (2006) *Nucleic acid switches and sensors*, Landes Bioscience/Eurekah.com and Springer Science+Business Media, Georgetown, TX and New York, NY.

5. Watson, J. D.; F. H. Crick. Molecular structure of nucleic acids: a structure for deoxyribose nucleic acid, *Nature*, **1953,** *171*, 737-738.

6. Carvalho, J. C. Derivation of the mass of the observable universe, *Int. J. Theor. Phys.*, **1995,** *34*, 2507-2509.

7. Holmstrom, E. D.; N. F. Dupuis; D. J. Nesbitt. Pulsed IR heating studies of single-molecule DNA duplex dissociation kinetics and thermodynamics, *Biophys. J.*, **2014,** *106*, 220-231.

8. Dupuis, N. F.; E. D. Holmstrom; D. J. Nesbitt. Single-Molecule Kinetics Reveal Cation-Promoted DNA Duplex Formation Through Ordering of Single-Stranded Helices, *Biophys. J.*, **2013,** *105*, 756-766.

9. Hodak, J. H.; C. D. Downey; J. L. Fiore; A. Pardi; D. J. Nesbitt. Docking kinetics and equilibrium of a GAAA tetraloop-receptor motif probed by single-molecule FRET, *Proc. Natl. Acad. Sci. USA*, **2005,** *102*, 10505–10510.

10. Holmstrom, E. D.; D. J. Nesbitt. Single Molecule FRET Studies of the Human Telomerase RNA Pseudoknot: Temperature/Urea Dependent Folding Kinetics and Thermodynamics, *J. Phys. Chem. B.*, **2014**.

11. Fiore, J. L.; E. D. Holmstrom; L. R. Fiegland; J. H. Hodak; D. J. Nesbitt. The Role of Counterion Valence and Size in GAAA Tetraloop-Receptor Docking/Undocking Kinetics, *J. Mol. Biol.*, **2012**.

12. Draper, D. E.; D. Grilley; A. M. Soto. Ions and RNA folding, *Annu. Rev. Biophys. Biomolec. Struct.*, **2005,** *34*, 221–243.

13. Leipply, D.; D. Lambert; D. E. Draper. Ion-RNA interactions: Thermodynamic analysis of the effects of mono- and divalent ions on RNA conformational equilibria, *Methods Enzymol.*, **2009,** *469*, 433-463.

14. Holmstrom, E. D.; J. L. Fiore; D. J. Nesbitt. Thermodynamic origins of monovalent facilitated RNA folding, *Biochemistry*, **2012,** *51*, 3732-3743.

15. Shelton, V. M.; T. R. Sosnick; T. Pan. Applicability of Urea in the Thermodynamic Analysis of Secondary and Tertiary RNA Folding, *Biochemistry*, **1999,** *38*, 16831-16839.

16. Lambert, D.; D. E. Draper. Effects of Osmolytes on RNA Secondary and Tertiary Structure Stabilities and RNA-Mg^{2+} Interactions, *J. Mol. Biol.*, **2007,** *370*, 993-1005.

17. Lambert, D.; D. E. Draper. Denaturation of RNA secondary and tertiary structure by urea: simple unfolded state models and free energy parameters account for measured m-values, *Biochemistry*, **2012,** *51*, 9014-9026.

18. Priyakumar, U. D.; C. Hyeon; D. Thirumalai; A. D. MacKerell. Urea Destabilizes RNA by Forming Stacking Interactions and Multiple Hydrogen Bonds with Nucleic Acid Bases, *J. Am. Chem. Soc.*, **2009,** *131*, 17759-17761.

19. Lambert, D.; D. Leipply; D. E. Draper. The osmolyte TMAO stabilizes native RNA tertiary structures in the absence of Mg^{2+}: Evidence for a large barrier to folding from phosphate dehydration, *J. Mol. Biol.*, **2010,** *404*, 138-157.

20. Breaker, R. R. Riboswitches and the RNA world, *Cold Spring Harb. Perspect. Biol.*, **2012,** *4*.

21. Garst, A. D.; A. L. Edwards; R. T. Batey. Riboswitches: structures and mechanisms, *Cold Spring Harb. Perspect. Biol.*, **2011,** *3*.

22. Kador, L.; D. E. Horne; W. E. Moerner. Optical-Detection and Probing of Single Dopant Molecules of Pentacene in a P-Terphenyl Host Crystal by Means of Absorption-Spectroscopy, *J. Phys. Chem.*, **1990,** *94*, 1237-1248.

23. Moerner, W. E.; L. Kador. Optical-Detection and Spectroscopy of Single Molecules in a Solid, *Phys. Rev. Lett.*, **1989,** *62*, 2535-2538.

24. Orrit, M.; J. Bernard. Single pentacene molecules detected by fluorescence excitation in a p-terphenyl crystal, *Phys. Rev. Lett.*, **1990,** *65*, 2716-2719.

25. Joo, C.; H. Balci; Y. Ishitsuka; C. Buranachai; T. Ha. Advances in single-molecule fluorescence methods for molecular biology, *Annu. Rev. Biochem.*, **2008,** *77*, 51-76.

26. Roy, R.; S. Hohng; T. Ha. A Practical Guide to Single-Molecule FRET, *Nat. Methods*, **2008,** *5*, 507-516.

27. Zhao, R.; D. Rueda. RNA folding dynamics by single-molecule fluorescence resonance energy transfer, *Methods*, **2009,** *49*, 112-117.

28. Förster, T. Zwischenmolekulare Energiewanderung und Fluoreszenz, **1948,** *437*, 55-75.

29. Einstein, A. Strahlungs-Emission und -Absorption nach der Quantentheorie, *Deutch. Phys. Ges.*, **1916,** *18*, 318-323.

30. Schuler, B.; E. A. Lipman; P. J. Steinbach; M. Kumke; W. A. Eaton. Polyproline and the "spectroscopic ruler" revisited with single-molecule fluorescence, *Proc. Natl. Acad. Sci. USA*, **2005,** *102*, 2754-2759.

31. Akiyama, B. M.; M. D. Stone. Assembly of Complex RNAs by Splinted Ligation, *Methods Enzymol.*, **2009,** *469*, 27-46.

32. Fiore, J. L.; E. D. Holmstrom; D. J. Nesbitt. Entropic Origin of Mg^{2+}-Facilitated RNA Folding, *Proc. Natl. Acad. Sci. USA*, **2012,** *109*, 2902-2907.

33. Fiore, J. L.; B. Kraemer; F. Koberling; R. Erdmann; D. J. Nesbitt. Enthalpy-Driven RNA Folding: Single-Molecule Thermodynamics of Tetraloop–Receptor Tertiary Interaction, *Biochemistry*, **2009,** *48*, 2550–2558.

34. Holmstrom, E. D.; D. J. Nesbitt. Real-time infrared overtone laser control of temperature in picoliter H_2O samples: "Nanobathtubs" for single-molecule microscopy, *J. Phys. Chem. Lett.*, **2010,** *1*, 2264–2268.

Chapter 2

Experimental Methods

Each scientific discipline has its own set of tools that are frequently used to investigate experimental problems. A single-molecule fluorescence microscopy tool kit is required for the vast majority of the scientific research described in this thesis. This chapter provides a detailed description of most of the experimental techniques and fundamental scientific concepts that have been used to generate the contents of this work.

2.1 Experimental Observation

Nearly every scientific experiment requires some form of observable that can be monitored to confirm or reject a particular hypothesis. A detailed and rigorous understanding of this necessity is essential for an objective interpretation of the experimental outcome. As mentioned previously, fluorescence is the preferred method of detection for most of the work described in this thesis.

2.1.1 Molecular Fluorescence

Molecular fluorescence is a useful physical phenomenon in that it provides the experimenter with the ability to very nearly observe chemical processes. Most generally, fluorescence refers to the emission of light from a substance (e.g., molecule) that has absorbed some form of electromagnetic radiation. This rather simple definition contains two profound scientific processes—absorption and emission—that have been studied by many of the great intellectuals of the past two centuries, perhaps most notably Albert Einstein(1). Absorption is a process that describes the interaction between light and matter, whereby the energy of an absorbed photon ($E_{\text{photon}} = hc/\lambda$) is transferred to the interacting matter (e.g., molecule). The efficiency of this process is dictated by the physical properties of both the light, as well as, the matter and is characterized by a parameter called the absorption cross section (σ). This can be thought of as a nanoscopic area presented by the molecule to the photons, where the zero-dimensional particles of light can only be described in terms of the average number of particles per area. Absorbing a photon becomes more likely as the number of them occupying this molecular cross section increases. The energy of the absorbed photon can be used to rearrange the electronic configuration of the molecule to energetically excited state.

Radiative relaxation occurs when an excited state molecule returns to the ground state and, in the process, emits lights. The energetic difference between these two states dictates the energy content (i.e., color) of the emitted photon—higher energy photons are blue, low energy photons are red. If this is the only available relaxation pathway to the ground state, then every single absorbed photon will give rise to an emitted photon, resulting in a quantum efficiency (Φ) of unity. However, there is another competing parallel pathway—*non*-radiative relaxation—that allows excited state molecules to return to the ground state *without* emitting a photon. In this process, the absorbed energy is released as heat, as opposed to a particle of light, which results in Φs of less than one. The Φ can also be defined by the rate constants associated with all of the excited-state processes in the molecule (Eq. 2.1), where k_{rad} is the spontaneous rate constant for radiative relaxation (emission) and $k_{nrad,i}$ is the rate constant for any of a number of non-radiative (i.e., non-emissive) relaxation processes.

$$\Phi = \frac{k_{rad}}{k_{rad} + \sum_i k_{nrad,i}} \qquad \text{(Eq. 2.1)}$$

The rate constants can be used to characterize the excited-state fluorescence lifetime ($\tau_{fluorescence}$, Eq. 2.2), which defines the average duration a molecule spends in the excited state (e.g., S_1) before returning to the ground state either though radiative or non-radiative relaxation.

$$\tau_{fluorescence} = \frac{1}{k_{rad} + \sum_i k_{nrad,i}} \qquad \text{(Eq. 2.2)}$$

These processes, and their associated time-scales, can be summarized in a Jablonski diagram (Figure 2.1).

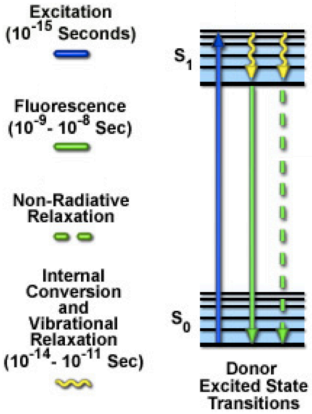

Figure 2.1 Jablonski energy level diagram depicting absorption (excitation) and emission (fluorescence) of photons.(http://www.microscopyu.com/articles/fluorescence/fret/fretintro.html)

For most molecules in nature, non-radiative processes dominate their radiative counterparts, giving rise to negligible Φs; it is only a very specific sub-set of molecules (i.e., fluorophores) with the right properties (i.e., large σ and high Φ) that have significant fluorescence. Examples of organic fluorophores that are of direct relevance to this work are the cyanine (e.g., Cy3 and Cy5) and rhodamine (e.g., RhoB, and Rho6G) dyes. The relevant photophysical properties (σ, $\tau_{fluorescence}$, Φ, k_{rad}) of these molecules are summarized in Table 2.1. Because the fundamentals of fluorescence are well understood, these fluorophores can be attached, or coupled, to nucleic acids to probe specific characteristics of the labeled system. For example, one could attach a cyanine dye to a fictitious RNA of interest to determine where it is located within a cell.

fluorophore	**absorption maximum (λ_{max}) nm**	**cross section (σ) at λ_{max} cm^2**	**fluorescence lifetime ($\tau_{fluoresence}$) ns**	**quantum yield (ϕ)**	**radiative rate constant ($k_{radiative}$) ns^{-1}**
Cy3-DNA*	550	5.7×10^{-16}	1.4	0.30	0.21
Cy5	650	9.5×10^{-16}	1.0	0.28	0.28
Rhodamine B	545	4.0×10^{-16}	1.74	0.33	0.19
Rhodamine 6G	530	4.4×10^{-16}	4.08	0.90	0.22

Table 2.1 Table of approximate photophysical properties associated with four fluorophores commonly used throughout this thesis. All reported values are for free dye molecules in buffered aqueous solutions, expect for Cy3-DNA*, where the conjugation to a nucleic acid significantly increases the quantum yield and fluorescence lifetime of the fluorophore.

2.1.2 Forster Resonance Energy Transfer (FRET)

Indeed, fluorescence itself is a useful tool for locating the spatial position of a molecule. However, in order to use this process as a read-out for questions more sophisticated than those related to location, changes in fluorescence properties must be measured. Most frequently these changes are related to the above photophysical parameters (Table 2.1); of particular relevance to this work are changes in the $\tau_{fluorescence}$. The previous examples of non-radiative relaxation were all *intramolecular* processes, however *intermolecular* processes can also significantly influence the $\tau_{fluorescence}$ of a dye. One example of this is Forster (sometimes Fluorescence) Resonance Energy Transfer (FRET). This phenomenon describes the non-radiative (i.e., non-emissive) transfer of energy from an energetically excited donor molecule to a neighboring acceptor molecule via near-field dipole-dipole coupling. The rate constant for this energy transfer process is dependent on a number of physical parameters (Eq. 2.3): (*i*) the relative orientation of the two interacting dipoles (κ^2), (*ii*) distance between the donor and acceptor fluorophores (r), (*iii*) the spontaneous rate constant for emission associated with the donor ($k_{rad,D}$), (*iv*) the spectral overlap integral between the emission spectrum of the donor and the molar extinction spectrum of the acceptor (J), the index of refraction (n) of the medium containing the two fluorophores (typically water n = 1.33), and Avagadro's Number (N_A).

$$k_{FRET} = \frac{9\, k_{rad,D}(\ln 10)\kappa^2 J}{128\, \pi^5 n^4 r^6 N_A} \qquad \text{(Eq. 2.3)}$$

The orientation factor, κ^2, is defined using Eq. 2.4,

$$\kappa^2 = \left(\cos\theta_t - 3\cos\theta_d\cos\theta_a\right)^2 \qquad \text{(Eq. 2.4)}$$

where θ_t is the dihedral angle between the two planes associated with the transition dipole moments of the donor emission and the acceptor absorption, and θ_d and θ_a are the angles between the line-of-centers connecting the two fluorophores and the donor emission and acceptor absorption transition dipole moments, respectively. This value can range from 0 to 4 depending upon the relative orientation of the coupled dipoles(2). A value of 2/3 is often used, which assumes that the time-averaged orientation of the two fluorophores isotropic. This assumption, while generally quite sound, starts to break down for slowly rotating dipoles, like fluorescent proteins, and can be completely invalid for fixed, or oriented, dipoles.

The efficiency of energy transfer from the donor to the acceptor (E_{FRET}) can be calculated (Eq. 2.5) in a similar fashion to the quantum efficiency (Eq. 2.1).

$$E_{FRET} = \frac{k_{FRET}}{k_{rad,D} + k_{FRET} + \sum_i k_{nrad,D,i}} \qquad \text{(Eq. 2.5)}$$

In certain systems, the presence of an acceptor can significantly decrease (i.e., quench) the $\tau_{fluorescence}$ and Φ of the donor fluorescent dye. However, if the acceptor is also a fluorophore, the loss of donor fluorescence due to energy transfer is conveniently offset by the resulting generation of excited-state acceptor fluorophores that can undergo typical spontaneous emission.

Again, a Jablonski diagram can be used to schematically illustrate the details of this process (Figure 2.2).

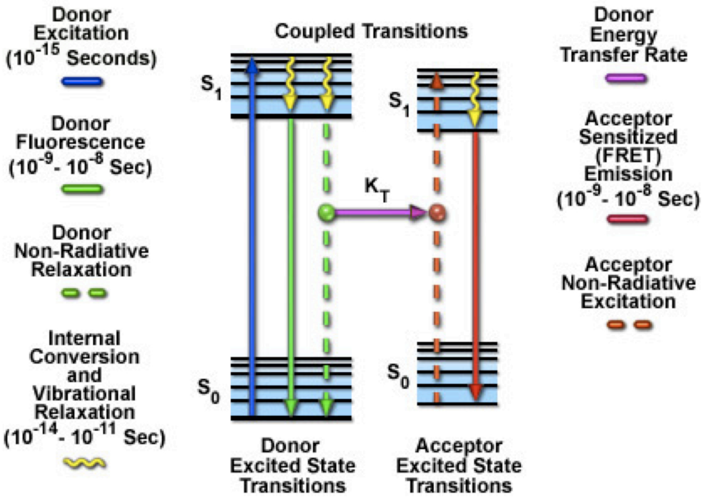

Figure 2.2 Jablonski energy level diagram depicting Fluorescence Resonance Energy Transfer (FRET). (http://www.microscopyu.com/articles/fluorescence/fret/fretintro.html)

The distance-dependence of FRET allows it to be used as a semi-quantitative ruler to measure distances of approximately 10-100 Å. For the Cy3-Cy5 donor-acceptor FRET pair used exclusively throughout this thesis, the distance corresponding to half-maximal E_{FRET} (R_0) is approximately 53 Å; when the donor and acceptor are proximal (i.e., $r < R_0$) E_{FRET} is high, when they are distal (i.e., $r > R_0$) E_{FRET} is low (Eq. 2.6).

$$E_{FRET} = \frac{R_o^6}{R_o^6 + r^6} \qquad \text{(Eq. 2.6)}$$

By attaching a FRET pair to a molecule of interest, not only can you determine its spatial location, but you can also determine the distance between the two fluorophores, which provides structural or conformational information about the molecule (Figure 2.3). Analogous to the example mentioned above, a fictitious FRET-labeled RNA within a cell may, perhaps, reveal that the molecules are in a closed structure (high E_{FRET}) in some areas of the cell and an open one (low E_{FRET}) in other areas.

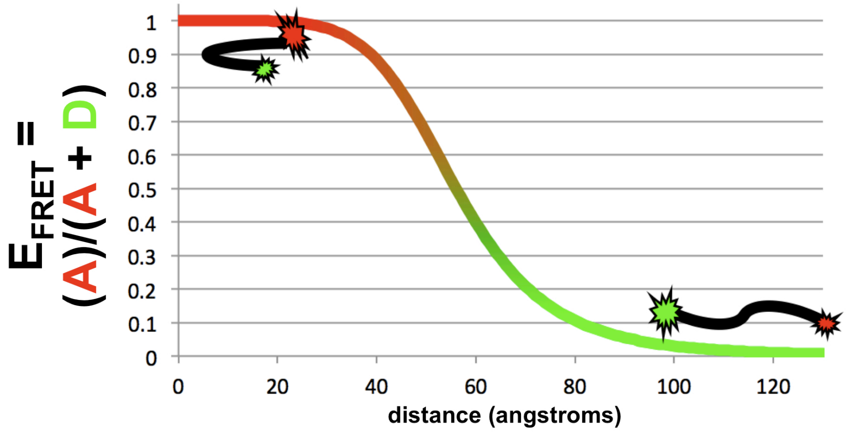

Figure 2.3 Distance dependence of FRET efficiency (E_{FRET}) for a fictitious biological molecule. Separation of the donor and acceptor fluorophores results in less efficient energy transfer.

2.2 Single-Molecule Confocal Microscope

Of course, the fluorescently labeled molecules are thousands of times smaller than the width of a human hair. A home-built single-molecule confocal fluorescence microscope is used to facilitate observation of these tiny objects (Figure 2.4). The experimental system was first built and characterized by a previous postdoctoral researcher in the lab (Dr. Jose Hodak), with some additional assistance from my former graduate student mentor (Dr. Julie Fiore). Details of the experimental apparatus are contained in this section (2.2) of the thesis; the thesis of Dr. Julie Fiore is also an excellent resource(3).

2.2.1 Excitation Path

The entire microscope system has been optimized for the use of the Cy3-Cy5 FRET pair, starting with the excitation source. A 532 nm (green) frequency doubled Nd:YAG laser is used to excite donor (Cy3) fluorophores. This excitation source was chosen to facilitate spectral filtering of excitation light (532 nm) and Cy3 emission ($\lambda_{max} \approx 570$ nm). The excitation source is pulsed at 20 MHz with a pulse width of ≈ 10 ps to enable the use of time-correlated single-photon counting techniques (TCSPC, see section 2.2.4). A half wave plate (λ/2) and broadband polarizing beam splitter are used to attenuate the laser power and ensure complete polarization of the laser output. The 1 mm intensity diameter ($1/e^2$) of the Gaussian laser beam is expanded to 12 mm using a Keplerian telescope containing lenses with focal lengths of f_1 = 25 mm and f_2 = 300 mm, respectively. A former graduate student—Dr. Tom Baker—provides a great description of proper techniques associated with measuring beam diameters in the experimental chapter of his thesis(4).

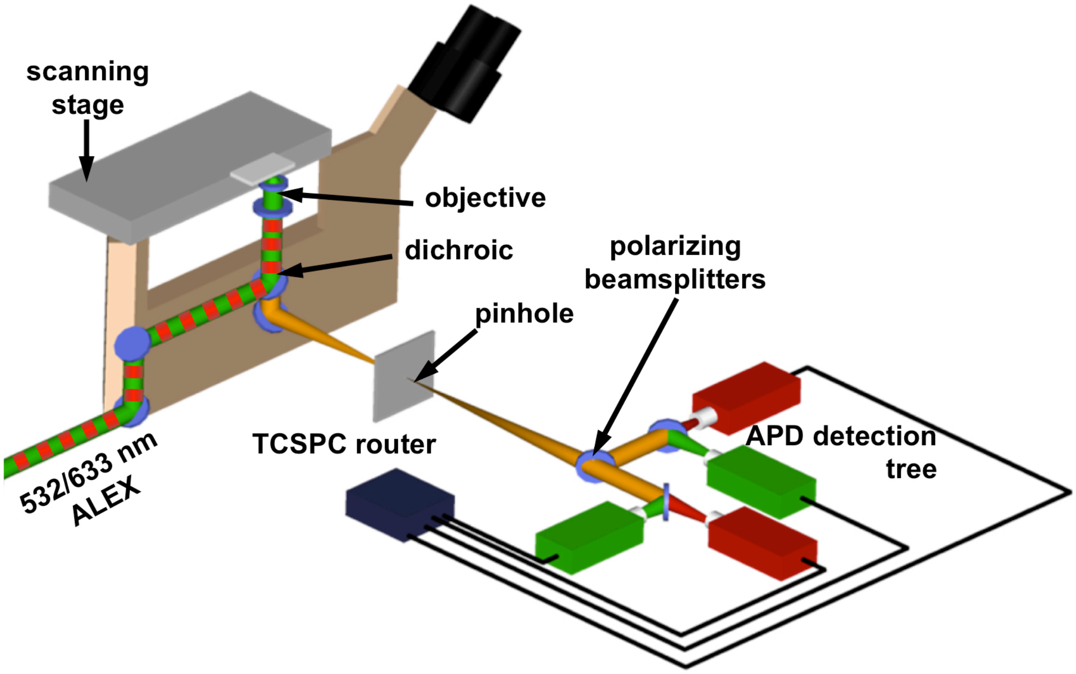

Figure 2.4 Cartoon cut-away diagram of the single-molecule microscope system used to conduct the research associated with this thesis.

Each green laser pulse triggers a red laser pulse from a 635 nm (red) laser diode (< 100 ps pulse FWHM) with an approximately 25 ns delay determined by the length of BNC cable between the two laser controllers. The time-delay and repetition rate of the two light sources result in almost perfectly interleaved laser pulses. The incorporation of a red excitation source to the experimental apparatus provides the ability to directly excite both donor and acceptor fluorophores via Alternating Laser EXcitation (ALEX)(5-8), which ensures that biomolecules contain both donor and acceptor fluorophores. The red laser (635 nm) is used to efficiently excite Cy5 ($\lambda_{\max} \approx 650$ nm), while still being easy to spectrally filter from both Cy3 ($\lambda_{\max} \approx 570$ nm) and Cy5 ($\lambda_{\max} \approx 670$ nm) fluorescence. The output of the red laser is directly coupled into a single-mode fiber-optic cable to clean up the beam shape, as suggested by the manufacturer. The light exits the cable via a beam collimator resulting in an intensity diameter ($1/e^2$) of ≈ 10 mm. The red and green laser beams are spatially overlapped using a dichroic mirror that transmits the green and reflects the red light. The two beams pass through a set of broadband neutral density filters to attenuate the optical power before being directed into the back port of an Olympus IX70 inverted microscope base.

2.2.2 Microscope and Sample Stage

Once the red and green beams are inside the microscope, they are reflected upward towards the back aperture ($d_{\text{aperture}} = 9.25$ mm) of the 1.2 N.A. water objective (UPLSAPO 60XW) via a custom 2-color dichroic mirror designed specifically to only reflect light from the two excitation sources (Di01-R532/635, Semrock, Inc). Because both the red and green beams sufficiently overfill (i.e., intensity diameter ($1/e^2$) > d_{aperture}) the back aperture, the optical elements within the objective can effectively focus the light to a single diffraction-limited Airy feature (Figure 2.5) at a working distance of 280 μm. The spatially dependent intensity of the Airy feature can be expressed via Eq. 2.7, where J_1 is a first-order Bessel function of the first kind, r is the radius from the optical axis, λ is the wavelength of light, and *N.A.* is the numerical aperture the optical system.

$$\frac{I(x)}{I_0} = \left(\frac{2J_1(x)}{x}\right)^2, \quad x \approx \frac{2\pi r N.A.}{n\,\lambda} \qquad \text{(Eq. 2.7)}$$

Accordingly, the radius that corresponds to the first zero of the Airy feature (r_{Airy}) is approximately equal to $0.61n\lambda/\text{N.A.}$, which corresponds to ≈ 360 nm for the present apparatus.

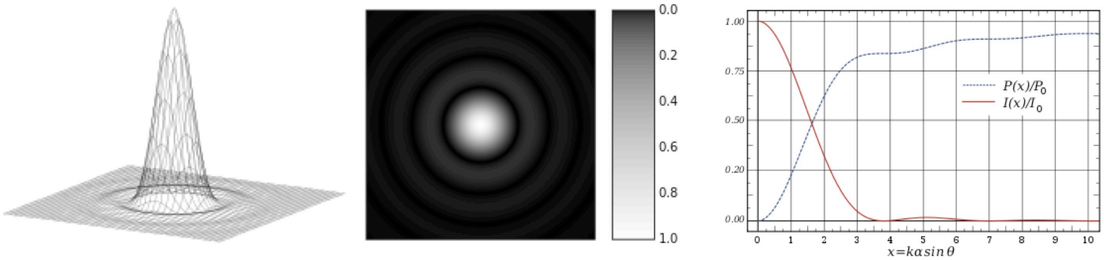

Figure 2.5 (left and middle) Visual depictions of the Airy disc associated with a diffraction-limited focus. (right) Graphical representation of the normalized radial intensity distribution (red solid line, $I(x)/I_o$) and the relative encircled power (blue dotted line, $P(x)/P_o$). Note $x = kasin(\theta) = 2\pi rN.A./\lambda$, as used in Eq. 2.7. (http://en.wikipedia.org/wiki/Airy_disk).

The sample holder (Section 2.3.1) is supported directly above the objective by a 3-D nano-positioning piezo-electric scanning stage, which is used to raster the sample in the plane of the nanoscopic focus in order to generate a microscopic image of the sample (Figure 2.6).

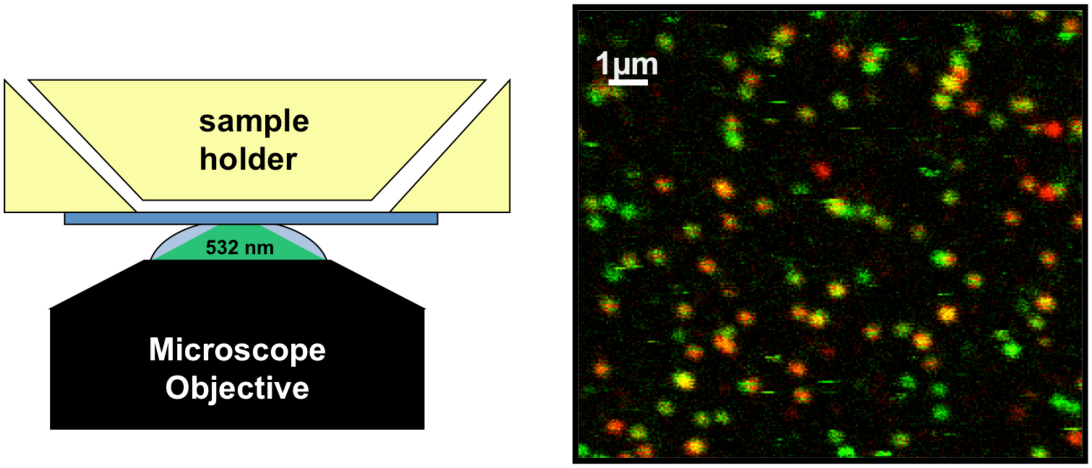

Figure 2.6 Sample surface image of immobilized fluorescence molecules using the 3-D nano-positioning peizo-electric scanning stage (not shown).

This practice facilitates localization of fluorescent molecules. Because of the size and surface density of the immobilized species, the fluorescent features (e.g., spots) associated with them are diffraction limited and only sparsely populate the surface of the sample. The stage can be used to position the sample such that a single fluorescent molecule will reside precisely at the center of the diffraction-limited focus. This exposes the fluorophores to the excitation sources resulting in the absorption and subsequent emission of photons. The emitted fluorescence is collected by the same objective (i.e., epifluorescence) and directed as a collimated beam of donor (Cy3) and acceptor (Cy5) fluorescence through the 2-color dichroic mirror, where it is focused by a tube lens (*f* =80 mm) and directed out the side-port of the microscope by a mirror.

2.2.3 Emission path

The entire emission path, starting directly from the side-port of the microscope base, is contained in a series of black matte optical tubes to prevent ambient room light from reaching the detectors. A pinhole is placed ≈ 80 mm outside of the side port in the image plane of the tube lens (*f* = 180 mm) within the microscope body. The aperture of the pinhole ($d_{pinhole}$ = 50 μm) is used to reject out-of-plane and off-axis. The 50 μm aperture is more than sufficient to capture the center spot of the Airy pattern after being magnified by the microscope objective ($60 \times d_{\mathrm{Airy}} \approx 42$ μm). Notably, this central feature contains ≈ 83 % of the total power of the Airy pattern (Eq. 2.8).

$$\frac{P(x)}{P_0} = 1 - \left(\frac{J_0(x)}{x}\right)^2 - \left(\frac{J_1(x)}{x}\right)^2, \; x \approx \frac{2\pi r N.A.}{n\,\lambda} \qquad \text{(Eq. 2.8)}$$

On-axis fluorescence in the focal plane passes through the pinhole, where it is collected by a lens and imaged onto the active area of the downstream detectors. Prior to reaching the detectors, the fluorescence is spatially separated, first by polarization (horizontal and vertical with respect to the laser table) using a polarizing beam cube (CVI PBSH-450-1300-100) and then by color (e.g., donor and acceptor fluorescence) via dichroic mirrors designed to transmit red and reflect green light (645DCXR, Chroma Technology). The last elements in the emission path prior to the detectors are band pass and long pass filters on the donor and acceptor emission paths, respectively. These optical elements facilitate rejection of photons from the excitation sources (532 nm and 635 nm) and ensure that only Cy3 or Cy5 fluorescence reaches each of the four detectors.

2.2.4 TCSPC Detection

Four avalanche photodiodes (APDs, SPCM-ARQ-14, Perkins-Elmer Optoelectronics) serve as the detection elements (1: donor horizontal, 2: acceptor horizontal, 3: donor vertical, and 4: acceptor vertical) for the Cy3 and Cy5 fluorescence. These remarkable devices provide the ability to detect single-photons with high efficiency ($\approx$ 65%) and enable time-correlated single-photon counting (TCSPC) capabilities. A synchronization signal associated with the repetition rate of the green laser (20 MHz) is directed to the TCSPC module (SPC-134, Becker & Hickl GmbH) to track the laser pulses. Coincident with the detection of a single photon, the APD starts a linear voltage ramp that stops when the next sync signal is received by the TCSPC module. Because the $\approx$ 25 ns between laser pulses is much longer than the $\tau_{\text{fluorescence}}$ of Cy3 and Cy5, the amplitude of the voltage and the known repetition rate of the green laser can be used to infer the arrival time (micro-time) of the photon relative to previous laser pulse that excited the fluorophore. The micro-times provide the ability to observe chemical dynamics on the 0.5 to 50 ns time scale (e.g., excited-state relaxation and rotational diffusion). Additionally, the TCSPC module also keeps track of the arrival time of individual photons with respect to the start of the observation period (macro-time). This provides the ability to observe the time-dependence of the photon arrival rate for any arbitrary time-bin greater than 50 ns, making it possible to monitor fluorescence changes resulting from longer time-scale chemical processes (e.g., translational diffusion or biomolecular folding) ranging from hundreds of nanoseconds (10^{-7} s) to thousands of seconds (10^{3} s).

2.2.5 Temperature Control

The above single molecule apparatus enables observation of chemical processes via fluorescence. The amount of information provided by this instrument is useful for tackling a wide range of scientific questions. However, precisely controlling the experimental sample-temperature can further increase this utility. Temperature is a useful experimental variable that, in conjunction with kinetics experiments, can be used to reveal the thermodynamic properties of a system. To this end, the above experimental apparatus has been retrofit with two different heating technologies, each capable of precisely and accurately controlling the sample temperature. A previous graduate student (Julie Fiore) incorporated the more user-friendly stage-heating capabilities, whereas the slightly more technical infrared-based optical heating capabilities have been implemented as part of the research associated with this thesis.

2.2.5.1 Bulk Heating Methods

Instead of placing the sample holder (Section 2.3.1) directly on the 3-D nano-positioning piezo-electric scanning stage, it is placed within an enclosed stage heater that, itself, rests on top of the scanning stage (Figure 2.7).

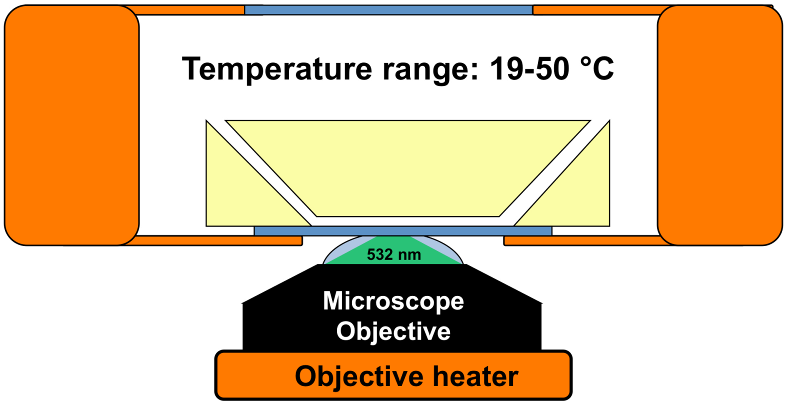

Figure 2.7 Diagram of the original, bulk, heating capabilities established by Dr. Julie Fiore (stage not shown).

Vacuum grease (Dow Corning) maintains efficient thermal contact between the sample holder and the stage heater. The objective is almost completely thermally isolated from the stage and must also be heated to minimize thermal gradients across the sample. This is accomplished by a resistively heated wire-based objective collar (Figure 2.7).Calibration of sample temperature with respect to the set point of both the stage and objective heaters is necessary to ensure accurate and precise temperature measurements. It is important to note that because of precious optical elements in the objective, heating rates should not exceed 1 °C/min so as to minimize the potentially damaging effects of thermal expansion. Furthermore, the temperature of the objective should not exceed 50 °C according to the manufacturer. Because of the high heat capacity associated with the objective, a 10 min wait is required for all of the elements to reach a steady-state temperature. In its current implementation, the bulk stage heating capabilities provide the ability to reliably control the sample temperature (± 0.2 °C), though not without some restriction—to use the words of my advisor, “There is no such thing as a free lunch!” These experimental restrictions are primarily related to the following three concepts. First, biological samples tend to rapidly degrade at elevated temperatures. This is particularly true for acid/base and metal ion-catalyzed cleavage of the phosphodiester backbone in RNA(9,10). Although sample heating is desirable, heating the entire sample will result in many unwelcome side effects related to sample degradation. Second, the large heat capacity of the objective mandates that heating must occur on the time-scale of 10 min, which, unfortunately, makes taking data laborious and time-consuming. Furthermore, these temporal constraints preclude the ability to use rapid changes in temperature to induce particular conformational transitions in nucleic acids. Lastly, thermal expansion of the objective limits the maximum attainable temperature, which impedes the study of ultra-stable nucleic acid interactions that require high (> 50 °C) experimental temperatures.

2.2.5.2 Infrared-based Heating

All of these hindrances associated with bulk stage heating can be alleviated thought the use of optical heating methods. Specifically, focused infrared light resonant with a combination band of the asymmetric and symmetric OH stretch in water can be used to vibrationally excite water molecules (Figure 2.8). These excited molecules will rapidly deposit the excess energy into the solution resulting in an increase in the sample temperature. A detailed description of the implementation and characterization of these heating capabilities is the topic of Chapters 3 and 4, which should be referenced for additional details.

In summary, 1443 nm continuous wave radiation is directly coupled into a single-mode fiber at the output of the laser diode. The infrared light exits the fiber at the top of an optical cage system via a beam collimator and propagates coaxially towards the sample and microscope objective with a beam intensity diameter ($1/e^2$) of ≈ 9 mm.

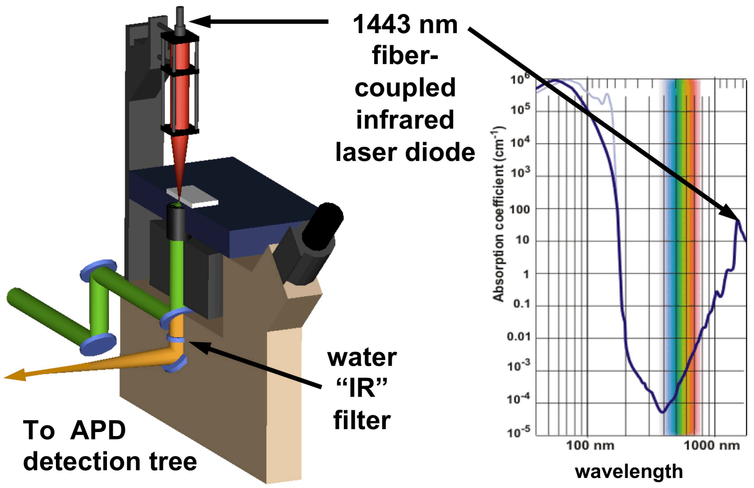

S. Prahl, Optical absorption of water.
http://omlc.ogi.edu/spectra/water/index.html

Figure 2.8 Cut-away cartoon of the infrared-based heating apparatus coupled to the existing inverted confocal fluorescence microscope.

A lens (f = 100 mm), approximately 10 cm from the focal plane of the microscope objective, is used to focus the infrared light to an intensity diameter ($1/e^2$) = 20 μm, which provides the thermal energy for the infrared heating capabilities. The implementation of these methods increase the range of accessible temperature to 20-90 °C, which represents a substantial improvement from the 20- 50 °C range associated with bulk heating methods. The infrared heating methods also result in substantially smaller heated volume ($\lesssim 10^{-11}$ L) than conventional heating methods ($\gtrsim 10^{-6}$ L), thus greatly reducing the effects of elevated temperatures on sample degradation. Lastly, and perhaps most importantly, the optical modulation of temperature provides the ability to alter the sample temperature on a ms time-scale rather than the hundreds of seconds necessary with the previous implementations of temperature control on the experimental apparatus.

2.3 Sample Preparation

Central to nearly every biological experiment is sample preparation, especially in systems where inadequate sample preparation can lead to misleading experimental results. Although the experiments described in this thesis are mostly insensitive to variations in sample preparation, some knowledge of this process is certainly useful. The following sections describe the processes associated with preparing both the sample and the sample holders

2.3.1 Sample Holder

The single-molecule experiments described herein make use of different sample holder variants that are all based on standard microscope cover slips. Corning No. 1½ 22 × 22 mm Zinc Titania (ZT) cover slips (Catalog No. 2870-22) were used until they were discontinued in 2012. Since then, Corning No. 1½ 22 × 22 mm Borosilicate (BS) cover slips (Catalog No. 2850-22) have proven to be a less-than-desirable replacement due to fact they require more stringent cleaning methods. Future efforts should be directed at finding a suitable replacement for the original ZT coverslips. Historically, all cover slips were soaked in 70% nitric acid over night, rinsed with HPLC grade-water, and dried with argon gas. This process is unnecessary for the ZT coverslips, as many experimental observables are insensitive to the cleaning procedures. However, this is not the case for the BS coverslips, which benefit from the nitric acid wash. Given the University's recent concern about both nitric acid and piranha cleaning methods (see CU Boulder EHS), a simple methanol rinse has, thus far, proven to be sufficient for clean glass surfaces.

The ready-to-use glass cover slips (either ZT or clean BS) can easily be incorporated into one of three styles of sample holder (Figure 2.9): (*i*) the "open-air" sample holder (*ii*) "sandwich" style, double-sided sticky tape sample holder, or (*iii*) PCTFE (polychlorotrifluoroethylene) polymer sample holder. The majority of work conducted by a former graduate student (Dr. Julie Fiore) made use of the PCTFE sample holders (see Dr. Julie Fiore's thesis). Given the time and material consumption required by these sample holders, both for cleaning and preparation, the other two, more crude and efficient samples holders quickly replaced them.

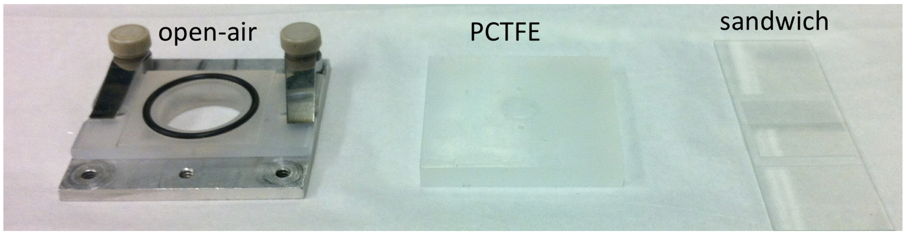

Figure 2.9 Image of the three types of sample holders used for fluorescence studies. See Section 2.3.1 for details.

The "open-air" style sample holder simply consists of a ready-to-use coverslip held in place by a machined aluminum coverslip holder. These were most often used for freely diffusing experiments (Section 2.4.1) of free dye molecules or fluorescently labeled molecules in solution. The "open-air" sample holders are also frequently used for alignment purposes. The "sandwich" style sample holder consists of two pieces of Scotch Brand (3M) double-sided sticky tape, lying parallel to each other, between a ready-to-use coverslip and a standard glass slide (1.0 mm thick 25×75 mm WVR microslides, No 48300-025). The open-ended ≈ 80 μm high channel, or tunnel, resulting from this configuration, which typically runs perpendicular to the long axis of the glass slide, provides the ability to flush, or more precisely, wick (via capillary action) different solutions into and out of the sample holder. This "sandwich" style sample holder can be supported directly above the objective, coverslip-side down, by any two lightweight objects of similar height (e.g., glass slides). Because of the ability to readily change solutions, these sample holders were the desired choice for nearly all surface-immobilized and some freely diffusing experiments involving fluorescent species.

2.3.2 Sample of Interest

Preparation of the actual experimental sample is obviously dependent on the type of experiment and, therefore, the style of sample holder. Freely diffusing experiments (Section 2.4.1) can be performed in the "sandwich" style sample holders, but are generally easier to conduct using the "open-air" style sample holders. For experiments requiring freely diffusing fluorophores, the dyes can be dissolved in HPLC grade H_2O at dilute concentrations, typically 0.1 – 1000 nM, depending on the photophysical properties of the fluorophore. An approximately 40 μl drop of solution can be placed directly on the ready-to-use coverslips of an "open-air" sample holder. These types of experiments are typically used for system alignment and characterization.

Unfortunately, a number of detrimental chemical transformations can occur when the fluorophore is in the excited electronic state. The products of these excited state reactions (e.g., triplet states and conformational isomers) have been shown to be associated, either directly or indirectly, with photophysical abnormalities. Molecular oxygen (O_2) plays an important role in a number of these excited state chemical transformations. Of particular relevance is the strong electrophile, single molecular oxygen ($^1O_2$), which rapidly reacts with the conjugated double bonds of organic fluorophores, rendering them non-fluorescent. Singlet molecular oxygen has also been known to oxidize nucleobases (e.g., guanosine), which can inhibit proper folding of nucleic acids. For these reasons, two different photophysical stabilizing systems are used in order to minimize the influence of O_2. Specifically, a biological antioxidant/triplet state quencher—TROLOX(11) (2 mM)—and an enzymatic oxygen scavenging system—PCA/PCD(12) (5 mM and 60 nM, respectively)—are incorporated into all of the smFRET sample solutions. This practice sufficiently increases the photostability of the fluorophores without influencing any of the measured properties associated with nucleic acid conformational transitions.

For experiments involving surface immobilized molecules (Section 2.4.2), the commonly used chemistry of the biotin-streptavidin ligand-binding system, is employed to non-covalently attach individual molecules to a ready-to-use coverslip at a surface density of less than 1 molecule per square micron. This is most efficiently accomplished using the “sandwich” style sample holders. The sample holder is initially flushed with approximately 200 µl of 10 mg/mL bovine serum albumin (BSA) containing 10% biotinylated-BSA and allowed to incubate for 10 min. This allows the BSA to non-specifically absorb to the surface of the glass coverslip. Then, another approximately 200 µl of 200 µg/mL streptavidin is flushed through the sample holder and allowed to incubate for 10 min. The incubation permits formation of the non-covalent ligand binding interaction between biotin and streptavidin, which immobilizes streptavidin to the surface of the coverslip. Conveniently, streptavidin is a tetrameric protein with four biotin binding sites, which allows this protein to also bind biotinylated nucleic acids. Approximately 200 µl of a 100 pM solution of these biotinylated, fluorescently labeled molecules is flushed through the channel of the “sandwich” style sample holder to achieve the desired surface densities (Figure 2.6, 2.10). After the nucleic acids have been immobilized to the surface of the coverslip, the desired imaging conditions (including TROLOX and PCA/PCD) can be flushed into the sample holder to permit prolonged observation of individual molecules.

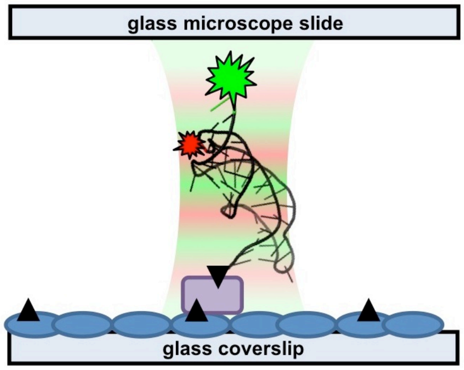

Figure 2.10 Schematic representation (not-to-scale) of the commonly used biotin-streptavidin surface immobilization technique. Approximately one out of ten BSA(blue ovals) molecules contains a biotin (black triangle) moiety. Streptavidin (purple rectangle) has four binding sites for biotin, which can be used to immobilize fluorescent nucleic acids to the glass coverslip.

2.4 Data Collection and Analysis

The single-molecule confocal fluorescence microscope, described above, is capable of a number of advanced fluorescence spectroscopy techniques ranging from time-dependent polarization anisotropy to fluorescence correlation spectroscopy. However, the majority of research contained within this document is carried out using only two such techniques—freely diffusing and surface immobilized experiments; both are well suited for single-molecule experiments.

2.4.1 Single-Molecule Freely Diffusing

The single-molecule freely diffusing (sometimes referred to as “burst”) experiments make use of a confocal microscope’s three-dimensional: (*a*) Excitation Probability Distribution (EPD)—determined by the microscope objective—and (*b*) Detection Probability Distribution

(DPD)—determined by the pinhole and detectors. The product of these two spatially dependent probability distributions—called the molecule detection function (MDF)—is used to define a region in space—termed the confocal volume—where the probability of detecting emitted fluorescence is greater than $1/e^2$ (13). For the current microscope setup, this region is approximately 0.36 femtoliters; one molecule in such a volume corresponds to a solution concentration of approximately 5 nM. By working with concentrations of fluorescent species much lower than this (i.e., 100 pM), one can ensure that most of the time the confocal volume is void of fluorescent species. However, when a fluorescent molecule stochastically diffuses through this volume (Figure 2.11), fluorescence well above background will be observed.

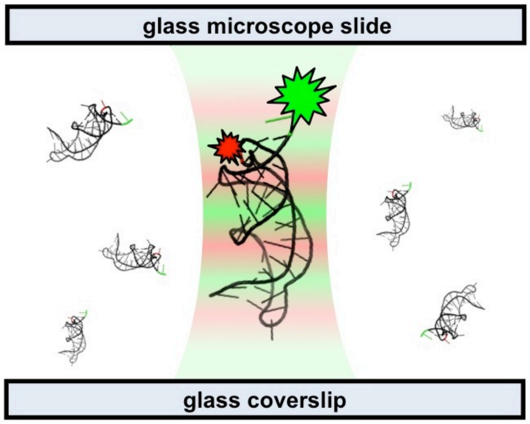

Figure 2.11 Schematic for freely-diffusing single-molecule experiments.

The duration of the burst of fluorescence is obviously limited by the diffusion constant of the species in the solution; for the nucleic acids studied in this thesis, this amounts to approximately 1 ms in the confocal volume. The short residence times minimize the concern for photobleaching, thus allowing for higher incident laser powers (i.e., 30-100 μW), which ensure that the fluorescent bursts are well above background and contain a sufficient number of photons for quantitative determination of E_{FRET}. Conveniently for single-molecule FRET experiments, the use of Alternating Laser EXcitation (ALEX) (see Section 2.2.1) provides the ability to determine the stoichiometry of the fluorescent busts such that only species with both a single Cy3 and Cy5 are considered for data analysis(5-8,14).

Numerous 60-second time trajectories, each containing approximately 500-1000 fluorescents bursts can readily be acquired using in-house software—SPCImage.exe—written originally by Dr. Vasiliy Fomenko using Lab windows/CVI(Figure 2.12). This software has since been updated and modified by Dr. Thomas Baker, Dr. Julie Fiore, Dr. Larry Fiegland, and myself.

Analysis of the data is performed using a second piece of in-house software also scripted primarily by Dr. Vasiliy Fomenko—vffta64.exe (Figure 2.13). Binning the macro-time photon arrival data at 1 ms (depending on the diffusion coefficient of the fluorescent species) allows for single time-bin bursts of fluorescence. Count rate thresholds (20-35 kHz) can be assigned for fluorescence bursts (Options > Burst Analysis) resulting from both the green and red lasers to ensure that only Cy3-Cy5 labeled fluorescent species are considered for analysis.

Lastly, all of the dually labeled fluorescent bursts are compiled together in a histogram, which depicts the distribution of E_{FRET} values associated with the given experiment. The resulting shape of the histogram, but not the amplitude, should be insensitive to the choice of red and green laser ALEX threshold. The histograms can be analyzed a variety of ways to derive equilibrium data and. More sophisticated techniques can even be used to extract kinetic data from such E_{FRET} histograms, as done by other members of the single-molecule community(15). The most frequently used method involves fitting the E_{FRET} distributions to a sum of Gaussians with an additional constraint determined by the total number of observed fluorescence bursts.

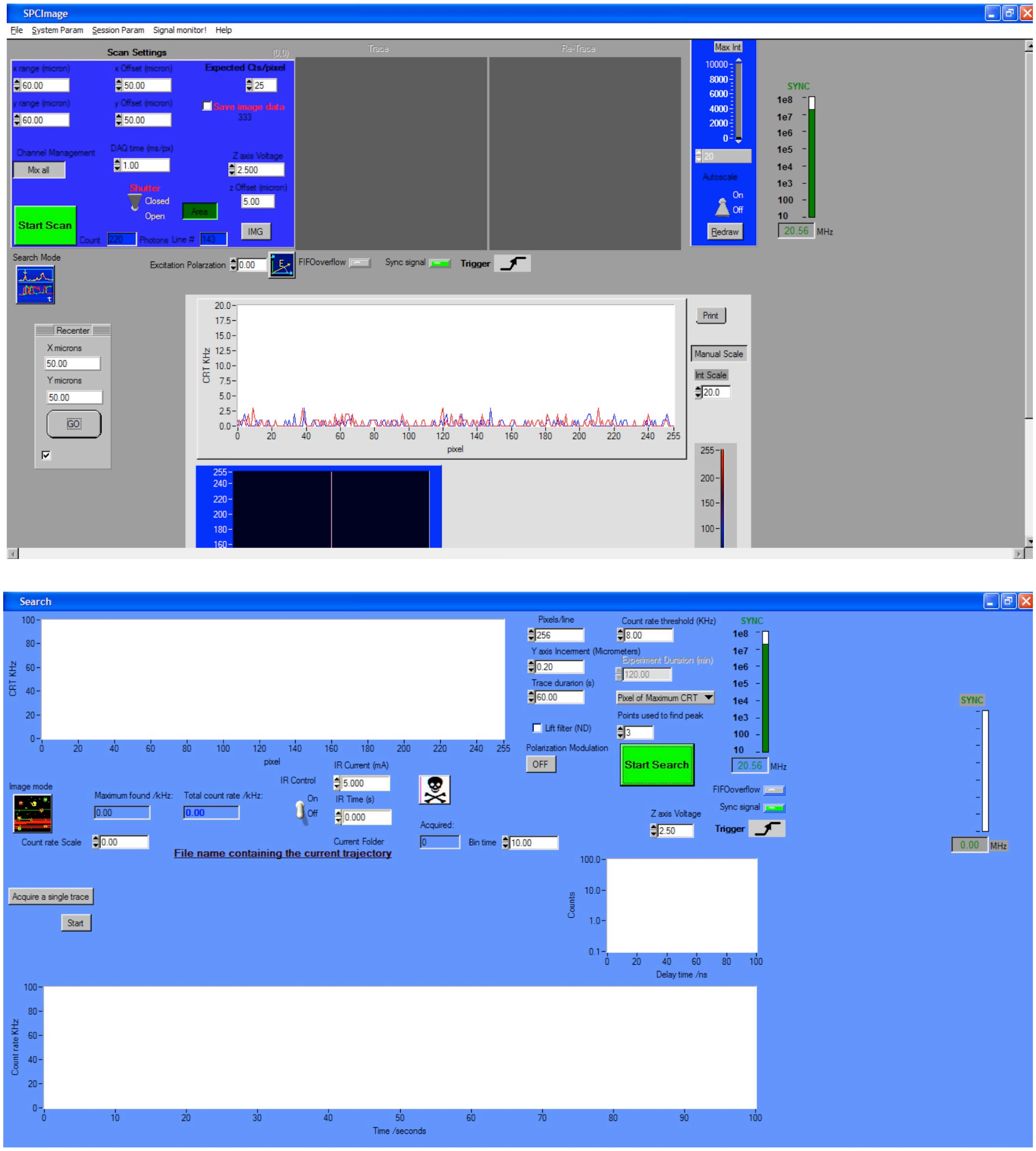

x range (micron): 60.00
x Offset (micron): 50.00
Expected Cts/pixel: 25
y range (micron): 60.00
y Offset (micron): 50.00
☐ Save image data 333
DAQ time (ms/px): 1.00
Z axis Voltage: 2.500
z Offset (micron): 5.00
Count: 220
Photons Line #: 143
Max Int: 20
SYNC: 20.56 MHz
Excitation Polarzation: 0.00
X microns: 50.00
Y microns: 50.00
Int Scale: 20.0

Pixels/line: 256
Count rate threshold (KHz): 8.00
Y axis Incement (Micrometers): 0.20
Experiment Durarion (min): 120.00
Trace durarion (s): 60.00
Pixel of Maximum CRT
Points used to find peak: 3
☐ Lift filter (ND)
Polarization Modulation: OFF
SYNC: 20.56 MHz
IR Control: Off
IR Current (mA): 5.000
IR Time (s): 0.000
Maximum found /kHz: 0.00
Total count rate /kHz: 0.00
Count rate Scale: 0.00
Acquired: 0
Bin time: 10.00
Z axis Voltage: 2.50
SYNC: 0.00 MHz

Figure 2.12 Images of the scanning (top) and time trajectory (bottom) windows of the SPCImage.exe software used to acquire fluorescence data.

2.4.2 Single-Molecule Surface Immobilized

The second, but perhaps most powerful, operational mode afforded by the inverted single-molecule scanning confocal fluorescence microscope involves acquisition of time-trajectories from individual surface-immobilized fluorescently-labeled nucleic acids (Figure 2.10).

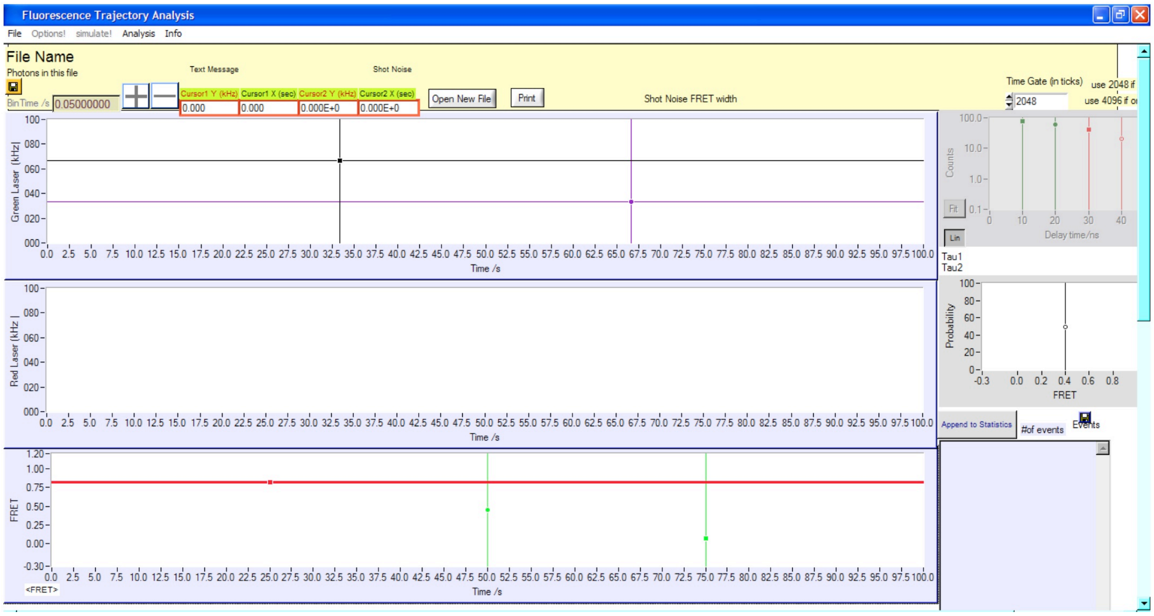

BinTime /s 0.05000000

Cursor1 Y (kHz) 0.000

Cursor1 X (sec) 0.000

Cursor2 Y (kHz) 0.000E+0

Cursor2 X (sec) 0.000E+0

Time Gate (in ticks) 2048

use 2048 if

use 4096 if o

Figure 2.13 Image of the vffta64.exe software use to analyze the data acquired via the SPCImage.exe program.

Because of the small area associated with the diffraction-limited focus of the excitation sources, the sample must be rastered over the objective to generate an image of the surface immobilized molecules (Figure 2.6). This can be accomplished using the SPCImage.exe software described above. Specifically, the software is used to control the 3-D nano-positioning piezo-electric scanning stage such that a 10 µm × 10 µm area of the sample is rastered in the plane of the focus resulting in a 256 × 256 pixel image of the surface, where each pixel results from approximately 2 ms of fluorescence integration. The resulting RGB false-colored surface representation can be used to re-position the scanning stage such that a single fluorescent species resides directly in the focus of the excitation sources. Using the SPCImage.exe software, time-traces can be acquired from the individual fluorescent species for the specified duration of time (Figure 2.12). Analysis of these surface-immobilized trajectories is also accomplished using the vffta64.exe software

(Figure 2.13). Because of the time-tagged data storage method, the bin time can be adjusted, post-acquisition, to achieve the desired balance of signal-to-noise and temporal resolution; typical bin times range from 5-1000 ms depending on the experimental system. The software can also be used to generate a corrected (16) E_{FRET} trajectory which is then integrated over time to generate a E_{FRET} histogram for the specific time-trace. A dwell time threshold can be placed at an E_{FRET} value that approximately represents the minimum between the two distributions. The software will generate a list of all of the threshold crossings and their corresponding dwell times. The dwell times can then be sorted based upon the transitions that gave rise to them (i.e., high $E_{FRET} \rightarrow$ low E_{FRET}, or low $E_{FRET} \rightarrow$ high E_{FRET}) and analyzed to determine the characteristic time constant (or rate constant) that describes the process responsible for the threshold crossing events.

2.5 Single Molecule Construct Design

Perhaps the single most important component of any single-molecule experiment is the preparation of a fluorescently labeled construct. First and foremost, suitable locations for synthetic modifications must be chosen so as to accurately report on conformational transitions within the nucleic acid without significantly perturbing any of the structural or dynamical properties of the molecule. This can be a particularly daunting task without the assistance of biochemical and structural data. Biochemical data can assist in identifying robust nucleotides that can tolerate significant perturbations (e.g., mutations, insertions, and deletions), while still maintaining wild-type activity. These locations are ideal for synthetic modifications like fluorescent dyes. Structural data can also be used to aid in construct design by providing a suitable model for intermolecular distances and the solvent-exposure of particular positions within the nucleic acid. Ideally, the labeling sites should allow nearly free rotation of the fluorophores and the desired conformational transition should modulate the distance between the fluorophores from >53 Å to <53 Å.

Once a construct has been conceptualized, synthesis must be carried out. For designs that consist of annealed oligonucleotides, the starting materials can be purchased from any of a number of commercial sources capable of custom nucleic acid synthesis. However, often times, more complicated steps are required to synthesize a suitable construct. For example, nucleic acid ligation may be required to "join" together two (or more) oligonucleotides. There are a number of useful (but challenging) ligation strategies that can be employed to accomplish such a task. In-house coupling of fluorophores to the nucleic acids may also be necessary for construct synthesis. These techniques are often described and provided by the manufacturer of the functionalized fluorophores. Upon successful synthesis of an RNA construct, great care should be taken to clean up and purify the product by removing undesirable fluorescent contaminants and excess reactants. This is best accomplished using High Performance Liquid Chromatography (HPLC). Once purified, samples should be stored at -70 °C in 50 mM HEPES buffer with ~100 mM monovalent cation concentration and 0.1 mM EDTA to prevent metal-ion catalyzed cleavage of the nucleic acids. Aliquots from the original stock solution (µM) can be made at ~ 25 nM and stored at -20 °C for day-to-day experimentation. A more detailed description of the procedures required to prepare each of the nucleic acid constructs covered in this thesis can be found in the experimental methods section of each of the corresponding chapters.

2.6 References

1. Einstein, A. Strahlungs-Emission und -Absorption nach der Quantentheorie, *Deutch. Phys. Ges.*, **1916,** *18*, 318-323.

2. van der Meer, B. W.; D. M. van der Meer; S. S. Vogel. Optimizing the Orientation Factor Kappa-Squared for More Accurate FRET Measurements, In *FRET – Förster Resonance Energy Transfer*, pp 63-104, Wiley-VCH Verlag GmbH & Co. KGaA.2013

3. Fiore, J. L. (2012) Single-Molecule Kinetic and Thermodynamic Studies of Cation-Facilitated RNA Folding: Isolated Tertiary Interactions, In *Chemical Physics*, University of Colorado, Boulder.

4. Baker, T. A. (2012) Confocal Microscopy Studies of Fluorescence Blinking of Semiconductor Quantum Dots, Metal Nanoparticle Photogeneration, and Multiphoton Photoemission from Thin Metal Films and Metal Nanoparticles, In *Chemistry*, University of Colorado, Boulder.

5. Kapanidis, A. N.; T. A. Laurence; N. K. Lee; E. Margeat; X. Kong; S. Weiss. Alternating-laser excitation of single molecules, *Acc. Chem. Res.*, **2005,** *38*, 523-533.

6. Kapanidis, A. N.; N. K. Lee; T. A. Laurence; S. Doose; E. Margeat; S. Weiss. Fluorescence-aided molecule sorting: Analysis of structure and interactions by alternating-laser excitation of single molecules, *Proc. Natl. Acad. Sci. USA*, **2004,** *101*, 8936-8941.

7. Lee, N. K.; A. N. Kapanidis; H. R. Koh; Y. Korlann; S. O. Ho; Y. Kim; N. Gassman; S. K. Kim; S. Weiss. Three-color alternating-laser excitation of single molecules: Monitoring multiple interactions and distances, *Biophys. J.*, **2007,** *92*, 303–312.

8. Lee, N. K.; A. N. Kapanidis; Y. Wang; X. Michalet; J. Mukhopadhyay; R. H. Ebright; S. Weiss. Accurate FRET Measurements within Single Diffusing Biomolecules using Alternating-Laser Excitation, *Biophys. J.*, **2005,** *88*, 2939-2953.

9. Forconi, M.; D. Herschlag. Metal ion-based RNA cleavage as a structural probe, *Methods Enzymol.*, **2009,** *468*, 91-106.

10. Lonnberg, T.; M. Luomala. Intracomplex general acid/base catalyzed cleavage of RNA phosphodiester bonds: the leaving group effect, *Org. Biomol. Chem.*, **2012,** *10*, 6785-6791.

11. Rasnik, I.; S. A. McKinney; T. Ha. Nonblinking and long-lasting single-molecule fluorescence imaging, *Nat. Methods*, **2006,** *3*, 891-893.

12. Aitken, C. E.; R. A. Marshall; J. D. Puglisi. An Oxygen Scavenging System for Improvement of Dye Stability in Single-Molecule Fluorescence Experiments, *Biophys. J.*, **2008,** *94*, 1826-1835.

13. Ruttinger, S.; V. Buschmann; B. Kramer; R. Erdmann; R. Macdonald; F. Koberling. Comparison and accuracy of methods to determine the confocal volume for quantitative fluorescence correlation spectroscopy, *J. Microsc. Oxford*, **2008,** *232*, 343-352.

14. Joo, C.; H. Balci; Y. Ishitsuka; C. Buranachai; T. Ha. Advances in single-molecule fluorescence methods for molecular biology, *Annu. Rev. Biochem.*, **2008,** *77*, 51-76.

15. Torella, J. P.; S. J. Holden; Y. Santoso; J. Hohlbein; A. N. Kapanidis. Identifying molecular dynamics in single-molecule FRET experiments with burst variance analysis, *Biophys. J.*, **2011,** *100*, 1568-1577.

16. Fiore, J. L.; J. H. Hodak; O. Piestert; C. D. Downey; D. J. Nesbitt. Monovalent and Divalent Promoted GAAA-Tetraloop–Receptor Tertiary Interactions from Freely Diffusing Single-Molecule Studies, *Biophys. J.*, **2008,** *95*, 3892-3905.

Chapter 3

Real-Time IR Overtone Laser Control of Temperature in Picoliter H_2O Samples: "Nano-Bathtubs" for Single Molecule Microscopy[*]

3.1 Introduction

Temperature arguably represents the most critical experimental variable for detailed thermodynamic/kinetic study of chemical and biological processes. Of particular interest, temperature control at the focus of a confocal microscope objective offers significant potential for kinetic exploration of nanoparticle(1,2) and biological(3-5) systems at the single molecule level. Such temperature control can in principle be achieved from "bulk" methods by heating the entire sample, stage, and objective with an enclosed stage-heater and heated objective collar. Though quite powerful, there are several important physical limitations to such a bulk heating approach. First of all, the time constants for heating/cooling of the stage and objective can be unacceptably long, requiring multiple minutes to achieve steady-state temperatures necessary for single-molecule fluorescence detection. Secondly, the speed of such bulk stage heating approaches preclude use of powerful temperature jump methods to activate a specific process of interest, such as denaturation/renaturation of proteins, melting of nucleotide interactions, annealing of nanomaterials, etc. Furthermore, elevated objective temperatures (> 50 °C) can soften optical cement and thereby destroy the precise lens alignment crucial to high numerical aperture photon collection. Finally, prolonged exposure to elevated temperatures may facilitate

---

[*] Adapted from: Holmstrom, Erik D.; Nesbitt, David J. *J. Phys. Chem. Lett.* ***2010**, 1, 2264-2268*

unwanted degradation of the entire sample, which can decrease length of observation times and increase background fluorescence.

Despite these challenges, there have been attempts to alleviate/overcome some of the shortcomings associated with bulk sample-heating, particularly with biological systems. Resistive joule-heating in microfluidic systems has been used to increase sample temperatures to > 90 °C and thereby induce polymerase chain reaction; (6-8) however constraining the heating to within a small sub-volume of the sample is difficult. Others have used the absorbance of water in the near-IR region to directly heat the surrounding medium(9-15). The use of IR light provides optical control of the heated volume, as well as large, programmable temperature changes over short periods of time. As a result, IR laser overtone heating is well poised to remedy a number of shortcomings associated with traditional stage-heating methods. Specifically, the use of resonant near-IR laser excitation of H_2O permits optically controlled, uniform heating of picoliter volumes in a well-defined confocal geometry. Furthermore, any residual transmitted IR laser intensity can be selectively blocked with high specificity by attenuation with a thin bulk-absorbing H_2O filter. As a result, the combination of uniform sample heating and exponential rejection of the heating light permits temperature-dependent studies of kinetics/thermodynamics while maintaining continuous, high fluorescence sensitivity necessary for single-molecule studies.

The thrust of the present work describes an IR-absorption based heating approach coupled with single-molecule fluorescence resonance energy transfer (smFRET) microscopy to simultaneously heat and observe folding of single RNA molecules. To accomplish thermal control of RNA samples, IR light is used to vibrationally excite the first overtone band ($v_{OH} = 2 \leftarrow 0$ at 1445 nm) of the OH-stretch in water (Figure 3.1). This non-contact heating method makes it possible to systematically control the temperature of small volumes of aqueous solution. The result is a confocal fluorescence microscopy apparatus capable of broad temperature control (T = 20-90 °C), high accuracy (± 0.5 °C) and heating rates in excess of 10^4 °C/sec, which offers enormous potential for thermodynamic/kinetic studies of conformational dynamics of biomolecules at the single-molecule level. The reliability and accuracy of this technique are tested by using the IR-absorption based heating to reproduce thermodynamic folding studies of the GAAA tetraloop–receptor from the *Tetrahymena* ribozyme(16).

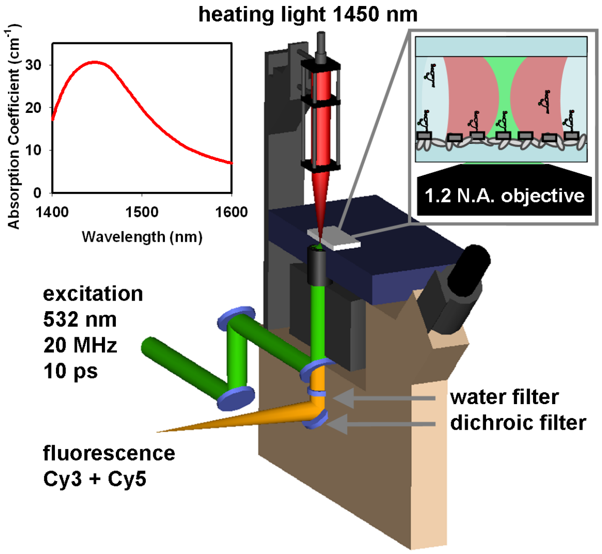

Figure 3.1 Cutaway diagram of IR absorption based heating apparatus. Inset shows the absorption coefficient (α) of water in the $v_{OH} = 2 \leftarrow 0$ overtone band region near 1.45 mm.

3.2 Results and Discussion

To achieve IR-absorption based temperature control of aqueous solutions, a fiber-coupled 1445 nm continuous-wave laser has been incorporated into an inverted fluorescence microscope (Figure 3.1) with a 532 nm pulsed laser excitation source. This apparatus is capable of color, polarization, and time-resolved single-photon(16). In the studies described herein, an XYZ-translation stage controlled optical-cage is used to focus (f = 100 mm) IR light down to a 17 μm (full width half maximum) diameter spot in the focal plane of (and coaxial with) the microscope objective. The IR laser power (P_{IR}) is controllable between 0-160 mW, with typical peak incident laser intensities of I_o » 47 kW/cm^2. At l = 1.445 µm, the absorption coefficient, $\alpha(l)$, is equal to = 30.3 cm^{-1} (17). For an H_2O sample depth of ≈ 150 mm, this corresponds to a Beers Law absorbance of $A \approx 1.05$ (base e) and nearly uniform local heating throughout the ≈ 35 pL sample volume. For an aqueous sample dominated by the heat capacity of water ($C_p(H_2O) = 4.184$ J/K/cm^3), this model predicts a maximum heating rate ($[\,\partial T/\partial t]_{(t\,=\,0)} = [\alpha(l) \times I^{\circ}\,]/C_p$) of 3.4×10^5 °C/sec.

A microscope objective collects the fluorescence from a donor/acceptor fluorophore-labeled RNA construct. The fluorescent photons are separated from the excitation source and directed towards the detection system using a dichroic mirror. Before detection, the fluorescent photons are spatially separated by color and polarity using various optical elements to accommodate FRET experiments (see Fiore et al.(16)). Detection of fluorescent photons is accomplished with single-photon avalanche photodiodes and a time-correlated single-photon counting (TCSPC) module(16). A thin 3 mm water filter located under the objective is used to prevent excess IR light not absorbed by the sample from reaching the detection system. Infrared light is attenuated with essentially complete efficiency ($T \approx 8 \times 10^{-10}$), and yet with minimal loss of sample fluorescence ($T \approx 0.9$).

An important associated challenge is accurate measurement of the sample temperature, which is accomplished using TCSPC methods to measure the temperature-dependent fluorescence lifetime (τ_{fluor}) of rhodamine B (18). To establish reliable calibration over the full range of interest (20-90 °C), the rhodamine B lifetimes are measured (*i*) in situ with TCSPC methods and (*ii*) benchmarked against studies in a temperature-controlled fluorometer. The fluorescence decay curves in both regimes are least squares fit to a convolution of single-exponential decay and a well-defined instrument response function to determine τ_{fluor} as a function of temperature.

Previous experiments exploiting this property of rhodamine B have focused mainly on either τ_{fluor} or fluorescence intensity, with the resulting empirical calibration curves typically interpolated as a means of inferring the solution temperature(13,19-21). We can take this analysis one step further by considering a realistic Arrhenius kinetic model for the temperature-dependence of rhodamine B. Specifically, it has been shown that the quantum yield (QY) of rhodamine B approaches unity as the temperature decreases(18). Additionally, it is also known that the rate constant for the non-radiative relaxation from the excited state (k_{nrad}) is strongly temperature-dependent and vanishes at low temperature(18,22). Based on the relationship between decay rate constants and fluorescence quantum yield ($\text{QY} = k_{rad}/[k_{rad} + k_{nrad}]$), these observations suggest the temperature dependence of τ_{fluor} to arise from the non-radiative rate, i.e. $k_{nrad}(T)$. This can be simply modeled as an activated process, with the temperature dependence of $k_{nrad}(T)$ dictated by the well known Arrhenius equation, i.e., $k_{nrad}(T) = A\exp(-E_a/kT)$. Analysis and results from such an Arrhenius model are summarized in a standard Arrhenius plot of $\ln[k_{nrad}(T)]$ versus $1/T$ (Figure 3.2). Over the range of temperatures observed, $\ln[k_{nrad}(T)]$ decreases linearly with $1/T$, which when fit to the Arrhenius equation yields an activation energy (E_a) for accessing the non-radiative decay channel of 7.2(1) kcal/mol. This is qualitatively consistent with previous Arrhenius analyses of non-radiative decay in methanol ($E_a = 5.2(4)$ kcal/mol), ethanol ($E_a = 5.0(4)$ kcal/mol) and 1-propanol ($E_a = 4.1(5)$ kcal/mol), which is clearly indicative of a reduction of E_a with decreasing solvent polarity (23). Of particular relevance to the present work, this expression provides physically-motivated calibration of τ_{fluor} as a function of solution temperature, and thereby a non-invasive measure of temperature for picoliter volumes of H_2O.

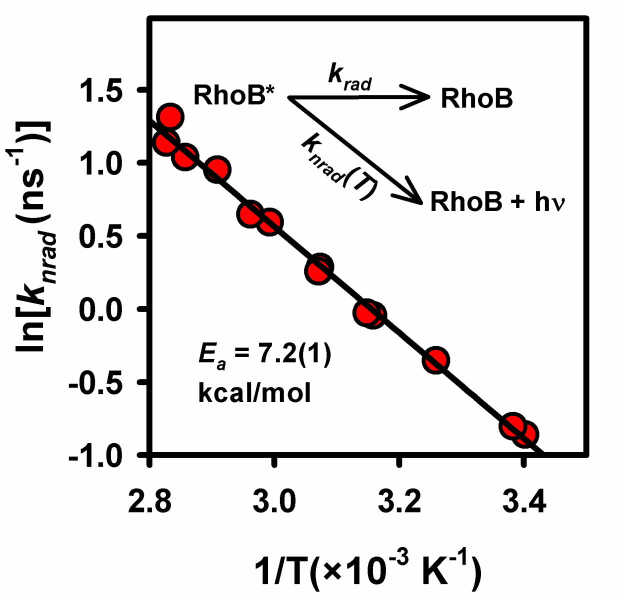

Figure 3.2 Arrhenius analysis of the non-radiative component $k_{nrad}(T)$ for temperature-dependent rhodamine B fluorescence rates. By explicitly measuring $k_{fl} = k_{rad} + k_{nrad}$ (T) and modeling k_{nrad} (T) as a thermally activated Arrhenius process, one can use TCSPC and the Arrhenius equation as a calibration curve for temperature.

As a quantitative demonstration of such a IR-absorption based heating method, we have also investigated equilibrium thermodynamics for RNA folding at the single-molecule level (16). Specifically, a donor/acceptor labeled RNA construct and smFRET are used to study the temperature-dependent folding/unfolding dynamics of the GAAA tetraloop-receptor tertiary interaction. Most importantly, this permits a direct comparison with previous single-molecule measurements of enthalpy and entropy based on bulk microscope stage-heating.

The equilibrium constant as well as the individual rate constants for folding/unfolding are determined using previously established methods(24). Figure 3.3 depicts a van't Hoff plots of R ln[K_{eq}] versus $1/T$ obtained from both the present study (IR-absorption heating) as well as previous work (bulk stage heating). Results from this work (ΔH° = 18(2) kcal/mol, ΔS° = 58(6) cal/mol/K) and bulk stage heating experiments (ΔHº = 17(2) kcal/mol, ΔSº = 56(5) cal/mol/K) are clearly in excellent agreement, with all thermodynamic quantities indistinguishable within experimental uncertainty. This represents strong confirmation that the present IR-laser absorption based heating methods can be used to obtain high quality kinetic/thermodynamic data on single-molecule samples.

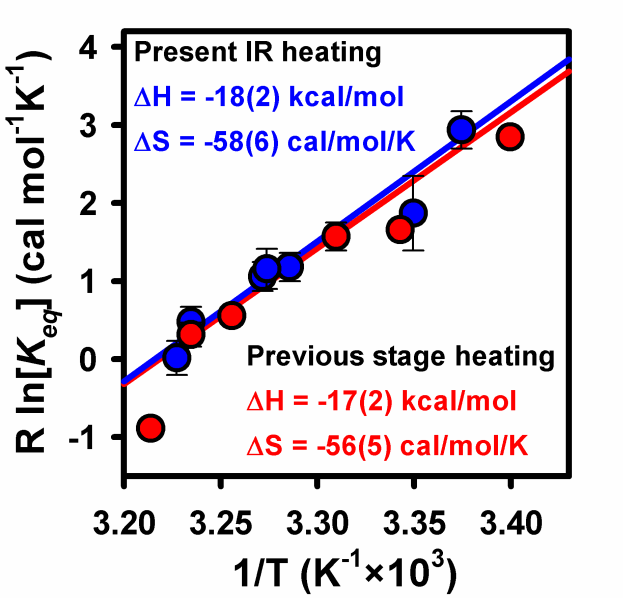

Figure 3.3 Van't Hoff plot of R ln[K_{eq}] vs 1/T for single molecule FRET studies of RNA folding provides ΔHº and ΔSº for the GAAA tetraloop–receptor tertiary interaction. Note the excellent agreement between the laser-overtone and stage-based heating techniques.

One critically important advantage of the IR laser heating method is the high temporal control of sample temperature, which we can address more quantitatively from the data. To determine a maximum rate and upper limit time-scale for heating, fluorescence from rhodamine B is measured as a function of time during abrupt heating/cooling cycles (Figure 3.4). To obtain sufficient accuracy in the fluorescence lifetime information, τ_{fluor} at each time point is determined from a least-squares exponential decay fit to 2000 photons, which at maximum fluorescence rates corresponds to a minimum bin time of ≈ 20 ms. The prompt decrease in τ_{fluor} reflects a correspondingly rapid increase in $k_{nrad}(T)$, which from the Arrhenius expression translates into an IR laser-induced jump of $\Delta T = 23.2(5)$ ºC. Interestingly, the characteristic rate for laser heating above ambient temperature is currently limited by the minimum bin time, with the data clearly establishing an *upper limit* for the heating process ($t_{heat} < 20$ ms). It is also worth noting that the ability to monitor confocal fluorescence *continuously* throughout the temperature jump event highlights a critical kinetic advantage of the present narrow band IR laser absorption heating technique over broad band IR-induced heating methods(12).

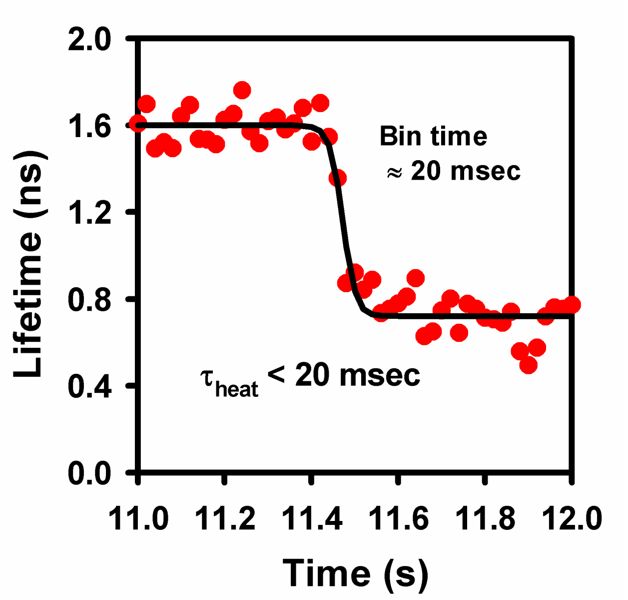

Figure 3.4 Time scale for IR-absorption based heating. By monitoring rhodamine B fluorescence lifetimes, one can directly measure characteristic times associated with laser heating of the sample. The characteristic heating time is currently limited by the time binning resolution of the data (< 20 ms), which is slower than, but consistent with, predictions (see Section 3.2 for details).

This analysis can be explored further based simply on conservation of energy and Newton's Law of cooling. If we at first assume no heat flow into/out of the illuminated sample volume, conservation of energy relates the time-dependent deposition of thermal energy ($\partial(\Delta Q)/\partial t = \alpha(l) \times I_o$) to the time-dependent change in local temperature ($\partial(\Delta T)/\partial t = C_p(H_2O)\ \partial(\Delta Q)/\partial t$). In this approximation, the temperature derivative is given by $\partial(\Delta T)/\partial t = (\alpha(l) \times I_o)/C_p(H_2O)$, which for 50 mW of IR light focused to an area of $A = \pi(17\ \mathrm{mm})^2/4$ at 1445 nm ($\alpha(l) = 30.3\ \mathrm{cm}^{-}$

^{1}) predicts a maximum initial rate of ≈ 1.1×10^5 °C/sec. It is worth noting that because of the relatively small absorbance per unit length, and therefore uniform heating conditions, this prediction is rather insensitive to the sample depth.

Of course, this initial rate is not maintained indefinitely due to thermal conduction and loss of heat to the surrounding medium, resulting in a steady-state temperature increase. This temperature change can be analyzed via Newton's law of cooling, $\partial(DT)/\partial t \propto -\Delta T$, which can be integrated to yield a single-exponential rise/fall to an asymptotic steady-state temperature, i.e., $\Delta T(t) = \Delta T_\infty \times [1 - \exp(-t/\tau_{\text{heat}})]$. This time constant ($\tau_{\text{heat}}$) will be a function of thermal-conduction efficiency away from the laser heated volume. However, t_{heat} can be simply re-expressed from the expression above to yield $\tau_{\text{heat}} = (\Delta T_\infty)/[\partial(\Delta T)/\partial t]_{(t=0)}$ in terms of (*i*) the maximum initial rate of temperature change ($[\partial(\Delta T)/\partial t]_{(t=0)}$) and (*ii*) the asymptotic temperature rise (ΔT_∞), which can be experimentally measured for a given P_{IR}. Note that since both ΔT_∞ and $[\partial(\Delta T)/\partial t]_{(t=0)}$ are approximately proportional to intensity, τ_{heat} will be largely insensitive to the incident P_{IR}.

More quantitatively, for a 43 mW IR laser focused to a sample area of $A = 235$ mm^2 in water, the asymptotic temperature rise is empirically found to be $\Delta T_\infty = 23.2(5)$ °C. From the above expression, this predicts $\tau_{\text{heat}} \approx 0.25$ ms, which is substantially faster but nevertheless consistent with the experimentally determined upper limit. We are currently extending these studies to digitally switched laser outputs, faster fluorescence rates, and shorter bin times to constrain this limit further. However, we anticipate that some of this discrepancy may be a result thermal gradients and heat flow. By way of evidence, the heating and cooling time constants from such a first-order model are predicted to be equal, whereas experimentally the *cooling* time is observed to be considerably longer ($\tau_{cool} \approx 320(20)$ ms) and easily measurable with a 20 ms bin time. One interpretation is that on the time scale of heating (> 20 ms) the heated volume closely resembles the profile of the incident IR laser beam. However, over longer times heat can diffuse radially away from the pseudo-column of water giving rise to a broad volume of heated water. As such, this large volume of water will cool down more slowly than it takes the small volume of water to heat up. Unfortunately, this broad heated region will expose more surface tethered molecules to elevated temperatures and potentially contribute to unwanted sample degradation and background fluorescence, but is still significant improvement from bulk sample heating. Nevertheless, this simple first-order analysis of rapid temperature changes suggests intriguing prospects for temperature jump capabilities and single-molecule kinetics on the msec time scale. Specifically, this technique coupled with smFRET provides the ability to observe, in real-time, intermediate states in the melting pathway of large non-coding RNAs.

3.3 Conclusions

In summary, we have presented results from a confocal method with high spatial (30 µm) temporal (< 20 ms) and thermal (± 0.5 K) control of aqueous smFRET samples based on excitation of the OH-stretch overtone with 1445 nm laser light. The benefits of this non-contact method of resonant IR laser heating are (*i*) much larger dynamic temperature range compared to more traditional stage-heating methods, as well as (*ii*) the ability for continuous sensitive monitoring of fluorescence at the single molecule level throughout the heating event. These temperatures increases can be accurately calibrated from the temperature-dependent fluorescence lifetimes of rhodamine B, making it particularly useful for quantitative studies of temperature-dependent kinetics/thermodynamics in a variety of systems.

Indeed, such resonant IR-laser absorption based heating techniques have very recently been adapted to wide-field microscopy experiment (10,11) demonstrating the applicability of the technique to single-cell *in vivo* studies. This work has furthered the application of IR absorption based heating to the field of single-molecule microscopy. In particular, the prospects for temporal control of picoliter sample temperatures down to the msec time scale with resonant absorption of the residual IR flux offers access to temperature jump experiments performed at the single molecule level and monitored in real-time.

3.4 Experimental Methods

The three-piece donor/acceptor labeled GAAA tetraloop–receptor construct, as well as all solution preparations, annealing and tethering protocols are as described previously;(16) only experimental modifications necessary for the current study are presented herein. Samples holders are created with standard glass slides and coverslips. Double-sided tape is placed across a clean glass slide creating two closely spaced parallel channels and sealed with a clean glass coverslip. In the first channel, fluorescence measurements of 500 nM rhodamine B (in water) under constant power illumination are used to determine $k_{nrad}(T)$ with < 1% error, from which the sample temperature can be calculated from the Arrhenius expression calibration curve (Figure 3.2). FRET trajectories from a series of single RNAs immobilized in the second channel are then collected under identical constant power illumination, simply by translating the glass slide assembly. As a control, independent tests with rhodamine B in *both* channels reveal no temperature difference within experimental uncertainty (± 0.5 K) that could potentially arise from variations in the glass or sample-holder preparation. For all of the above experiments, the microscope stage is not temperature controlled and thus is confined to the ambient room temperature. As such, all temperature changes are a result of increases in laser power.

3.5 References

1. Li, S.; K. Zhang; J. M. Yang; L. W. Lin; H. Yang. Single quantum dots as local temperature markers, *Nano Lett*, **2007,** *7*, 3102–3105.

2. Valerini, D.; A. Creti; M. Lomascolo; L. Manna; R. Cingolani; M. Anni. Temperature dependence of the photoluminescence properties of colloidal CdSe/ZnS core/shell quantum dots embedded in a polystyrene matrix, *Phys. Rev. B*, **2005,** *71*, 235409.

3. Bartley, L. E.; X. W. Zhuang; R. Das; S. Chu; D. Herschlag. Exploration of the Transition State for Tertiary Structure Formation Between an RNA Helix and a Large Structured RNA, *J. Mol. Biol.*, **2003,** *328*, 1011–1026.

4. Hohng, S.; T. J. Wilson; E. Tan; R. M. Clegg; D. M. J. Lilley; T. J. Ha. Conformational flexibility of four-way junctions in RNA, *J. Mol. Biol.*, **2004,** *336*, 69–79.

5. Kato, H.; T. Nishizaka; T. Iga; K. Kinosita, Jr.; S. Ishiwata. Imaging of thermal activation of actomyosin motors, *Proc. Natl. Acad. Sci. USA*, **1999,** *96*, 9602–9606.

6. de Mello, A. J.; M. Habgood; N. L. Lancaster; T. Welton; R. C. R. Wootton. Precise temperature control in microfluidic devices using Joule heating of ionic liquids, *Lab on a Chip*, **2004,** *4*, 417-419.

7. Hu, G. Q.; Q. Xiang; R. Fu; B. Xu; R. Venditti; D. Q. Li. Electrokinetically controlled real-time polymerase chain reaction in microchannel using Joule heating effect, *Anal. Chim. Acta*, **2006,** *557*, 146–151.

8. Zhao, Q. L.; Q. A. Huang; Y. C. Lin. Design and numerical analysis of a joule-heating-induced continuous-flow polymerase chain reaction microchip, *J. Micro-Nanolithogr. MEMs and MOEMs*, **2009,** *8*, 021101.

9. Braun, D.; A. Libchaber. Trapping of DNA by thermophoretic depletion and convection, *Phys. Rev. Lett.*, **2002,** *89*, 188103.

10. Ebbinghaus, S.; A. Dhar; D. McDonald; M. Gruebele. Protein folding stability and dynamics imaged in a living cell, *Nat. Methods*, **2010,** *7*, 319-323.

11. Schoen, I.; H. Krammer; D. Braun. Hybridization kinetics is different inside cells, *Proc. Natl. Acad. Sci. USA.*, **2009,** *106*, 21649-21654.

12. Zhao, R.; E. Alemán; D. Rueda. Laser Assisted Single-molecule Refolding, *Biophys. J.*, **2009,** *96*, Biophys. Soc. proceedings 9a.

13. Slyadnev, M. N.; Y. Tanaka; M. Tokeshi; T. Kitamori. Photothermal temperature control of a chemical reaction on a microchip using an infrared diode laser, *Anal. Chem.*, **2001,** *73*, 4037–4044.

14. Mao, H. B.; J. R. Arias-Gonzalez; S. B. Smith; I. Tinoco; C. Bustamante. Temperature control methods in a laser tweezers system, *Biophys. J.*, **2005,** *89*, 1308–1316.

15. Peterman, E. J. G.; F. Gittes; C. F. Schmidt. Laser-induced heating in optical traps, *Biophys. J.*, **2003,** *84*, 1308–1316.

16. Fiore, J. L.; B. Kraemer; F. Koberling; R. Erdmann; D. J. Nesbitt. Enthalpy-Driven RNA Folding: Single-Molecule Thermodynamics of Tetraloop–Receptor Tertiary Interaction, *Biochemistry*, **2009,** *48*, 2550–2558.

17. Wieliczka, D. M.; S. S. Weng; M. R. Querry. Wedge shaped cell for highly absorbent liquids: Infrared optical constants of water, *Appl. Opt.*, **1989,** *28*, 1714–1719.

18. Karstens, T.; K. Kobs. Rhodamine B and rhodamine 101 as reference substances for fluorescence quantum yield measurements, *J. Phys. Chem.*, **1980,** *84*, 1871–1872.

19. Muller, C. B.; K. Weiss; A. Loman; J. Enderlein; W. Richtering. Remote temperature measurements in femto-liter volumes using dual-focus-Fluorescence Correlation Spectroscopy, *Lab on a Chip*, **2009,** *9*, 1248-1253.

20. Robinson, T.; Y. Schaerli; R. Wootton; F. Hollfelder; C. Dunsby; G. Baldwin; M. Neil; P. French; A. Demello. Removal of background signals from fluorescence thermometry measurements in PDMS microchannels using fluorescence lifetime imaging, *Lab on a Chip*, **2009,** *9*, 3437–3441.

21. Ross, D.; M. Gaitan; L. E. Locascio. Temperature measurement in microfluidic systems using a temperature-dependent fluorescent dye, *Anal. Chem.*, **2001,** *73*, 4117–4123.

22. Arbeloa, F. L.; T. L. Arbeloa; M. J. T. Estevez; I. L. Arbeloa. Photophysics of Rhodamines - Molecular-Structure and Solvent Effects, *J. Phys. Chem.*, **1991,** *95*, 2203–2208.

23. Casey, K. G.; E. L. Quitevis. Effect of solvent polarity on nonradiative processes in xanthene dyes: Rhodamine B in normal alcohols, *J. Phys. Chem.*, **1988,** *92*, 6590.

24. Downey, C. D.; J. L. Fiore; C. D. Stoddard; J. H. Hodak; D. J. Nesbitt; A. Pardi. Metal ion dependence, thermodynamics, and kinetics for intramolecular docking of a GAAA tetraloop and receptor connected by a flexible linker, *Biochemistry*, **2006,** *45*, 3664–3673.

Chapter 4

Pulsed Infrared-Heating Studies of Single Molecule DNA Duplex Dissociation Kinetics and Thermodynamics[*]

4.1 Introduction

Over the years, single-molecule fluorescence techniques have proven to be quite powerful by allowing researchers to monitor the kinetics and dynamics of individual biomolecules in real-time. These techniques have resulted in a number of important scientific advances regarding a wide variety of biological systems(1). One of the most common applications of single-molecule fluorescence, Förster Resonance Energy Transfer (FRET), has been particularly advantageous for the observation of distinct conformational transitions(2,3). Although direct observation of biomolecular dynamics provides valuable kinetic and mechanistic insight into the particular conformational transitions, even more information can be obtained by combining such single-molecule FRET (smFRET) experiments with control of other biophysically relevant variables such as applied force and temperature(4-11). For example, the addition of explicit temperature control to smFRET experiments can provide thermodynamic information not only on the free energy change, but also the enthalpy and entropy changes associated with the observed processes(4,9). In particular, efficient integration of high resolution spatial and temporal control of temperature with existing single-molecule fluorescence technology represents a significant advance and offers novel quantitative thermodynamic details about biomolecular dynamics (12).

---

[*] Adapted from: Holmstrom, Erik D.; Dupuis, Nicholas F.; Nesbitt, David J. *Biophys J.* ***2014**, 106, 220-231*

The most widely used method with which to control the temperature of an aqueous sample on a single-molecule fluorescence microscope is though the use of an objective-stage heating system(4,7,9). However, there are three major problems associated with such a heating technique: (*i*) a limited range of accessible temperatures (<45 °C) resulting from temperature restrictions on high numerical aperture objectives, (*ii*) large heated volume determined by the size of the sample, and (*iii*) long equilibration times limited by thermal conduction. Recently, a number of techniques have been developed that use focused near-infrared light to directly(10,12-16) or indirectly(17,18) modulate the temperature of aqueous samples. The indirect heating methods are based on infrared absorptions by thin metal films on glass substrates, which then transfer heat to the aqueous solutions. The direct heating techniques all rely on the fact that water molecules have a modest ability to absorb near-infrared light(19), which excites various vibrational modes of the liquid water and effectively increases the local temperature. Of specific interest in this work is the absorption band near 1440 nm corresponding to the $(\nu_1\nu_2\nu_3) = (1,0,1)$ combination state for one quantum of both symmetric and asymmetric OH stretching excitation. These infrared-heating techniques can alleviate many of the limitations associated with the objective-stage heating systems, specifically by providing a broader range of available temperatures and vastly superior spatio-temporal control of temperature(10,12,18,20). Though indirect infrared heating techniques have been well-described(17), none of the direct techniques have been quantitatively characterized, which represents the first major aim of this work.

As a second target, we focus on specific applications in single molecule biophysics. Although the emergence of infrared-based heating methods has alleviated many deficiencies of conventional stage heating techniques, it also has revealed experimental restrictions associated with continuous observation of single-molecules at elevated temperatures (e.g., > 45 °C). Two particularly important restrictions arise from: (*i*) the temperature-dependent dissociation of the non-covalent bond between biotin and streptavidin (21) and (*ii*) the temperature-dependent quantum yields of common single-molecule organic fluorophores(22,23). Due to the unusually high binding affinity of biotin-streptavidin ($K_d \approx 5\times10^{-14}$ mol/L) and the extremely slow dissociation rate ($k_{diss} \approx 3.8\times10^{-6}\ s^{-1}$ at 37 °C), this ligand binding interaction has been widely used in single-molecule experiments for surface immobilization to microscope coverslips(24-27). However, as is necessarily the case with all activated rate processes, the rate constant for dissociation of the biotin-streptavidin interaction increases exponentially with temperature, which can therefore result in rapid depletion of surface immobilized molecules. Key advances in this area of specialized surface immobilization techniques have been fueled by powerful `click' chemistry, which can be used to *covalently* attach single molecules to sample substrates in situations that require stable surface immobilization (28,29).

However, there is one universal difficulty associated with performing smFRET studies at elevated temperatures that represents a more serious experimental problem. In particular, all conventional organic dyes have fluorescence quantum yields that are dramatically reduced at high temperatures. This is predominantly due to rapid growth in the *non-radiative* decay rate constant, which competes efficiently with the *radiative* pathway and therefore makes observation of single fluorophores challenging at temperatures > 45 °C. There have been a variety of recent efforts that help address this problem, ranging from: (*i*) the use of semiconductor nanoparticles (e.g., quantum dots) with much higher absorption cross sections, (*ii*) more efficient collection of fluorophore emission by immobilizing individual molecules on colloidal spheres (30), and (*iii*) development of intrinsically brighter fluorophores by conjugation with photophysical stabilizing agents(31). Although such techniques represent possible directions for addressing issues of fluorophore quenching at elevated temperatures, they also add significantly to experimental complexity, particularly for single molecule studies of biophysical interest. Despite these advances, there remains a considerable need for alternative microscopy methods that can offer access to biomolecular dynamics at temperatures where visualization of common organic fluorophores is challenging. The second aim of this paper is to describe ongoing efforts to help address this issue.

This article is organized into two major sections corresponding to the two parallel aims described above. The first thrust describes a detailed characterization of an all-optical infrared laser based heating technique (12) for single molecule microscopy, which offers quantitative analysis of the thermal, spatial, and temporal characteristics. When compared with conventional microscope stage heating methods, three advantages regarding optical temperature control are apparent: (*i*) larger range of accessible temperatures, (*ii*) extreme localization of thermal load to picoliter volumes and (*iii*) orders of magnitude faster heating rates. As a complementary second thrust, the high spatial/temporal control of the infrared heating is exploited for high-temperature smFRET kinetic measurements**.** In particular, we present results from a "proof-of-principle" demonstration, whereby rapid heating/cooling cycles are used to obtain detailed kinetic/thermodynamic information on the dissociation of 21 bp DNA duplex. Interestingly, the results clearly reveal non-monoexponential temporal behavior in the dissociation kinetics that are used to develop a simple kinetic model based on simultaneous "fraying" from each end of the DNA duplex. Additionally, such a model is capable of describing duplex dissociation for both long (>10 bp) and short (< 10 bp) DNA sequences.

4.2 Overtone Infrared Laser Based Heating Technique

Details of the infrared heating system used throughout the present study can be found in previously published material(12) and can be quickly summarized here. Specifically, the TEM_{00} Gaussian beam profile from a continuous wave laser diode with peak wavelength of 1443 nm is fiber-coupled into an optical cage system containing a beam collimator (output spot size, ω = 4.5(3) mm) and focusing lens (f = 100 mm) to form a suitably small waist (ω_o = 10.0(4) mm, FWHM ≈ 17 μm) for local heating near the focal plane. A precision three-axis translation stage then translates the optical cage with respect to the diffraction-limited focus of a 532 nm excitation laser beam (Figure 4.1a), which illuminates the sample in the opposite direction through the objective of an inverted fluorescence microscope.

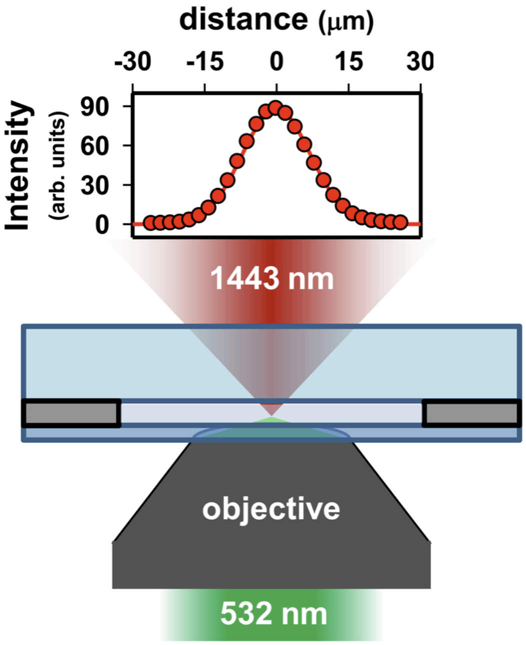

Figure 4.1 Schematic representation of the infrared heating apparatus illustrating the coaxially aligned foci of the infrared (red) and excitation (green) lasers within a standard sample holder (not to scale). The intensity plot depicts the experimentally measured radial intensity profile at the focus of the infrared laser (ω_o = 10.04(4) μm).

Beers law absorption (α_{1443}= 30.3 cm^{-1}) of infrared radiation induces vibrational OH stretch combination band excitation (ν_1, ν_2, ν_3) = (1,0,1) of the solvent water molecules, which relax on the sub-ns time scale and thus yield a rapid increase in solution temperature in the laser focal region. The following experiments have been performed with such an apparatus to experimentally quantify each of the three major proclaimed advantages associated with infrared heating: (*i*) larger range of temperatures, (*ii*) smaller heated volumes, and (*iii*) faster heating.

4.2.1 *In Situ* Measurement and Dynamic Range of Accessible Temperatures

One crucial aspect of the infrared heating apparatus is clearly the magnitude of the induced temperature change. As described previously (12), these temperatures can be accurately obtained by measuring the temperature-dependent fluorescent lifetime [τ_{fluor}(T)] of Rhodamine B(32,33) when the heating and excitation foci are spatially overlapped. The essence of the method relies on the fact that k_{fluor}(T) is simply the sum of a temperature-independent radiative process, k_{rad}, and a temperature-dependent non-radiative relaxation, k_{nrad}(T)(34). Furthermore, k_{nrad}(T) can be accurately modeled using Eyring transition state theory (Figure 4.2, *inset*), reflecting that non-radiative relaxation is enhanced by tilting the peripheral tertiary amino groups away from the plane of conjugation (34). If we invert this procedure, experimental extraction of k_{nrad}(T) for Rhodamine B provides an *in situ* “thermometer” for the local temperature in the sample region.

Specifically, time-correlated single-photon counting (TCSPC) methods are used to acquire the fluorescence decay curve of Rhodamine B in the confocal detection volume of the 532 nm excitation laser. The k_{fluor}(T) is then determined by single-exponential fits convoluted over the instrument response function of the excitation source, with k_{nrad}(T) obtained by subtracting the known k_{rad} value from k_{fluor}(T). The resulting k_{nrad}(T) can be used to predict confocal temperatures to within ≈ 0.5 °C, based on the previously determined Eyring transition state parameters for Rhodamine B in water (Figure 4.2, *inset*)(12). Over the range of incident infrared laser powers (P_{laser} = 0-135 mW) focused to a waist of w_0 = 10.0(4) μm at a distance 15 μm above the glass cover slip, the present experimental apparatus allows for rapid, systematically controlled temperature increases from ΔT = 0 - 80 °C, as illustrated in Figure 4.3a. These results unambiguously demonstrate a range of experimental temperatures significantly larger than accessible by conventional stage-objective heating systems.

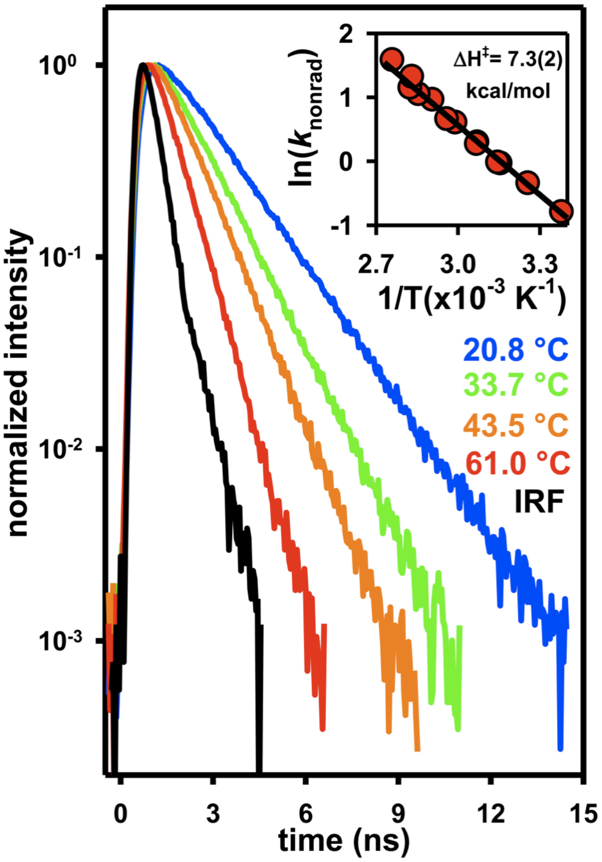

Figure 4.2 Fluorescent decay profile for Rhodamine B as a function of temperature. The linearity of the fluorescence decay over three orders of magnitude attests to the single-exponential behavior of Rhodamine B. The inset represents the Eyring analysis of the temperature-dependent non-radiative rate constant for Rhodamine B (see Section 4.2.1 for details), which is used to determine the temperature rise in the diffraction-limited confocal volume of the sample.

4.2.2 High Resolution Spatial Control of Temperature

The second major advantage associated with infrared heating methods is the high degree of spatial localization for the induced temperature changes. In order to quantify this, we first characterize the intensity distribution of the IR-heating laser at the beam waist. This can be accomplished by measuring the IR laser light transmitted though a 5 μm circular pinhole translated on a piezoelectric stage. The resulting plot of measured intensity vs. lateral displacement (Figure 4.1a) clearly depicts a TEM_{00} beam, which can be nicely fitted with a Gaussian beam waist of $\omega_o = 10.04(4)$ μm. This is also in very good agreement with expectations of $\omega_o = 10.3$ μm, based on the propagation of a Gaussian beam at the fiber collimator output ($\omega_o = 4.5(3)$ μm) that is focused to a waist by a 100 mm focal length lens.

To experimentally determine the steady-state radial temperature-profile, the optical cage system, and thus the IR laser light, is translated horizontally away from the coaxial position established by the excitation beam. Rhodamine B fluorescence lifetimes are then monitored by TCSPC as a function of distance on the translation stage micrometer. The measured values of $k_{fluor}(T)$ are then used to calculate ΔT as a function of the radial separation between the heating and excitation sources, as summarized in Figure 4.3b. The data clearly demonstrate that under steady state heating conditions, the temperature increase is localized in the radial dimension (FWHM ≈ 55 μm). Additionally, the data also establish that the radial temperature profile is significantly broader than the incident laser beam. At distances near (i.e. < 5 μm) the axis of heating, the temperature gradient (≈ 0.1 °C/μm) is much smaller than the experimental uncertainty associated with temperature determination (≈ 0.5 °C), which conveniently results in an essentially uniform temperature profile near the heating axis. It is important to note that the temperature begins to gradually decreases at distances further from the heating axis. This slow radial decay of temperature is consistent with the inverse logarithmic dependence of the radial temperature profile associated with a one-dimensional temperature source and is a result of the elongated column of heat provided by attenuation of the focus infrared beam as it propagates through the sample.

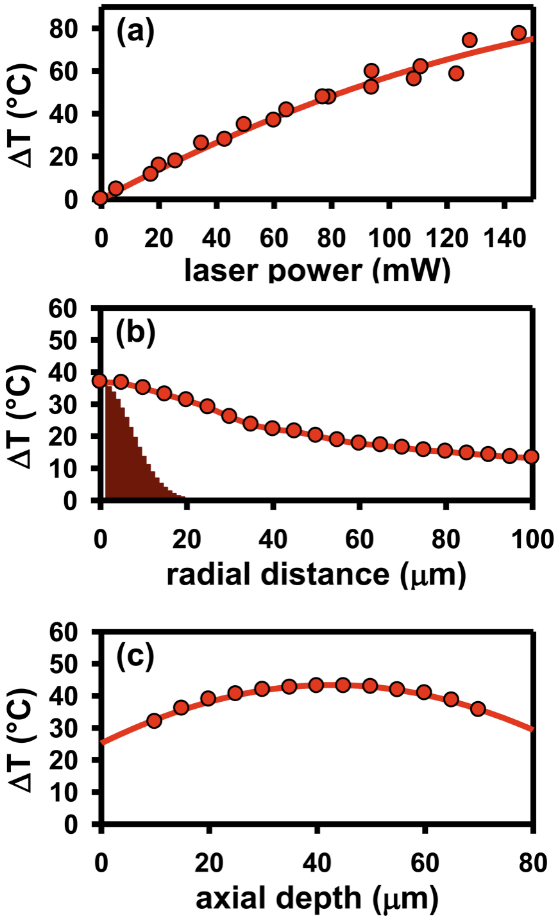

Figure 4.3 Experimentally measured steady state temperature rise (Δ*T*) as a function of **(a)** incident laser power as well as **(b)** radial and **(c)** axial distances from the laser focal point. The solid red region in **(b)** represents the radial intensity profile of the infrared laser beam scaled to the maximum Δ*T*. Note the clear broadening of the temperature profile beyond the laser excitation region, which arises largely from thermal diffusion away from the heating axis.

By way of further characterization of the spatial temperature profile, ΔT has been measured along the vertical axis of the infrared laser, as summarized in Figure 4.3c. It is interesting to note that the measured temperature profiles are relatively flat with a gradual maximum near the midpoint, and therefore only a small vertical gradient exists between the two glass boundary surfaces. The reason for this is that overtone absorption strengths for water lie in an ideal intermediate regime, whereby the 85 μm sample thickness is appreciably smaller than the 1/*e* optical penetration depth (330 μm), and yet not so small as to non-linearly attenuate laser propagation through the sample. As a result, the on-axis thermal heat deposition is nearly linear with distance, which implies nearly uniform heat load in each axial volume element. Most importantly, it is worth noting that the spatial characterization of heated volume demonstrates that the present apparatus confines the temperature rise to extremely small volumes ($\approx 10^{-10}$ L). This represents a significant improvement relative to conventional bulk heating methods and furthermore, with sufficiently dilute sample conditions, extendable down to the heating of a single molecule construct.

4.2.3 Rapid Temperature Modulation

The last major advantage offered by infrared overtone laser heating is control of sample temperature in the time domain, which is only limited by diffusion of heat. To provide expectations for the magnitude(s) of such heating and cooling times, we consider the following elementary physical model. The rate of deposition of thermal energy into a laser illuminated water cylinder of height Dl and cross sectional area A and bounded by an ambient temperature heat bath (T_0) is

$$\partial Q/\partial t = \alpha \Delta l \, I_{laser}, \tag{Eq. 4.1a}$$

where α is the normal base *e* absorption coefficient. By conservation of energy, this thermal deposition must equal the time-dependent change in temperature ($\partial(T - T_0)/\partial t = \partial \Delta T/\partial t$) divided by the heat capacity ($C_p A\Delta l$) of the sample volume $V = A\Delta l$. This immediately yields the simple equation

$$(\partial \Delta T/\partial t)_0 = \alpha \mathrm{I}_{\mathrm{laser}}/[\mathrm{C_p\,A}] \qquad \text{(Eq. 4.1b)}$$

for the instantaneous rate of heating at $t = 0$. Furthermore, Newton's Law of Cooling implies that this initial rate of temperature increase (°C/s) must be linearly proportional to the asymptotic temperature differential (ΔT_∞) when steady state conditions are achieved, with coefficient of proportionality given by the exponential rise time. The combination of these relations predicts a characteristic $1/e$ time for cooling (or heating) given by

$$\tau_{\mathrm{heat}} = \Delta T_\infty /(\partial \Delta T/\partial t)_0, \qquad \text{(Eq. 4.1c)}$$

One simple qualitative prediction from Eq. 4.1c is that since both $(\Delta T/\partial t)_0$ and ΔT_∞ scale approximately linearly with laser power, the time constant for heating (or cooling) of a localized sample surrounded by material at T_0 should be insensitive to incident laser power and depend only on the sample heat capacity undergoing this ΔT_∞. A second more quantitative prediction is that for typical conditions of laser power ($\mathrm{I}_{\mathrm{laser}} \approx 135$ mW), absorption cross section ($\alpha = 30.3$ cm^{-1}), and beam area ($A \approx \omega_0^2 \approx 10^{-6}$ cm^2), the initial heating rates for the sample volume are remarkably swift, on the order of 1×10^6 °/s! Finally, for a typical asymptotic temperature gain under such conditions of $\Delta T = 80$ °C, Eq. 4.1c suggests a $1/e$ time constant for heating on the submillisecond time scale.

In order to determine the experimental time-scales associated with heating and cooling aqueous solutions using focused infrared light, time-dependent trajectories of freely diffusing Rhodamine B (575 nM) have been collected as a function of heating duration (Δt). For a given Δt, each trajectory exhibits a rapid rise to steady-state temperature ΔT_∞, at which point the deposition of thermal energy into system is perfectly balanced by loss of heat to the surroundings (e.g., objective, stage, air). At the end of the heating duration, the heat source is turned off and the sample rapidly cools back to T_0 to complete a single heating/cooling cycle (Figure 4.4a).

Since the data are collected by TCSPC, the trajectories can be sorted into bins of 100 consecutive photons, with each bin converted into a exponential fluorescence decay rate $k_{fluor}(T)$ by maximum-likelihood estimation (35). As describe in Section 4.2.1, these $k_{fluor}(T)$ values can be corrected for the purely radiative contribution and converted into temperatures trajectories ΔT(t) from the $k_{nrad}(T)$ Arrhenius expression for Rhodamine B (Figure 4.2). The heating/cooling behavior of such a temperature trajectory is shown in Figure 4.4a for a heating duration of 500 ms and P_{laser} = 60 mW, which clearly reveals an extremely sharp increase in the sample temperature.

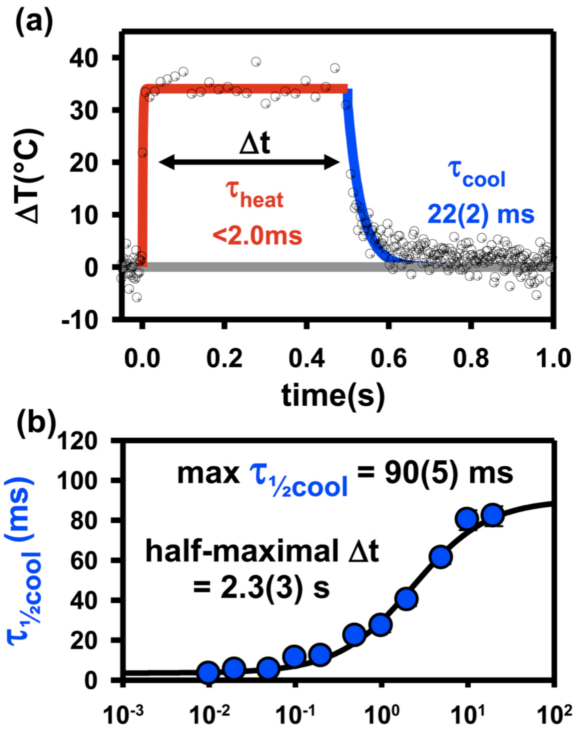

Figure 4.4 Real time observation of the infrared heating and cooling behavior, as obtained by time-correlated single photon fluorescence measurements of Rhodamine B in the confocal excitation region. **(a)** Sample temperature trajectory (black ⊗'s) resulting from a 50 mW heating pulse with a duration of 500 ms. The solid lines represent multi-exponential fits used to calculate the half-maximal times for heating (solid red) and cooling (solid blue). **(b)** A linear-log plot demonstrating the dependence of cooling time constant on the heating duration, which suggests that the system achieves a steady state thermal distribution on the few second time scale.

Though too rapid to resolve with 100 photon time bin steps, the time to half-maximal temperature increase ($\tau_{½heat}$) suggests a heating time constant ≤ 1 ms, in good qualitative agreement with the above predictions.

Closer inspection of Figure 4.4a reveals that the cooling profile after the laser is switched off is noticeably broadened with respect to the rise. Specifically, for a laser heating duration of $\Delta t = 500$ ms, $\tau_{½cool} \approx 22(2)$ ms whereas $\tau_{½heat} \approx 1$ ms. It is worth stressing that this is *not* inconsistent with the *equal* times predicted above from Newton's Law of Cooling (Eq. 4.1c). The reason is clearly evident in Figure 4.3b. Lateral thermal conduction away from the laser illumination region during the approach to steady state necessarily *increases* the surrounding temperature to well above T_0. It is then the presence of this additional "heat reservoir" adjacent to the laser heated region that slows the eventual diffusive cooling process back to ambient values. As expected from such a bulk diffusion process, these decays also deviate considerably from single exponential, which makes characterization by $\tau_{½}$ values a more useful concept.

One clear prediction from this model is that the cooling times should be strongly dependent on the heating duration. Such a compilation of data is presented in Figure 4.4b, which displays the cooling time ($\tau_{½cool}$) vs. duration of the heating laser (Δt). The results (in log time units) are consistent with an approximately proportional growth in $\tau_{½cool}$ with Δt, that eventually saturate at some steady state value for the cooling process. The intercept of this initial linear region is 3(1) ms, which is qualitatively consistent with Newton's Law of Cooling expectations that $\tau_{½heat} \approx \tau_{½cool}$ for sufficiently short heating durations. Most importantly, such exceptionally short values for $\tau_{½heat}$ (and, at sufficiently small Δt, also for $\tau_{½cool}$) represent an enormous improvement ($>10^4$ fold) from the typical time scales of minutes associated with conventional stage-objective heating methods. As will become clear in the following section, this offers several critical advantages for single molecule studies of biophysical kinetics, in particular enabling high temperature single-molecule kinetic measurements without the need for temperature-stable fluorescent dyes.

4.3 A Test Application: Single Molecule Kinetics of DNA Duplex Dissociation

As clearly outlined in the introductory sections, the use of IR overtone laser based methods for controlled heating of picoliter volumes within an aqueous samples has considerable potential for applications in a confocal single molecule microscopy. In particular, the above discussion has revealed at least two fundamental complications associated with continuous observation of individual, fluorescently labeled molecules at elevated temperatures: (*i*) the temperature-dependent rate of dissociation for the biotin-streptavidin surface immobilization technique (21,36) and (*ii*) the temperature dependent fluorescent lifetime of commonly used single-molecule fluorophores (22,23). Because of the novel ability to rapidly modulate the local temperature of aqueous solutions, pulsed heating experiments can in fact be used to circumvent both of these difficulties. On the one hand, rapid T modulation achieves a enormously reduced duty cycle for surface heating over bulk heating techniques, which dramatically reduces parallel loss of the single molecule biotin–strepavidin attachment. On the other hand, the rapid heating and cooling also greatly limits kinetic effects due to time spent in transition, which permits subsequent FRET dye interrogation under cool, high quantum yield conditions. The following pulsed heating experiments, based on a similar proof-of-principle demonstration for laser assisted single-molecule refolding (LASR)(10), are used to demonstrate the ability to make high temperature kinetics measurements of DNA duplex dissociation, tethered to a coverslip with biotin-streptavidin interactions, without the need for thermally stable fluorophores.

4.3.1 Laser Heating Induced Duplex DNA Dissociation Kinetics

In order to exploit these IR laser heating methods to investigate the temperature-dependent dissociation kinetics of duplex DNA, a synthetically modified DNA construct has been designed with two highly stable conformations—duplex or closed—that can be easily distinguished via FRET (Figure 4.5a).

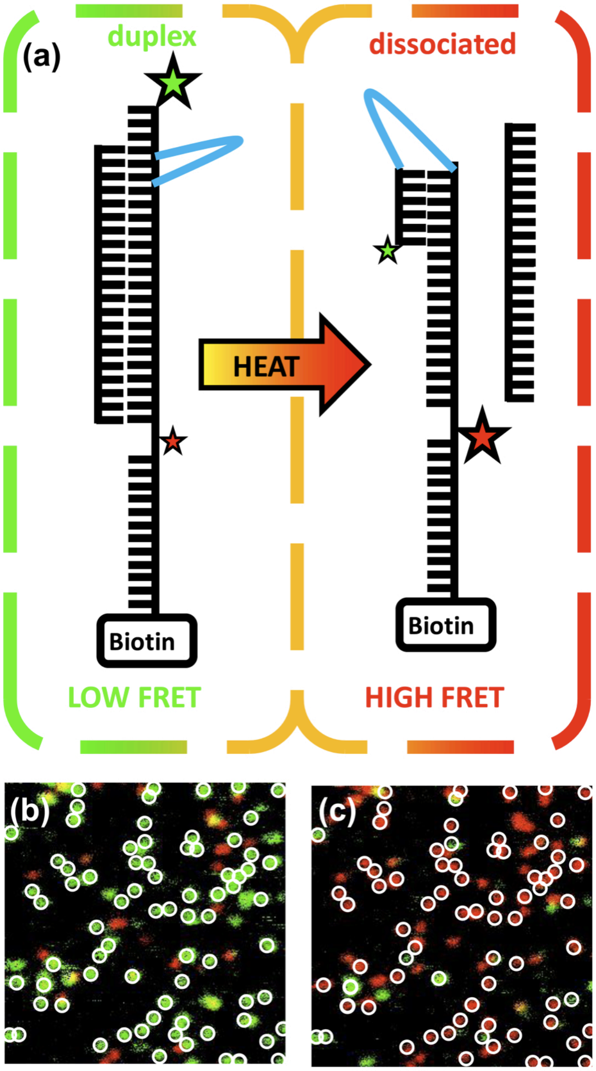

Figure 4.5 (a) Diagram of the duplex DNA fluorescent construct used for the dissociation experiments. Green and red stars represent the Cy3 and Cy5 FRET pair used in the experiments. The solid cyan line corresponds to the PEG_{18} internal linker within the construct to easily allow the construct to form the closed conformation. **(b)** ALEX surface image (10 µm × 10 µm) prior to and **(c)** after exposure to a pulse of infrared light. White circles represent the mask used to measure survival probability (see Section 4.3.1 for details).

The duplex is formed by hybridization of two oligonucleotides—reporter and splint. The reporter oligo has: (*i*) a 6 base pair self complementary sequence separated by a $(PEG)_{18}$ linker, (*ii*) Cy3 and Cy5 fluorescent dyes and (*iii*) a 3' biotin to permit tethering to the surface via biotin-streptavidin interactions. The splint oligo simply contains 21 nt that are complementary to the reporter oligo. Formation of the duplex conformation is accomplished by hybridization of the reporter and splint oligos, which spatially separates the Cy3 and Cy5 dyes, resulting in low FRET efficiency ($E_{FRET} \approx 0.1$, green). Upon dissociation of the splint, the reporter oligo is able to rapidly form the closed conformation, whereby the first six nucleotides at the 5' end quickly base pair with nucleotides 7-12 at the 3' end of the PEG linker (Figure 4.5a). The transition from duplex to closed conformations greatly reduces the radial distance between the Cy3-Cy5 FRET pair, resulting in more efficient FRET ($E_{FRET} \approx 1.0$, red). The basic experimental technique is therefore to use a raster-scanning confocal microscope to image the FRET states under room temperature conditions, before and after the IR laser has induced transient heating of the sample up to a tunable but well characterized temperature for a given time duration.

Prior to a IR laser induced heating episode, alternating laser excitation methods (ALEX, see Materials and Methods) are used to scan images (10 μm × 10 μm) of the sample surface, which reveal that nearly all of the dually labeled surface-immobilized molecules are in the (low FRET state (green) duplex conformation (Figure 4.5b). Upon exposure to the IR laser heating pulse (Δt =10 s, T=72.3(5) °C) centered on the image, the same surface shows that nearly every duplex has undergone dissociation, as indicated by the abundance (> 90%) of molecules in the closed (red, high E_{FRET}) conformation (Figure 4.5c). As mentioned previously, the nearly uniform temperature profile near the heating axis conveniently results in all of the molecules in the 10 μm × 10 μm images experiencing the same temperature. Additional evidence for the spatially localized heating and duplex dissociation is demonstrated more dramatically in FRET images of larger 80 µm × 80 µm scans (as shown in Figure 4.6) where the temperature gradient is no longer negligible. These larger images reveal a clear dividing line between the inner circular region with *dissociated* duplexes (red, high FRET) and the surrounding area with fully intact duplexes (green, low FRET). The reason is that duplex constructs in the inner circular region have been heated to temperatures with sufficiently large rate constants to have significant dissociation probability during the 10 s heating duration.

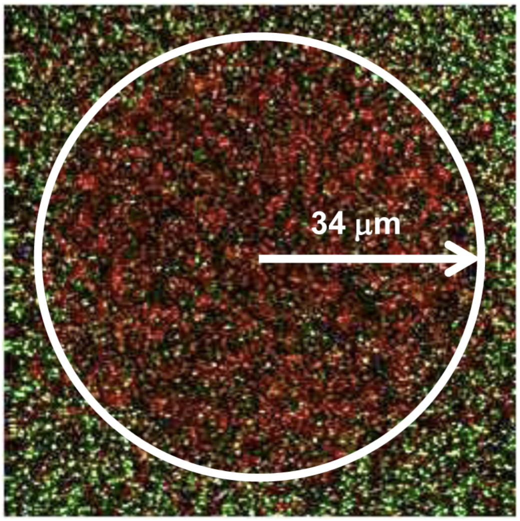

Figure 4.6 ALEX scanned image (80 µm × 80 µm) of the fluorescent DNA duplex constructs after heating the center of the image to 72.3(5) °C for 10 sec. Note the clear circular region of high FRET molecules (red), corresponding to duplex constructs that have undergone dissociation, while the surrounding low FRET species (green) remain in the duplex conformation.

As a result, most molecules heated by the infrared laser reside in the closed conformation (red, high FRET), while those around the periphery remain in the duplex conformation (green, low E_{FRET}). Long-term exposure to elevated temperatures is capable of inducing duplex dissociation in a 21 bp DNA double helix, with the same duplexes more or less indefinitely stable at room temperature. Therefore, we exploit the excellent spatial, temporal and thermal control of the IR overtone heating laser to systematically tune the (*i*) temperature change and (*ii*) heating duration

(Δt) in order to extract the temperature-dependence of the DNA duplex dissociation rate constant.

The degree of duplex dissociation for a given heating duration (Δt) and steady-state temperature (T) can be quantified via the single molecule survival probability, $S(\Delta t,T)$, corrected for loss of construct from view due to other channels such as photobleaching and disruption of the biotin-streptavidin linkage. To extract $S(\Delta t,T)$, one generates a mask (Figure 4.5b) that identifies the number of individually immobilized molecules prior to the heating pulse with both Cy3/Cy5 dyes and in the duplex conformation ($N_{\text{duplex}}[0]$). After exposure to the heating cycle, the sample area is overlaid with the same mask (Figure 4.5c), in order to determine the number of remaining molecules in the duplex conformation ($N_{\text{duplex}}[\Delta t,T]$) as well as the very small number N' (where $N' << N_{\text{duplex}}[0]$) removed via parallel pathways such as photobleaching or irreversible dissociation of the biotin –strepavidin linkage. Corrected for these loss channels (e.g., $N'_{\text{duplex}}[0] = N_{\text{duplex}}[0] - N'$), the survival probability $S(\Delta t,T)$ can simply be calculated via.

$$S(\Delta t,T) = N_{\text{duplex}}[\Delta t,T]/\, N'_{\text{duplex}}[0] \qquad \text{(Eq. 4.2)}$$

The survival probability is monitored as a function of heating duration (Dt) and temperature (T) in order to probe the underlying kinetics mechanism of temperature-induced dissociation of a 21bp DNA duplex.

In order to correctly analyze these heating pulse experiments, one must make two kinetic assumptions. The first is that the duplex dissociation kinetics are negligible at room temperature, and only contribute during the heating episode. This is readily confirmed by the fact that surface immobilized constructs do not change FRET states over many hours in the absence of the heating laser. The second assumption is that the dissociation event is irreversible, with the liberated splint strand unable to re-form the duplex conformation. Since duplex association is a bimolecular process, this assumption is clearly valid, as the dissociated splint strand quickly diffuses into the bulk to form a solution of vanishingly low concentration.

Pulsed-heating experiments are performed to measure the survival probability as a function of the heating pulse steady-state temperature (T = 55.2(5) to 64.9(5) °C) and duration (Δt = 50-1000 ms). The results of these experiments clearly demonstrate that measured values of the $S(\Delta t,T)$ remain near unity for sufficiently short heating durations (< 100 ms) regardless of pulse temperature. As the heating duration increases, $S(\Delta t,T)$ decreases with a distinctly sigmoidal shape, i.e., with the initial $\partial^2 S/ \partial^2 t < 0$ and a clear inflection point uncharacteristic of purely single exponential decay kinetics. The impact of heating duration on the kinetics is quite clear from Figure 4.7a, with the time scale for achieving half-maximal survival probabilities decreasing rapidly with increasing temperature. It is worth stressing that such a heating protocol makes it possible to obtain kinetic information at elevated temperatures using standard fluorescent dyes, since the fluorescence photons are harvested only under room temperature conditions where high quantum yields have been reestablished.

We next consider the simple kinetic models necessary to describe these observed $S(\Delta t,T)$ plots for each of the four heating series. First of all, it is important to note that for any dissociation process over a single rate-limiting barrier (e.g. duplex → hairpin). For such a process, the survival probability would be described by a simple single-exponential decay (Eq. 4.3) with a rate constant, $k_{diss}(T)$, that depends on the steady-state temperature of the heating pulse.

$$S(\Delta t,T) = e^{-\Delta t\, k_{diss}(T)} \qquad \text{(Eq. 4.3)}$$

However, this model would predict a conventional convex shape (i.e., with initial $\partial^2 S/\partial^2 t > 0$) lacking an inflection point and inconsistent with the data. Instead, the experimental survival probabilities clearly reveal an anomalous “lag time” at short heating durations (Figure 4.7a), which necessarily requires description by a *higher* than first order kinetic model. The simplest such model is that of consecutive first-order reactions (e.g., $\mathbf{D_0} \rightarrow \mathbf{D_1} \rightarrow \mathbf{C}$) where $\mathbf{D_0}$ and $\mathbf{D_1}$ represents some partially dissociated duplex conformation (i.e., still low FRET), whereas **C** corresponds to the spectroscopically distinguishable closed (high FRET) conformation accessible only by dissociation of the full duplex.

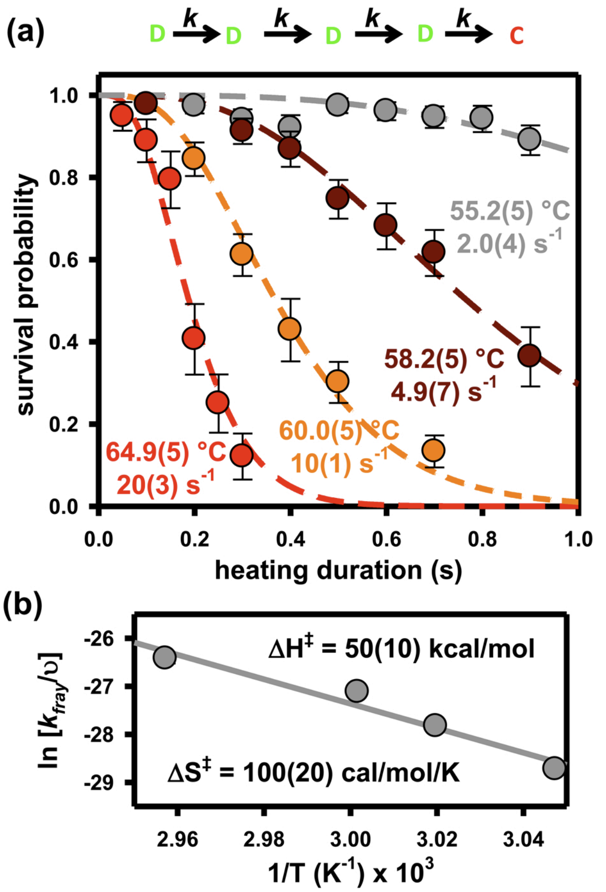

Figure 4.7 (a) DNA duplex survival probability data, $S(\Delta t,T)$, as a function of heating duration, Δt, at four steady-state heating pulse temperatures. Dashed lines represent least squares fit to a consecutive first order reaction model, which yields n = 4.1(3) sequential reaction steps with an assumed identical rate constant. Notice the rapid increase in this rate constant with increasing temperature, which implies a large endothermic component the transition state barrier. **(b)** Eyring transition state analysis of the temperature-dependent rate constant, suggesting a highly endothermic ($\Delta H^{\ddagger}$ = 50(10) kcal/mol) and entropically rewarding ($\Delta S^{\ddagger}$ = 100(20 cal/mol/K) component of the free energy barrier for each of the fraying events.

In such a kinetic model, the "lag time" arises from the first order kinetics of $\mathbf{D_0}$ needing to form $\mathbf{D_1}$ prior to forming the detected species **C**. Even more likely, there could be a series of *n* such intermediate species (e.g., $\mathbf{D_0} \rightarrow \mathbf{D_1} \cdots\rightarrow \mathbf{D}_n \rightarrow \mathbf{C}$), which impact both the lag time as well as the cooperative sharpness of the sigmoidal behavior. If all *n* of the rate constants associated with the steady-state temperature of the heating pulse, $k(T)$, are all nearly identical, the solution to this *n*-step first order consecutive kinetic model can be solved exactly to yield

$$S(\Delta t, T) = \frac{\Gamma(n, k(T)\Delta t)}{\Gamma(n)} \qquad \text{(Eq. 4.4)}$$

where $\Gamma(n)$ and $\Gamma(n,k(T)\Delta t)$ are the gamma function and incomplete gamma function, respectively. Successful examples of the application of sequential chemical reaction models to biological systems include both DNA helicases(37,38), as well as strand exchange induced by RecA(39). Application of this model to the present experiments involves fitting the data in Figure 4.7a to extract the two fitted parameters: (*i*) the rate constant for each of the steady-state temperatures associated with the infrared heating pulse, $k(T)$, and (*ii*) the number of consecutive steps, *n*. The results of a least-squares analysis of the data yield $n = 4.1(3)$, which in the context of such a model would suggest that there may be four consecutive steps prior to complete duplex dissociation. Furthermore, the values of $k(T)$ increase dramatically with relatively small increase in temperature, which would be consistent with the four sequential steps having to surmount strongly endothermic free energy barriers. Other more complex kinetic models can of course fit the data. However, the success of this simple consecutive first order reaction picture with $n \approx 4$ proves a useful starting point, from which insights into the duplex dissociation event may be developed further below.

4.4 Duplex Dissociation Model

Since the discovery of the dsDNA structure (40), there has considerable effort directed toward understanding the fundamental kinetics and thermodynamics for duplex dissociation and association events (41). A significant amount of work has been directed at characterizing the forward association process, in particular highlighting the importance of pre-helical structures for oligonucleotide strands forming the duplex(42-44). For corresponding studies of the duplex dissociation process, however, there has been much less consensus regarding the explicit dissociation mechanism, with conflicting reports of single-exponential(45-47), stretched-exponential(48), and bi-exponential kinetic behavior(49,50) for different oligo length systems and experimental conditions. The present single molecule heating results confirm that the DNA duplex dissociation kinetics are distinctly non-single exponential for a 21 bp DNA duplex. Specifically, the "lag time" dissociation behavior observed in these studies is fundamentally inconsistent with that of an isolated rate process over a single transition state barrier. Instead, the dissociation kinetics are more correctly described by an first order consecutive model with $n \approx 4$ matching rate constants that increase rapidly with temperature.

This suggests a simple, physically motivated mechanism for duplex dissociation; specifically, "fraying" of the 21 bp DNA duplex can occur from *either* of the two ends of the helix. Before developing this model further, it is first important to note the pitch of the DNA double helix is about 10 bp per 360° (51) and largely restricted by base-stacking interactions(52). Thus, for a DNA duplex longer than 10 bp, simple structural constraints make it physically difficult to dissociate without major disruption of the helical pitch. This alone would suggest that duplexes longer than 9 bp must initially peel apart (i.e., "fray") at one or both ends to generate a sufficiently short duplex that can then undergo rapid dissociation in a single step. For the 21 bp

DNA duplexes in this study, this would require fraying of at least 12 bp. Although fraying can occur entirely from one end, dissociation preceded by symmetrical fraying of at least 6 base pairs from *each* end would be much more highly favored by simple Poisson considerations. Specifically, the statistical ratio between N base pairs fraying from *two* ends vs 2N base pairs fraying from *one* end is readily shown to be $(2N)!/(N!)^2$, which for N = 6 is already 924:1.

Similar ideas in the literature have been used to help interpret dissociation(45) and end-fraying(53-55) dynamics of DNA duplexes. These studies of end-fraying dynamics at temperatures well below the melting point of the DNA duplex have been able to measure small changes in the terminal base pairs that occur on the 10^{-7} s time-scale. Of course, the present analysis associated with the *n*-step consecutive first-order kinetic model is clearly not sensitive to individual bp fraying steps, but instead appears to be consistent with approximately four fraying steps with 3-5 base pair disruptions in each (see Figure 4.8). For the four consecutive fraying events, Poisson considerations suggest that fraying from both ends would be six-fold times more likely than fraying entirely from one end. Additionally, with more than 3 base pair disruptions in each of the observed fraying events, it is not surprising that the time-scale for this process is orders of magnitude slower than what has been measured for single base pair fraying dynamics(53,54). Therefore, it is reasonable to suggest that the 21 bp DNA duplex used in these pulsed heating experiments dissociates via the following pathway: Two fraying events, of 3-5 bp each, must occur at the two ends of the DNA duplex, giving rise to a highly frayed intermediate with only a small number (1-9) of remaining base pairing interactions. This intermediate is then able to dissociate in a rapid (i.e. non-rate-limiting) step into the two individual oligonucleotides, as schematically depicted in Figure 4.8.

We note that this highly simplified analysis of the duplex dissociation kinetics is based on a series of rate-limiting steps due to fraying from both ends of the helix to fewer than 10 remaining bp, followed by rapid dissociation of the remaining duplex. Recently published single-molecule experiments have investigated the association/dissociation kinetics of smaller DNA duplexes (6-9 bp) as a function of temperature (56).

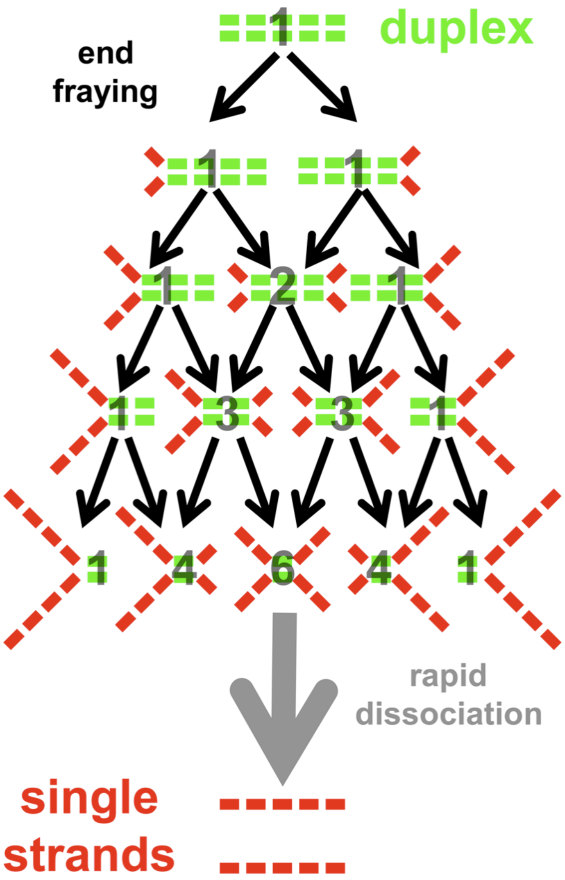

Figure 4.8 Model depicting the “consecutive fraying at both ends” mechanism for duplex dissociation. The colored bars represent short segments of the 21 bp DNA duplex that are either associated (green) or dissociated (red). The transparent black numbers correspond to the relative abundance of each partially dissociated species as predicted by a binomial distribution. After four consecutive fraying events, the single remaining associated (green) segment of the duplex is sufficiently frayed to undergo a final rapid dissociation step (see Section 4.4 for details).

The results of these experiments strongly support the assumption of rapid single-exponential survival probabilities for short DNA duplex that at elevated temperatures. Specifically, if one extrapolates to the higher temperatures (65 °C) in the present study, the temperature-dependent single-exponential rate constants for duplex dissociation would be > 10^4 s^{-1}. This is already considerably faster than the range of rate constants obtained in Figure 4.7 and thus consistent with the notion of rate-limiting symmetrical fraying to the center from both ends, prior to a rapid (non-rate limiting) dissociation step. As a final topic, the measured temperature-dependence of the $n \approx 4$ sequential fraying rate constants can be used to extract thermodynamic information about the fraying process itself. Specifically, from Eyring transition state theory, the experimentally measured duplex dissociation rate constant is given by

$$k(T) = \upsilon e^{(-\Delta G^{\ddagger}/kT)} = \upsilon e^{(-\Delta H^{\ddagger}/kT)} e^{(-\Delta S^{\ddagger}/k)} \qquad \text{(Eq. 4.5)}$$

where υ is some characteristic vibrational attempt frequency for the fraying event. We can therefore formulate an Eyring transition state plot of $\ln[k/\upsilon]$ vs 1/T to provide key additional information on the enthalpy (slope) and entropy (intercept) components of the free energy barrier. Such an analysis is shown in Figure 4.7b, which predicts a large enthalpic transition state barrier of $\Delta H^{\ddagger} = 50(10)$ kcal/mol and is consistent with breaking several base pair interactions in each of the four fraying events for the DNA duplex. Indeed, for a mean dissociation enthalpy of ≈ 8.4 kcal/mol/bp obtained from nearest neighbor modeling(57), this would be consistent with an average of ≈ 6(1) base pair disruptions in each of the 4 consecutive fraying processes. Similarly, the corresponding entropy change from such an Eyring plot is found to be large and positive, $\Delta S^{\ddagger} = 100(20)$ cal/mol/K, which from a nearest neighbor modeling of the average entropy (22.4 cal/mol/K/bp) would suggest disruption of ≈ 4.5(9) base pairs in each of the 4 fraying events. Although such an analysis is clearly not intended to be quantitative, these values are at least consistent with end fraying of the DNA duplex down to a small of base pairs prior to a final (non-rate-limiting) dissociation event**.** Clearly an interesting next step would be to further explore such dissociation kinetics as a function of sequence and length of the DNA duplexes, which would be necessary to further refine such a multi-step consecutive fraying mechanism for duplex oligonucleotide dissociation.

4.5 Conclusions

This work provides a detailed description and quantitative characterization of the overtone laser infrared-absorption heating method for applications in single molecule fluorescence studies, which highlight several key advantages over conventional bulk heating microscopy methods. First of all, the technique provides controlled and highly reproducible experimental access to sample temperatures from 20 °C up to the boiling point ($\Delta T \approx 80$ °C), greatly exceeding the operating temperature ranges accessible by conventional stage-objective heating. Secondly, use of high quality TEM_{00} mode laser sources permits exceptionally high spatial control and confinement of the heated volume, with typical sample regions on the order of 10^{-10} liters or less. Finally, this optical laser-based infrared heating system is able to achieve controlled rises in sample temperatures with a half-maximal heating time of about 1 ms, which is many tens of thousand times faster than the minute to hour time scales of conventional stage-based methods.

Additionally, this work demonstrates the greater utility of this optical laser heating technique by performing pulsed heating experiments. Specifically, single-molecule dissociation kinetics of single DNA duplexes have been studied by elevating the sample temperature by a well-characterized amount for a well-characterized duration. Most importantly, the rapid heating and cooling properties of the system offer the ability to access kinetics at high sample temperatures without the need for temperature-stable fluorescent dyes. These temperature cycling dissociation studies provide useful kinetic insight into the mechanism by which a 21 bp

DNA duplex undergoes dissociation. In particular, the kinetic data reveal a clear sigmoidal time lag in the appearance of the dissociated duplex. This is qualitatively inconsistent with any single exponential rate process and indeed is more consistent with $n \approx 4$ sequential first order pathways. The current working model for this behavior is that DNA dissociation over this range of duplex lengths is constrained by the helical twist, which makes dissociation occur from a short interior region resulting from rapid "fraying" at both ends toward the middle. Specifically, fraying inward with two separate rate processes from each end is shown to be six-fold more probable than all four processes occurring from a single end, with rapid dissociation occurring when the duplex is sufficiently frayed from both ends. In summary, the results of this study provide a "proof-of-principle" demonstration for pulsed laser heating studies of single-molecule kinetics with high spatial ($< 10^{-10}$ liter) and temporal (≈ 1 ms) control of sample temperatures, as well as help elucidate the role of sequential, first order kinetic pathways in the dissociation of DNA duplexes.

4.6 Experimental Methods

4.6.1 Fluorescent Oligonucleotides

A synthetically-modified, double-stranded DNA construct is purchased from a commercial supplier. The construct consists of two oligonucleotides. The first oligonucleotide (reporter strand) sequence is: 5'-|Cy3| CCC TTG |$(PEG)_{18}$| CAA GGG CTC AGA CGA GTG |internal Cy5| AAA AAA AAA AAA |Biotin|-3'. The second oligonucleotide (splint strand) sequence is: 5'-CAC TCG TCT GAG CCC TTG CAA-3'. The 36 nt reporter strand is annealed to the 21 nt splint strand that is complementary with nucleotides 4-24 of the reporter strand, forming a continuous 21 bp DNA duplex (Figure 4.5a).

4.6.2 Sample Preparation

All experiments are performed in 1-2 mm wide channels created by two pieces of 85 µm thick double-sided sticky tape between a 170 µm thick glass coverslip and a 1 mm thick glass microscope slide. Samples containing 575 nM Rhodamine B in water are used to measure the temperature in all experiments designed to characterize the infrared-heating system.

4.6.3 Fluorescence Microscope

All fluorescence data are acquired on a previously described inverted confocal microscope(58). Briefly, a pulsed (10 ps, 20 MHz) excitation source (532 nm) is directed into the back aperture of a 1.2 NA water-immersion objective via a dichroic mirror, with the resulting fluorescence emission collected from the diffraction-limited excitation volume by the same objective. The fluorescence photons are then spatially separated by dichroics and polarization beam splitters onto four single-photon avalanche photodiodes (APDs), where a time-correlated single-photon counting (TCSPC) module records the arrival time of each photon with respect to both the most recent laser pulse (microtime) as well as the start of the experiment (macrotime). The microtime data are used for fluorescence lifetime measurements, while the macrotime data permit one to reconstruct time trajectories of fluorescence intensity, E_{FRET}, lifetime, and temperature with arbitrary choice of temporal binning.

4.6.4 Duplex Dissociation Experiments

For all duplex dissociation experiments the pre-annealed reporter-splint DNA duplex is immobilized to the glass surfaces using previously establish biotin-streptavidin surface immobilization techniques. The PCD/PCA oxygen-scavenging system is used to increase the photophysical stability of the Cy3/Cy5 FRET pair(59). All experiments are performed at room temperature (≈ 23.2 °C) in a buffer containing: 50 mM hemisodium HEPES, 100 mM NaCl, 100 μM EDTA, 2.0 mM TROLOX, 5.0 mM PCA, 100 nM PCD, 10 mM KOH, pH 7.5. Duplex dissociation data is collected using a second excitation source to perform Alternating Laser EXcitation (ALEX) imaging(60,61). Briefly, a red (636 nm) pulsed excitation source triggers on the green (532 nm) 20 MHz primary excitation source. A 25 ns delay places the red laser pulses exactly half way between green laser pulses. ALEX provides the ability to filter molecules by fluorescence, in order to ensure that only data obtained from dually-labeled fluorescent DNAs are considered in the analysis.

4.7 References

1. Joo, C.; H. Balci; Y. Ishitsuka; C. Buranachai; T. Ha. Advances in single-molecule fluorescence methods for molecular biology, *Annu. Rev. Biochem.*, **2008,** *77*, 51-76.

2. Roy, R.; S. Hohng; T. Ha. A Practical Guide to Single-Molecule FRET, *Nat. Methods*, **2008,** *5*, 507-516.

3. Zhao, R.; D. Rueda. RNA folding dynamics by single-molecule fluorescence resonance energy transfer, *Methods*, **2009,** *49*, 112-117.

4. Holmstrom, E. D.; J. L. Fiore; D. J. Nesbitt. Thermodynamic origins of monovalent facilitated RNA folding, *Biochemistry*, **2012,** *51*, 3732-3743.

5. Tarsa, P. B.; R. R. Brau; M. Barch; J. M. Ferrer; Y. Freyzon; P. Matsudaira; M. J. Lang. Detecting force-induced molecular transitions with fluorescence resonant energy transfer, *Angew. Chem. Int. Ed.*, **2007,** *46*, 1999-2001.

6. Shroff, H.; B. M. Reinhard; M. Siu; H. Agarwal; A. Spakowitz; J. Liphardt. Biocompatible force sensor with optical readout and dimensions of 6 nm(3), *Nano Lett.*, **2005,** *5*, 1509-1514.

7. Fiore, J. L.; B. Kraemer; F. Koberling; R. Erdmann; D. J. Nesbitt. Enthalpy-Driven RNA Folding: Single-Molecule Thermodynamics of Tetraloop–Receptor Tertiary Interaction, *Biochemistry*, **2009,** *48*, 2550–2558.

8. Graneli, A.; C. C. Yeykal; R. B. Robertson; E. C. Greene. Long-distance lateral diffusion of human Rad51 on double-stranded DNA, *Proc. Natl. Acad. Sci. USA*, **2006,** *103*, 1221-1226.

9. Fiore, J. L.; E. D. Holmstrom; D. J. Nesbitt. Entropic Origin of Mg^{2+}-Facilitated RNA Folding, *Proc. Natl. Acad. Sci. USA*, **2012,** *109*, 2902-2907.

10. Zhao, R.; M. Marshall; E. A. Aleman; R. Lamichhane; A. Feig; D. Rueda. Laser-assisted single-molecule refolding (LASR), *Biophys. J.*, **2010,** *99*, 1925-1931.

11. Gross, P.; G. Farge; E. J. G. Peterman; G. J. L. Wuite. Combining optical tweezers, single-molecule fluorescence microscopy, and microfluidics for studies of DNA-protein interactions, *Method Enzymol.*, **2010,** *475*, 427-453.

12. Holmstrom, E. D.; D. J. Nesbitt. Real-time infrared overtone laser control of temperature in picoliter H_2O samples: "Nanobathtubs" for single-molecule microscopy, *J. Phys. Chem. Lett.*, **2010,** *1*, 2264–2268.

13. Braun, D.; A. Libchaber. Trapping of DNA by thermophoretic depletion and convection, *Phys. Rev. Lett.*, **2002,** *89*, 188103.

14. Slyadnev, M. N.; Y. Tanaka; M. Tokeshi; T. Kitamori. Photothermal temperature control of a chemical reaction on a microchip using an infrared diode laser, *Anal. Chem.*, **2001,** *73*, 4037–4044.

15. Mao, H. B.; J. R. Arias-Gonzalez; S. B. Smith; I. Tinoco; C. Bustamante. Temperature control methods in a laser tweezers system, *Biophys. J.*, **2005,** *89*, 1308–1316.

16. Peterman, E. J. G.; F. Gittes; C. F. Schmidt. Laser-induced heating in optical traps, *Biophys. J.*, **2003,** *84*, 1308–1316.

17. Zondervan, R.; F. Kulzer; H. van der Meer; J. A. Disselhorst; M. Orrit. Laser-driven microsecond temperature cycles analyzed by fluorescence polarization microscopy, *Biophys. J.*, **2006,** *90*, 2958-2969.

18. Yuan, H.; T. Xia; B. Schuler; M. Orrit. Temperature-cycle single-molecule FRET microscopy on polyprolines, *Phys. Chem. Chem. Phys.*, **2011,** *13*, 1762-1769.

19. Wieliczka, D. M.; S. S. Weng; M. R. Querry. Wedge shaped cell for highly absorbent liquids: Infrared optical constants of water, *Appl. Opt.*, **1989,** *28*, 1714–1719.

20. Hung, M. S.; O. Kurosawa; M. Washizu. Single DNA molecule denaturation using laser-induced heating, *Mol. Cell. Probes*, **2012,** *26*, 107-112.

21. Holmberg, A.; A. Blomstergren; O. Nord; M. Lukacs; J. Lundeberg; M. Uhlen. The biotin-streptavidin interaction can be reversibly broken using water at elevated temperatures, *Electrophoresis*, **2005,** *26*, 501-510.

22. Sanborn, M. E.; B. K. Connolly; K. Gurunathan; M. Levitus. Fluorescence properties and photophysics of the sulfoindocyanine Cy3 linked covalently to DNA, *J. Phys. Chem. B.*, **2007,** *111*, 11064-11074.

23. Marras, S. A. Selection of fluorophore and quencher pairs for fluorescent nucleic acid hybridization probes, *Methods Mol. Biol.*, **2006,** *335*, 3-16.

24. Hyre, D. E.; I. Le Trong; E. A. Merritt; J. F. Eccleston; N. M. Green; R. E. Stenkamp; P. S. Stayton. Cooperative hydrogen bond interactions in the streptavidin-biotin system, *Protein Sci.*, **2006,** *15*, 459-467.

25. Selvin, P. R.; T. Ha, (Eds.) (2008) *Single-molecule Techniques: A Laboratory Manual*, Cold Spring Harbor Laboratory Press, Cold Spring Harbor, NY.

26. Lamichhane, R.; A. Solem; W. Black; D. Rueda. Single-molecule FRET of protein-nucleic acid and protein-protein complexes: Surface passivation and immobilization, *Methods*, **2010,** *52*, 192-200.

27. Akabayov, B.; A. Henn; G. Nautrup-Pedersen; M. Elbaum; I. Sagi. (2002) Immobilization of RNA: application to single molecule spectroscopy, In *Molecular,*

Cellular and Tissue Engineering, 2002. Proc. IEEE-EMBS Special Topic Conference, pp 71-72.

28. Janissen, R.; L. Oberbarnscheidt; F. Oesterhelt. Optimized straight forward procedure for covalent surface immobilization of different biomolecules for single molecule applications, *Colloid. Surface B.*, **2009,** *71*, 200-207.

29. Aleman, E. A.; H. S. Pedini; D. Rueda. Covalent-bond-based immobilization approaches for single-molecule fluorescence, *ChemBioChem*, **2009,** *10*, 2862-2866.

30. Schwartz, J. J.; S. Stavrakis; S. R. Quake. Colloidal lenses allow high-temperature single-molecule imaging and improve fluorophore photostability, *Nat. Nanotechnol.*, **2010,** *5*, 127-132.

31. Altman, R. B.; D. S. Terry; Z. Zhou; Q. Zheng; P. Geggier; R. A. Kolster; Y. Zhao; J. A. Javitch; J. D. Warren; S. C. Blanchard. Cyanine fluorophore derivatives with enhanced photostability, *Nat. Methods*, **2012,** *9*, 68-71.

32. Chen, Y. Y.; A. W. Wood. Application of a temperature-dependent fluorescent dye (Rhodamine B) to the measurement of radiofrequency radiation-induced temperature changes in biological samples, *Bioelectromagnetics*, **2009,** *30*, 583-590.

33. Karstens, T.; K. Kobs. Rhodamine B and rhodamine 101 as reference substances for fluorescence quantum yield measurements, *J. Phys. Chem.*, **1980,** *84*, 1871–1872.

34. Casey, K. G.; E. L. Quitevis. Effect of solvent polarity on nonradiative processes in xanthene dyes: Rhodamine B in normal alcohols, *J. Phys. Chem.*, **1988,** *92*, 6590.

35. Maus, M.; M. Cotlet; J. Hofkens; T. Gensch; F. C. De Schryver; J. Schaffer; C. A. M. Seidel. An experimental comparison of the maximum likelihood estimation and nonlinear least squares fluorescence lifetime analysis of single molecules, *Anal. Chem.*, **2001,** *73*, 2078-2086.

36. Nesbitt, D. J.; N. F. Dupuis; E. D. Holstrom. Single Molecule Studies of Streptavidin-Biotin Dissociation at Elevated Temperatures, *Biophys. J.*, **2012,** *102*, 270a.

37. Lucius, A. L.; N. K. Maluf; C. J. Fischer; T. M. Lohman. General methods for analysis of sequential "n-step" kinetic mechanisms: application to single turnover kinetics of helicase-catalyzed DNA unwinding, *Biophys. J.*, **2003,** *85*, 2224-2239.

38. Park, J.; S. Myong; A. Niedziela-Majka; K. S. Lee; J. Yu; T. M. Lohman; T. Ha. PCRA helicase dismantles RecA filaments by reeling in DNA in uniform steps, *Cell*, **2010,** *142*, 544-555.

39. Ragunathan, K.; C. Joo; T. Ha. Real-time observation of strand exchange reaction with high spatiotemporal resolution, *Structure*, **2011,** *19*, 1064-1073.

40. Watson, J. D.; F. H. C. Crick. Molecular structure of nucleic acids - a structure for deoxyribose nucleic acid, *Nature*, **1953,** *171*, 737-738.

41. Porschke, D.; O. C. Uhlenbeck; F. H. Martin. Thermodynamics and kinetics of helix-coil transition of oligomers containing GC base pairs, *Biopolymers*, **1973,** *12*, 1313-1335.

42. Dewey, T. G.; D. H. Turner. Laser temperature jump study of solvent effects on poly(adenylic acid) stacking, *Biochemistry*, **1980,** *19*, 1681-1685.

43. Freier, S. M.; K. O. Hill; T. G. Dewey; L. A. Marky; K. J. Breslauer; D. H. Turner. Solvent Effects on the Kinetics and Thermodynamics of Stacking in Poly(Cytidylic Acid), *Biochemistry*, **1981,** *20*, 1419-1426.

44. Dewey, T. G.; D. H. Turner. Laser temperature-jump study of stacking in adenylic acid polymers, *Biochemistry*, **1979,** *18*, 5757-5762.

45. Ikuta, S.; K. Takagi; R. B. Wallace; K. Itakura. Dissociation kinetics of 19 base paired oligonucleotide-DNA duplexes containing different single mismatched base pairs, *Nucleic Acids Res.*, **1987,** *15*, 797-811.

46. Sauer-Budge, A. F.; J. A. Nyamwanda; D. K. Lubensky; D. Branton. Unzipping kinetics of double-stranded DNA in a nanopore, *Phys. Rev. Lett.*, **2003,** *90*, 238101.

47. Liphardt, J.; B. Onoa; S. B. Smith; I. Tinoco, Jr.; C. Bustamante. Reversible unfolding of single RNA molecules by mechanical force, *Science*, **2001,** *292*, 733-737.

48. Biancaniello, P. L.; A. J. Kim; J. C. Crocker. Long-time stretched exponential kinetics in single DNA duplex dissociation, *Biophys. J.*, **2008,** *94*, 891-896.

49. Gunnarsson, A.; P. Jonsson; V. P. Zhdanov; F. Hook. Kinetic and thermodynamic characterization of single-mismatch discrimination using single-molecule imaging, *Nucleic Acids Res.*, **2009,** *37*, e99.

50. Tawa, K.; W. Knoll. Mismatching base-pair dependence of the kinetics of DNA-DNA hybridization studied by surface plasmon fluorescence spectroscopy, *Nucleic Acids Res.*, **2004,** *32*, 2372-2377.

51. Sinden, R. R. (1994) *DNA Structure and Function*, Academic Press, San Diego, CA.

52. Yakovchuk, P.; E. Protozanova; M. D. Frank-Kamenetskii. Base-stacking and base-pairing contributions into thermal stability of the DNA double helix, *Nucleic Acids Res.*, **2006,** *34*, 564-574.

53. Porschke, D. A direct measurement of the unzippering rate of a nucleic acid double helix, *Biophys. Chem.*, **1974,** *2*, 97-101.

54. Nikolova, E. N.; H. M. Al-Hashimi. Preparation, resonance assignment, and preliminary dynamics characterization of residue specific 13C/15N-labeled elongated DNA for the study of sequence-directed dynamics by NMR, *J. Biomol. NMR*, **2009,** *45*, 9-16.

55. Porschke, D. Model calculations on the kinetics of oligonucleotide double helix coil transitions. Evidence for a fast chain sliding reaction, *Biophys. Chem.*, **1974,** *2*, 83-96.

56. Dupuis, N. F.; E. D. Holmstrom; D. J. Nesbitt. Single-Molecule Kinetics Reveal Cation-Promoted DNA Duplex Formation Through Ordering of Single-Stranded Helices, *Biophys. J.*, **2013,** *105*, 756-766.

57. SantaLucia, J. A unified view of polymer, dumbbell, and oligonucleotide DNA nearest-neighbor thermodynamics, *Proc. Natl. Acad. Sci. USA*, **1998,** *95*, 1460-1465.

58. Hodak, J. H.; C. D. Downey; J. L. Fiore; A. Pardi; D. J. Nesbitt. Docking kinetics and equilibrium of a GAAA tetraloop-receptor motif probed by single-molecule FRET, *Proc. Natl. Acad. Sci. USA*, **2005,** *102*, 10505–10510.

59. Aitken, C. E.; R. A. Marshall; J. D. Puglisi. An Oxygen Scavenging System for Improvement of Dye Stability in Single-Molecule Fluorescence Experiments, *Biophys. J.*, **2008,** *94*, 1826-1835.

60. Kapanidis, A. N.; T. A. Laurence; N. K. Lee; E. Margeat; X. Kong; S. Weiss. Alternating-laser excitation of single molecules, *Acc. Chem. Res.*, **2005,** *38*, 523-533.

61. Lee, N. K.; A. N. Kapanidis; Y. Wang; X. Michalet; J. Mukhopadhyay; R. H. Ebright; S. Weiss. Accurate FRET Measurements within Single Diffusing Biomolecules using Alternating-Laser Excitation, *Biophys. J.*, **2005,** *88*, 2939-2953.

Chapter 5

Thermodynamic Origins of Monovalent-Facilitated RNA Folding*

5.1 Introduction

Over the last ten years, the number of structures and functions attributed to specific non-coding RNA sequences has grown significantly(1) and radically advanced the field of RNA biology. These structures are the result of a number of smaller molecular interactions (e.g., tertiary interactions), which stabilize the global conformation of RNAs(2). However, it is important to note that these structures, although extremely helpful, represent only static images of RNA in a near minimum energy conformation. Under more physiological conditions, these molecules can be richly dynamic and occupy a broad ensemble of thermally accessible structures(3-5). The conformational dynamics of RNA tertiary interactions contribute to the diverse array of functionality(6).

Since RNA molecules are anionic biopolymers, they are always accompanied with counterions in solution regardless of conformation. These counterions interact favorably with the electrostatic potential of the RNA giving rise to an "ion atmosphere." For RNA to achieve a specific three-dimensional conformation it must undergo any number of structural transitions, most of which result in a more compact structure. Additional cation uptake into the ion atmosphere can help alleviate the enhanced intramolecular columbic repulsion associated with a more compact conformation. A number of studies suggest that entropic considerations are largely responsible for cation-facilitated stabilization of folded structures(7-9). One explanation

---

* Adapted from: Holmstrom, Erik D; Fiore, Julie L; Nesbitt, David J. *Biochemistry.* ***2012**, 51, 3732-3743*

for this entropic promotion is as follows. As an RNA undergoes a structural transition to a more charge-dense state, additional counterions are brought from the bulk solution to the pre-existing ion atmosphere as a result of the elevated charge density. This restricts the translational freedom of those ions and thus gives rise to an entropic penalty associated with “unmixing” the solution. At higher bulk concentrations, it is less entropically costly to unmix counterions that were taken up during the folding transition, thus reducing the entropic cost of the folding transition. Single-molecule experiments provide a relatively unexplored technique that can be used to quantitatively measure the salt-dependence of RNA folding thermodynamics and represents the major focus of this work.

The cytosol contains cations of multiple valencies, each of which can interact with the electrostatic potential of the RNA and thus facilitate folding(4,10-12). A number of RNAs are capable of adopting stable, native, tertiary structures in solutions consisting solely of monovalent ions(13-16). Focusing on monovalent-facilitated folding provides a crucial conceptual simplification for both experiment and theory by avoiding complications associated with mixed solutions of monovalent, divalent, and higher valence cations. In turn, these simple models serve as critical benchmarks for accurately testing our ability to predict thermodynamics of RNA folding under realistic cellular conditions.

Much work has been directed at understanding the role that monovalent ions play in the folding of structured RNAs(17-20). Generally, monovalents are capable of interacting with RNAs through a variety of distance-dependent modes, ranging from totally diffuse to completely chelated. The most direct mode of interaction is chelation of an ion(21,22), whereby the ion loses multiple water molecules in its primary sphere of hydration in order to make direct, stabilizing contact with the electronegative atoms of the RNA. These specific ion interactions are not dominant and therefore have a minimal effect on net charge neutralization for a single RNA in solution(23), though with potentially more significant effects on enzymatic activity(21). Diffuse ions have the most indirect mode of interaction with RNA. These ions interact only with the electrostatic potential of the RNA giving rise to the above-mentioned ion atmosphere(24). Of course there exists many other ways in which ions can interact with the RNA (e.g., indirect hydrogen bonding via the hydration layers associated with the solvated ion), but all of them fall between the extremes of chelated and diffuse ions. This work contributes to the understanding of how the various monovalent cation-RNA interactions alter the thermodynamics associated with formation of an isolated tetraloop–receptor tertiary interaction.

5.2 Molecular Model

RNAs are well known to fold in a hierarchical manner, with secondary structure forming on a relatively rapid time scale (ms to ms), followed by slower folding of the tertiary structure (ms to s). Thus, a commonly proposed framework in which to view equilibrium folding of RNA is: (25,26)

$$\mathbf{U} \Leftrightarrow \mathbf{I} \Leftrightarrow \mathbf{F}$$

where the unfolded state (**U**) corresponds to an RNA without extensive secondary interactions, and the intermediate state (**I**) describes an RNA with well formed secondary structure(27). The **I** state then proceeds to form tertiary interactions on much longer time scales, resulting in the final folded state, **F**. The present work focuses exclusively on tertiary interactions by making two additional assumptions: (*i*) secondary structure formation (**U ⇔ I)** is rapid relative to formation of tertiary contacts and (*ii*) experimental conditions are such that the equilibrium constant between **U** and **I** is much greater than unity. These assumptions allow for further simplification of the kinetic framework to

$$\mathbf{I} \Leftrightarrow \mathbf{F}$$

where the equilibrium constant (K_{eq}) is defined as the ratio of k_{fold} ($\mathbf{I} \Rightarrow \mathbf{F}$) to k_{unfold} ($\mathbf{I} \Leftarrow \mathbf{F}$). In this two-state equilibrium, both the macroscopic states **I** and **F** are likely composed of an ensemble of microscopic states. The Boltzmann-weighted averages of the ensembles are used to describe the macroscopic states, thus allowing for interpretations based on the two-state unimolecular equilibrium. This simplified two-state model proves sufficient to describe the formation of an individual tertiary interaction for the RNA construct in the present study.

The model RNA used to explore tertiary interactions in monovalent ion atmospheres is a synthetic RNA construct that isolates the GAAA tetraloop–receptor interaction (Figure 5.1)(28), as observed in the P4-P6 domain of the *Tetrahymena* ribozyme(29).

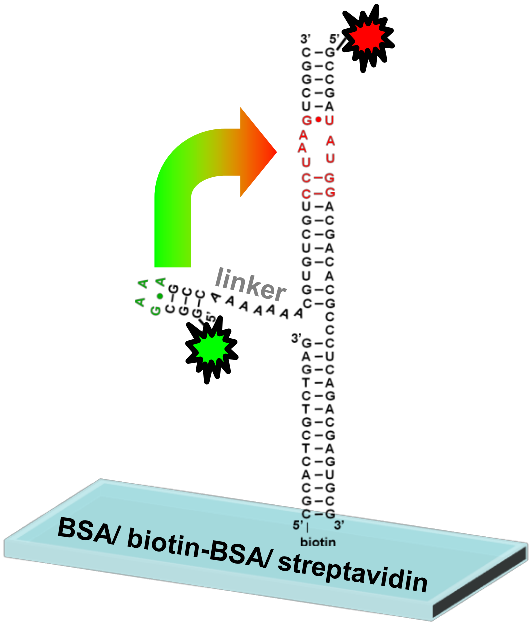

Figure 5.1 Schematic of the three-piece donor/acceptor label RNA construct. The isolated GAAA tetraloop–receptor serves as a model system to investigate the thermodynamics and kinetics of monovalent-facilitated formation of tertiary interactions in structured RNAs.

The construct is built from a three-piece oligonucleotide assembly that allows the GAAA tetraloop (green), tethered by a flexible poly-A_7 linker, to freely dock/undock into the 11 nt receptor domain (red). This tertiary interaction(30,31) has undergone extensive biochemical and biophysical characterization(32-36) making it a prime RNA folding motif for detailed kinetic/thermodynamic investigation. There also exists a significant amount of structural data for this RNA folding motif from a variety of RNA systems(21,32,37-40). Most relevantly, the tetraloop–receptor interaction is stably formed in solutions containing only monovalent ions(10), thus eliminating the complications associated with mixed monovalent and divalent ions in solution, and therefore making it an ideal RNA model to address the effect of monovalent cations on the formation of tertiary interactions. Additionally, the "binary" (folded/unfolded) nature of this tertiary interaction (Figure 5.2a) makes the isolated construct used in this study particularly useful by eliminating potential complications due to cooperative folding effects between multiple tertiary interactions.

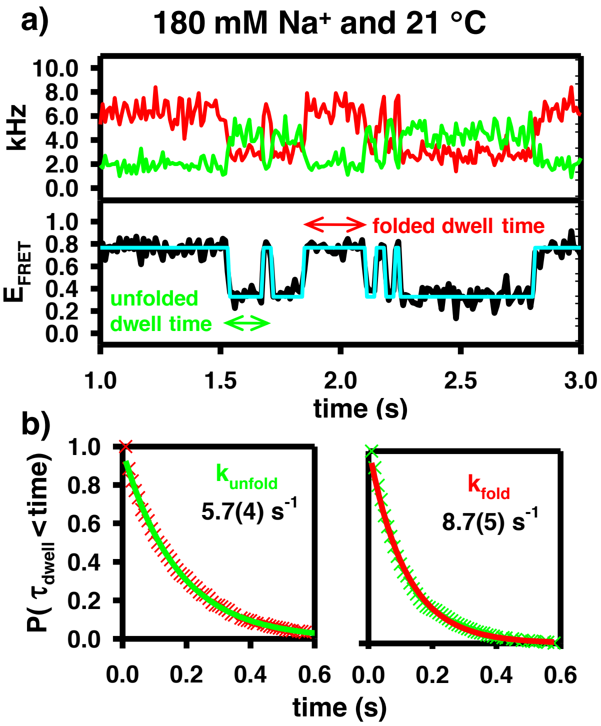

Figure 5.2 (a) Sample time trajectories for the model construct. A hidden Markov fit to the FRET trajectory is used to demonstrate the two-state behavior of folding process. **(b)** Cumulative distribution function (CDF) of the dwell times demonstrates single-exponential behavior and are used to extract unimolecular rate constants for folding and unfolding.

Lastly, the simplicity of the construct allows for the use of synthetic modifications (e.g. biotin and fluorescent dyes) necessary for single-molecule fluorescence resonance energy transfer (smFRET) experiments (Figure 5.1)(10,28,35,36). See Materials and Methods for details.

The smFRET experiments used throughout this work are conducted using a confocal fluorescent microscope equipped with time-correlated, two-color detection of single photons. This techniques provides the ability to measure, in real-time and under equilibrium conditions, the amount of time of a single molecule spends in a given conformation (Figure 5.2a)(41,42). In the framework of the previously described two-state model, the cumulative distribution function (CDF) of durations spent in either state (τ_{dwell}) will be exponentially distributed, determined by the characteristic decay constant k_{unfold} or k_{fold} (Figure 5.2b)(43-45). At a specific monovalent concentration and temperature, therefore, smFRET can be used to measure k_{fold}, k_{unfold}, and K_{eq} for the GAAA tetraloop–receptor interaction. In the present work, analysis of the equilibrium constants as a function of both temperature and [Na^+] is used to extract standard state thermodynamics ($\Delta G°$, $\Delta H°$, $\Delta S°$) for this isolated tertiary interaction. Additionally, the temperature dependence of the forward and reverse rate constants (k_{fold}, k_{unfold}) is used to obtain information about the enthalpic ($\Delta H^{\ddagger}$) and entropic ($\Delta S^{\ddagger}$) components of the free energy barrier ($\Delta G^{\ddagger}$) as a function of [Na^+].

5.3 Results

5.3.1 Folding Kinetics and Standard State Free Energy of Folding

As shown in the titration data in Figure 5.3a, increasing [Na^+] both *accelerates* k_{fold} and *decelerates* k_{unfold}, which clearly favors formation of products (**F**) over reactants (**I**) and therefore increases K_{eq}. In terms of free energy, addition of Na^+ increases favorability of forming the tertiary interaction, i.e., $\Delta[\Delta G°] < 0$ (Figure 5.3b). At 130 mM Na^+, the reaction is slightly unfavorable at ($\Delta G°$[298 K] = 0.4(1) kcal/mol), whereas at 830 mM Na$^+$, folding becomes appreciably favored ($\Delta G°$[298 K] = -2.0(1) kcal/mol). Clearly, the free energy, and therefore ln[K_{eq}], has a non-liner dependence on [Na$^+$].

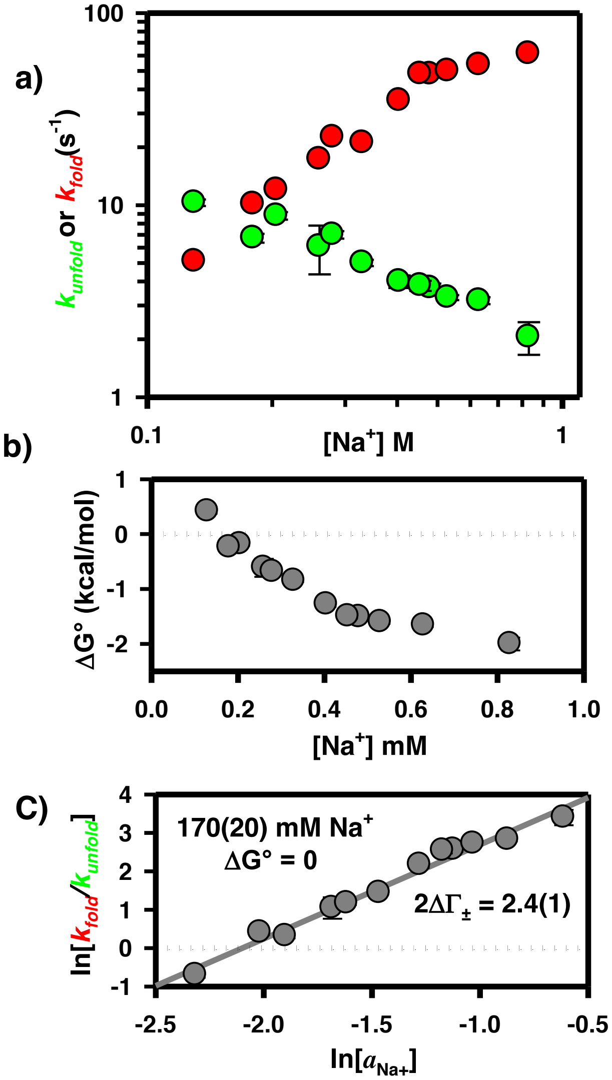

Figure 5.3 (a) Na$^+$-dependent kinetics for the formation of the GAAA tetraloop–receptor interaction. Increasing [Na$^+$] yields a significant enhancement of the folding rate constant (k_{fold}) and a subtle reduction in the rate constant for the unfolding process (k_{unfold}). **(b)** The dependence of the free energy on [Na$^+$] and **(c)** preferential interaction coefficient analysis for the formation of the tertiary interaction, which yields an ion pair uptake of $2\Delta\Gamma_\pm = 2.4(1)$ and no change in free energy at [Na$^+$] = 170(20) mM.

These data, when considered in the context of the physically-motivated theoretical framework provided by preferential interaction coefficients, can be used to create a more informative depiction of the Na^+-dependence of K_{eq} (7,46). Based on this model-free description of RNA-ion interactions, the logarithm of the equilibrium constant ($\ln[K_{eq}]$) should scale *linearly* with the logarithm of the thermodynamic activity of the monovalent ion ($\ln[a_{Na+}]$). From such an analysis, the slope ($2\Delta\Gamma_{\pm}$) corresponds to the net change in the number of ion pairs associated with the ion atmosphere as a result of the folding transition. This is well demonstrated by a linear fit of $\ln[K_{eq}]$ vs $\ln[a_{Na+}]$ where the slope yields a net uptake of approximately 2.4(1) ion pairs (Figure 5.3c). This plot also demonstrates that at 170(20) mM Na^+ formation of the tertiary interaction results in no free energy change. It should be noted that because $\ln[K_{eq}]$ is proportional to Gibbs free energy, $\Delta G° = \Delta H° - T\Delta S°$, it seems a reasonable anticipation that both $\Delta H°$ and $T\Delta S°$ might also scale linearly with $\ln[a_{Na+}]$.

The purpose of this work is to investigate the thermodynamics associated with the formation of the GAAA tetraloop–receptor interaction as a function of monovalent salt concentration. Therefore, it will be useful to develop the language used to describe the range of experimental [Na^+]. Specifically, this work will refer to RNA molecules in 180 mM Na^+ as being under "free energy neutral" conditions where $\Delta G° \approx 0$ kcal/mol. Progressively higher concentrations of Na^+ (i.e., 330 mM, 480 mM, and 630 mM) correspond to progressively more "free energy favorable" conditions as $\Delta G°$ decreases below zero with addition of Na^+.

5.3.2 Standard State Enthalpy and Entropy of Folding

The observed *increase* in k_{dock} and *decrease* in k_{undock} represent the fundamental kinetic basis for Na^+-promoted folding (Figure 5.3a). However, in order to provide a more insightful description of the free energy folding pathway from **I** to **F**, it is also important to understand the thermodynamic contributions (i.e. enthalpic and entropic) to monovalent-facilitated folding. This can be best accomplished by temperature dependent van't Hoff analysis of K_{eq}(36), which allows the free energy ($\Delta G°$) to be partitioned into the enthalpy ($\Delta H°$) and entropy ($\Delta S°$) changes associated with folding at a particular [Na$^+$] (Figure 5.4a). Specifically, in a plot of ln[K_{eq}] vs. $1/T$ the slope and intercept are equal to $-\Delta H°/R$ and $\Delta S°/R$, respectively.

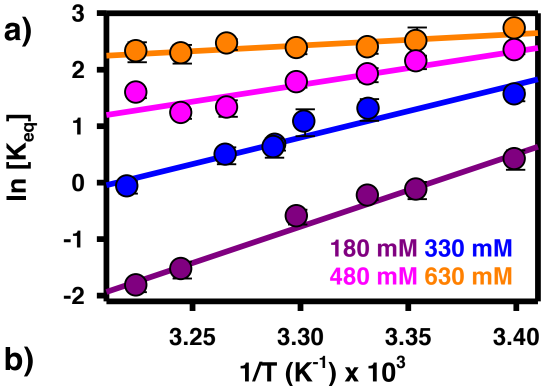

b)

[Na+] mM	ΔH° kcal/mol	ΔS° cal/mol/K
180	-26(2)	-86(6)
330	-19(3)	-60(8)
480	-12(2)	-36(8)
630	-4(1)	-8(4)

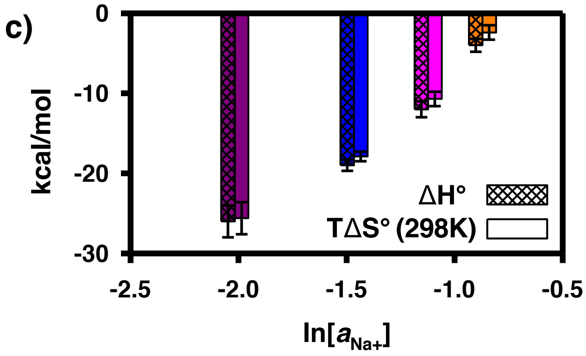

Figure 5.4 (a) van't Hoff analysis of the tetraloop–receptor interaction at four [Na$^+$]. Increasing [Na$^+$] increases both the $\Delta H°$ (decreasing slope) and the $\Delta S°$ (increasing vertical intercept) for the formation of the tertiary interaction. **(b)** Table of thermodynamic parameters from the van't Hoff analysis. **(c)** Bar graph to visually display the change in $\Delta H°$ and $\Delta S°$ as a function of ln[a_{Na+}].

Under free energy neutral conditions of 180 mM, the van't Hoff plot in Figure 5.4a reveals the folding process to be quite exothermic ($\Delta H°$ = -26(2) kcal/mol). This is entirely consistent with the formation of 11 hydrogen bonds in the **F** state, which are absent in the **I** state(37). In principle, an additional source of exothermicity could be the site-specific chelation of a monovalent ion in the folded conformation. Indeed, there is some structural evidence that supports a proposed monovalent binding site within the tetraloop–bound receptor domain(21). However, these chelation interactions are considerably stronger and thus likely already saturated well below the present working conditions. Therefore, changes in [Na^+] over the range of 180 to 630 mM will not significantly affect how monovalent chelation contributes to the folding thermodynamics. Under the same free energy neutral experimental conditions, the van't Hoff analysis reveals a folding process that is entropically penalized ($\Delta S°$ = -86(6) cal/mol/K). This loss of disorder associated with formation of the **F** state is quite reasonable given that the non-canonical hydrogen bonds within the receptor domain are more conformationally restricted after the formation of tertiary contacts. Furthermore, formation of the tertiary interaction restricts the conformational freedom of the poly-A_7 linker. Lastly, the large entropic cost to folding is also the result of ion uptake as the RNA undergoes a structural transition. Based on these experimentally measured values of $\Delta H°$ and $\Delta S°$, the calculated Gibbs free energy for the folding process at 180 mM Na^+ is nearly zero ($\Delta G°$[298 K] = -0.4(9) kcal/mol), which is consistent with the predictions from the preferential interaction coefficient analysis (Figure 5.3b).

These three thermodynamic parameters (i.e., $\Delta G°$, $\Delta H°$, $\Delta S°$) at 180 mM now establish a baseline with respect to increasing monovalent concentrations. If the effect of Na^+-facilitated folding were purely related to ion uptake from solution (e.g. unmixing), one would predict that increasing [Na^+] would have no affect on the enthalpy of folding (i.e. $\Delta[\Delta H°] = 0$). Surprisingly, both the folding entropy *and* enthalpy increase with increasing [Na^+] (Figure 5.4). The van't Hoff plot for the equilibrium docking reaction at 330 mM Na^+ (and higher) demonstrates a *less positive* slope ($\Delta[\Delta H°] > 0$) when compared to free energy neutral conditions. Specifically, the exothermicity of folding continues to *diminish* with further increases in [Na^+]. Indeed, under the most free energy favorable conditions, formation of the tertiary interaction is much less exothermic ($\Delta H°$ =-4(1) kcal/mol). A similar and slightly over-compensating trend is also apparent when probing changes in the standard state *entropy* of folding (i.e., intercepts of the van't Hoff plot) as a function of [Na^+]. Increasing [Na^+] gives rise to a large *increase* in entropy change ($\Delta[\Delta S°] > 0$) for folding. At 630 mM Na^+, the entropic penalty for folding is greatly reduced ($\Delta S°$ = -8(4) cal/mol/K). As apparent in Figure 5.4c, both $\Delta H°$ and $T\Delta S°$ scale linearly with ln[Na^+].

Finally, the Van't Hoff analysis in Figure 5.4a demonstrates that increasing [Na^+] systematically increases *both* $\Delta H°$ and $\Delta S°$, but that at a fixed temperature, increasing [Na^+] increases the equilibrium constant and thus decreases $\Delta G°$. In order to have decreasing free energy ($\Delta[\Delta G°] < 0$) with increasing [Na^+], the rate of increase for $T\Delta S°$ must be larger than the rate of increase for $\Delta H°$ (Figure 5.4c). This implies that an increase in monovalent cation concentration enhances tetraloop–receptor folding via a reduction of the entropic penalty that slightly over-compensates for the loss in exothermicity. Stated simply, the well-known increase in stability of the tetraloop–receptor tertiary interaction with increasing monovalent cation concentration is in fact the result of entropic considerations. It is also interesting to note that rather large changes in $\Delta H°$ and $\Delta S°$ give rise to relatively small changes in $\Delta G°$. This *nearly* compensatory nature of $\Delta[\Delta H°]$ and $\Delta[\Delta S°]$ is intriguing and may provide a way to tune the temperature sensitivity of biochemically relevant processes (e.g., RNA folding) without significantly perturbing the equilibrium constant.

5.3.3 Transition State Thermodynamics

This trend of increasing $\Delta H°$ and $\Delta S°$ with increasing [Na$^+$] clearly provides surprising information about thermodynamic changes between reactants (**I**) and products (**F**). Taken one step further, a parallel investigation of the *transition state barrier* can provide additional insight into how the monovalent ion atmosphere affects the GAAA tetraloop–receptor interaction. Specifically, the temperature dependence of k_{fold} and k_{unfold} can be analyzed in the context of transition state theory (TST) to provide thermodynamic details about access to the transition state from the intermediate (**I**) and folded (**F**) states, respectively(47,48). Although more sophisticated treatments exist in the literature(49), for present purposes we consider TST in its simplest form of activated complex theory. This treatment invokes two key assumptions: (*i*) a well defined transition state dividing surface, beyond which the reactants proceed toward products without recrossing and *(ii)* a transition state in quasi-equilibrium with the reactants. The transition state expression for the folding rate constant can then be rigorously written as

$$k_{fold} = \frac{k_b T}{h} \frac{(q^{\ddagger}_{perp})}{(q^{\mathbf{I}}_{perp})(q^{\mathbf{I}}_{para})} e^{\frac{-\Delta U^{\ddagger}_{fold}}{k_b T}} \qquad \text{(Eq. 5.1)}$$

where k_b, T, and h are Boltzmann's constant, temperature and Planck's constant respectively.

In Eq. 5.1, $q^{\mathbf{I}}_{perp}$ and $q^{\mathbf{I}}_{para}$ represent partition functions for the **I** state in all degrees of freedom (i.e., both *perpendicular* and *parallel* to the reaction coordinate), whereas $q^{\ddagger}_{perp}$ represents the corresponding partition function at the transition state, including only degrees of freedom *perpendicular* to the reaction coordinate. Additionally, $\Delta U^{\ddagger}_{fold}$ corresponds to the potential energy barrier between the **I** state and the transition state. Eq. 5.1 can be conveniently expressed in terms of the Gibbs free energy barrier ($\Delta G^{\ddagger}_{fold}$) by rewriting the ratio of the partition functions associated with the perpendicular degrees of freedom as Eq 5.2.

$$\frac{(q^{\ddagger}_{perp})}{(q^{\mathbf{I}}_{perp})} = e^{\frac{\Delta S^{\ddagger}_{fold}}{k_b T}} \qquad \text{(Eq. 5.2)}$$

If pressure-volume work is assumed to be negligible (i.e., $\Delta H = \Delta U$) and $q^{\mathbf{I}}_{para}$ to be in the high temperature limit (i.e., k_bT/hn), the TST equation reduces to the simple activated complex expression:

$$k_{fold} = \nu e^{\frac{-\Delta G^{\ddagger}_{fold}}{k_b T}} \qquad \text{(Eq. 5.3)}$$

where n corresponds to the attempt frequency—parallel to the reaction coordinate—for approaching the transition state. Eq. 5.3 can be readily expressed as an Eyring plot, ln[k_{fold}/ν] vs $1/T$, whose slope and intercept correspond to the transition state enthalpy ($-\Delta H^{\ddagger}_{fold}/R$) and entropy ($\Delta S^{\ddagger}_{fold}/R$), respectively. Though commonly misinterpreted as such, note that the attempt frequency (υ) is *not* the same as k_bT/h, and in fact an accurate determination of n requires far more detailed knowledge of the true folding potential surface than currently available. The present analysis uses $\upsilon \approx 1\times10^{13}$ sec^{-1} as an approximate order of magnitude for hydrogen bond formation/breaking rates. However, it is important to stress that the choice of ν only introduces a constant *offset* to the barrier entropy ($\Delta S^{\ddagger}_{fold}$) and has no effect on the barrier enthalpy ($\Delta H^{\ddagger}_{fold}$). Furthermore, the choice of n also has no effect on the *change* in barrier entropy ($\Delta[\Delta S^{\ddagger}_{fold}]$) as a function of [Na$^+$], which is of particular interest for the analysis and interpretation of the present results.

5.3.4 Temperature Dependence of k_{fold}

An Eyring plot of the folding rate constants (Figure 5.5a) at 180 mM Na^+ depicts a slightly positive slope, indicating that formation of the transition state under free energy neutral conditions is slightly exothermic ($\Delta H^{\ddagger}_{fold}$ = -3(2) kcal/mol), which is consistent with recent studies of a similar RNA construct under similar conditions(50).

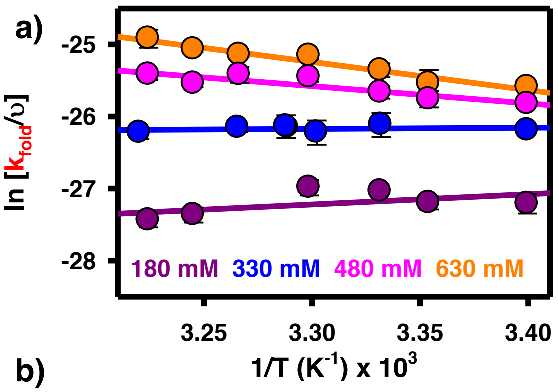

b)

$[Na^+]$ mM	$\Delta H^{\ddagger}_{fold}$ kcal/mol	$\Delta S^{\ddagger}_{fold}$ cal/mol/K
180	-3(2)	-64(7)
330	0.3(7)	-53(2)
480	5(1)	-35(3)
630	7.7(8)	-25(3)

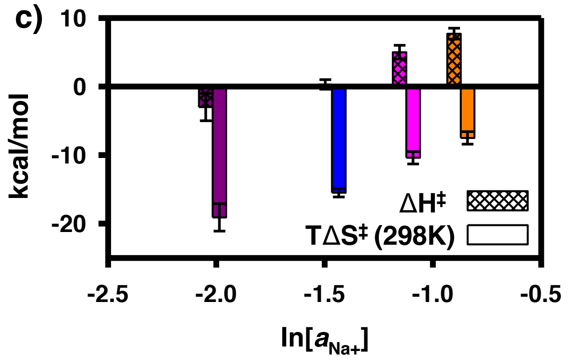

Figure 5.5 (a) Transition state theory (TST) analysis of the rate constant associated with formation of the tetraloop–receptor interaction (k_{fold}) as a function of temperature. **(b)** Table of thermodynamics parameters from the TST analysis. **(c)** Bar graph depicting the change in $\Delta H^{\ddagger}_{fold}$ and $\Delta S^{\ddagger}_{fold}$ at four values of $\ln[a_{Na+}]$.

The lack of an endothermic component of the free energy barrier suggests the transition state is structurally similar to the **I** state, i.e., the transition state is "early" with respect to reactants. Again, if monovalent-facilitated folding were solely a result of entropic terms associated with unmixing of the solution, one would expect the enthalpic component of the free energy barrier to be insensitive to [Na$^+$]. Surprisingly, for increasing [Na$^+$], the slope of the Eyring plot becomes significantly more negative ($\Delta[\Delta H^{\ddagger}_{fold}] > 0$), indicating the emergence of *an endothermic* barrier, which is often associated with formation of a less early transition state. This is best demonstrated at 630 mM Na$^+$, where the enthalpy for forming the transition state is significantly positive ($\Delta H^{\ddagger}_{fold} = 7.7(8)$ kcal/mol). One source of an endothermic folding barrier at elevated [Na$^+$] could be associated with preferential stabilization of non-native contacts that must break prior to forming the transition state.

Additionally, the intercepts of the Eyring plot (Figure 5.5a) demonstrate that the entropy change associated with formation of the transition state also increases ($\Delta[\Delta S^{\ddagger}_{fold}] > 0$) with [Na$^+$]. For example, at 180 mM Na$^+$, transition state formation is a heavily penalized process ($\Delta S^{\ddagger}_{fold} = -64(7)$ cal/mol/K). By 630 mM Na$^+$, however, this penalty is dramatically reduced ($\Delta S^{\ddagger}_{fold} = -25(3)$ cal/mol/K). These combined results suggest that: (*i*) folding under free energy neutral conditions is predominantly rate-limited by a conformational search (e.g., $-T\Delta S^{\ddagger}_{fold} > \Delta H^{\ddagger}_{fold} \approx 0$ kcal/mol) and (*ii*) while under most free energy favorable conditions, folding is rate-limited by an increased amount of structural rearrangements and reduced conformational search (e.g., $-T\Delta S^{\ddagger}_{fold} \approx \Delta H^{\ddagger}_{fold} > 0$kcal/mol).Again, it should be noted that both $\Delta H^{\ddagger}_{fold}$ and $T\Delta S^{\ddagger}_{fold}$ appear to scale linearly with the ln[Na$^+$] (Figure 5.5c).

Based on the simple relationship between Gibbs free energy, entropy, and enthalpy, we can now describe the free energy barrier as a function of monovalent ion concentration.

Increasing the folding favorability of the experimental conditions gives rise to a *strong* increase in the entropic and enthalpic components of the free energy barrier. Similar to what was noted above for the standard state folding thermodynamics, these large changes yield a much more subtle effect on the transition state free energy barrier. Specifically, $\Delta G^{\ddagger}_{fold}$ [298 K] decreases only by ≈ 0.9 kcal/mol (from 16.1(8) kcal/mol to 15.2(7) kcal/mol) between free energy neutral and the most free energy favorable conditions. This drop in barrier height is the result of a dramatic increase in entropic rewards (≈ 11.6 kcal/mol at 298 K) that slightly outweighs the increase in enthalpic cost (≈ 10.7 kcal/mol) associated with formation of the transition state (i.e., $\Delta[T\Delta S^{\ddagger}_{fold}] > \Delta[\Delta H^{\ddagger}_{fold}]$). As a central result, this implies that the Na^+-accelerated k_{fold} of the GAAA tetraloop–receptor interaction (Figure 5.3a) occurs via a subtle reduction of the folding free energy barrier, which results from *entropic facilitation* barely overcoming *enthalpic suppression*.

In order to determine if the poly-A_7 linker has any appreciable effect on the thermodynamics of tetraloop–receptor folding, a poly-U_7 linker is used to replace the poly-A_7 linker of the original construct (Supplemental Figure S5.1). As was the case with the original poly-A_7 construct, addition of Na^+ resulted in an acceleration of k_{fold} and a deceleration of k_{unfold}. A simple van't Hoff analysis (Supplemental Figure S5.2) with the poly-U_7 RNA construct reveals the same trends as the poly-A_7 RNA construct, i.e., increasing $[Na^+]$ from 80 to 330 mM increases $\Delta H°$ from -26 to -13 kcal/mol. This reduction of exothermicity was subtly overcompensated by an increase in $\Delta S°$ from -88 to -38cal/mol/K. Furthermore, a corresponding Eyring analysis of the forward rate constant indicates that increasing $[Na^+]$ *also* increases both $\Delta H^{\ddagger}_{\text{fold}}$ and $\Delta S^{\ddagger}_{\text{fold}}$ (Supplemental Figure S5.3)—the same trend observed for the poly-A_7 construct. The additional analysis of the poly-U_7 construct suggests that, although the linker may subtly change the thermodynamics of folding at a given [Na^+], the observed trends in the A_7-linker based construct are dominated by the GAAA tetraloop–receptor tertiary interaction.

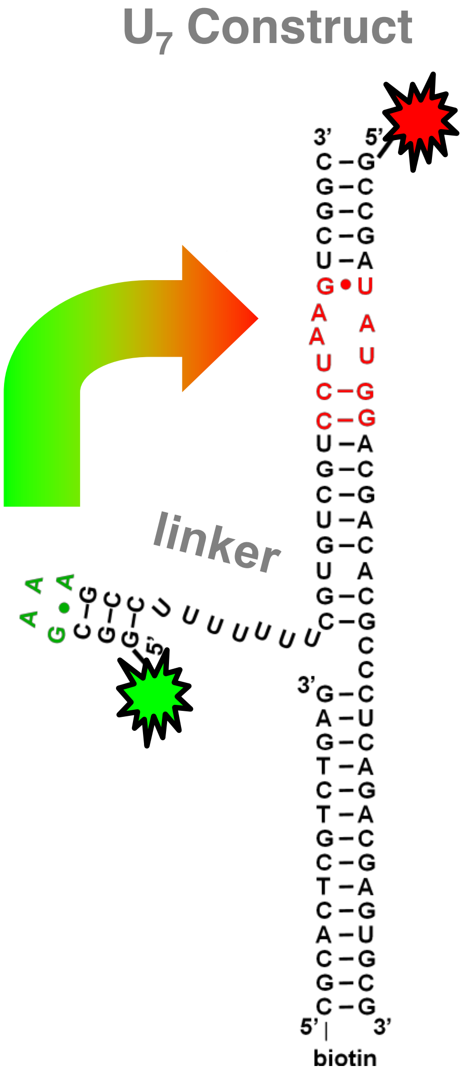

Supplemental Figure S5.1 Schematic of the three-piece donor/acceptor label RNA construct. The poly-U_7 linker is used to determine the effect of the linker on the folding thermodynamics.

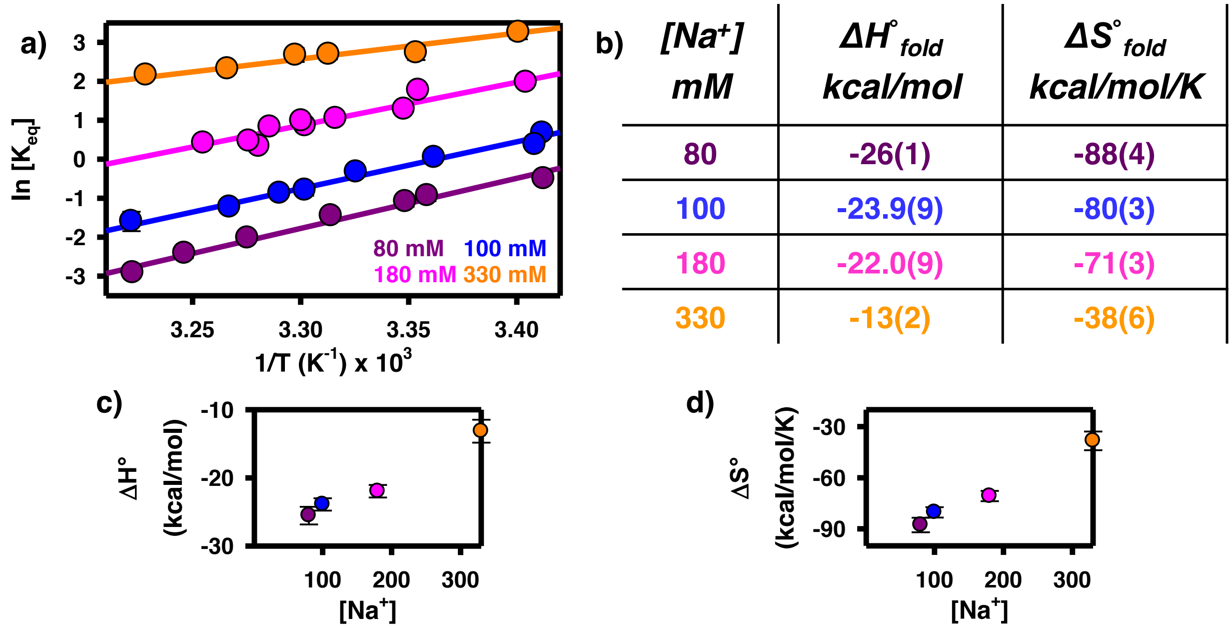

[Na$^+$] mM	ΔH°_{fold} kcal/mol	ΔS°_{fold} kcal/mol/K
80	-26(1)	-88(4)
100	-23.9(9)	-80(3)
180	-22.0(9)	-71(3)
330	-13(2)	-38(6)

Supplemental Figure S5.2 (a) van't Hoff analysis of tetraloop–receptor interaction at four [Na$^+$] with the poly-U$_7$ linker. Increasing [Na$^+$] increases both the $\Delta H°$ (decreasing slope) and the $\Delta S°$ (increasing vertical intercept) for the formation of the tertiary interaction. **(b)** Table of thermodynamic parameters from the van't Hoff analysis. **(c)** Visual display of changes in $\Delta H°$ and $\Delta S°$ as a function of ln[Na$^+$].

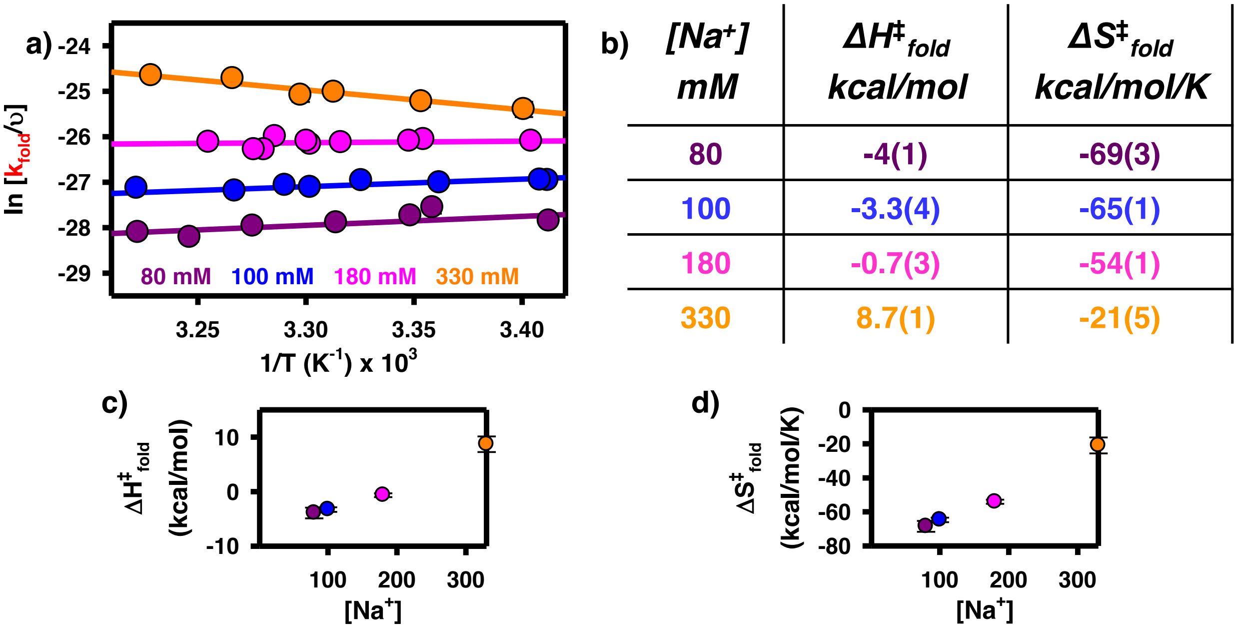

[Na$^+$] mM	$\Delta H^{‡}_{fold}$ kcal/mol	$\Delta S^{‡}_{fold}$ kcal/mol/K
80	-4(1)	-69(3)
100	-3.3(4)	-65(1)
180	-0.7(3)	-54(1)
330	8.7(1)	-21(5)

Supplemental Figure S5.3 (a) Transition state theory (TST) analysis of the rate constant associated with formation of the tetraloop–receptor interaction (k_{fold}) as a function of temperature with the poly-U$_7$ linker based construct **(b)** Table of thermodynamics parameters from the TST analysis **(c)** Bar graph depicting the change in $\Delta H^{‡}_{fold}$ and $\Delta S^{‡}_{fold}$ at four values of ln[Na$^+$].

5.4 Discussion

5.4.1 Folding Pathways and Ion Atmospheres

The free energy barrier thermodynamic data can be used in conjunction with the previously extracted standard state thermodynamic data to provide additional insight into the "reaction coordinate" for tetraloop–receptor folding as a function of [Na^+]. As summarized schematically in Figure 5.6, the reaction coordinate follows the folding pathway from left to right, where the horizontal distance between the **I** state and the transition state qualitatively represents how "early" or "late" the free energy barrier is along the reaction coordinate.

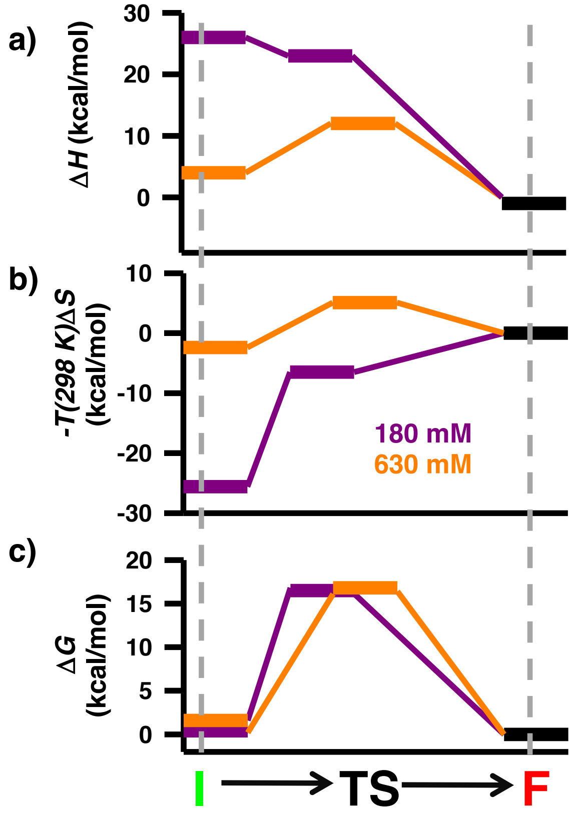

Figure 5.6 Complete thermodynamics reaction coordinates for the formation of the GAAA tetraloop–receptor tertiary interaction. The three panels depict the: **(a)** enthalpy, **(b)** entropy, and **(c)** free energy along the reaction coordinate at 180 and 630 mM Na^+. The horizontal distance between states qualitatively represents how "early" or "late" they are along the reaction coordinate (see Section 5.4 for details).

For all **F** states in the plot, the absolute energies are referenced to 0 kcal/mol. This choice is made because the **F** state is least likely to be influenced by [Na$^+$], and it will therefore more clearly demonstrates changes to the folding pathway(51). First, the implications of the 180 mM reaction coordinate will be considered.

5.4.2 Folding in a Free Energy Neutral Monovalent Ion Atmosphere

The path of the reaction coordinate under free energy neutral conditions (Fig 5.6, purple) is easily interpreted, and serves as a baseline for comparison to the 630 mM Na$^+$ reaction coordinate. Formation of a number of tertiary contacts in the **F** state, and perhaps specific chelation of a monovalent ion, makes the folding process strongly exothermic. Furthermore, the measured $\Delta H°$ values reported herein are in decent agreement with previously reported values using a complementary technique(50). Specifically, the measured exothermicity of the poly-U$_7$ construct at 180 mM Na$^+$ is almost exactly half of published values for a dual tetraloop–receptor construct at 200 mM KCl; the poly-A$_7$ construct is slightly more than half as exothermic.

The absence of any significant endothermic component of the free energy barrier (i.e., an early transition state) suggests most of the standard state enthalpic gains occur as the transition state forms the **F** state (Figure 5.6a, purple), which is again supported by previous work(50). The strong entropic component of the free energy barrier at 180 mM Na$^+$ suggests that there is a significant conformational search of the receptor by the tetraloop, which represents the rate-limiting step in transition state formation. Previous structural studies of the receptor domain have identified a high degree of conformational disorder within the free receptor, which is absent once the full tertiary interaction has formed(37). Therefore, the loss of entropy associated with the formation of the transition state, and subsequently the **F** state, can in part be attributed to the restricted orientation of the base pairs within the 11-nucleotide receptor (Figure 5.6b, purple).

Other contribution to the loss of entropy for folding under free energy neutral conditions come from: (*i*) localizing the tetraloop near the receptor and (*ii*) the subsequent uptake of ions from the bulk to the ion atmosphere in order to compensate for the increased charge density of both the transition state and the **F** state. This leads to a proposed compact transition state where the tetraloop is proximal to the receptor and a few additional monovalent ions have been localized around the RNA. Furthermore, the nucleotides within the receptor must have transiently adopted a conformation from the ensemble of unfolded microstates that is "aligned" for the formation of hydrogen bonds with the GAAA tetraloop.

Our identification of (*i*) an early transition state and (*ii*) a large entropic barrier in the GAAA tetraloop–receptor interaction supports two emerging paradigm for RNA folding. First, our findings under free energy neutral conditions support the observation that transition states for tertiary interactions are often early (*40, 47, 48,*(48,52), (50)); that is to say that there is little to no enthalpic component to the free energy barrier ($\Delta H^{\ddagger}_{fold} \approx 0$). Furthermore, the idea of an early transition state implies that the structure of the transition state more closely resembles the **I** state than the **F** state. The second paradigm supported by the thermodynamics observations under free energy neutral conditions is that RNA folding is accompanied by a large entropic component of the free energy barrier ($\Delta S^{\ddagger}_{fold} < 0$) resulting from a conformational search. This idea was first proposed in regard to the slow folding of ribozymes from group I(52) and group II (53) introns, where the notion of contact order was used to explain the large entropic barrier to folding. The idea of a rate-limiting conformational search and a large $\Delta S^{\ddagger}_{fold}$ has since been supported by experiments on the hairpin ribozyme(44,54,55) and the GAAA tetraloop–receptor(48,50). More importantly, however, this work provides a quantitative framework for understanding how the entropic and enthalpic components of the free energy barrier change with increasing monovalent cation concentrations.

5.4.3 Folding in a "Free Energy Favorable" Monovalent Ion Atmosphere

Increasing the [Na^+] dramatically alters the folding pathway associated with formation of the tertiary interaction (Figure 5.6, orange). At elevated [Na^+] the standard state entropy and enthalpy for folding are significantly increased as well as the entropic and enthalpic components of the free energy barrier. Mg^{2+}-induced increases to $\Delta S°$ and $\Delta H°$ been observed in both the P4-P6 domain of the *Tetrahymena* ribozyme as well various GAAA tetraloop–receptor construct (48,56,57). However, support for the same trend with monovalent ions is less apparent in the literature. A great deal of work has concluded that for duplex denaturation there is little to no monovalent-dependence of $\Delta H°$(8,58) concluding that entropy is the only thermodynamic term that is dependent on monovalent ion concentration. However, other have seen significant increases in $\Delta H°$ for helix formation with increasing monovalent salt concentration(59), suggesting that both entropy and enthalpy must be changing with addition of monovalent salt. With regard to the formation of the GAAA tetraloop–receptor interaction, recent studies of a bimolecular, dual tetraloop–receptor RNA construct were not able to unambiguously determine whether the observed monovalent-induced stability was the result of entropic or enthalpic considerations(50). However, they note that over the range of 100-300 mM KCl the $\Delta[\Delta S°]$ accounts for 134-166% of the overall $\Delta[\Delta G°]$, which clearly implies that the increase in $\Delta H°$ must be 34-66% of the overall $\Delta[\Delta G°]$, which is certainly qualitatively consistent with our observations that both enthalpy and entropy change and that the increase in $\Delta S°$ slightly overcomes the increase in $\Delta H°$.

These results, perhaps, suggest that addition of salt may indeed increase the observed $\Delta H°$ of formation. Although these bimolecular, dual tetraloop–receptor constructs do contain the GAAA tetraloop–receptor interaction from the *Tetrahymena* ribozyme, the context of the interaction is quite different. The duality of the construct and the significantly enhanced degree of helical packing upon formation of the interaction make truly rigorous comparisons with the construct used for this study challenging at best. The degree to which $\Delta H°$ for various RNA folding motifs is affected by monovalent salt concentrations is likely a result of how many alternative conformations are easily accessible within the ensemble of microstates associated with the **I** state. Nevertheless, in the examples above, addition of monovalent salt increases the overall favorability of folding by increasing the $\Delta S°$ of formation.

In conjunction with the present work, these observations support a potential paradigm fundamental to tertiary interactions and perhaps even RNA folding, whereby additional monovalent cations facilitate folding by reducing the entropic penalty ($\Delta[\Delta S°] > 0$) at the potential cost of reducing the folding exothermicity ($\Delta[\Delta H°] > 0$). The qualitatively established free energy barrier thermodynamics for the GAAA tetraloop–receptor are used to *further* support this paradigm by providing a physical picture based on the molecular structure of the tertiary interaction, as described below.

It is important to remember that discussion of structural changes pertains primarily to either of the Boltzmann-weighted macroscopic states; it is likely that these structural changes reflect a shift in the energetic distribution of the ensemble of microscopic states. As illustrated by the orange traces in Figures 5.6a and 5.6b, formation of the transition state in the most free energy favorable conditions is accompanied by an *enthalpic cost* and an *entropic penalty*. The enthalpic cost associated with transition state formation is attributed to preferentially stabilized non-native intramolecular contacts within the unbound receptor domain (**I**) that must be broken prior to forming the transition state. One such contact from structural models of the free tetraloop–receptor domain, is that of base U19 (numbering from ref (37)). An NMR solution structure of the free receptor domain(37) depicts a conformation where U19 participates in one hydrogen-bonding interaction with U5 and is basestacked between G20 and A6 (Figure 5.7).

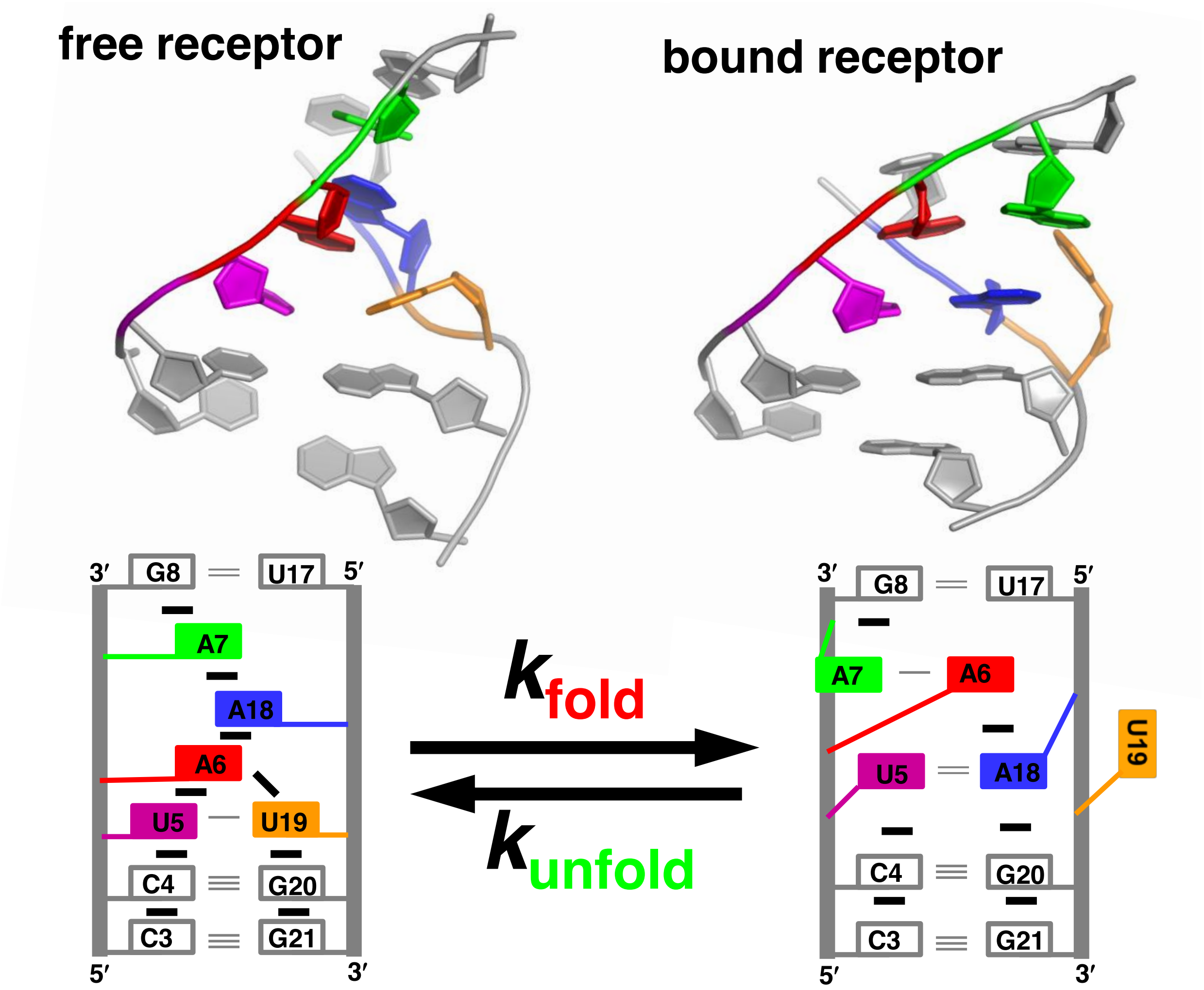

Figure 5.7 Structural representation of the free and bound receptor domain. Bases that undergo significant structural rearrangement upon forming the tetraloop–receptor interaction are color-coded. Bases of the GAAA tetraloop are not shown to emphasize changes within the receptor domain (see Section 5.4.3 for details).

Structural models of the bound receptor domain show that in the presence of the GAAA tetraloop the U19-U5 hydrogen bond and all of the basestacking interactions with U19 are absent as U19 is flipped outside of the receptor to accommodate the tetraloop(29). The reduction of the entropic barriers results from the **I** state being preorganized at high [Na^+] by non-native contacts, thus removing the entropic cost associated with forming an "aligned" receptor conformation. The remaining entropic penalty for forming the transition state at 630 mM Na^+ is likely associated with bringing the tetraloop in close proximity to the receptor and ion uptake associated with the increased charge density. Taken together, these conclusions can be used to portray a more detailed image of the transition state. Specifically, the tetraloop is (*i*) proximal to the receptor, which is (*ii*) in a conformation "aligned" for formation of the tertiary interaction and (*iii*) has U19 flipped outside of the receptor to accommodate the GAAA tetraloop.

This putative model of the transition state is also in accord with the observed changes in $\Delta H^{\ddagger}_{fold}$ and $\Delta S^{\ddagger}_{fold}$ with increasing [Na^+]. At 180 mM Na^+, the interactions involving U19 in the free receptor are only poorly stabilized. Addition of Na^+ preferentially stabilizes these interactions within the free receptor (**I**), which gives rise to an increase in $\Delta H^{\ddagger}_{fold}$ associated with hydrogen-bond breakage, unbasestacking, and base flipping—all prior to forming the transition state. The increase in $\Delta S^{\ddagger}_{fold}$ comes from the fact that stabilizing the non-native interactions pre-organizes the receptor, thus reducing the amount of organization (i.e., entropy loss) required to form the transition state. An additional source of increasing $\Delta S^{\ddagger}_{fold}$ could be global compaction of the RNA at elevated [Na^+], which is supported by a Na^+-dependent undocked FRET position(35). This would reduce the accessible volume for the unbound tetraloop, thus making it less entropically costly to localize the tetraloop proximal to the receptor in order to form the transition state. As additional support for this molecular model, recent electron paramagnetic resonance (EPR) experiments with spin-labeled nucleotides have demonstrated that increasing the cation concentration by itself does not promote the unbasestacked conformation of U19(60). Indeed, only in the presence of GAAA tetraloop is the U19 base able to adopt a stable conformation where it is flipped outside of the receptor domain, which further supports the proposed origin of monovalent-facilitated folding of the GAAA tetraloop–receptor interaction.

The tertiary contacts within the unbound receptor associated with U19 are used to explain the observed changes in the free energy barrier to folding. However, it is possible that interactions with solution may also contribute. Recent experiments have highlighted the importance of phosphate backbone dehydration in RNA folding transitions(61). With this in mind, solvent rearrangement may serve as potential explanation for the monovalent-induced changes to the folding thermodynamics. However, one must have a detailed understanding for how changing the monovalent concentration affects the entropic and enthalpic components of phosphate backbone dehydration. Fortunately, the total amount of buried phosphate surface area for the tetraloop–receptor interaction used in this study (≈ 67 Å^2) is much smaller than more biologically relevant RNAs making the energetics associated with desolvation much smaller in magnitude than it may have otherwise been(61).

One last explanation for the strong salt-dependence of both the enthalpic and entropic terms pertains to the polynucleotide linker used to create the unimolecular tetraloop–receptor construct. Theoretically, increasing the monovalent concentration could preferentially stabilize a rigid, base-stacked conformation within the poly-A_7 linker(62). If so, elevated monovalent concentrations could result in an additional enthalpic loss (and entropic reward), arising from the need to disrupt this rigid base-stacked linker.

Control experiments can be performed to test and rule out this alternative explanation. The poly-U_7 single strand RNA linker is thought to only be rigid and structured at low ionic strengths (e.g., < 50 mM monovalent)(63) or at low temperatures (T< 10 °C)(64). As a result the poly-U_7 linker should act as a more flexible, passive, linker that is less susceptible to Na^+-facilitated base-stacking. A comparison of the results of the poly-U_7 construct with the rigourusly determined values of the poly-A_7 construct clearly suggests the polynucleotide linker has only a minimal contribution to the absolute thermodynamic values, and that the observed changes in all measured thermodynamic values ($\Delta H°$, $\Delta S°$, $\Delta H^{\ddagger}_{fold}$, and $\Delta S^{\ddagger}_{fold}$) follow the same trend with increasing [Na^+]. One interesting observation is that at both 180 and 330 mM Na^+, formation of the GAAA tetraloop–receptor interaction is *more* exothermic for the poly-A_7 RNA construct than for the poly-U_7 RNA construct (i.e., $\Delta H°[A_7] < \Delta H°[U_7]$) (Figure 5.4b and Supplemental Figure S5.2b). This suggests that perhaps the poly-A_7 linker forms and maintains a few base-stacking interactions along the folding pathway. We note that the effect of single stranded linkers and base-stacking in RNA folding is a particularly important problem for: (*i*) H-type pseudoknot formation (*ii*) other single-stranded regions of larger functional RNAs (e.g., the template boundary element of human telomerase RNA), and (*iii*) oligonucleotide duplex formation. Consequently, future work directed at elucidating differences in folding kinetics and thermodynamics due to changes in single-strand structure would be particularly relevant.

5.4.4 Dependence on Monovalent Cation Identity

One issue with RNA folding studies is the potential role of monovalent identity. For example, the use of K^+ vs Na^+ cations has been shown to affects rates of RNA catalysis, and has been attributed to specific binding of K^+(21). We can easily test for monovalent identity effects with parallel folding studies as a function of [K^+]. Interestingly, the corresponding K^+ vs. Na^+

titrations reveal completely negligible differences in the folding kinetics of the GAAA tetraloop–receptor construct as summarized in Figure 5.8(65), which is consistent with existing studies of a GAAA tetraloop–receptor construct(18).

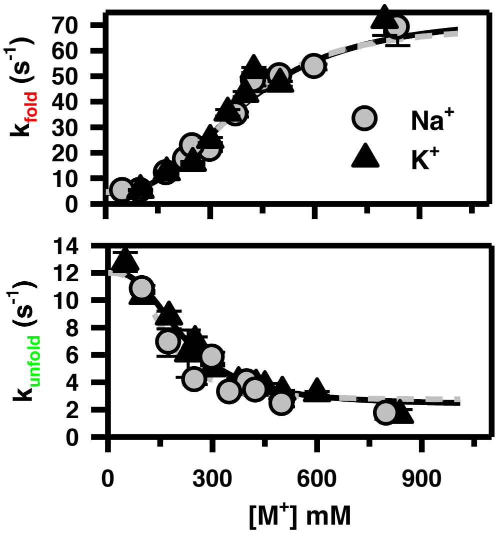

Figure 5.8 Monovalent-identity and folding kinetics for the formation of the GAAA tetraloop–receptor interaction. Increasing monovalent concentration provides a significant enhancement of the folding rate constant (k_{fold}) and a subtle reduction in the rate constant for the unfolding process (k_{unfold}). No significant difference is observed between Na^+ and K^+.

Furthermore, temperature-dependent kinetic experiments identical to those described for Na^+ reveal that all thermodynamic parameters for Na^+ and K^+ promoted folding are identical within experimental uncertainty (Figure 5.9). The insensitivity to monovalent identity suggests that the effects observed are common to both Na^+ and K^+, thus demonstrating the broader applicability of the proposed model for monovalent-facilitated RNA folding.

5.5 Conclusion

The present work describes the use of smFRET experiments to better understand the origins of monovalent-facilitated formation of an RNA tertiary interaction. The kinetic origin of this enhanced folding results from a large acceleration of k_{fold} and a subtle deceleration of k_{unfold} at elevated [Na^+]. The large 14-fold change in the forward folding rate constant is the result of a modest ($\Delta[\Delta G^{\ddagger}_{fold}] \approx$ -1 kcal/mol) decrease in the height of the free energy barrier associated with the folding reaction. This reduction in the free energy barrier is relatively small compared to the much larger changes in both the enthalpic ($\Delta[\Delta H^{\ddagger}_{fold}] \approx$ 11 kcal/mol) and entropic ($\Delta[T(298K)\Delta S^{\ddagger}_{fold}] \approx$ 12 kcal/mol) components.

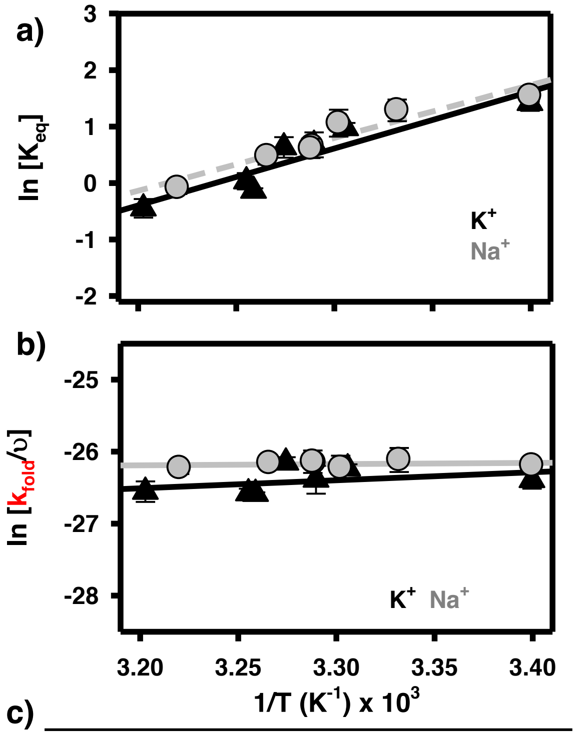

c)

330 mM	ΔH°_{fold} kcal/mol	ΔS°_{fold} kcal/mol/K
K+	-20(4)	-65(12)
Na+	-19(3)	-60(8)

d)

330 mM	$\Delta H^{\ddagger}_{fold}$ *kcal/mol*	$\Delta S^{\ddagger}_{fold}$ *kcal/mol/K*
K+	2(2)	-60(8)
Na+	0.3(7)	-53(2)

Figure 5.9 (a) van't Hoff analysis of tetraloop–receptor interaction comparing [Na$^+$] and [K$^+$]**(b)** Eyring analysis of tetraloop–receptor interaction comparing [Na$^+$] and [K$^+$]. **(c,d)** Table of thermodynamic parameters from the van't Hoff and Eyring analyses. As depicted, folding behavior is largely independent of monovalent cation identity.

Indeed, the growth of a strong enthalpic component to the free energy barrier with increasing $[Na^+]$ is in surprising opposition to what would be predicted if monovalent-enhanced stability of tertiary interactions were solely the result of a reduction of the entropic penalty associated with ion uptake or unmixing. Nevertheless, the growth of an endothermic barrier makes *entropy* the thermodynamic parameter responsible for increased favorability of folding at high monovalent concentrations. We postulate that these rather dramatic changes in the entropic and enthalpic components of the free energy barrier may result from monovalent-induced structural changes within the receptor domain. Specifically, we propose base unstacking and flipping of U19, along with the resulting structural changes, as one possible explanation worthy of further exploration. The results contained within this work support the emerging paradigm that suggests RNA folding is predominately rate-limited under free energy neutral conditions by a conformational search (e.g., $-T\Delta S^{\ddagger}_{fold} > \Delta H^{\ddagger}_{fold} \approx 0$ kcal/mol) and that addition of monovalent cations reduces the conformational search of RNAs at the potential cost of stabilizing alternative conformations (e.g., $-T\Delta S^{\ddagger}_{fold} \approx \Delta H^{\ddagger}_{fold} > 0$ kcal/mol). A thorough examination of other tertiary interactions such as H-type pseudoknots, larger non-coding RNAs (e.g riboswitches) and perhaps even duplex formation would be useful to demonstrate the universality of such a paradigm. Additionally, this work provides detailed experimental benchmarks for the thermodynamics associated with formation of tertiary interactions in RNA. These benchmarks can be used to test rigorous theoretical modeling of simple but ubiquitous RNA tertiary interactions in the presence of monovalents ions. Finally, this work clearly highlights important directions for future investigations of the more complex effects associated with mixed-valence cation solutions more relevant to that of the cellular environment.

5.6 Experimental Methods

5.6.1 Experimental Apparatus

Excitation of fluorescent molecules is accomplished by focusing light from a pulsed (20 MHz, 10 ps) 532 nm laser to a diffraction-limited spot in the sample with a 1.2 N.A. water emersion objective. The same objective collects the photons from the sample and directs them to a detection system using a dichroic mirror. A small pinhole rejects fluorescence from outside the confocal volume thereby reducing background signal. Photons from donor/acceptor fluorescence are separated by wavelength and polarization using dichroic filters and polarization beam splitters. The photons are then detected on single-photon avalanche photodiodes (see ref (36) for details). Photon arrival time information is sent to a time-correlated single-photon counting module where the fluorescence microtime (i.e. delay with respect to the laser pulse) and macrotime (time with respect to the start of the experiment) of each incoming photon is recorded.

5.6.2 Temperature Control

Two methods are used to provide temperature control of smFRET samples. The first involves the use of a microscope stage heater and a heated objective collar to uniformly heat the entire sample (see ref (36) for details). The second involves the use of a newly adapted IR-laser absorption based heating technique (see ref (66) for details). This technique provides the ability to control the local temperature of an aqueous sample using focused light from a fiber-coupled 1440 nm continuous-wave laser. While the stage heating method is used for a majority of the data collection, IR-laser based heating is also explored at all reported values of [Na^+]. The two heating methods used in the present work produce kinetic and thermodynamics results that have previously been determined to be indistinguishable from one another(66).

5.6.3 RNA and Sample Preparation

All nucleic acid sequences for the tetraloop–receptor constructs have been purchased commercially. The full construct consists of three strands of oligonucleotides (Figure 5.1): (*i*) a 5′ Cy3 labeled RNA strand containing the GAAA tetraloop sequence *ii*) a 5′ Cy5 labeled RNA strand with a 3′ overhang *iii*) a 5′ biotinylated DNA strand complementary to the 3′ overhang of the Cy5 strand. The three strands are annealed and purified using solutions and buffers described in previously work(10). Thermodynamic and kinetic data was collected using solutions consisting of: 50 mM hemisodium HEPES, 5.0 mM PCA, 100 nM PCD, 2.0 mM Trolox, 0.1 mM EDTA at pH 7.5 with varying concentrations of NaCl (100-800 mM) to achieve the desired [Na^+]. Note the [Na^+] comes from added NaCl, buffer, and the oxygen scavenging system—PCA/PCD.

5.7 Acknowledgment

We would like to thank Drs. Arthur Pardi and Christopher D. Downey for their contributions to the RNA construct design.

5.8 References

1. Mattick, J. S.; I. V. Makunin. Non-coding RNA, *Hum. Mol. Genet.*, **2006,** *15*, R17-R29.

2. Butcher, S. E.; A. M. Pyle. The molecular interactions that stabilize RNA tertiary structure: RNA motifs, patterns, and networks, *Acc. Chem. Res.*, **2011,** *44*, 1302-1311.

3. Ditzler, M. A.; D. Rueda; J. J. Mo; K. Hakansson; N. G. Walter. A rugged free energy landscape separates multiple functional RNA folds throughout denaturation, *Nucl. Acids Res.*, **2008,** *36*, 7088-7099.

4. Steiner, M.; D. Rueda; R. K. O. Sigel. Ca^{2+} induces the formation of two distinct subpopulations of group II intron molecules, *Angew. Chem. Int. Ed. Engl.* , **2009,** *48*, 9739-9742.

5. Xie, Z.; N. Srividya; T. R. Sosnick; T. Pan; N. F. Scherer. Single-molecule studies highlight conformational heterogeneity in the early folding steps of a large ribozyme, *Proc. Natl. Acad. Sci. USA*, **2004,** *101*, 534-539.

6. Zhuang, X. W.; H. Kim; M. J. B. Pereira; H. P. Babcock; N. G. Walter; S. Chu. Correlating structural dynamics and function in single ribozyme molecules, *Science*, **2002,** *296*, 1473–1476.

7. Record, M. T.; W. T. Zhang; C. F. Anderson. Analysis of effects of salts and uncharged solutes on protein and nucleic acid equilibria and processes: A practical guide to recognizing and interpreting polyelectrolyte effects, Hofmeister effects, and osmotic effects of salts, *Adv. Protein. Chem.*, **1998,** *51*, 281-353.

8. Privalov, P. L.; O. B. Ptitsyn; Birshtei.Tm. Determination of stability of DNA double helix in an aqueous medium, *Biopolymers*, **1969,** *8*, 559-571.

9. Manning, G. S. Application of polyelectrolyte limiting laws to helix-coil transition of DNA .1. Excess univalent cations, *Biopolymers*, **1972,** *11*, 937-947.

10. Downey, C. D.; J. L. Fiore; C. D. Stoddard; J. H. Hodak; D. J. Nesbitt; A. Pardi. Metal ion dependence, thermodynamics, and kinetics for intramolecular docking of a GAAA tetraloop and receptor connected by a flexible linker, *Biochemistry*, **2006,** *45*, 3664–3673.

11. Heilman-Miller, S. L.; J. Pan; D. Thirumalai; S. A. Woodson. Role of counterion condensation in folding of the Tetrahymena ribozyme II. Counterion-dependence of folding kinetics, *J. Mol. Biol.*, **2001,** *309*, 57–68.

12. Heilman-Miller, S. L.; D. Thirumalai; S. A. Woodson. Role of counterion condensation in folding of the Tetrahymena ribozyme. I. Equilibrium stabilization by cations, *J. Mol. Biol.*, **2001,** *306*, 1157–1166.

13. Nixon, P. L.; D. P. Giedroc. Energetics of a strongly pH dependent RNA tertiary structure in a frameshifting pseudoknot, *J. Mol. Biol.*, **2000,** *296*, 659–671.

14. Takamoto, K.; Q. He; S. Morris; M. R. Chance; M. Brenowitz. Monovalent cations mediate formation of native tertiary structure of the Tetrahymena thermophila ribozyme, *Nat. Struct. Biol.*, **2002,** *9*, 928-933.

15. Uchida, T.; K. Takamoto; Q. He; M. R. Chance; M. Brenowitz. Multiple monovalent ion-dependent pathways for the folding of the L-21 Tetrahymena thermophila ribozyme, *J. Mol. Biol.*, **2003,** *328*, 463-478.

16. Ke, A.; F. Ding; J. D. Batchelor; J. A. Doudna. Structural roles of monovalent cations in the HDV ribozyme, *Structure*, **2007,** *15*, 281-287.

17. Jiang, Y. F.; M. Xiao; P. Yin; Y. Zhang. Monovalent cations use multiple mechanisms to resolve ribozyme misfolding, *RNA*, **2006,** *12*, 561-566.

18. Lambert, D.; D. Leipply; R. Shiman; D. E. Draper. The influence of monovalent cation size on the stability of RNA tertiary structures, *J. Mol. Biol.*, **2009,** *390*, 791-804.

19. Shiman, R.; D. E. Draper. Stabilization of RNA tertiary structure by monovalent cations, *J. Mol. Biol.*, **2000,** *302*, 79–91.

20. Uchida, T.; Q. He; C. Y. Ralston; M. Brenowitz; M. R. Chance. Linkage of monovalent and divalent ion binding in the folding of the P4-P6 domain of the Tetrahymena ribozyme, *Biochemistry*, **2002,** *41*, 5799-5806.

21. Basu, S.; R. P. Rambo; J. Strauss-Soukup; J. H. Cate; A. R. Ferre-D'Amare; S. A. Strobel; J. A. Doudna. A specific monovalent metal ion integral to the AA platform of the RNA tetraloop receptor, *Nat. Struct. Biol.*, **1998,** *5*, 986–992.

22. Wang, Y. X.; M. Lu; D. E. Draper. Specific ammonium ion requirement for functional ribosomal-RNA tertiary structure, *Biochemistry*, **1993,** *32*, 12279-12282.

23. Draper, D. E. RNA folding: Thermodynamic and molecular descriptions of the roles of ions, *Biophys. J.*, **2008,** *95*, 5489-5495.

24. Anderson, C. F.; M. T. Record. Salt nucleic-acid interactions, *Annu. Rev. Phys. Chem.*, **1995,** *46*, 657–700.

25. Tinoco, I.; C. Bustamante. How RNA folds, *J. Mol. Biol.*, **1999,** *293*, 271–281.

26. Sosnick, T. R.; T. Pan. RNA folding: Models and perspectives, *Curr. Opin. Struct. Biol.*, **2003,** *13*, 309–316.

27. Woese, C. R.; S. Winker; R. R. Gutell. Architecture of ribosomal-RNA: "Constraints on the sequence of Tetraloops", *Proc. Natl. Acad. Sci. USA*, **1990,** *87*, 8467-8471.

28. Hodak, J. H.; C. D. Downey; J. L. Fiore; A. Pardi; D. J. Nesbitt. Docking kinetics and equilibrium of a GAAA tetraloop-receptor motif probed by single-molecule FRET, *Proc. Natl. Acad. Sci. USA*, **2005,** *102*, 10505–10510.

29. Cate, J. H.; A. R. Gooding; E. Podell; K. H. Zhou; B. L. Golden; C. E. Kundrot; T. R. Cech; J. A. Doudna. Crystal structure of a group I ribozyme domain: Principles of RNA packing, *Science*, **1996,** *273*, 1678–1685.

30. Batey, R. T.; R. P. Rambo; J. A. Doudna. Tertiary motifs in RNA structure and folding, *Angew. Chem. Int. Ed.*, **1999,** *38*, 2327–2343.

31. Costa, M.; F. Michel. Frequent use of the same tertiary motif by self-folding RNAs, *Embo. J.*, **1995,** *14*, 1276–1285.

32. Vander Meulen, K. A.; J. H. Davis; T. R. Foster; T. Record; S. E. Butcher. Thermodynamics and folding pathway of tetraloop receptor-mediated RNA helical packing, *J. Mol. Biol.*, **2008,** *384*, 702-717.

33. Young, B. T.; S. K. Silverman. The GAAA tetraloop-receptor interaction contributes differentially to folding thermodynamics and kinetics for the P4-P6 RNA domain, *Biochemistry*, **2002,** *41*, 12271–12276.

34. Sattin, B. D.; W. Zhao; K. Travers; S. Chut; D. Herschlag. Direct measurement of tertiary contact cooperativity in RNA folding, *J. Am. Chem. Soc.*, **2008,** *130*, 6085–6087.

35. Fiore, J. L.; J. H. Hodak; O. Piestert; C. D. Downey; D. J. Nesbitt. Monovalent and Divalent Promoted GAAA-Tetraloop–Receptor Tertiary Interactions from Freely Diffusing Single-Molecule Studies, *Biophys. J.*, **2008,** *95*, 3892-3905.

36. Fiore, J. L.; B. Kraemer; F. Koberling; R. Erdmann; D. J. Nesbitt. Enthalpy-Driven RNA Folding: Single-Molecule Thermodynamics of Tetraloop–Receptor Tertiary Interaction, *Biochemistry*, **2009,** *48*, 2550–2558.

37. Butcher, S. E.; T. Dieckmann; J. Feigon. Solution structure of a GAAA tetraloop receptor RNA, *Embo. J.*, **1997,** *16*, 7490–7499.

38. Davis, J. H.; M. Tonelli; L. G. Scott; L. Jaeger; J. R. Williamson; S. E. Butcher. RNA helical packing in solution: NMR structure of a 30 kDa GAAA tetraloop-receptor complex *J. Mol. Biol.*, **2005,** *351*, 371–382.

39. Heus, H. A.; A. Pardi. Structural features that give rise to the unusual stability of RNA hairpins containing GNRA loops, *Science*, **1991,** *253*, 191-194.

40. Jucker, F. M.; H. A. Heus; P. F. Yip; E. H. M. Moors; A. Pardi. A network of heterogeneous hydrogen bonds in GNRA tetraloops, *J. Mol. Biol.*, **1996,** *264*, 968-980.

41. Aleman, E. A.; R. Lamichhane; D. Rueda. Exploring RNA Folding One Molecule at a Time, *Curr. Opin. Chem. Biol.*, **2008,** *12*, 647-654.

42. Bokinsky, G.; X. W. Zhuang. Single-molecule RNA folding, *Acc. Chem. Res.*, **2005,** *38*, 566–573.

43. Blanco, M.; N. G. Walter. Analysis of complex single-molecule FRET time trajectories, *Methods Enzymol.*, **2010,** *472*, 153-178.

44. Bartley, L. E.; X. W. Zhuang; R. Das; S. Chu; D. Herschlag. Exploration of the Transition State for Tertiary Structure Formation Between an RNA Helix and a Large Structured RNA, *J. Mol. Biol.*, **2003,** *328*, 1011–1026.

45. Zhou, Y. J.; X. W. Zhuang. Robust reconstruction of the rate constant distribution using the phase function method, *Biophys. J.*, **2006,** *91*, 4045-4053.

46. Leipply, D.; D. Lambert; D. E. Draper. Ion-RNA interactions: Thermodynamic analysis of the effects of mono- and divalent ions on RNA conformational equilibria, *Methods Enzymol.*, **2009,** *469*, 433-463.

47. Bokinsky, G.; D. Rueda; V. K. Misra; M. M. Rhodes; A. Gordus; H. P. Babcock; N. G. Walter; X. W. Zhuang. Single-molecule transition-state analysis of RNA folding, *Proc. Natl. Acad. Sci. USA*, **2003,** *100*, 9302–9307.

48. Fiore, J. L.; E. D. Holmstrom; D. J. Nesbitt. An Entropic origin of Mg^{2+}-Facilitated RNA Folding, *Proc. Natl. Acad. Sci. USA*, **2011**, (Accepted).

49. Hanggi, P.; P. Talkner; M. Borkovec. Reaction-rate theory - 50 years after Kramers, *Rev. Mod. Phys.*, **1990,** *62*, 251-341.

50. Vander Meulen, K. A.; S. E. Butcher. Characterization of the kinetic and thermodynamic landscape of RNA folding using a novel application of isothermal titration calorimetry, **2011,** *DOI:10.1093/nar/gkr894*.

51. Davis, J. H.; T. R. Foster; M. Tonelli; S. E. Butcher. Role of metal ions in the tetraloop-receptor complex as analyzed by NMR, *RNA*, **2007,** *13*, 76-86.

52. Buchmueller, K. L.; A. E. Webb; D. A. Richardson; K. M. Weeks. A collapsed non-native RNA folding state, *Nat. Struct. Biol.*, **2000,** *7*, 362-366.

53. Swisher, J. F.; L. H. J. Su; M. Brenowitz; V. E. Anderson; A. M. Pyle. Productive folding to the native state by a group II intron ribozyme, *J. Mol. Biol.*, **2002,** *315*, 297-310.

54. Silverman, S. K.; T. R. Cech. An early transition state for folding of the P4-P6 RNA domain, *RNA*, **2001,** *7*, 161–166.

55. Pljevaljcic, G.; D. Klostermeier; D. P. Millar. The tertiary structure of the hairpin ribozyme is formed through a slow conformational search, *Biochemistry*, **2005,** *44*, 4870-4876.

56. Szewczak, A. A.; E. R. Podell; P. C. Bevilacqua; T. R. Cech. Thermodynamic stability of the P4-P6 domain RNA tertiary structure measured by temperature gradient gel electrophoresis, *Biochemistry*, **1998,** *37*, 11162–11170.

57. Vander Meulen, K. A.; S. E. Butcher. Characterization of the kinetic and thermodynamic landscape of RNA folding using a novel application of isothermal titration calorimetry, *Nucl. Acids Res.*, **2012,** *40*, 2140-2151.

58. Holbrook, J. A.; M. W. Capp; R. M. Saecker; M. T. Record. Enthalpy and heat capacity changes for formation of an oligomeric DNA duplex: Interpretation in terms of coupled processes of formation and association of single-stranded helices, *Biochemistry*, **1999,** *38*, 8409-8422.

59. Takach, J. C.; P. J. Mikulecky; A. L. Feig. Salt-dependent heat capacity changes for RNA duplex formation, *J. Am. Chem. Soc.*, **2004,** *126*, 6530-6531.

60. Qin, P. Z.; J. Feigon; W. L. Hubbell. Site-directed spin labeling studies reveal solution conformational changes in a GAAA tetraloop receptor upon Mg^{2+}-dependent docking of a GAAA tetraloop, *J. Mol. Biol.*, **2005,** *351*, 1-8.

61. Lambert, D.; D. Leipply; D. E. Draper. The osmolyte TMAO stabilizes native RNA tertiary structures in the absence of Mg^{2+}: Evidence for a large barrier to folding from phosphate dehydration, *J. Mol. Biol.*, **2010,** *404*, 138-157.

62. Breslauer, K. J.; J. M. Sturtevant. Calorimetric investigation of single stranded base stacking in ribo-oligonucleotide-A7, *Biophys. Chem.*, **1977,** *7*, 205-209.

63. Seol, Y.; G. M. Skinner; K. Visscher. Elastic properties of a single-stranded charged homopolymeric ribonucleotide, *Phys. Rev. Lett.*, **2004,** *93*, 118102.

64. Michelson, A. M.; C. Monny. Polynucleotides .8. Base stacking in polyuridylic acid, *Proc. Natl. Acad. Sci. U.S.A.*, **1966,** *56*, 1528-1534.

65. Fiore, J. L.; E. D. Holmstrom; L. R. Feigland; J. H. Hodak; D. J. Nesbitt. The Role of Counterion Valence and Size in the GAAA Tetraloop-Receptor Docking/Undocking Kinetics, **2011**, (In preperation).

66. Holmstrom, E. D.; D. J. Nesbitt. Real-time infrared overtone laser control of temperature in picoliter H_2O samples: "Nanobathtubs" for single-molecule microscopy, *J. Phys. Chem. Lett.*, **2010,** *1*, 2264–2268.

Chapter 6

Kinetic and Thermodynamic Origins of Osmolyte-Influenced Nucleic Acid Folding[*]

6.1 Introduction

The folding free energy for nucleic acid is significantly influenced by the presence of cosolutes. Some of the most prominent cosolutes are metal ions, which are known to be important for a large number of nucleic acid conformational transitions ranging in complexity from short, single-strand oligonucleotides to large, highly organized RNAs like the large ribosomal subunit(1,2). However, metal ions are not the only cosolutes that can alter the energetics of nucleic acid folding. Many highly soluble organic small molecules—known as osmolytes—can also affect the stability of various nucleic acid structural motifs(3).

Early work on the biological importance of osmolytes has demonstrated that they help living cells respond to changes in osmotic pressure(4,5). However, numerous experiments have shown that high concentrations of osmolytes can either *facilitate* or *inhibit* folding of nucleic acids and proteins, depending on the chemical nature of the osmolyte. As intracellular concentrations change in response to osmotic stress, the effects of these cosolutes on the energetics of structured proteins and nucleic acids must therefore be counterbalanced in order to maintain homeostasis. Previous biological studies have validated this idea by demonstrating that some organisms are able to adjust intracellular concentrations of stabilizing osmolytes to offset the effect of urea(6,7).

---

[*] To be submitted

Because osmolytes are known to alter the stability of biomolecules, a large number of scientific investigations have centered on studying their ability to influence protein (8-11) and nucleic acid (12-17) conformational transitions. Urea is one of the most prominent osmolytes and tends to *destabilize* folded proteins(18-20) and nucleic acids(21-23), where as trimethylamine N-oxide (TMAO) is an osmolyte that has been shown to *stabilize* these biomolecules(13,22,24,25). Recently, the interactions between osmolytes and nucleic acids have begun to attract the same degree of attention as their protein-based analogues. To follow suit, this work reports on the first, to our knowledge, detailed kinetic investigation of the topic using single-molecule fluorescence techniques.

Over the years, a number of experimental and theoretical efforts regarding TMAO(13,26) and urea(14,27) have brought about a more physical understanding of such nucleic acid-osmolyte interactions. Inspired by quantitative thermodynamic work on proteins(11), recent bulk ensemble studies indicate that osmolytes can interact with any of the three components of a nucleic acid—base, sugar, and phosphate(12-14). Specifically, these ensemble experiments have demonstrated that urea *destabilizes* RNA folding transitions by forming *favorable* interactions with all three constituents, which *increase* in strength from urea-phosphate to urea-nucleobase(14). Because the unfolded conformations of most nucleic acids tend to have more solvent accessible surface area (SASA), the presence of urea will therefore tend to *preferentially stabilize* such *unfolded* conformations relative to those that are *folded* and more compact (Figure 6.1). This results in a net *increase* in the free energy change ($\Delta G°_{fold}$) between the unfolded and folded conformation, which is driven primarily by SASA-mediated burial of nucleobases. For this reason, urea is referred to as a *destabilizing* osmolyte. Conversely, the presence of the osmolyte TMAO gives rise to precisely the opposite effect, specifically a net decrease in $\Delta G°_{fold}$.

This results primarily from *unfavorable* interactions between the osmolyte and the various surfaces of a nucleic acid, which range in strength from TMAO- phosphate to the rather weak TMAO-sugar interactions(13). As described above, nucleic acids tend to become more compact when they fold and, as a result, phosphate SASA is often buried. Therefore, the presence of TMAO yields a *preferential destabilization* of the *unfolded* species, which results in a net *stabilization* of the folding transition (Figure6.1). Hence, TMAO is characterized as a *stabilizing* osmolyte.

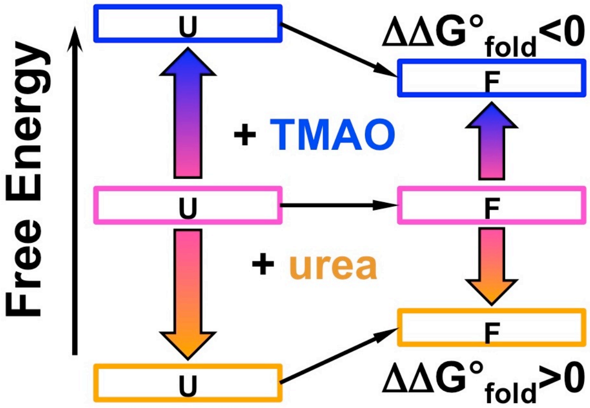

Figure 6.1 Free energy diagram representing the effect of TMAO or urea on the stability of the unfolded (**U**) or folded (**F**) structures of a nucleic acid. TMAO has a *more unfavorable* interaction with the *unfolded* structure than the *folded* structure, which results in a net *decrease* in $\Delta G°_{\mathrm{fold}}$. Urea has a *more favorable* interaction with the *unfolded* conformation than *folded* conformation, which gives rise to a net *increase* in $\Delta G°_{\mathrm{fold}}$.

To date, most experimental studies that investigate the influence of osmolytes on structured nucleic acid have been based on ensemble techniques (e.g., calorimetry or UV-spectroscopy) that only provide information about the equilibrium constant between folded and unfolded species (e.g., K_{eq} = [folded]/[unfolded]=). Although these techniques have been extremely informative, they lack the ability to partition the observed *equilibrium* effects into components related to the folding/unfolding *kinetics* (e.g., $K_{eq} = k_{fold}/k_{unfold}$). Because of this, the *kinetic* origin of osmolyte-influenced nucleic acid folding is not well known and is, therefore, the major focus of this study.

Single-molecule methods(28) are ideally suited to address these questions by providing kinetic information about the folding and unfolding rate constants of various nucleic acid conformational transitions. To this end, single-molecule fluorescence resonance energy transfer (29-32) (smFRET) is used to determine the *kinetic* origins of TMAO-*facilitated* and urea-*inhibited* nucleic acid folding. Specifically, two fluorescently labeled constructs (Figure 6.2) serve as models systems for both types of nucleic acid folding transitions—secondary (2°) structure formation (e.g., duplex association/dissociation) and tertiary (3°) structure formation (e.g., loop docking/undocking). The first model construct is a previously characterized(33) 8 bp DNA duplex that is used to elucidate the role of osmolytes in the formation of nucleic acid 2° structures (Figure 6.2a,b). The second is an RNA construct that isolates the GAAA tetraloop—tetraloop receptor (TL-TLR) interaction from the *Tetrahymena* ribozyme. This ubiquitous loop-bulge interaction has undergone extensive biophysical characterization at the single-molecule level (34-40) and is used to study the influence of osmolytes on RNA 3° structure formation (Figure 6.2b,c). Using smFRET techniques to study these model systems, we show that the kinetic origin of TMAO-*facilitated* nucleic acid folding arises from an *increase* in k_{fold} and a corresponding *decrease* in k_{unfold} for both 2° and 3° structure formation. The precise *opposite* is true for the kinetic origin of urea-*inhibited* nucleic acid structure formation, which results from a *decrease* in k_{fold} and an *increase* in k_{unfold}, regardless of the nucleic acid construct.

6.2 Results

The two nucleic acid constructs are chosen to serve as model systems for a variety of reasons. First and foremost, they broadly represent the two types of structure formation in nucleic acids—secondary (2°) and tertiary (3°). Specifically, canonical Watson-Crick interactions within a double helix are one of the defining characteristics of nucleic acid 2° structures.

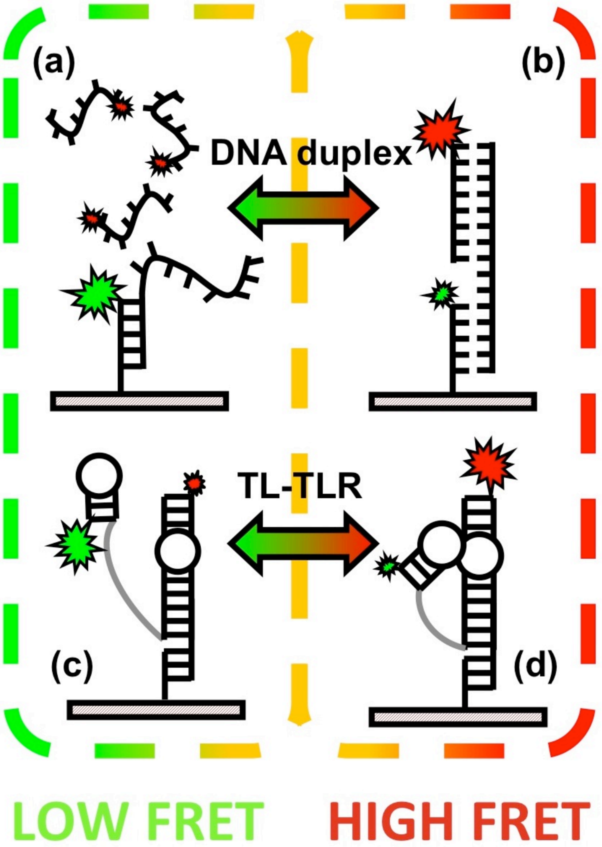

Figure 6.2 Cartoon representation of the two smFRET nucleic acid constructs used throughout the study. The DNA duplex construct (**a** and **b**) is intended to be a model system for nucleic acid secondary structure, where as the TL-TLR construct (**c** and **d**) serves as a model for tertiary interactions in structured RNAs. For both constructs, formation of the interaction (**b** and **d**), referred to as folding, results in an increase in E_{FRET}(**a** and **c**).

Alternatively, the interaction between the GAAA tetraloop and the tetraloop receptor (TL-TLR) contains both non-canonical hydrogen bonding and base stacking between a loop and an internal bulge, which are among some of the distinguishing features of 3° structures. These tertiary contacts frequently orient and stabilize the global architecture and three-dimensional conformation of large structured nucleic acids. An additional reason for using these two constructs as model systems is that both the 8 bp DNA duplex(33) and the TL-TLR have been previously characterized using single-molecule techniques(34-40), which establishes a well-understood baseline for the folding kinetics in the absence of osmolytes. Lastly, both interactions are capable of forming in the absence of Mg^{2+}. This allows the equilibrium constant for the two conformational transitions to easily be adjusted via the [KCl] and also limits the number of cosolutes in solution, therefore reducing the potential for complex cooperative effects observed in more complex solutions.

6.2.1 Folding in the Absence of Osmolytes

Individual time-trajectories for surface immobilized TL-TLR constructs demonstrate two-state behavior (Figure 6.3a) with well-defined high and low FRET states (e.g., docked ⇔ undocked). The 8bp DNA duplex exists in a bimolecular equilibrium (e.g., strand 3+ dsDNA scaffold ⇔ duplex) with a concentration-dependent rate constant for duplex association. To facilitate determination of this rate constant, experiments are performed at a fixed concentration (200 nM) of the freely diffusing Cy5, as previously reported(33). Surface immobilized trajectories of the 8bp duplex also exhibit two-state behavior (Figure 6.3b). The well-separated FRET states for each of the two constructs make it easy to determine dwell times using a previously described thresholding routine(39). The experimentally measured dwell times are analyzed via a cumulative distribution function(41-43) to determine the rate constants for each construct, which establishes a point-of-comparison for experiments that are conducted using solutions containing high concentrations of osmolytes. For ease of discussion, the *forward* rate constant for both systems (i.e. duplex association and tetraloop docking) will be referred to as the *folding* rate constant (k_{fold}), whereas the *reverse* rate constant will be referred to as the *unfolding* rate constant (k_{unfold}).

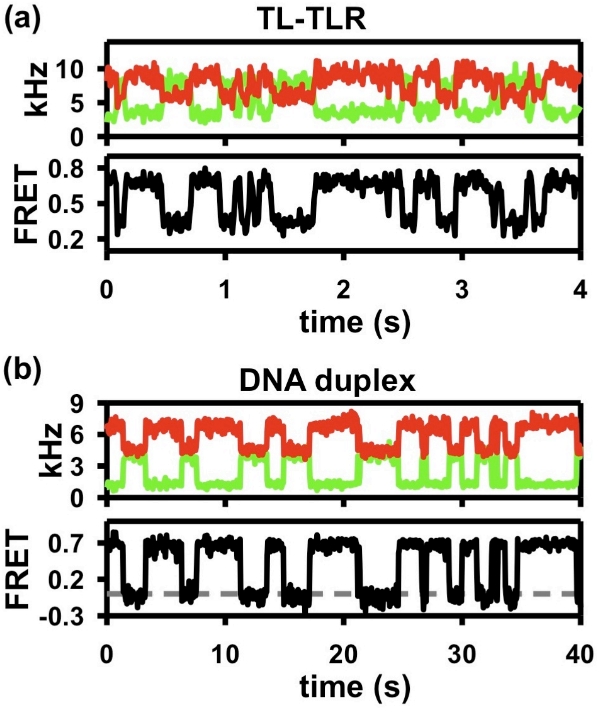

Figure 6.3 Representative donor (green) and acceptor (red) fluorescence trajectories for **(a)** the TL-TLR and **(b)** the DNA duplex. Fluorescence data is use to calculate the FRET trajectories (black), which are then analyzed to measure the folding (k_{fold}) and unfolding (k_{unfold}) rate constants for each of the nucleic acid constructs.

To further facilitate kinetic and thermodynamic comparisons between constructs, KCl concentrations are adjusted so that ΔG° in the absence of any osmolytes is ≈ 0 for both folding transitions (i.e., 50 mM and 100 mM for the TL-TLR and 8 bp DNA duplex, respectively). The following four sections highlight the important kinetic and thermodynamic observations associated with osmolyte-influenced nucleic acid folding.

6.2.2 Osmolyte-Dependent Folding Kinetics

Titrations of both TMAO and urea clearly demonstrate the kinetic origin of osmolyte-influenced nucleic acid folding (Figure 6.4). The presence of TMAO *increases* k_{fold} (Figure 6.4a) and *decreases* k_{unfold} (Figure 6.4b) for both nucleic acid constructs. Together, these *kinetic* effects contribute to an *increase* in K_{eq} and more *favorable* folding.

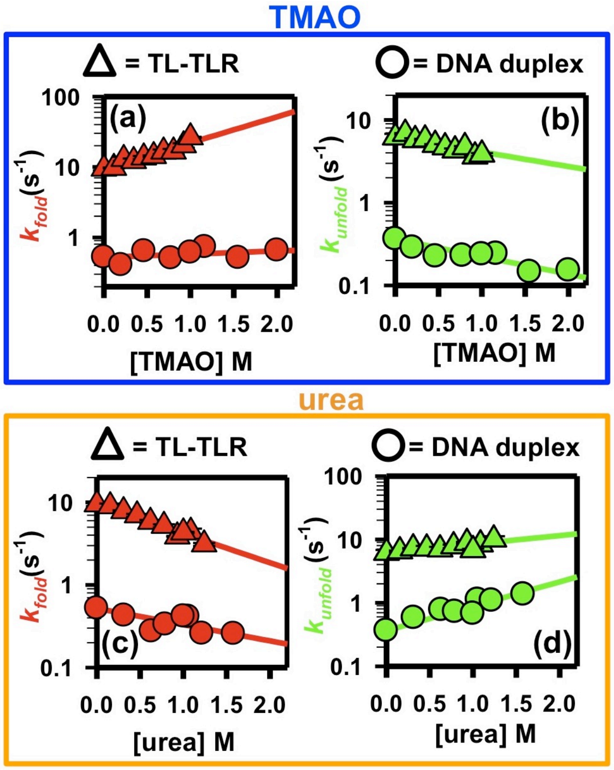

Figure 6.4 Kinetic origin of osmolyte- influenced nucleic acid folding. The *stabilizing* osmolyte TMAO (blue box) *increases* the **(a)** folding rate constant (k_{fold}, red) and *decreases* the **(b)** unfolding rate constant (k_{unfold}, green) for both the GAAA tetraloop—receptor (triangle) and DNA duplex (circle) constructs. The *destabilizing* osmolyte, urea, *decreases* the **(c)** folding rate constant (k_{fold}, red) and *increases* the **(d)** unfolding rate constant (k_{unfold}, green) for both constructs.

The exact *opposite* effect results from the presence of urea, where elevated concentrations *decrease* k_{fold} (Figure 6.4c) and *increase* k_{unfold} (Figure 6.4d) for both the 8 bp DNA duplex and the TL-TLR. Interestingly, the qualitative trends highlighted above are quantitatively different. These distinctions are exemplified by the following two observations: (*i*) TMAO *accelerates* k_{fold} for the TL-TLR more effectively that it does for the 8 bp DNA duplex (Figure 6.4a, red triangles vs circles) and (*ii*) urea *decelerates* k_{unfold} for the 8 bp DNA duplex more effectively that it does for the TL-TLR (Figure 6.4d, green triangles vs circles).

6.2.3 Osmolyte-Dependent Folding Free Energies (*m*-value analysis)

With knowledge of both rate constants, the free energy change for folding ($\Delta G^\circ_{\mathrm{fold}}$) can readily be calculated from the equilibrium constant ($K_{\mathrm{eq}} = k_{\mathrm{fold}}/k_{\mathrm{unfold}}$) using the Gibbs equation ($\Delta G^\circ = -RT\ln[K_{\mathrm{eq}}]$). As empirically observed for nucleic acids(21,44,45) and proteins(46,47), the folding free energy change is linearly-dependent on osmolyte concentration (Figure 6.5). This dependence ($\partial\Delta G^\circ/\partial$[osmolyte]) is often characterized by the *m*-value, which serves as a measure of the folding transition's sensitivity to the presence of an osmolyte. From these *m*-values, it is apparent that: (*i*) TMAO is much more effective at *stabilizing* the TL-TLR than the 8 bp DNA duplex and (*ii*) urea *destabilizes* both model constructs by an equal amount (Figure 6.5).

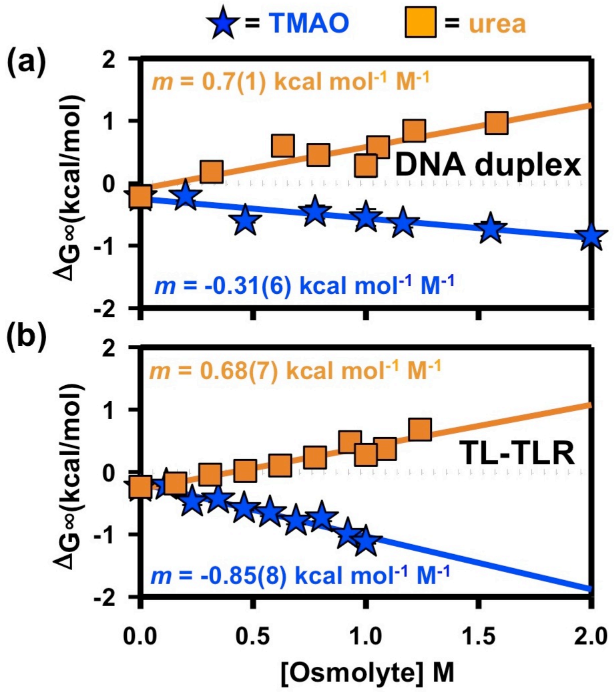

Figure 6.5 Osmolyte-dependent folding free energy change for **(a)** the DNA duplex and **(b)** the TL-TLR constructs. For both constructs, addition of TMAO (blue stars) always *stabilizes* the folding transitions, where as addition of urea (orange squares) *destabilizes* the folding transitions as indicated by the dependence of ΔG° on the osmolyte concentration.

Both of these observations are in complete accordance with previous equilibrium-based ensemble studies, which reveal that urea can effectively *destabilize* both 2° and 3° interactions, where as TMAO primarily *stabilizes* 3° structure formation. Additionally, this experimental agreement further validates the use of single-molecule experiments to study osmolyte-influenced nucleic acid conformational transitions with the intent to partition *equilibrium* effects into their *kinetic* components.

6.2.4 Osmolyte-Dependent Thermodynamics for the 8 bp DNA Duplex

To more rigorously understand the kinetic origin of osmolyte-influenced folding of nucleic acids, temperature-dependent single-molecule experiments have been performed to parse the free energy change into its enthalpic and entropic components ($\Delta G° = \Delta H° - T\Delta S°$)(40,48). Briefly, the inverse temperature-dependence of ln[K_{eq}] can be used to provide information about ΔH° and ΔS° for the two model systems in the form of a van't Hoff analysis. Similarly, the inverse temperature-dependence of ln[*k*] provides information about the enthalpic and entropic components of the free energy barrier ($\Delta H^{‡}$ and $\Delta S^{‡}$) in what is referred to as an Eyring analysis. In a plot of ln[K_{eq}] vs 1/T (Figure 6.6), the slope represents $-\Delta H°/R$ and the intercept, corresponds to $\Delta S°/R$, where R is the Gas constant ($\approx$ 1.987 cal mol^{-1} K^{-1}). For the 8 bp DNA duplex, neither of the 1M osmolyte solutions substantially changes ΔH° (Figure 6.6a). This indicates that the *thermodynamic* origin of TMAO- and urea-influenced 2° structure formation is predominately *entropic*. Furthermore, the Eyring analyses demonstrate that there is a much larger change in $\Delta S^{‡}_{unfold}$ than $\Delta S^{‡}_{fold}$, which implies that this *entropic* origin is associated with the *unfolding* process (Supplemental Figure S6.1b). Explicitly stated, TMAO *stabilizes* the 8 bp DNA duplex by making the unfolding barrier *less* entropically rewarding. Conversely, urea *destabilizes* this conformational transition by making the unfolding barrier *more* entropically rewarding. As a testament to the validity of these single-molecule experiments, the thermodynamics results for the 8 bp DNA duplex are in excellent agreement with the corresponding kinetic data, which demonstrates that both osmolytes more prominently affect k_{unfold} rather than k_{fold} (Figure 6.4, circles).

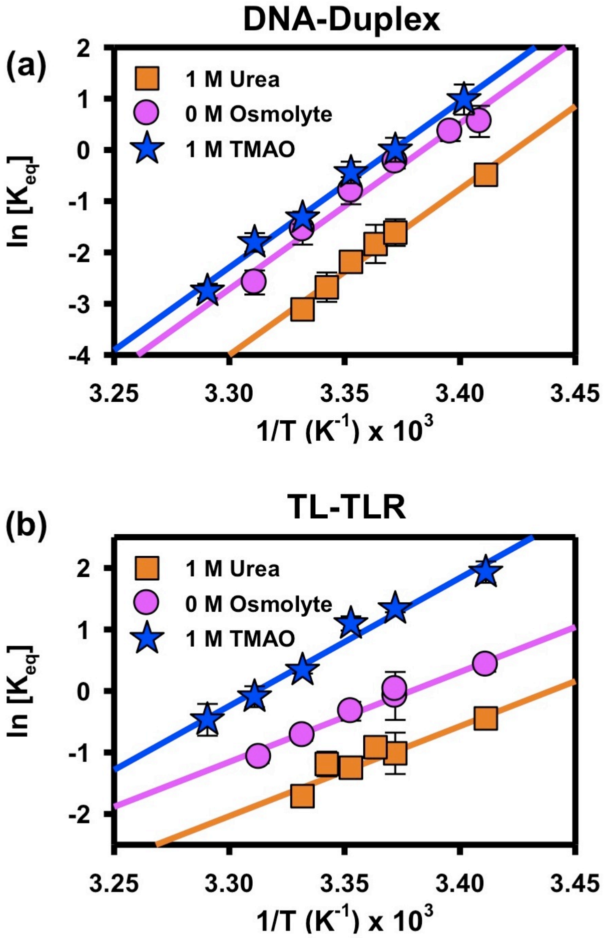

Figure 6.6 van't Hoff plots for the osmolyte- influenced folding of both **(a)** the DNA duplex and **(b)** the TL-TLR interaction. Solid lines in **(a)** correspond to a global fit with a common slope, as discussed in the text, to reduce parameter correlation between the three data sets: 1 M TMAO (blue stars), 0 M osmolyte (pink circles), and 1 M urea (orange squares). The solid lines for the TL-TLR interaction **(b)** are also the result of a global fit of the 0 M osmolyte and 1 M urea data sets in order to reduce parameter correlation, while the solid line for the 1M TMAO data set represents an independent fit of the data. See Table 6.1 for values of the fitted parameters.

	8bp DNA-Duplex			TL-TLR		
[Osmolyte] M	Δ*H*° kcal mol^{-1}	Δ*H*° kcal mol^{-1}	Δ*S*° cal mol^{-1} K^{-1}	Δ*H*° kcal mol^{-1}	Δ*H*° kcal mol^{-1}	Δ*S*° cal mol^{-1} K^{-1}
1 M TMAO	-65(6) [a]	-65(3) [b]	-218.1(2) [c]	41(3) [a]	n/a	-137(11) [a]
0 M Osmolyte	-63(6) [a]	-65(3) [b]	-218.8(2) [c]	-31(3) [a]	-29(2) [b]	-97.07(8) [c]
1 M Urea	-65(5) [a]	-65(3) [b]	-221.5(2) [c]	-28(4) [a]	-29(2) [b]	-99.82(8) [c]

[a]-Enthalpy or entropy values from independent linear fits to the van't Hoff plots of ln[K_{eq}] vs 1/T
[b]-Enthalpy values from a global fit of the datasets with a common enthalpy change (slope)
[c]-Entropy values from a global fit of the datasets with a common enthalpy change (slope)

Table 6.1 Values for the van't Hoff analysis of the osmolyte-influenced folding nucleic acids. Additional information about the methods of data analysis for the van't Hoff plots can be found in Section 6.3.4. See Figure 6.6 for experimental data.

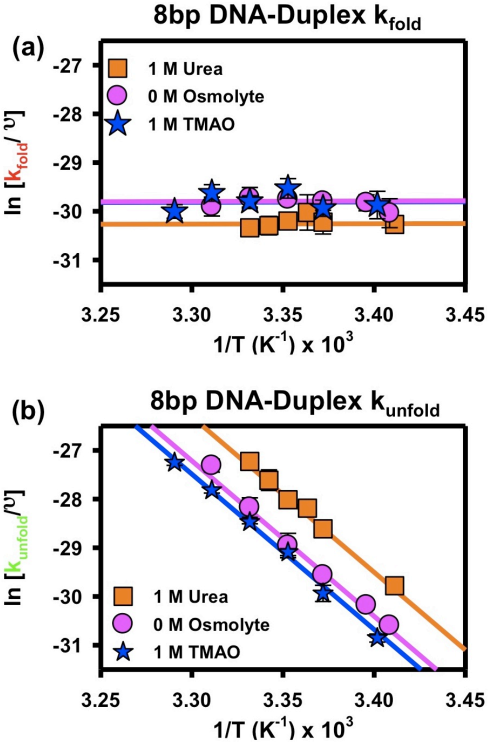

(c) **DNA duplex**

[Osmolyte] M	Δ*H*°$_{fold}$ kcal mol^{-1}	Δ*H*°$_{fold}$ kcal mol^{-1}	Δ*S*°$_{fold}$ cal mol^{-1} K^{-1}
1 M TMAO	2(2) [a]	0 (1) [b]	-59.86(7) [c]
0 M Osmolyte	-1(2) [a]	0(1) [b]	-59.82(6) [c]
1 M Urea	0(2) [a]	0(1) [b]	-60.75(7) [c]

[Osmolyte] M	Δ*H*°$_{unfold}$ kcal mol^{-1}	Δ*H*°$_{unfold}$ kcal mol^{-1}	Δ*S*°$_{unfold}$ cal mol^{-1} K^{-1}
1 M TMAO	64(2) [a]	63.4(7) [b]	154.66(2) [c]
0 M Osmolyte	63(2) [a]	63.4(7) [b]	155.20(3) [c]
1 M Urea	62(2) [a]	63.4(7) [b]	156.99(2) [c]

[a]-Enthalpy or entropy values from independent linear fits to the transition state theory plots of ln[k/ν] vs 1/T
[b]-Transition state enthalpy change for a global fit of the datasets with a common slope
[c]-Transition state entropy change for the datasets with a fixed and common transition state enthalpy change

Supplemental Figure S6.1 Temperature-dependent kinetic data for the **(a)** folding and **(b)** unfolding rate constants for the DNA duplex. The data are analyzed using transition state theory. Solid lines in correspond to a global fit with a common slope, as discussed in the text, to reduce parameter correlation. The large entropic offset in the temperature-dependence of the unfolding rate constants **(b)** suggests that most of the change in ΔS° arises from changes in the entropic barrier to unfolding ($\Delta S^{\ddagger}_{unfold}$). The data table **(c)** contains values for the transition state theory analysis of the temperature-dependent kinetic data for the DNA duplex. Fitting methods are identical to those used in the van't Hoff analysis (Figure 6.6), which is discussed in Section 6.3.4.

6.2.5 Osmolyte-Dependent Thermodynamics for the TL-TLR

The van't Hoff and Eyring analyses of the TL-TLR highlight key similarities and differences between the two osmolytes. Additionally, when compared to results of the thermodynamic studies of the 8 bp DNA duplex, these observations also highlight similarities and differences between the two types of conformational transitions. As was the case for the urea-*inhibited* folding of the 8 bp DNA duplex, the presence of 1 M urea has little affect on the ΔH° for the TL-TLR interaction (Figure 6.6b), which, again, indicates that *entropy* is the thermodynamic parameter responsible for destabilization. However, *unlike* the 8bp DNA duplex, most of this change in ΔS° arises from the *folding* process (Supplemental Figure S6.2). The urea-dependent thermodynamics for the TL-TLR construct are remarkably well supported by the corresponding kinetics, which demonstrate that *destabilization* occurs primarily via a *reduction* of k_{fold} (Figure 6.4c, triangles). Together, the kinetic and thermodynamic results from the TL-TLR experiments imply that urea *destabilizes* this interaction by *increasing* the *entropic* cost associated with the *folding* free energy barrier.

Interestingly, elevated concentrations of TMAO change both the ΔH° (slope) and the ΔS° (intercept) associated with formation of the TL-TLR interaction (Figure 6.6b), which is also demonstrated in Eyring analyses (Supplemental Figure S6.2a). This is surprising because TMAO does not affect the ΔH° for the 8bp DNA duplex. The prominence of both an *enthalpic* and *entropic* component to TMAO-*facilitated* formation of the TL-TLR suggests that this osmolyte interacts differently with the two nucleic acid constructs, presumably as a result of considerably different changes in the phosphate SASA.

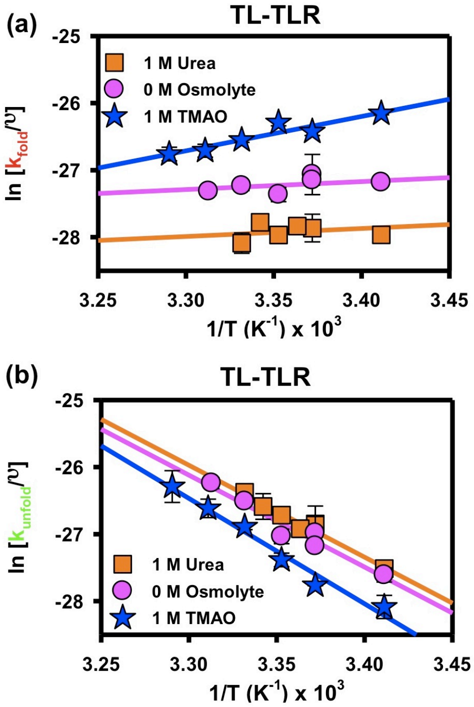

(c) **TL-TLR**

[Osmolyte] M	ΔH°_{fold} kcal mol^{-1}	ΔH°_{fold} kcal mol^{-1}	ΔS°_{fold} cal mol^{-1} K^{-1}
1 M TMAO	-10(2) [a]	n/a	-87(7) [a]
0 M Osmolyte	-4(3) [a]	-2(2) [b]	-61.97(8) [c]
1 M Urea	-1(3) [a]	-2(2) [b]	-63.36(8) [c]

[Osmolyte] M	$\Delta H^{\circ}_{unfold}$ kcal mol^{-1}	$\Delta H^{\circ}_{unfold}$ kcal mol^{-1}	$\Delta S^{\circ}_{unfold}$ cal mol^{-1} K^{-1}
1 M TMAO	31(2) [a]	n/a	50(7) [a]
0 M Osmolyte	27(3) [a]	-65(3) [b]	-38.00(8) [c]
1 M Urea	27(3) [a]	-65(3) [b]	-38.29(2) [c]

[a]-Enthalpy or entropy values from independent linear fits to the transition state theory plots of ln[k/ν] vs 1/T

[b]-Transition state enthalpy change for a global fit of the datasets with a common slope

[c]-Transition state entropy change for the independent datasets with a fixed and common transition state enthalpy change

Supplemental Figure S6.2 Temperature- dependent kinetic data for the **(a)** folding and **(b)** unfolding rate constants for the TL-TLR. The data are analyzed using transition state theory. Solid lines for 1 M urea (orange squares) and 0 M osmolyte (pink circles) correspond to a global fit with a common slope, as discussed in the text, to reduce parameter correlation. The large entropic offset for 1 M urea in the temperature-dependence of the folding rate constant **(a)** suggests that most of the change in ΔS° arises from changes in the entropic barrier to folding ($\Delta S^{\ddagger}_{fold}$). The distinct thermodynamic behavior of TMAO- facilitated formation of the TL-TLR interaction is discussed in the text. The data table **(c)** contains values for the transition state theory analysis of the temperature-dependent kinetic data for the DNA duplex. Fitting methods are identical to those used in the van't Hoff analysis (Figure 6.6), which is discussed in Section 6.3.4.

6.3 Discussion

Ensemble thermal denaturation experiments have demonstrated that the *m*-value, which is a measure of the sensitivity of ΔG° to osmolyte concentration, is correlated with the differences in solvent accessible surface area (SASA) between the folded and unfolded structures. Specifically, the *m*-values for TMAO and urea are primarily mediated by changes in phosphate and nucleobase SASA, respectively. Vapor pressure osmometry (VPO) experiments have revealed that TMAO primarily forms *unfavorable* interactions with the phosphate backbone, and to a lesser extent, the nucleobases of a nucleic acid(13). This is different from the *favorable* interaction between urea and the nucleobase of an oligonucleotide(14). Accordingly, TMAO will preferentially *destabilize* conformations with more phosphate SASA, whereas urea will better *stabilize* structures with greater base SASA (Figure 6.1). Unfolded conformations commonly have more phosphate and base SASA than their folded counterparts, which means that TMAO will *stabilize* nucleic acid folding transitions, whereas urea will *destabilize* them (Figure 6.1).

6.3.1 TMAO-Dependent Folding Free Energies

The folding/unfolding rate constants (Figure 6.4) are used to calculate equilibrium constants ($K_{eq} = k_{fold}/k_{unfold}$), which are used to determine the osmolyte-dependence of the free energy change for folding (*m*-value). These results clearly indicate that TMAO is better able to stabilize 3° (e.g., TL-TLR), rather than 2° (e.g., DNA duplex), structural transitions (Figure 6.5). Previous calculations based on structural models of duplex nucleic acids predict *very little* change in phosphate SASA upon formation of a double helix(12), which would render TMAO an ineffective *stabilizing* osmolyte. However, VPO experiments(13) indicate that there are some weak, but still energetically *unfavorable*, interactions between TMAO and nucleobases that would result in a net *stabilization* of the duplex based on the change in nucleobase SASA. Conversely, the *substantial* change in phosphate SASA (≈ 67 Å^2) for the TL-TLR receptor interaction (13) clearly explains why TMAO is more effective at *stabilizing* this structural transition. These results bolster the notion that, when changes in phosphate SASA are *substantial*, TMAO can efficiently *stabilize* conformational transitions. However, when these changes are *miniscule*, TMAO can still *facilitate* folding, although less efficiently, based on differences in nucleobase SASA.

6.3.2 Urea-Dependent Folding Free Energies

Surprisingly, the *m*-values for the TL-TLR and 8 bp DNA duplex interactions are very similar (Figure 6.5), which suggests nearly identical changes in nucleobase SASA for the two folding transitions. Additionally, previous ensemble experiments on similar constructs under comparable conditions yield qualitatively consistent *m*-values for urea-*inhibited* folding. A10 bp RNA duplex at 0.5 M NaCl has an *m*-value = 0.74(4) kcal mol^{-1} molar^{-1}(21) and a bimolecular, dimeric TL-TLR construct has an extrapolated *m*-value ≈ 0.64 kcal mol^{-}molal^{-1} at 85 mM KCl (14). Both of these previously measured values are within the experimental uncertainty of the single-molecule measurements reported in this study. The excellent agreement between *m*-values measured using single-molecule techniques and UV-melting experiments further supports the notion that urea is a strongly *destabilizing* osmolyte for both 2° and 3° folding transitions, which results primarily from *favorable* interactions with the nucleobase SASA of nucleic acids. Despite the similar *m*-values, which are related to the folding *equilibria*, the pronounced structural differences between the TL-TLR and the 8bp DNA duplex make the urea-dependence of the *rate constants* very different.

6.3.3 Kinetic Origins of Osmolyte-Influenced Nucleic Acid Folding

This work details the first, to our knowledge, demonstration of the *kinetic* origins associated with osmolyte-influenced nucleic acid folding. The observed *increase* in stability of folded nucleic acid structures at elevated concentrations of TMAO is the result of an *increase* in k_{fold} (Figure 6.4a) and a *decrease* in k_{unfold} (Figure 6.4b). Alternatively, the *decrease* in stability associated with addition of urea occurs because of a *decrease* in k_{fold} (Figure 6.4c) and an *increase* in k_{unfold} (Figure 6.4d).

The ideology of preferential interactions with base, sugar, and phosphate SASA of nucleic acids can also be applied to osmolyte-dependence of the *rate constants*. Such an analysis provides information about changes in SASA that result from forming the transition state. For example, the observation that k_{fold} for the 8 bp DNA duplex construct is only *slightly increased* by the presence of TMAO (Figure 6.4a, circles) indicates that there is very little reduction in phosphate SASA upon reaching the transition state. Conversely, the k_{fold} for TL-TLR construct *strongly accelerated* by TMAO (Figure 6.4a, triangles), which implies that there is a considerable reduction in phosphate SASA that occurs while crossing the folding free energy barrier.

Similarly, the urea-dependence of the rate constants can be used to make inferences about where along the reaction coordinate the burial of nucleobase SASA occurs for the two different conformational transitions. Because k_{fold} for the TL-TLR interaction is much more sensitive to urea than k_{unfold} (Figures 6.4c, 6.5d) it evident that most of the change in nucleobase SASA occurs prior to formation of the transition state. This is in contrast with previous smFRET studies of urea-induced denaturation of other RNA folding motifs (i.e., the human telomerase RNA pseudoknot(49), the adenine riboswitch(50), and the P4-P6 domain of the *Tetrahymena* ribozyme(42)) where addition of urea predominantly affects the unfolding rate constant. It is interesting to note that the GAAA tetraloop—tetraloop receptor is one of two tertiary interactions in the P4-P6 domain and that the inconsistencies between these two RNA constructs are likely the result of vastly different folding reaction coordinates, specifically regarding changes in nucleobase SASA.

Not only do these results demonstrate the kinetic origins of osmolyte-influenced nucleic acid folding (Figure 6.4), but also that osmolytes, specifically TMAO and urea, can be experimental tools capable of providing low-resolution information about changes in SASA across the entire folding landscape. Accordingly, the large amount of nucleobase and phosphate SASA buried upon formation of the transition state for the TL-TLR interaction is evidence for a transition state where the GAAA tetraloop and the receptor are proximal to one another. Such a structural depiction is certainly consistent with independent single-molecule experiments that propose a compact transition state for the GAAA tetraloop—receptor interaction(40).

6.3.4 Osmolyte-Dependent Entropy Changes for the 8bp DNA Duplex

Temperature-dependent smFRET experiments have been preformed to obtain insights into the *enthalpic* and *entropic* components (i.e., thermodynamics origin) of osmolytes-influenced nucleic acid folding. As indicated by the vertically-offset, parallel data sets in the van't Hoff plots for the 8 bp DNA duplex (Figure 6.6a), neither 1 M TMAO nor 1 M urea significantly alter the folding enthalpy. This observation demonstrates that ΔH° is insensitive to the presence of osmolytes (Table 6.1) and that the predominant source of the osmolyte-dependent ΔG° (*m*-value) results from *entropic* considerations. Previous calorimetric experiments that examined the effect of *destabilizing* osmolytes (e.g., urea) on DNA melting have similarly concluded that *entropic* terms dominate, giving rise to the observed *decrease* in duplex stability (15). Additionally, computational simulations of an RNA hairpin (e.g., 2° structure) in the presence of TMAO suggest that, if the interaction between the two is *unfavorable*, then TMAO will acts as a small molecular crowding agent (26), that *entropically stabilizes* the *folded* conformation(51). With these findings in mind, it is important to note that our single-molecule thermodynamics results further support the established notion that, for 2° structure formation, the osmolyte-induced change in ΔG° results from *entropic* terms (Figure 6.6a). This notion suggest that the free energy change associated with expulsion of TMAO or urea from the buried surfaces of 2° structure conformational transition is dominated by *entropic* rewards, or costs, respectively.

To more quantitatively explore the osmolyte-dependence of the entropy change associated with duplex formation and to reduce parameter correlation between ΔH° and ΔS° (52), the van't Hoff plots are globally fit with common slopes and independent intercepts (Table 6.1). The resulting values of ΔS° are able to explain ≈ 80% of the osmolyte-dependence of ΔG°(295 K), which is entirely consistent with the notion of an *entropic* origin for urea-*inhibited* or TMAO-*facilitated* duplex formation. An Eyring analysis of the temperature-dependent rate constants (Supplemental Figure S6.1) unites the *kinetic* and *thermodynamic* origins of these processes by demonstrating that most of the change in ΔS° is associated with the *entropic* component of the *unfolding* free energy barrier (i.e., $\Delta S^{\ddagger}_{\text{unfold}}$), rather than the folding barrier (i.e., $\Delta S^{\ddagger}_{\text{unfold}}$). Stated more generally, TMAO *stabilizes* nucleic acid 2° structure formation by *decreasing* k_{unfold}, which occurs because of a *decrease* in the *entropic reward* associated with the *unfolding* barrier. Conversely, urea *destabilizes* 2° structure formation by *increasing* k_{unfold}, which results from a *more entropically rewarding unfolding* barrier.

6.3.5 Osmolyte-Dependent Entropy Changes for the TL-TLR

When analyzed in the same fashion as the 8bp DNA duplex data, the temperature-dependent van't Hoff analysis of the TL-TLR data makes it evident that addition of 1 M urea primarily results in an *entropic destabilization* of this 3° interaction (Figure 6.6b). The results from the common-slope analysis reveal that the urea-induced changes to ΔS° account for ≈ 74% of the *m*-value at 295 K (Table 6.1). Furthermore, most of the change in ΔS° is associated with the *folding* barrier (Supplemental Figure S6.2). This observation is entirely internally consistent with the *kinetic* origin of urea-*inhibited* folding of the TL-TLR, which revealed that k_{fold} is more prominently affected than k_{unfold} (Figure 6.4c,d, triangles). Together, the *kinetic* and *thermodynamic* results suggest that urea *destabilizes* the TL-TLR by predominantly *decreasing* k_{fold} via an *increase* in the *entropic cost* associated with the *folding* barrier. That is to say, as the RNA folds, urea is expelled from the buried nucleobase SASA, which is predominately an entropically costly process.

Single-molecule urea-induced denaturation studies of an RNA pseudoknot(49) also demonstrate a largely *entropic destabilization*, that results from a strong *increase* in k_{unfold} rather than a *decrease* in k_{fold}, as observed for the TL-TLR. This observation suggests that individual tertiary interactions likely have kinetics whose dependencies on urea are quantitatively different, but that the *destabilization* by urea is *always entropic* in origin. Because of the canonical base pairing in both the RNA pseudoknot and the 8 bp DNA duplex, it is, perhaps, unsurprising that urea predominately affects k_{unfold} for these two folding transitions (RNA pseudoknot and DNA duplex), as they are very similar with respect to changes in nucleobase SASA.

Although the *kinetic* origin of TMAO-*facilitated* formation of the TL-TLR is qualitatively similar to that of the 8bp DNA duplex (i.e., k_{fold} increase and k_{unfold} decreases), the *thermodynamics* of this process are noticeably different. Specifically, the presence of 1 M TMAO significantly changes the ΔH° for the TL-TLR construct as evidenced by a more positive slop on the van't Hoff plot (Figure 6.6b). As a reminder, this effect is not observed in the 8bp DNA duplex (Figure 6.6a). The fitted results reveal that both ΔH° and ΔS° *decrease* with the addition of 1 M TMAO (Table 6.1), which mandates a thermodynamically distinct mechanism of *stabilization* for the TL-TLR than that of the 8bp DNA duplex. One of the most pronounced differences between the two folding transitions is the amount of phosphate SASA burial. Therefore, it is reasonable to conclude that, for folding transition where there is a substantial change in phosphate SASA (e.g., 3° structure formation), the expulsion of TMAO from these surfaces is both *exothermic* and *entropically costly*. For the TL-TLR interaction, most of the change in phosphate SASA occurs prior to formation of the transition state (Figure 6.4a,b and Supplemental Figure S6.2). Because the TMAO-induced *decrease* in $\Delta H^{\ddagger}_{\text{fold}}$ is greater than the *decrease* in $T\Delta S^{\ddagger}_{\text{fold}}$ (Supplemental Figure S6.2), addition of 1 M TMAO results in a net *increase* in k_{fold} at 295 K. The distinct difference in the *thermodynamic* origins for TMAO-*stabilized* folding of the 8 bp DNA duplex and the TL-TLR construct highlights the two potential modes by which TMAO can interact with nucleic acids: (*i*) *strong unfavorable* interactions between TMAO and the phosphate backbone driven by both *entropy* and *enthalpy* that results in *stabilization* nucleic acid folding transitions with *substantial* changes in phosphate SASA and (*ii*) *weak unfavorable*, predominately *entropic* interactions between TMAO and the nucleobase that *stabilize* nucleic acid folding transitions with *miniscule* changes in phosphate SASA.

Although these single-molecule experiments explicitly demonstrate the kinetic and thermodynamic effects of TMAO and urea on two model constructs, it remains unknown how general these observations are, both with respect to different osmolytes (e.g., glycine betaine, proline, sucrose, etc.) and different nucleic acid structural motifs (e.g., pseudoknots, G-quadruplexes, kissing loops, etc.). Further exploration of the role of osmolytes in nucleic acid folding transitions, guided by single-molecule experiments that focus on the kinetics and thermodynamics origins, will help uncover a more comprehensive understanding of the complexities associated with biomolecules in cosolute-rich cellular environments.

6.4. Conclusions

Single-molecule fluorescence techniques have been used to observe the effect of *stabilizing* (TMAO) and *destabilizing* (urea) osmolytes on the folding/unfolding rate constants for both an 8 bp DNA duplex and the GAAA tetraloop—tetraloop receptor motif. The results demonstrate that, regardless of the type of the nucleic acid conformational transition (i.e., secondary or tertiary), TMAO always *stabilizes* nucleic acid structure formation by *increasing* the folding rate constant and *decreasing* the unfolding rate constant. Conversely, urea always *destabilizes* nucleic acid structure formation by *decreasing* the folding rate constant and *increasing* the unfolding rate constant. The magnitudes of these osmolyte-induced changes to the folding/unfolding rate constants are dependent on the amount and type (e.g., nucleobase) of solvent accessible surface area (SASA) that is buried for each of the conformational transition.

Complementary temperature-dependent single-molecule kinetic studies of the 8bp DNA duplex reveal that osmolyte-induced *stabilization* or *destabilization* results almost entirely from changes to the *entropic* component of the free energy barrier for *unfolding*. For the TL-TLR interaction, these studies demonstrate that urea *destabilizes* the structural equilibrium by *increasing* the *entropic penalty* associated with the *folding* barrier. This is markedly different than the *thermodynamic* origin of TMAO-*facilitated* formation of this structural motif, where an *increase* in *exothermicity* overcomes an *increase* in *entropic cost* associated the *folding* free energy barrier. Together, these two effects results in a pronounced *acceleration* of the *folding* rate constant.

As a whole, the experimental observations from this study represent a thorough characterization of both the kinetic and thermodynamic origins of osmolyte-influenced nucleic acid conformational transitions. Such a detailed characterization demonstrates how osmolytes can be used as biochemical tools to map out changes in SASA during a particular folding transition. Lastly, this work begins to unveil how small neutral organic molecules that are found in cells and biological tissues may potentially influence the structural dynamics of functional nucleic acids. Accordingly, future single-molecule efforts should be direct at studying the effect of other biologically relevant osmolytes like those that function in the renal medulla of the kidney(53) (e.g., glycine betaine, sorbitol, and taurine).

6.5 Experimental Methods

6.5.1 Nucleic Acids

The assembly of the smFRET DNA duplex construct has been described previously(33), and needs only a brief explanation. This construct consists of three custom oligonucleotides (Figure 6.2a,b). Strand 1 (5′-biotin-$(CA)_8$-Cy3-3′) has a biotin moiety for surface immobilization and a donor fluorophore for fluorescence resonance energy transfer (FRET). This is annealed to strand 2 (5′-TTG TTG GGT T$(TG)_8$-3′) to form a 16 bp dsDNA scaffold with a 10 nt 5′ overhang. Strand 3 (5′-CCCAACCAA-Cy5-3′) contains a 3′ acceptor dye, which, when present in solution, can hybridize with the 5′overhang region (Figure 6.2b). Throughout such a hybridization event, the Cy5 fluorophore of strand 3 remains in close proximity to the Cy3 fluorophore, allowing for efficient transfer of energy ($E_{FRET} \approx 0.7$) from the donor to the accepter. After dissociation of strand 3 from the overhang region, diffusion rapidly increases the distance between the donor and acceptor fluorophores (Figure 6.2a), which results in essentially zero energy transfer efficiency ($E_{FRET} \approx 0$). This gives rise to two possible FRET states for the 8bp DNA duplex construct—associated (Figure 6.2b, high E_{FRET}) and dissociated (Figure 6.2a, low E_{FRET}).

The GAAA tetraloop—tetraloop receptor (TL-TLR) model system is a modified version (51) of a previously described construct(39), where a synthetic polyethylene glycol (PEG) linker is used to localize the GAAA tetraloop near its cognate receptor. This construct is built from three custom oligonucleotides (Figure 6.2c,d). The Cy3 labeled RNA that contains the GAAA tetraloop (bold sequence) (5′-Cy3-GGC **GAA A**GC C-PEG$_6$-CGU GUC GUC CUA AGU CGG C-3′) is annealed to a Cy5 labeled RNA (5′-Cy5-GCC GAU AUG GAC GAC ACG CCC CUC AGA CGA GUG CG-3′) to form the 11 nt receptor domain (underlined sequence). This results in a 14 nt 3′ overhang that can hybridize to a complementary DNA containing a 5′ biotin (5′-Biotin-CGC ACT CGT CTG AG-3′) for surface immobilization. Once completely annealed, this three-piece construct serves as a FRET labeled, biotinylated TL-TLR construct. Formation of this interaction reduces the distance between the donor and acceptor fluorophores, which increases the efficiency of energy transfer from $E_{FRET} \approx 0.3$ to $E_{FRET} \approx 0.7$. This results in two distinct conformations for the TL-TLR construct—docked (Figure 6.2d, high E_{FRET}) and undocked (Figure 6.2c, low E_{FRET}).

6.5.2 Solution and Sample Preparation

Surface immobilization is accomplished via biotin-streptavidin chemistry. To attach the nucleic acids to a glass coverslip, the sample holder (10 μL) is consecutively flushed with 200 μL of the following three solutions: (*i*) 10 mg/mL bovine serum albumin (BSA) containing 10% biotinylated-BSA, (*ii*) 200 μg/mL streptavidin, and (*iii*) 100 pM biotinylated fluorescently labeled nucleic acid. This procedure provides reproducible immobilization with surface densities of approximately 1 molecule per μm^2. Prior to imaging with the fluorescence microscope, the sample holder is flushed with 200 μL of an imaging buffer (50 mM hemisodium HEPES, 5.0 mM PCA, 10 mM KOH, 100 nM PCD, 2.0 mM Trolox, 0.1 mM EDTA at pH 7.5) containing the desired concentrations of osmolytes (0-2 M) and KCl (either 50 mM or 100 mM). The enzymatic oxygen scavenging system of PCD and PCA (54) is used to enhanced the photostability of the cyanine dyes. For experiments involving the 8 bp DNA duplex, the imaging buffer also contains

200 nM freely diffusing Cy5 oligonucleotide, which permits observation of the bimolecular process.

6.5.3 smFRET Microscope

All smFRET experiments are performed on an inverted confocal fluorescence microscope with a N.A. = 1.2 water objective (Figure 6.7).

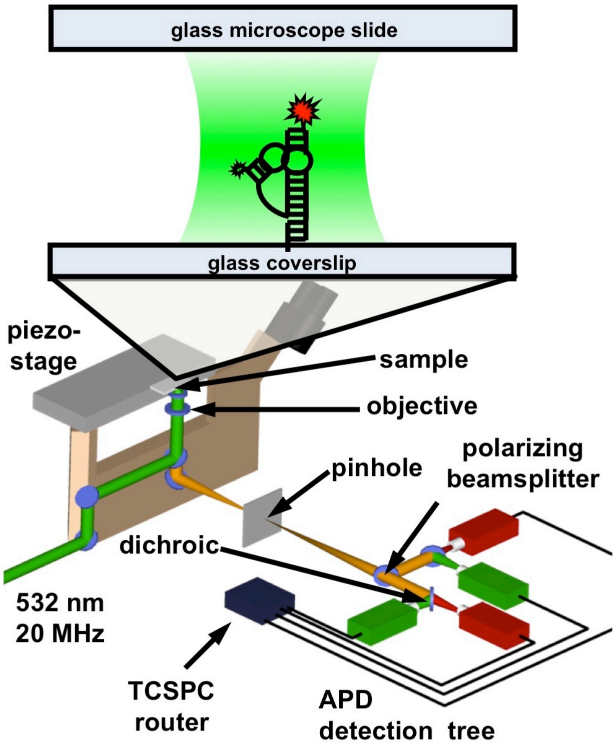

Figure 6.7 Schematic representation of the inverted confocal fluorescence microscope used to acquire smFRET trajectories. Individual molecules are immobilized to the glass coverslip using standard biotin-streptavidin chemistry. Excitation and emission is achieved using standard epifluorescence techniques. Fluorescent photons are focused through a confocal pinhole before being separated by color and polarization and directed onto 4 single photon avalanche photodiodes. Upon detection, the arrival times of individual photons are recorded and sent to a time-correlated single-photon counting (TCSPC) router where they are used to generate trajectories of donor and acceptor fluorescence.

A 20 MHz repetition rate, 532 nm laser beam overfills the limiting aperture of the optical system resulting in a diffraction-limited laser spot at the focus of the objective, which is used to directly excite the donor fluorophores of surface immobilized RNA constructs. Fluorescent photons are collected using a standard epifluorescence configuration before being separated by color (i.e., donor and acceptor) and polarization and directed onto four single photon avalanche photo diodes (APDs). A Time-Correlated Single-Photon Counting (TCSPC) module records the arrival of each detected photon. This information is used to construct time-traces of the donor (I_D) and acceptor (I_A) fluorescence intensity (Figure 6.3), which can readily be converted to FRET trajectories using Eq. 6.1, where α is a term that corrects for various components of collection efficiency (e.g., direct excitation, crosstalk see ref (35) for further information).

$$E_{FRET} = \left(1 - \frac{\alpha_A Q_A I_D}{\alpha_D Q_D I_A}\right) \Big/ \left(1 + \frac{Q_A I_D}{Q_D I_A}\right) \qquad \text{(Eq. 6.1)}$$

Dwell times are determined from the FRET trajectories using a previously described thresholding routine(34). Rate constants are extracted from cumulative distribution plots of dwell times(41-43) by performing a linear least-squares fit to a single-exponential decay. Temperature control of the sample is accomplished using commercially available stage and objective heaters, as described previously(38).

6.6 References

1. Draper, D. E. A guide to ions and RNA structure, *RNA*, **2004,** *10*, 335-343.

2. Klein, D. J.; P. B. Moore; T. A. Steitz. The contribution of metal ions to the structural stability of the large ribosomal subunit, *RNA*, **2004,** *10*, 1366-1379.

3. Kurz, M. Compatible solute influence on nucleic acids: many questions but few answers, *Saline Systems*, **2008,** *4*, 6.

4. Yancey, P. H.; M. E. Clark; S. C. Hand; R. D. Bowlus; G. N. Somero. Living with water stress: evolution of osmolyte systems, *Science*, **1982,** *217*, 1214-1222.

5. Record, M. T., Jr.; E. S. Courtenay; D. S. Cayley; H. J. Guttman. Responses of E. coli to osmotic stress: large changes in amounts of cytoplasmic solutes and water, *Trends Biochem. Sci.*, **1998,** *23*, 143-148.

6. Yancey, P. H.; G. N. Somero. Counteraction of urea destabilization of protein structure by methylamine osmoregulatory compounds of elasmobranch fishes, *Biochem. J.*, **1979,** *183*, 317-323.

7. Record, M. T., Jr.; E. S. Courtenay; S. Cayley; H. J. Guttman. Biophysical compensation mechanisms buffering E. coli protein-nucleic acid interactions against changing environments, *Trends Biochem. Sci.*, **1998,** *23*, 190-194.

8. Liu, Y.; D. W. Bolen. The peptide backbone plays a dominant role in protein stabilization by naturally occurring osmolytes, *Biochemistry*, **1995,** *34*, 12884-12891.

9. Timasheff, S. N. Control of protein stability and reactions by weakly interacting cosolvents: the simplicity of the complicated, *Adv. Protein Chem.*, **1998,** *51*, 355-432.

10. Courtenay, E. S.; M. W. Capp; R. M. Saecker; M. T. Record, Jr. Thermodynamic analysis of interactions between denaturants and protein surface exposed on unfolding: interpretation of urea and guanidinium chloride m-values and their correlation with changes in accessible surface area (ASA) using preferential interaction coefficients and the local-bulk domain model, *Proteins*, **2000,** *4*, 72-85.

11. Courtenay, E. S.; M. W. Capp; C. F. Anderson; M. T. Record, Jr. Vapor pressure osmometry studies of osmolyte-protein interactions: implications for the action of osmoprotectants in vivo and for the interpretation of "osmotic stress" experiments in vitro, *Biochemistry*, **2000,** *39*, 4455-4471.

12. Lambert, D.; D. E. Draper. Effects of Osmolytes on RNA Secondary and Tertiary Structure Stabilities and RNA-Mg^{2+} Interactions, *J. Mol. Biol.*, **2007,** *370*, 993-1005.

13. Lambert, D.; D. Leipply; D. E. Draper. The osmolyte TMAO stabilizes native RNA tertiary structures in the absence of Mg^{2+}: Evidence for a large barrier to folding from phosphate dehydration, *J. Mol. Biol.*, **2010,** *404*, 138-157.

14. Lambert, D.; D. E. Draper. Denaturation of RNA secondary and tertiary structure by urea: simple unfolded state models and free energy parameters account for measured m-values, *Biochemistry*, **2012,** *51*, 9014-9026.

15. Spink, C. H.; N. Garbett; J. B. Chaires. Enthalpies of DNA melting in the presence of osmolytes, *Biophys. Chem.*, **2007,** *126*, 176-185.

16. Hong, J.; M. W. Capp; C. F. Anderson; R. M. Saecker; D. J. Felitsky; M. W. Anderson; M. T. Record, Jr. Preferential interactions of glycine betaine and of urea with DNA: implications for DNA hydration and for effects of these solutes on DNA stability, *Biochemistry*, **2004,** *43*, 14744-14758.

17. Felitsky, D. J.; J. G. Cannon; M. W. Capp; J. Hong; A. W. Van Wynsberghe; C. F. Anderson; M. T. Record, Jr. The exclusion of glycine betaine from anionic biopolymer surface: why glycine betaine is an effective osmoprotectant but also a compatible solute, *Biochemistry*, **2004,** *43*, 14732-14743.

18. Bennion, B. J.; V. Daggett. The molecular basis for the chemical denaturation of proteins by urea, *Proc. Natl. Acad. Sc.i USA*, **2003,** *100*, 5142-5147.

19. Greene, R. F., Jr.; C. N. Pace. Urea and guanidine hydrochloride denaturation of ribonuclease, lysozyme, alpha-chymotrypsin, and beta-lactoglobulin, *J. Biol. Chem.*, **1974,** *249*, 5388-5393.

20. Tanford, C. Isothermal Unfolding of Globular Proteins in Aqueous Urea Solutions, *J. Am. Chem. Soc.*, **1964,** *86*, 2050-&.

21. Shelton, V. M.; T. R. Sosnick; T. Pan. Applicability of Urea in the Thermodynamic Analysis of Secondary and Tertiary RNA Folding, *Biochemistry*, **1999,** *38*, 16831-16839.

22. Canchi, D. R.; A. E. Garcia. Cosolvent Effects on Protein Stability, *Annu. Rev. Phys. Chem.*, **2013**.

23. Schwinefus, J. J.; M. J. Kuprian; J. W. Lamppa; W. E. Merker; K. N. Dorn; G. W. Muth. Human telomerase RNA pseudoknot and hairpin thermal stability with glycine betaine and urea: Preferential interactions with RNA secondary and tertiary structures, *Biochemistry*, **2007,** *46*, 9068-9079.

24. Cho, S. S.; G. Reddy; J. E. Straub; D. Thirumalai. Entropic Stabilization of Proteins by TMAO, *J. Phys. Chem. B*, **2011,** *115*, 13401-13407.

25. Wang, A. J.; D. W. Bolen. A naturally occurring protective system in urea-rich cells: Mechanism of osmolyte protection of proteins against urea denaturation, *Biochemistry*, **1997,** *36*, 9101-9108.

26. Pincus, D. L.; C. Hyeon; D. Thirumalai. Effects of trimethylamine N-oxide (TMAO) and crowding agents on the stability of RNA hairpins, *J. Am. Chem. Soc.*, **2008,** *130*, 7364-7372.

27. Priyakumar, U. D.; C. Hyeon; D. Thirumalai; A. D. MacKerell. Urea Destabilizes RNA by Forming Stacking Interactions and Multiple Hydrogen Bonds with Nucleic Acid Bases, *J. Am. Chem. Soc.*, **2009,** *131*, 17759-17761.

28. Tinoco, I.; R. L. Gonzalez. Biological mechanisms, one molecule at a time, *Gene Dev.*, **2011,** *25*, 1205-1231.

29. Roy, R.; S. Hohng; T. Ha. A practical guide to single-molecule FRET, *Nat. Methods*, **2008,** *5*, 507-516.

30. Li, P. T.; J. Vieregg; I. Tinoco, Jr. How RNA Unfolds and Refolds, *Annu. Rev. Biochem.*, **2008,** *77*, 77-100.

31. Bokinsky, G.; X. Zhuang. Single-Molecule RNA Folding, *Acc. Chem. Res.*, **2005,** *38*, 566-573.

32. Aleman, E. A.; R. Lamichhane; D. Rueda. Exploring RNA folding one molecule at a time, *Curr. Opin. Chem. Biol.* **2008,** *12*, 647-654.

33. Dupuis, N. F.; E. D. Holmstrom; D. J. Nesbitt. Single-Molecule Kinetics Reveal Cation-Promoted DNA Duplex Formation Through Ordering of Single-Stranded Helices, *Biophys. J.*, **2013,** *105*, 756-766.

34. Downey, C. D.; J. L. Fiore; C. D. Stoddard; J. H. Hodak; D. J. Nesbitt; A. Pardi. Metal ion dependence, thermodynamics, and kinetics for intramolecular docking of a GAAA tetraloop and receptor connected by a flexible linker, *Biochemistry*, **2006,** *45*, 3664–3673.

35. Fiore, J. L.; J. H. Hodak; O. Piestert; C. D. Downey; D. J. Nesbitt. Monovalent and Divalent Promoted GAAA-Tetraloop–Receptor Tertiary Interactions from Freely Diffusing Single-Molecule Studies, *Biophys. J.*, **2008,** *95*, 3892-3905.

36. Fiore, J. L.; E. D. Holmstrom; L. R. Feigland; J. H. Hodak; D. J. Nesbitt. The Role of Counterion Valence and Size in the GAAA Tetraloop-Receptor Docking/Undocking Kinetics, **2012**, *J. Mol. Biol.,* **2012,** 423, 198-216.

37. Fiore, J. L.; E. D. Holmstrom; D. J. Nesbitt. Entropic origin of Mg2+-facilitated RNA folding, *Proc. Natl. Acad. Sci. USA*, **2012,** *109*, 2902-2907.

38. Fiore, J. L.; B. Kraemer; F. Koberling; R. Erdmann; D. J. Nesbitt. Enthalpy-Driven RNA Folding: Single-Molecule Thermodynamics of Tetraloop–Receptor Tertiary Interaction, *Biochemistry*, **2009,** *48*, 2550–2558.

39. Hodak, J. H.; C. D. Downey; J. L. Fiore; A. Pardi; D. J. Nesbitt. Docking kinetics and equilibrium of a GAAA tetraloop-receptor motif probed by single-molecule FRET, *Proc. Natl. Acad. Sci. USA*, **2005,** *102*, 10505–10510.

40. Holmstrom, E. D.; J. L. Fiore; D. J. Nesbitt. Thermodynamic Origins of Monovalent Facilitated RNA Folding, *Biochemistry*, **2012,** *51*, 3732-3743.

41. Blanco, M.; N. G. Walter. Analysis of complex single-molecule FRET time trajectories, *Methods Enzymol.*, **2010,** *472*, 153-178.

42. Bartley, L. E.; X. W. Zhuang; R. Das; S. Chu; D. Herschlag. Exploration of the Transition State for Tertiary Structure Formation Between an RNA Helix and a Large Structured RNA, *J. Mol. Biol.*, **2003,** *328*, 1011–1026.

43. Zhou, Y. J.; X. W. Zhuang. Robust reconstruction of the rate constant distribution using the phase function method, *Biophys. J.*, **2006,** *91*, 4045-4053.

44. Sclavi, B.; S. Woodson; M. Sullivan; M. R. Chance; M. Brenowitz. Time-resolved synchrotron X-ray "footprinting", a new approach to the study of nucleic acid structure and function: application to protein-DNA interactions and RNA folding, *J. Mol. Biol.*, **1997,** *266*, 144-159.

45. Pan, J.; D. Thirumalai; S. A. Woodson. Folding of RNA involves parallel pathways, *J. Mol. Biol.*, **1997,** *273*, 7-13.

46. Pace, C. N. The stability of globular proteins, *CRC Crit. Rev. Biochem.*, **1975,** *3*, 1-43.

47. Myers, J. K.; C. N. Pace; J. M. Scholtz. Denaturant m values and heat capacity changes: relation to changes in accessible surface areas of protein unfolding, *Protein Sci.*, **1995,** *4*, 2138-2148.

48. Fiore, J. L.; E. D. Holmstrom; D. J. Nesbitt. Entropic Origin of Mg^{2+}-Facilitated RNA Folding, *Proc. Natl. Acad. Sci. USA*, **2012,** *109*, 2902-2907.

49. Holmstrom, E. D.; D. J. Nesbitt. Single-molecule fluorescence resonance energy transfer studies of the human telomerase RNA pseudoknot: temperature-/urea-dependent folding kinetics and thermodynamics, *J. Phys. Chem. B*, **2014,** *118*, 3853-3863.

50. Dalgarno, P. A.; J. Bordello; R. Morris; P. St-Pierre; A. Dube; I. D. Samuel; D. A. Lafontaine; J. C. Penedo. Single-molecule chemical denaturation of riboswitches, *Nucleic Acids Res.*, **2013,** *41*, 4253-4265.

51. Dupuis, N. F.; E. D. Holmstrom; D. J. Nesbitt. Molecular-crowding effects on single-molecule RNA folding/unfolding thermodynamics and kinetics, *Proc. Natl. Acad. Sci. USA,* **2013**. (in Press)

52. Cornish-Bowden, A. Enthalpy-entropy compensation: a phantom phenomenon, *J. Biosci.*, **2002,** *27*, 121-126.

53. Burg, M. B. Coordinate regulation of organic osmolytes in renal cells, *Kidney Int.*, **1996,** *49*, 1684-1685.

54. Aitken, C. E.; R. A. Marshall; J. D. Puglisi. An Oxygen Scavenging System for Improvement of Dye Stability in Single-Molecule Fluorescence Experiments, *Biophys. J.*, **2008,** *94*, 1826-1835.

Chapter 7

Single Molecule FRET Studies of the Human Telomerase RNA Pseudoknot: Temperature/Urea Dependent Folding Kinetics and Thermodynamics[*]

7.1 Introduction

Conventional DNA replication presents a serious problem for the ends of linear chromosomes. Each successive replication event results in the loss of genetic material at the ends of these long DNA duplexes, which has come to be known as the end replication problem (1). One of nature's solution to this problem is a ribonucleoprotein (RNP) complex, telomerase, that functions to maintain the long-term fidelity of eukaryotic chromosomes(2,3). This task is accomplished by processively adding multiple replicates of a species-specific DNA sequence to the ends of the chromosomes, which results in the formation of telomeres(4). Not only does repetitive elongation of telomeres buffer the natural shortening of chromosomes that occurs during DNA replication, but the presence of the telomeres allows for recruitment of a number of specific DNA binding proteins that are capable of protecting the chromosome ends from other potentially damaging cellular processes.

Proper telomere maintenance is essential for highly proliferative cells (e.g. stem cells) and is partially responsible for cellar immortality. Unfortunately, the marvels of telomerase are also beneficial for the highly proliferative constituents of cancerous tumors, with up-regulation of telomerase activity observed in > 85% of oncogenic cells(5). Indeed, the ability to repress telomerase activity offers a broadly applicable target for cancer therapeutics, while the ability to

---

[*] Adapted from: Holmstrom, Erik D; Nesbitt, David J. *J. Phys. Chem. B.* ***2014****, 118, 3853-3863*

enhance telomerase activity has applications in stem cell-based regenerative medicine. In order for medicinal applications to target telomerase activity more precisely, a deeper understanding of the complete RNP is essential. Until recently, mechanistic information about telomerase holoenzyme activity has proven quite challenging to obtain, though single-molecule studies of model systems have recently started to elucidate some key structural and mechanistic aspects of telomerase function (6-10). Specifically, these efforts have started to unveil details associated with the functional importance of the pseudoknot domain and the global conformation of the RNA in catalytically active enzymes; however, much of the detailed biophysics of telomerase activity still remains poorly understood.

What is known about telomerase is that the RNP consists primarily of two crucial structural components, though additional species-specific components have been shown to be required in various systems (11). The first is a protein subunit, telomerase reverse transcriptase (TERT), which is responsible for catalyzing the addition of telomeric repeats to the ends of eukaryotic chromosomes(12). The second component is telomerase RNA (TR), which, among other things, provides the template for this RNA-dependent DNA synthesis (12). One of the few highly conserved domains within TR is the core domain, which is essential for both RNP assembly and activity (13-19). It has been shown that within this domain there is a functionally critical region that forms a pseudoknot motif. In general, a pseudoknot is formed when the nucleotides in the loop of an RNA hairpin make stable, typically canonical, base pairing interactions with the free nucleotides of a single stranded region elsewhere in the RNA. The pseudoknot base pairing interactions (P3) found in human TR (hTR) are formed, in part, between the nucleotides in the loop of the P2 hairpin and the single stranded nucleotides of J2a/3 (Figure 7.1a). A number of NMR experiments have determined the molecular structure of a minimal wild-type (WT) hTR pseudoknot (Figure 7.1b) and various mutants(20-24). These structural experiments, together with recent single-molecule experiments(25,26) and computational folding models (27,28), indicate that the WT pseudoknot exists in equilibrium between a partially unfolded hairpin and a folded pseudoknot (PK) with a stable and conserved triple helix (Figure 7.1c).

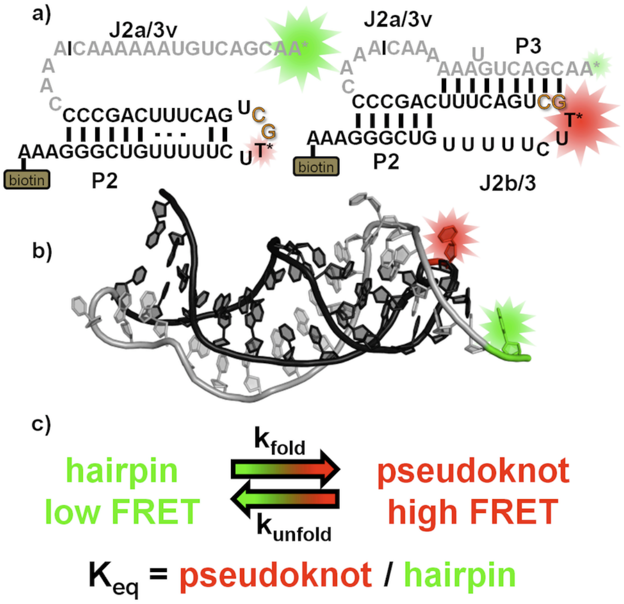

Figure 7.1 Details of the human telomerase RNA pseudoknot **a)** Secondary structure diagrams of the minimal pseudoknot motif in a partially unfolded (hairpin) conformation and a folded (pseudoknot) conformation. The GC→AG mutation at the orange nucleotides in the psuedoknot region corresponds to the genetic disorder dyskeratosis congenita. Green (Cy3) and red (Cy5) stars indicate the location of two fluorophores, where size of the stars reflect FRET efficiency between the two dyes and the black vertical bar represents the ligation site. **b)** Model solution structure of the minimal pseudoknot motif, with the same color scheme as the secondary structure diagram. **c)** Schematic equilibrium between the pseudoknot and hairpin conformations.

Such detailed investigations of the pseudoknot region of hTR have been used in conjunction with existing mutational studies to develop several models for the functional importance of this structural motif. To date, however, substantial accumulation of evidence in support of (or against) any of these model predictions has remained elusive, which therefore represents substantial motivation for the present work.

In this study, single-molecule fluorescence resonance energy transfer (smFRET) techniques(29,30) are used to further characterize the kinetics and thermodynamics of two minimal hTR PK constructs: (*i*) the wild-type (WT hTR PK) and (*ii*) a mutant thereof that is associated with the genetic disorder dyskeratosis congenita (DKC hTR PK). These smFRET experiments provide a remarkably quantitative methodology for observing molecular dynamics of biomolecules. Single-molecule techniques are extremely advantageous for kinetic studies of RNA folding in that they are able to resolve conformational dynamics unobservable in more traditional ensemble measurements. The ability to measure the kinetics of RNA folding at equilibrium and in real-time significantly increases the amount of information attainable from the experimental system(31-33). Furthermore, the temperature-dependence of these smFRET studies can be exploited to extract the enthalpic and entropic components associated with free energies(34-37). Lastly, experiments that utilize urea as a chemical denaturant provide important quantitative information about the free energy stability of the pseudoknot motif (36,38). The results of this study and the associated implications are discussed with regard to: (*i*) the folding pathway of the minimal RNA pseudoknot motif, (*ii*) the use of urea as a general tool for probing the single molecule kinetics and thermodynamics of RNA folding, and (*iii*) the molecular function and various disease states of telomerase.

7.2 Results

7.2.1 Freely Diffusing Burst Measurements

In the standard fluorescence-imaging buffer (see materials and methods), the wild-type (WT) human telomerase RNA pseudoknot (hTR PK) appears to exist in a single high FRET conformation (E_{FRET} = 0.95(1), FWHM = 0.11(1))(Figure 7.2a, black). This E_{FRET} corresponds to a length of R ≈ 32(1) Å which, when one considers the flexible carbon linkers (≈ 5 Å) connecting each of the two fluorescent dyes to the RNA, is consistent with the modeled distance (≈ 22 Å, ref (20)) between the two nucleotides nearest to the fluorophores. Therefore, the observed high FRET state is the result of a stably folded pseudoknot.

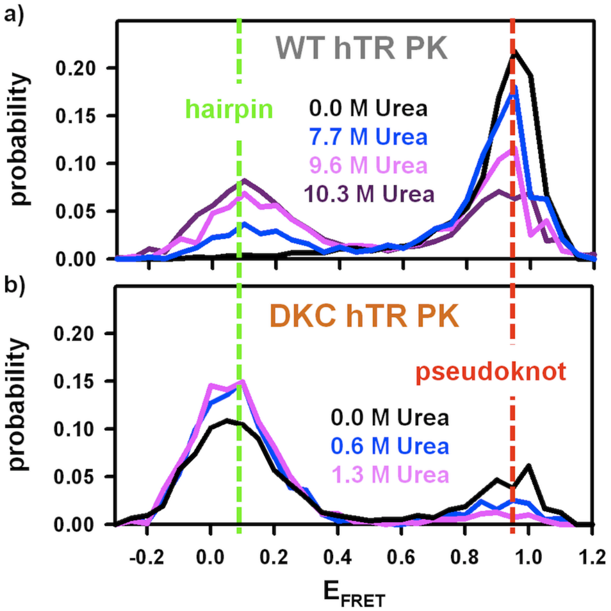

Figure 7.2 Freely diffusing FRET histograms of **a)** the wild-type human telomerase RNA pseudoknot and **b)** the dyskeratosis congenita mutant of the human telomerase RNA pseudoknot. The urea titrations demonstrate strong shifts in the pseudoknot-hairpin equilibrium behavior for both constructs.

This is in stark contrast to the equilibrium distributions of FRET states associated with the DKC hTR PK (Figure 7.2b, black). Under the same experimental conditions, the dyskeratosis congenita (DKC) hTR PK adopts two conformations: (*i*) a high FRET conformation (E_{FRET} = 0.94(2), FWHM = 0.14(2)), indistinguishable from the pseudoknot structure for WT hTR PK and (*ii*) a low FRET conformation (E_{FRET} = 0.07(1), FWHM = 0.19(1)), indicative of a substantial increase in donor-acceptor distance. From the $1/R^6$ dependence of FRET efficiency on distance, this low FRET value corresponds to ≈ 80(2) Å of separation between the two dyes and is indeed consistent with the hairpin conformation.

To better assess the stability of the WT hTR PK and to explore other partially folded or unfolded conformations, freely diffusing experiments have been performed as a function of urea concentration (Figure 7.2a). Upon addition of 7.7 M urea, a second conformation with low FRET (E_{FRET} = 0.11(1), FWHM = 0.20(1)) begins to appear, which is essentially indistinguishable from the low FRET conformation of the DKC hTR PK under non-denaturing conditions (Figure 7.2a, blue and Figure 7.2b, black). This suggests that the low FRET state for WT hTR PK in the presence of high urea concentrations is almost identical to the extended hairpin structure that the DKC hTR PK occupies under non-denaturing conditions. For the WT hTR PK, the relative population of molecules in the hairpin conformation continues to increases with increasing denaturant concentration up to the solubility limit of urea (≈ 10.3 M). This same trend is apparent for the DKC hTR PK, however it occurs over a much more dilute range of urea concentrations (Figure 7.2b). Both smFRET constructs are able to reversibly and completely redistribute between the low and high FRET states depending upon urea and monovalent cation concentration. Such behavior is consistent with a simple, two-state, unimolecular equilibrium between the pseudoknot and hairpin conformations.

An alternatively labeled RNA construct (WT^{alt} hTR PK) has been designed to further validate that the WT hTR PK exists in a hairpin-pseudoknot equilibrium under all urea concentrations (Supplemental Figure S7.1a). For this construct, the fluorophore labeling specifically probes disruption and formation of the P2 region of the pseudoknot, rather than the P3 region sampled with the conventional labeling scheme. The WT^{alt} hTR PK exists solely in a high FRET conformation at both 0 M urea (E_{FRET} = 0.95(1), FWHM = 0.09(1)) and 10.3 M urea (E_{FRET} = 0.95(1), FWHM = 0.13(1)), which confirms that the observed dynamics in the conventional construct are indeed the result of disruption and formation of the P3 region of the WT hTR PK (Supplemental Figure S7.1b).

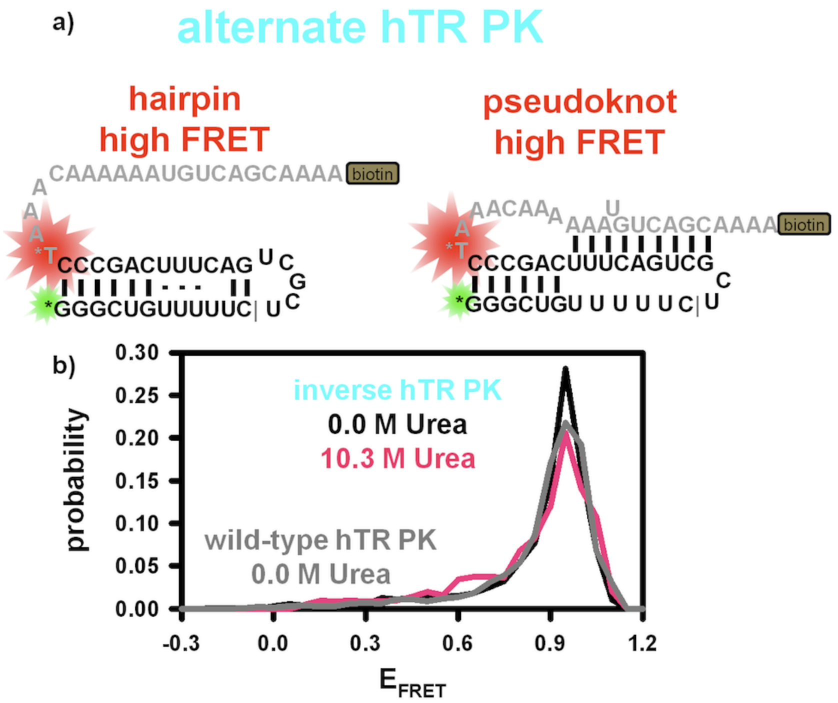

Supplemental Figure S7.1 a) Details of the alternative labeling scheme for the wild-type human telomerase RNA pseudoknot secondary structure. The minimal pseudoknot motif is in a partially unfolded (hairpin) conformation and a folded (pseudoknot) conformation. The green (Cy3) and red (Cy5) stars indicate the location of the two fluorophores, while the size of the stars represents the FRET efficiency between the two dyes. The grey vertical bar represents the location of the ligation site (see Section 7.5.1 for details) **b)** Freely diffusing FRET histograms of alternate wild-type human telomerase RNA pseudoknot. The nearly identical FRET values at high and low urea concentrations confirm that: (*i*) the P2 region of the pseudoknot remains intact under all experimental conditions and (*ii*) the dynamics associated with the conventional constructs results from formation/disruption of the P3 region of the pseudoknot.

Given that a unimolecular equilibrium can be used to accurately describe the hairpin-pseudoknot transition of both the WT and DKC hTR PK constructs used in this study, the ratio of the relative population of the pseudoknot and hairpin conformations yields the equilibrium constant (K_{eq} = [pseudoknot]/[hairpin]) for the two species (Figure 7.1c). The equilibrium constant can easily be converted to the standard state Gibb's free energy change associated with transitioning between the two conformations (i.e., $\Delta G° = -RT\ln[K_{eq}]$). As previously observed in other RNA systems(36,38,39), the free energy change depends linearly on the urea concentration (Figure 7.3). Although the slopes (*m*-values) for the two constructs are not identical (see Discussion), the pronounced linearity of both plots at high and low urea concentrations makes it reasonable to assume linear behavior across all urea concentrations. As a result, a simple linear extrapolation to 0 M urea should yield the ΔG°(295 K) values associated with hairpin-to-pseudoknot transitions under non-denaturing conditions (ΔG°_{DKC} = 0.26(4) kcal/mol, ΔG°_{WT} = –4.2(2) kcal/mol).

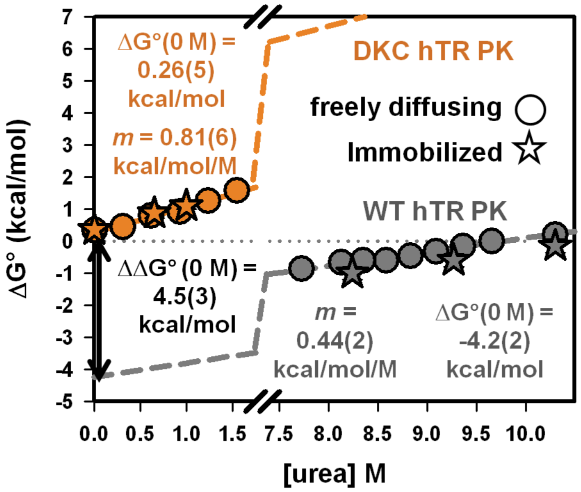

Figure 7.3 Urea dependence of the free energy change for forming the pseudoknot from the hairpin conformation for the wild-type human telomerase RNA pseudoknot (grey) and the dyskeratosis congenita mutant (orange) of the human telomerase RNA pseudoknot. Linear extrapolation to 0 M urea yields the 4.5(3) kcal/mol differential folding free energy between the WT and mutant pseudoknot under non-denaturing conditions.

7.2.2 Surface Immobilized Images

ALEX-filtered, raster-scanned surface images of immobilized molecules qualitatively recapitulate the results of the freely diffusing experiments (Figure 7.4). Under non-denaturing conditions, the WT hTR PK molecules exist entirely in the high FRET (pseudoknot) conformation (Figure 7.4a), while the DKC hTR PK molecules are distributed between the two conformations, with the low FRET (hairpin) state being slightly more populated (Figure 7.4c).

Upon closer inspection, however, the surface immobilized images provide partial information on the *lifetime* associated with the pseudoknot and hairpin conformations. Specifically, the uniformity of color for each diffraction-limited spot (Figure 7.4a,c,d) suggests that dwell times for the pseudoknot and hairpin conformations are, on average, longer than the ≈ 10 s time scale sampled in rastering across each of the ≈ 10 horizontal rows of pixels that comprise a single fluorescent spot.

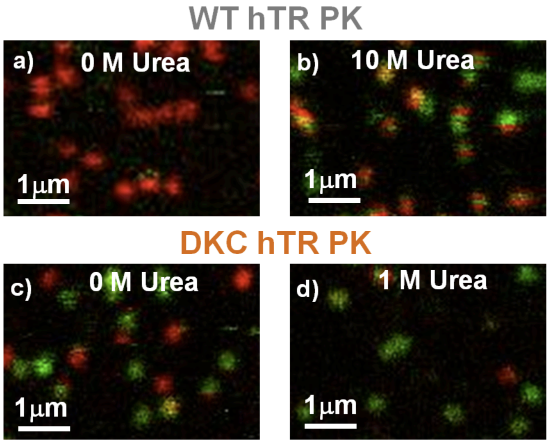

Figure 7.4 Images of surface immobilized molecules for the wild-type **a,b)** and dyskeratosis congenita **c,d)** pseudoknots. Each diffraction limited fluorescence spot represents the location of an individual dually labeled RNA molecule. The urea dependence of the images yields kinetic information about the two different pseudoknot constructs (see Section 7.2.2 for details).

This contrasts subtly but quite significantly with images for WT hTR PK at 10.3 M urea (Figure 7.4b), where individual fluorescent spots exhibit both red and green contributions, but only with complete rows of either fully red or green pixels. Such color continuity in the horizontal but not necessarily vertical dimension suggests that switching must take place on a time-scale that is *i*) clearly faster than 10 second overall scan time, but apparently also *ii*) slower than the ≈ 10 ms it takes to scan across ≈ 10 horizontal pixels within a single row for a given fluorescence spot.

7.2.3 Surface Immobilized Time Trajectories

To obtain more quantitative kinetic information about the rate constants for transitioning between the pseudoknot and hairpin conformations, donor-acceptor fluorescence time trajectories are acquired for individual surface immobilized molecules (Figure 7.5a,c).

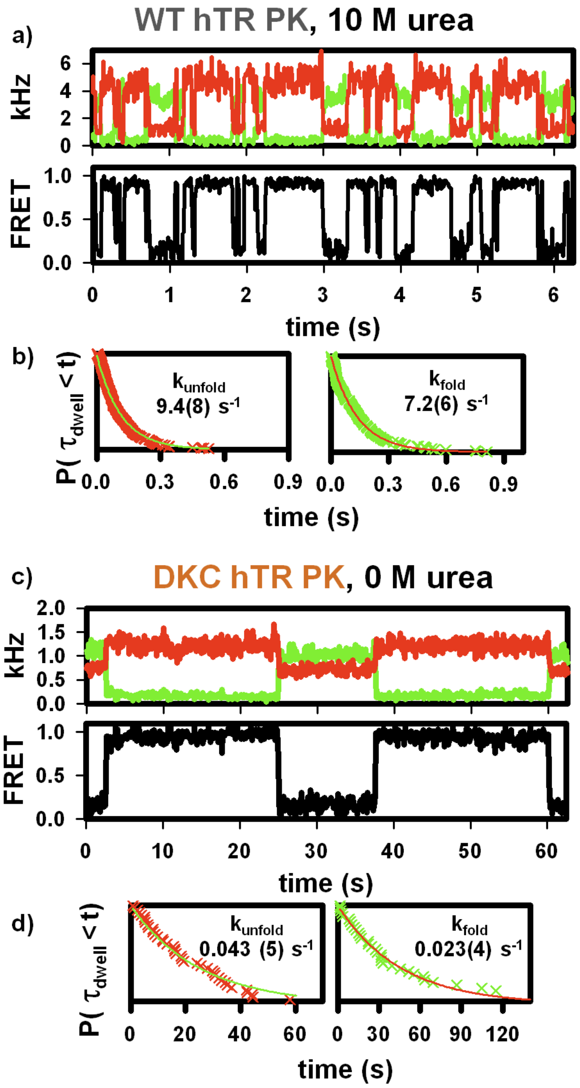

Figure 7.5 Surface immobilized folding and unfolding kinetics for the **a)** wild-type pseudoknot and **c)** the mutant human telomerase RNA pseudoknots under denaturing and non-denaturing conditions, respectively. Rate constants are determined from exponential fits to cumulative distribution plots of dwell times for the **b)** wild-type and **d)** dyskeratosis congenita pseudoknots.

The fluorescence trajectories can easily be converted to FRET trajectories that cleanly demonstrate the two-state behavior for both RNAs, with FRET values consistent with the freely diffusing experiments above. For such a two-state equilibrium system, the dwell times associated the pseudoknot and hairpin states should be distributed exponentially, with characteristic time constants corresponding to rate constants for unfolding (k_{unfold}, pseudoknot → hairpin) or folding (k_{fold}, pseudoknot ← hairpin) (Figure 7.1c). This expectation is nicely confirmed for both WT (Figure 7.5b) and DKC (Figure 7.5d) RNAs under denaturing and non-denaturing conditions, respectively. Clearly, both pseudoknot and hairpin dwell times are distributed exponentially with well-defined single exponential rate constants.

The FRET time trajectories for the WT hTR PK under *non-denaturing* conditions are overwhelmingly dominated by the high FRET state. Given the finite observation window of fluorescent molecules prior to photobleaching (≈ 100 sec), only a few conformational transitions have been observed under non-denaturing conditions. This prevents quantitative determination of dwell times and therefore rate constants associated with the WT construct under non-denaturing conditions. However, the fact that very few time trajectories exhibit even a single unfolding event during a 100 s photobleaching lifetime suggests an upper-limit for the unfolding rate constant of $\approx 0.01\ \mathrm{s}^{-1}$.

To achieve a better understanding of the WT hTR PK folding kinetics, surface immobilized time trajectories have been acquired under *denaturing* conditions (Figure 7.5a). Interestingly, high urea concentrations strongly increase the unfolding rates without substantially influencing the folding rates (Table 7.1a, Figure 7.6a). From the kinetics experiments, it is also possible to readily extract equilibrium constants for the pseudoknot-hairpin system ($K_{\mathrm{eq}} = k_{\mathrm{fold}}/k_{\mathrm{unfold}}$), based on the assumption of a two-state system. As expected, the surface immobilized equilibrium constant data, derived from folding/unfolding kinetics, are in excellent agreement with the freely diffusing experiments (Figure 7.3). Such agreement between surface immobilized and freely diffusing data sets provides additional evidence to support that surface immobilization does not perturb the conformation dynamics for either the WT or DKC constructs.

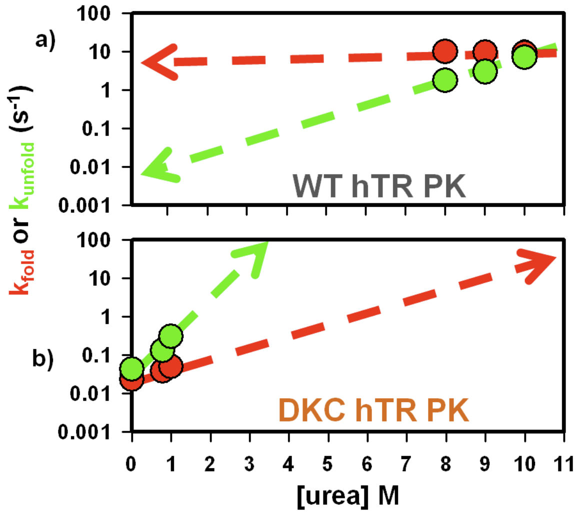

Figure 7.6 Log-linear plot of the urea-dependent folding and unfolding kinetics for the **a)** wild-type and **b)** dyskeratosis congenita pseudoknots. For both constructs, the unfolding rate constant is substantially more sensitive to addition of urea than the folding rate constant, which suggests that most of the change in base solvent accessible surface area (SASA) occurs after formation of the transition state. Lines indicate trends and are not actual fits to the data.

The linear dependence of the folding free energy change on urea concentration (Figure 7.3) can be used to develop a more quantitative understanding for the folding kinetics of the WT hTR PK under non-denaturing conditions. Specifically, the extrapolation of $\Delta G°$ to 0 M urea in Figure 7.3 yields $\Delta G°_{WT}(295\ K) = -4.2(2)$ kcal/mol, which would imply $K_{eq} = k_{fold}/k_{unfold} \approx 1100$ and thus a highly stable WT pseudoknot. Experimentally, the *folding* rate constant is observed to be mostly insensitive urea concentration, which would imply any urea-dependence of $\Delta G°$ is due primarily to changes in the *unfolding* rate constant. Therefore, a urea-*independent* folding rate constant of $\approx 10\ s^{-1}$ from Figure 7.6a would suggest an unfolding rate constant of $\approx 0.009\ s^{-1}$ at 0

M Urea (Table 7.1a), which is certainly consistent with the ≈ 0.01 s^{-1} upper limit established by photostability of the present donor-acceptor FRET pair.

a) **WT hTR PK**

[urea] M	k_{fold} s^{-1}	k_{unfold} s^{-1}	K_{eq}
8.0	10(1)	1.8(3)	5.7(6)
9.0	9.8(3)	3(1)	3(1)
10.0	9.4(8)	7.2(6)	1.3(2)
0.0	*10*[a]	*0.009*[a]	*1100*[a]

[a] - estimated values based on the urea-insensitive folding rate constant and the extrapolated free energy at 0 M urea(see text for details)

b) **DKC hTR PK**

[urea] M	k_{fold} s^{-1}	k_{unfold} s^{-1}	K_{eq}
0.0	0.023(5)	0.043(3)	0.5(1)
0.8	0.038(5)	0.13(1)	0.29(4)
1.0	0.05(1)	0.3(1)	0.15(5)

Table 7.1 Rate and equilibrium constants for the **a)** wild-type and **b)** mutant forms of the human telomerase RNA pseudoknot under varying urea concentrations. For both RNA pseudoknot constructs, the rate constant for forming the pseudoknot from the hairpin conformation is largely insensitive to urea concentration.

In contrast with the WT construct, each trajectory for the DKC hTR PK construct under *non-denaturing* conditions undergoes multiple conformational transitions between the two FRET states (Figure 7.5c), which permits accurate determination of dwell times and rate constants (Figure 7.5d). As was the case for the WT hTR PK, addition of urea has only a small effect on k_{fold} while substantially increasing k_{unfold} (Table 7.1, Figure 7.6b). It is worth noting that the above kinetic measurements for the DKC hTR PK under *non-denaturing* conditions serve as a valuable benchmark for the corresponding rate constants for WT hTR PK *extrapolated* to 0 M urea. Interestingly, such a comparison reveals that the net 4.5(3) kcal/mol *destabilization* of the mutant DKC pseudoknot is achieved by a combination of much *slower* folding (≈ 400x) and only slightly *faster* (≈ 5x) unfolding rate constants (Table 7.1).

7.2.4 van't Hoff Thermodynamics

Via direct measurement of the equilibrium constant, these single molecule studies have thus far focused on standard Gibbs free energy change (ΔG°) as the primary, experimentally determined, thermodynamic parameter. However, temperature-dependent information about the equilibrium constant can be used to deconstruct Gibbs free energy changes into enthalpic (ΔH°) and entropic (ΔS°) components. Furthermore, the observation that ΔG° is linearly dependent on urea concentration makes it reasonable to assume that the two additive components of $\Delta G° = \Delta H° - T\Delta S°$ might also be linearly dependent on urea, which facilitates additional thermodynamic comparisons between the wild type and mutant RNA constructs.

In freely diffusing experiments, the equilibrium constant for the WT hTR PK has been measured at temperatures ranging from 20.0(1) °C to 33.0(1) °C for three different urea concentrations (7.7 M, 8.4 M, and 9.1 M). At all urea concentrations, *increasing* the temperature results in *unfolding* of the pseudoknot, thus reducing the equilibrium constant. As shown in Figure 7.7a, a van't Hoff plot ($\ln[K_{eq}]$ vs 1/T) of the data is used to infer the entropy ($\Delta S° =$ intercept × R) and enthalpy ($-\Delta H° =$ slope × R) change associated with pseudoknot formation. It is interesting to note the nearly identical slopes for each of the plots, i.e., enthalpy changes (ΔH°) associated with pseudoknot formation are largely *insensitive* to urea. Along with more quantitative results from a non-linear least squares fit (Table 7.2a), these data sets provide clear evidence that the *addition of urea primarily decreases the folding entropy* ($\Delta\Delta S° < 0$), with a negligible effect on the folding enthalpy ($\Delta\Delta H° \approx 0$). To further break parameter correlation and thereby more precisely examine the dependence of ΔS° on urea, these van't Hoff data sets have been re-fitted with a common enthalpic slope. As shown in Figure 7.7b, the resulting entropy changes are linearly dependent on urea concentrations and predict ΔS° = -250.2(6) cal/molK at 0 M urea. In conjunction with the urea-independent ΔH° = -78.2(6) kcal/mol, this limiting ΔS° value corresponds to ΔG°(295 K) = -4.4(6) kcal/mol under non-denaturing conditions.

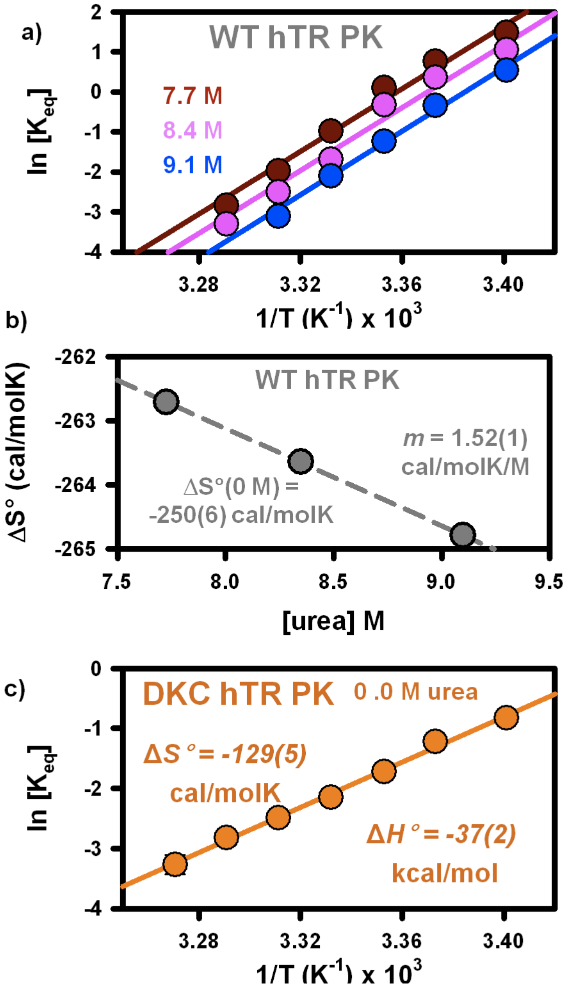

Figure 7.7 Single-molecule van't Hoff analyses. **a)** A plot of the temperature-dependence of the equilibrium constant of the wild-type human telomerase RNA pseudoknot at three urea concentrations. The identical slopes indicate a urea-*independent* folding enthalpy, while the constant vertical offset indicates a urea-*dependent* entropy. **b)** A plot of the urea-dependent entropy suggests a linear dependence of folding entropy on urea concentration. **c)** van't Hoff analysis of the mutant pseudoknot under non-denaturing conditions. All entropy and enthalpy changes can be found in Table 7.2.

It is worth noting that this is experimentally indistinguishable from the ΔG°(295 K) = -4.2(2) kcal/mol value obtained from extrapolation of the freely diffusing data (Figure 7.3a), which provides additional support for analyses of this conformational transition based on a linear dependence of free energy and entropy on urea.

WT hTR PK

a)

[urea] M	Δ*H*° kcal/mol	Δ*S*° cal/molK
9.1	-79(2)	-267(4)
8.4	-78(2)	-262(6)
7.7	-78(1)	-261(4)
0.0	*-78.2(6)*[b]	*-250(6)*[c]

[B] values from common slope analysis (see text for details)

[c] extrapolated values from the linear dependence of the entropy change on urea concentration (see text for details)

DKC hTR PK

b)

[urea] M	Δ*H*° kcal/mol	Δ*S*° cal/molK
0.0	*-37(2)*	*-129(5)*

Table 7.2 Thermodynamics parameters from the single-molecule van't Hoff analyses. **a)** Entropy and enthalpy changes for the wild-type human telomerase pseudoknot at various urea concentrations. ΔH° and ΔS° are (*i*) insensitive or (*ii*) linearly dependent on urea concentration, respectively. Together they predict folding thermodynamics under non-denaturing conditions. **b)** Enthalpy and entropy changes for the dyskeratosis congenita mutant form of the human telomerase RNA pseudoknot under non-denaturing conditions.

To enable thermodynamic comparison between the two RNA pseudoknot constructs under non-denaturing conditions, temperature-dependent equilibrium constants for DKC hTR PK have also been measured. The resulting van't Hoff plot (Figure 7.7c) predicts ΔS° = -129(5) cal/mol/K and ΔH° = -37(2) kcal/mol at 0 M Urea (Table 7.2b). Such a van't Hoff analysis of the DKC hTR PK data predicts ΔG°(295 K) = 1(2) kcal/mol at 0 M Urea, which is also consistent with the ΔG°(295 K) = 0.26(5) kcal/mol value obtained from the freely diffusing data (Figure

7.3b). Lastly, comparison of the WT and DKC constructs reveals that pseudoknot formation in the mutant is both half (≈ 47%) as exothermic and half (≈ 51%) as entropically costly, which makes formation of the WT pseudoknot more favorable thermodynamically.

7.3 Discussion

The above studies demonstrate the well-behaved, two-state nature of both the wild-type (WT) and dyskeratosis congenita (DKC) variants of the minimal hTR PK, which is consistent with recent smFRET findings (26). As a function of experimental conditions, both constructs are able to switch completely and reversibly between readily distinguishable low and high FRET states. This observation supports the existence of a two-state pseudoknot-hairpin unimolecular equilibrium for both the WT and DKC constructs (23). Implications of the kinetic and thermodynamic parameters associated with this equilibrium are discussed in detail below.

7.3.1 Folding Free Energies

For solution conditions used throughout these studies, which appropriately mimic physiological concentrations of free monovalent ion, the two RNA constructs exhibit vastly different $\Delta G°(295\ K)$ values for pseudoknot formation. The free energy of folding for the WT hTR PK is -4.2(2) kcal/mol, as determined by a linear extrapolation to 0 M urea (Figure 7.3a), which should be compared to 0.26(5) kcal/mol for the DKC variant. Such a substantial stability difference between the WT and DKC constructs ($\Delta\Delta G°(295K) = 4.5(3)$ kcal/mol) is qualitatively consistent with existing thermal denaturation studies (6.6 kcal/mol) and theoretical calculations (6 kcal/mol) (23), especially accounting for differences in solution conditions (e.g. salt, pH, temperature) associated with each value. Furthermore, the overall sign of this shift is in the expected direction, with the 2 nt non-complementary substitution resulting in *less favorable* formation of the pseudoknot.

It is instructive to explore how ΔΔG°(295 K) between the WT and DKC constructs (4.5(3) kcal/mol) manifests itself in the kinetics of the hairpin-pseudoknot unimolecular equilibrium. As noted previously, the presence of the DKC mutation results in a *large reduction* (≈ 400-fold) and yet only a *modest increase* (≈ 5-fold) in the folding and unfolding rate constants, respectively. In conjunction with the overall ΔΔG°, such kinetic information can be used to build a simple free energy reaction coordinate for the hairpin-pseudoknot folding transition (Figure 7.8).

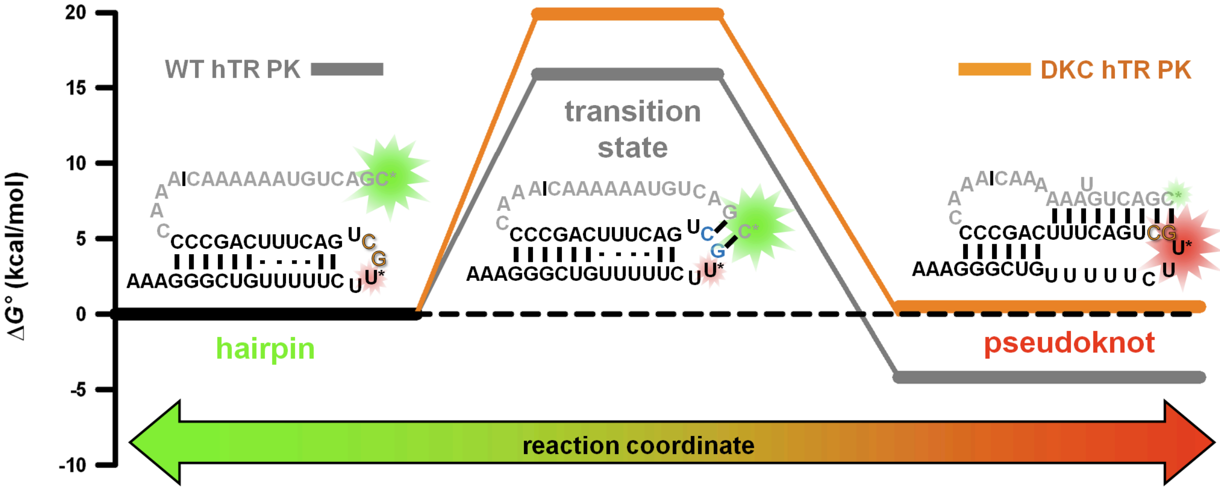

Figure 7.8 Free energy landscape for formation of the pseudoknot from the hairpin conformation. Secondary structure diagrams for the wild-type human telomerase RNA pseudoknot are shown, including the predicted structure of the transition state where only a few nucleotides from the P3 region of the pseudoknot have formed (see Section 7.3.1 for details).

Specifically, the measured rate constants data are used to estimate the free energy barrier for folding from transition state theory (Eq. 7.1), which would be consistent with a 15-20 kcal/mol transition state barrier along the reaction coordinate for typical attempt frequency of $\nu \approx 10^{13}$ s^{-1}.

$$\Delta G^{\ddagger} = -RT \ln\left(\frac{k}{\nu}\right) \qquad \text{(Eq. 7.1)}$$

It is worth noting, however, that $\Delta G^{\ddagger}$ depends only logarithmically on ν; thus, any differential *changes* in free energy barriers predicted from Eq. 7.2

$$\Delta\Delta G^{\ddagger} = RT \ln\left(\frac{k^{\mathrm{WT}}}{k^{\mathrm{DKC}}}\right) \qquad \text{(Eq. 7.2)}$$

should specifically remain completely independent of any such *ad hoc* and/or estimated choices for the prefactor, ν. From this expression, the changes associated with the folding and unfolding rate constants for the DKC mutant correspond to a 3.6 kcal/mol *increase* and a 0.9 kcal/mol *decrease* in the folding and unfolding free energy barriers, respectively.

Furthermore, we can extract additional physical insights into these changes in barrier height from a Φ-analysis (36,40). Specifically, for a given pair of modifications (e.g., DKC and WT), Φ represents the fraction of the free energy barrier change for folding ($\Delta\Delta G^{\ddagger}{}_{\mathrm{fold}}$) that results per unit change in the overall equilibrium stability ($\Delta\Delta G°$) as shown in Eq. 7.3.

$$\Phi = \frac{\Delta\Delta G^{\ddagger}{}_{\mathrm{fold}}(295\mathrm{K})}{\Delta\Delta G^{o}(295\mathrm{K})} \qquad \text{(Eq. 7.3)}$$

A Φ-analysis for the DCK and WT hTR pseudoknots demonstrates that 80% of the $\Delta\Delta G°(295\ \mathrm{K})$ comes from *decreasing* the DKC folding rate constant. This implies that the WT nucleotides at the positions associated with the DKC mutation (i.e., G108 and C109) play an important role in *lowering* the free energy transition state barrier for folding. Furthermore, the results of the Φ-analysis can be used to provide insights into the structure of the transition state for this conformational transition. Specifically, this strongly suggests that the WT hTR PK constructs at the transition state already have well-formed stabilizing contacts (e.g., base stacking and hydrogen bonding) at nucleotides G108 and C109.

7.3.2 Urea-dependent Free Energies and Rate Constants

Denaturation of nucleic acids is thought to occur because of favorable interactions between urea and the base "solvent accessible surface area" (SASA)(41). For RNA in a conformational equilibrium, the presence of urea preferentially stabilizes the structure with the most base SASA—typically unfolded and/or less compact. This manifests itself as a linear dependence of the folding free energy change on urea concentration ($\partial\Delta G°/\partial[\text{urea}]$), which is often referred to as the *m*-value (38,42). Consequently, one would expect the *m*-value for RNA folding to be positively correlated with the amount of base SASA *buried* due to a folding transition, as has been shown in several studies(38,39). It is therefore interesting to note that the *m*-values for the WT and DKC constructs differ in a counterintuitive direction. Specifically, due to two fewer base pairing interactions in the P3 region, pseudoknot formation might be anticipated to lead to *less* base SASA burial in DKC vs. WT hTR PK. As a result, one would expect WT hTR PK folding to be *more* sensitive to urea, when in fact it is nearly half as sensitive (WT: $m = 0.44(2)$ kcal/mol/M, DKC: $m = 0.81(6)$ kcal/mol/M). The precise origin of this difference is not well understood. However, these results certainly indicate unexpected differences in base SASA burial, which could potentially result from structural differences between: (*i*) the WT and DKC hairpin conformations and (*ii*) the WT and DKC pseudoknot conformations that may be related to the formation of base triples in the WT hTR PK. Together these structural differences could give rise to larger base SASA burial in the DKC hTR PK, which would be consistent with the experimentally observed *m*-values.

This *m*-value analysis can be similarly applied to the folding kinetics, by assuming that the urea-dependence of the *rate constants* is also related to the amount of base SASA burial associated with formation of the transition state that separates the two conformations(36). For both the hTR PK constructs, the very modest urea-dependence of the folding rate constant suggests that there is little base SASA burial associated with forming the transition state from the hairpin conformation. In conjunction with the observation that nucleotides 108 and 109 are important for fast folding, the urea-independent folding rate constant for the hTR PK imply a transition state where only the last two base pairs in P3 (e.g., G108 and C109) are formed, leaving the remainder of the bases in J2a/3 solvent exposed (Figure 7.8). Minimal burial of base SASA resulting from formation of the transition state from the hairpin conformation provides the rational for a largely urea-insensitive folding rate constant, as observed experimentally. Accordingly, most of the total base SASA burial takes place *after* the transition state during formation of the remainder of the P3 pseudoknot, which gives rise to a substantial dependence of the *unfolding* rate constant on urea concentration. Interestingly, similar conclusions have been made in quite different RNA constructs (36,43), which: (*i*) suggest that urea may generally destabilize all RNA tertiary folding transitions by selectively accelerating the *unfolding* rate constant and (*ii*) support the notion that many transition states for RNA tertiary folding may be conformationally aligned, yet still devoid of significant base SASA burial (e.g., minimal hydrogen-bonding and base stacking).

7.3.3 Urea-Dependent Entropies and Enthalpies

The measured urea-independent enthalpy for WT pseoduknot formation ($\Delta H° = -78.2(6)$ kcal/mol) is remarkably close to both theoretical calculations (-78.9 kcal/mol (44)) and previous experimental observations using ensemble techniques (-72.7 kcal/mol (22,23)). Such quantitative agreement serves as strong support for the use of urea as a valuable tool to study highly stable RNAs at the single-molecule level under denaturing conditions. Additionally, van't Hoff analysis as a function of urea yields new insights into the thermodynamic origin of urea-induced denaturation of the hTR PK. For example, the near complete insensitivity of ΔH° to urea provides experimental evidence that destabilization associated with urea is predominantly due to changes in ΔS°. This entropic origin of urea destabilization, together with the observation that urea has little effect on the folding rate constant, suggests that the majority of the denaturing power of urea results from *increasing* the entropic reward associated with forming the transition state from the pseudoknot conformation. Simply stated, urea destabilizes the WT hTR PK by making unfolding more entropically beneficial. This is a surprising observation, given that the proposed mechanism for urea denaturation of nucleic acids results from favorable hydrogen bonding between urea and the base SASA of RNA. The lack of any substantial enthalpic component to urea denaturation therefore must imply nearly perfect cancellation of any differential exothermicity between the competing urea-base and base-base interactions. Additionally, the determination of a urea-*independent* enthalpy change and a linear urea-*dependent* entropy change make it feasible to compare the folding thermodynamics between the WT and DKC hTR PK constructs used throughout this work (Figures 7.7a,c, and Table 7.2).

One additional surprising observation is that the increase in folding free energy (ΔΔG° = 4.5(3) kcal/mol) associated with the WT vs. DKC mutant results from a fortuitous near cancellation between much larger changes of both the folding enthalpy (ΔΔH° ≈ 41 kcal/mol) and entropy (ΔΔS° ≈ 121 kcal/mol/K, TΔΔS° ≈ 37 kcal/mol). An approximately 50% reduction in the enthalpic and entropic components of pseudoknot formation is certainly unexpected, but clearly indicates that substantial thermodynamics differences exist between the WT and the DKC hTR PK. These large entropic and enthalpic differences may be related to the vastly different *m*-values associated with the two constructs. As mentioned previously, it is likely that the WT and DKC constructs have different pseudoknot conformations. Specifically, the DKC hTR PK may not be able to from the well-defined triple-helical structure of the WT sequence. If this were the case, then pseudoknot formation in the DKC construct would lack the additional exothermicity as well as the entropic cost associated with forming the five base triples within the WT triple helix, resulting in the large ΔΔH° and ΔΔS° values that are observed experimentally. Unfortunately, differentiation between these two types of folding conformations (i.e., pseudoknot vs. triple-helix) is not possible with the current FRET constructs, but clearly identifies an interesting direction for future structural efforts.

7.4 Conclusions

Single molecule FRET experiments have been used to cleanly observe folding transitions in a minimal RNA pseudoknot (PK) designed to mimic the wild-type motif within the human telomerase RNA. These experiments are compared and contrasted with experiments conducted on a second minimal human telomerase RNA pseudoknot that contains a 2 nt non-complementary substitution mutation implicated in the telomerase-associated genetic disorder—dyskeratosis congenital (DKC). These experiments have demonstrated that the wild-type pseudoknot is substantially more stable (ΔΔG = 4.5(3) kcal/mol) than the mutant. Single-molecule kinetic studies of these constructs have identified the kinetic origin of this differential stability as being the result of: (*i*) a substantially reduced folding rate constant and (*ii*) a moderately increased unfolding rate constant, both of which contribute to destabilization of the fully folded mutant pseudoknot conformation. With the help of urea-induced denaturation, smFRET experiments have been used to elucidate the free energy landscape and various structural aspects of the folding reaction coordinate. Lastly, single-molecule van't Hoff analyses highlight a potential folding pathway wherein the mutant pseudoknot is unable to form the functionally important triple-helix structure known to exist in the wild-type RNA. Together, these results suggest that the disease mechanism associated with this particular genetic mutation is related to a combination of: (*i*) differential stabilities of the wild-type and mutant pseudoknot conformations, (*ii*) differential folding/unfolding kinetics associated with the pseudoknot-hairpin unimolecular equilibrium for the wild-type and mutant RNAs, and (*iii*) the potential lack of the a RNA triple helix in the mutant pseudoknot. Precise determination of the detailed mechanism of telomerase and the associated disease states would benefit substantially from extensions of these single-molecule experiments on minimal hTR pseudoknots to more holoenzyme-like systems that more closely recapitulate telomerase activity and function.

7.5 Experimental Methods

7.5.1 Construct Design

To generate suitable FRET labeled wild-type (WT hTR PK) and mutant (DKC hTR PK) psuedoknot constructs for single molecule studies, we exploit the powerful and increasingly common technique of RNA ligation (45-48). For the wild type construct, two synthetically modified oligonucleotides—strands 1 and strand 2—are purchased commercially (Integrated DNA Technologies, Inc). Strand 1 contains both a 5′ biotin moiety for surface immobilization as well as a internal amino modified dT (dT*) at position 106 (numbering from full length hTR(13)) for fluorescent labeling: (5′-biotin-AAA GGG CUG UUU UUC U[dT*]G CUG ACU UUC AGC CCC AAA-3′). This rC→dT* substitution was chosen to be the site of internal fluorophore labeling for three reasons: (*i*) this nucleotide is one of the least conserved positions in this region of the human TR pseudoknot motif (20), (*ii*) functional studies of the hTR PK have shown that a complementary mutation of C106 did not affect *in vitro* activity of telomerase (13,49), and (*iii*) structural models of the minimal WT hTR PK depict this nucleotide as being completely solvent exposed and devoid of hydrogen-bonding interactions with any of the surrounding functional groups (20). The amino-modified nucleotide within strand 1 is reacted with NHS-ester functionalized Cy5 dye (GE Healthcare) following the manufacturer's suggested protocol. Removal of unreacted Cy5 dyes is accomplished via micro centrifuge spin columns (Thermo Fisher Scientific, Inc). The second oligonucleotide, strand 2, contains a terminal 3′ Cy3 attached via phosphoramidite chemistry: (5′-phosphate-CAA AAA AUG UCA GCA A-Cy3-3′). Based on modifications to existing RNA ligation techniques (48,50), strands 1 and 2 are annealed together by heating to 85 °C at a 1:3 molar ratio in 50 mM hemisodium HEPES, 100 mM NaCl, pH 7.5 and allowed to slowly cool to 37 °C. T4 RNA ligase I (New England BioLabs, Inc.) is then added to the mixture following the manufacturer's recommended procedures, with the reaction held at 37 °C for 2 hours to allow for maximal ligation of the two strands (Figure 7.1). The product is purified via HPLC using a reverse phase column (Agilent Technologies) resulting in completely ligated RNA constructs containing Cy3, Cy5, and the biotin functional group.

The mutant DKC hTR PK construct is created in a similar fashion, with the only exception being that strand 1 for the DKC hTR PK contains the GC→AG mutation at positions 108-109 associated with the genetic disorder dyskeratosis congenita. A second wild-type construct with alternative labeling locations (WT^{alt} hTR PK) serves as a control to demonstrate that the observed conformational transitions are due to disruption and formation of the P3, rather than P2, region of the pseudoknot (Supplemental Figure S7.1). This WT^{alt} hTR PK construct is synthesized using the same procedures described above with two different oligonucleotides: (strand 1^{alt}: 5′-Cy3-GGG CUG UUU UUC-3′ and strand 2^{alt}: 5′-phosphate-UCG CUG ACU UUC AGC CC[dT*] AAA CAA AAA AUG UCA GCA AAA-biotin-3′). These alternate oligonucleotides shift the Cy 3 and Cy5 labeling sites from nucleotides 50 and 17 in the WT hTR

PK to nucleotides 1 and 30 in the WT^{alt} hTR PK (numbering from 5′-end of the smFRET constructs used within this study).

7.5.2 Single-molecule Microscope

All single-molecule experiments are performed with an inverted confocal fluorescence microscope (Olympus Corporation) outfitted with a 1.2 NA water-immersion objective (Olympus Corporation)(Figure 7.9).

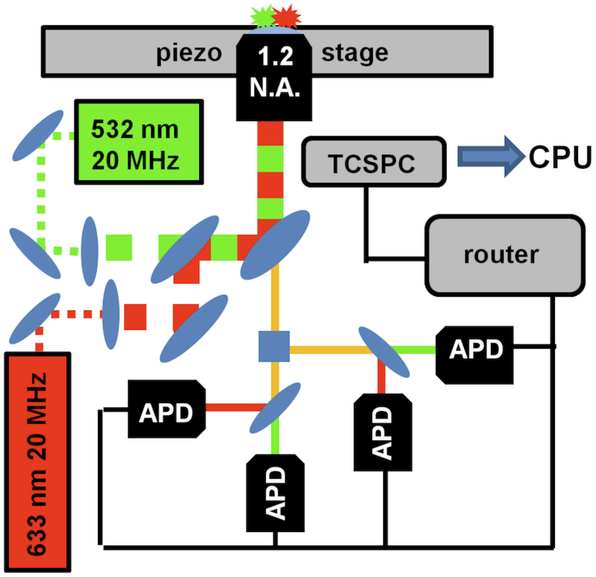

Figure 7.9 Single-molecule fluorescence microscope. Diagram of the experimental setup and data collection (see Section 7.5.2 for details).

Direct excitation of the Cy3 (donor) fluorophore is accomplished via a pulsed (20 MHz) 532 nm laser (Time Bandwidth Products Inc.). As needed, direct excitation of the Cy5 fluorophore (acceptor) can also be accomplished with a pulsed 635 nm laser diode (PicoQuant GmbH) triggered with a fixed 25 ns delay with respect to the 532 nm donor excitation pulse. The light from both excitation sources is coaxially aligned and directed into the back aperture of the objective, resulting in spatially overlapped laser foci and the ability for Alternating Laser

EXcitation methods (ALEX)(51-53) to verify presence of both donor and acceptor dyes on any given single molecule construct.

Photons are collected by the same objective in epifluorescence and focused through a spatial pinhole (50 μm) aligned for optimal fluorescence collection from the laser excitation volume. After passing through the pinhole, the light is spatially separated by polarization (i.e., perpendicular, parallel) and color (i.e., donor, acceptor) before being re-focused onto one of four single-photon avalanche photo diodes (APD, PerkinElmer Inc.) coupled to a time-correlated single-photon counting (TCSPC) module (Becker & Hickl GmbH) (Figure 7.9). The arrival of each fluorescence photon is recorded with respect the exciting laser pulse (microtime) and start of the experiment (macrotime). The stream of photon macrotimes is used to construct a donor-acceptor fluorescence time trajectory, which is a visual representation of the raw data collected in both the freely diffusing and surface immobilized smFRET experiments (see below). Conversely, the photon microtimes are used to construct fluorescence lifetime profiles of the two dyes, which, among other things, can be used to ensure isotropic rotational diffusion of the donor and acceptor fluorophores and thus the absence of any dye–RNA interactions.

7.5.3 Freely Diffusing smFRET Experiments

Freely diffusing experiments, similar to two-color coincidence detection one-color excitation experiments (8,54), are performed at relatively high average laser powers (≈ 75 μW) with low RNA concentrations (≈ 125 pM). At these concentrations there is, on average, significantly fewer than one RNA molecule in the confocal excitation volume at any time (Figure 7.10a). As an individual RNA in solution stochastically passes through the excitation volume of the focused laser beams, a short (< 1ms) burst of fluorescence is emitted that corresponds to the resonance time of the RNA in the confocal volume (Figure 7.10b). Sorting photon arrival times via ALEX methods provides the crucial ability to restrict analysis only to constructs containing both non-photobleached donor and acceptor fluorophores. This is accomplished by assigning a threshold of 20 KHz on the minimum photon count rate for a given fluorescent burst to ensure sufficient determination of E_{FRET}, with the reported values insensitive within quoted uncertainties to changes in such a choice of threshold.

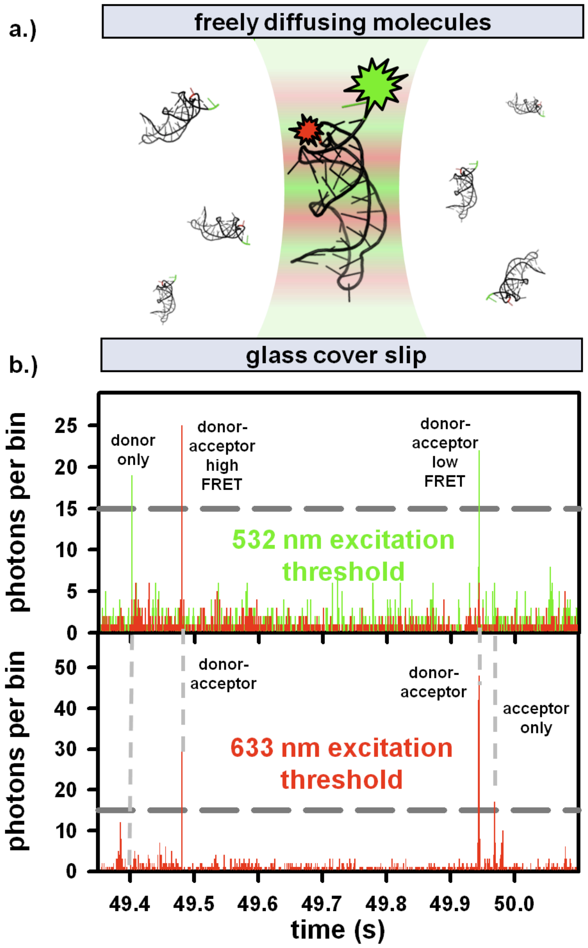

Figure 7.10 Freely diffusing experiments. **a)** Schematic representation of single-molecules freely diffusing in and around the overlapping excitation volumes of the red and green lasers (see Materials and Methods for details). **b)** Freely diffusing data of the human telomerase RNA pseudoknot obtained using ALEX methods, with the four possible outcomes for the fluorescent molecules. ALEX filtering permits events from dually labeled donor-acceptor molecules to be selectively considered for data analysis.

Data analysis is accomplished by calculating E_{FRET} values for all ALEX sorted bursts with both the donor and acceptor dyes present, which are then used to construct a histogram representing equilibrium distribution of E_{FRET} for the hTR PK molecules under a given set of experimental conditions(55). From the minimum ($E_{FRET} \approx 0.55$) in such a bimodal distribution (Figure 7.2), it is easy to determine which fluorescent bursts arise from molecules in the hairpin (unfolded, $E_{FRET} < 0.55$) or pseudoknot (folded, $E_{FRET} > 0.55$) conformation. Due to sample purity and the use of ALEX methods, the number of high and low E_{FRET} bursts is directly proportional to the concentration of each of the conformers at equilibrium; thus the ratio of high and low E_{FRET} burst frequencies provides direct experimental access to the equilibrium constant (Figure 7.1c).

7.5.4 Surface Immobilized smFRET Experiments

For surface immobilized experiments, molecules are non-covalently attached to the surface via biotin-streptavidin chemistry, with a typical surface coverage of less than one molecule per square micron. To generate an image of the surface immobilized molecules, a piezo-electric stage raster scans a 10 × 10 μm region of the sample with respect to the microscope objective to generate a 256 × 256 pixel image. Each diffraction-limited feature in the image corresponds to the fluorescence from a single surface-immobilized molecule. The stage is then used to position the sample so that the laser light is focused at the center of an individual fluorescence spot, from which the fluorescence can be continuously observed in real-time. Again, the use of ALEX filtered surface images ensure that only dually labeled molecules are considered for data analysis. As mentioned previously, the collected donor and acceptor photon streams are used to construct both fluorescence and E_{FRET} time trajectories, which for surface-immobilized experiments depict individual molecules actively switching between conformations with distinct FRET efficiencies. Rate constants for these conformational transitions are calculated by constructing cumulative distribution plots of the dwell times for the pseudoknot ($E_{FRET} > 0.55$) and hairpin ($E_{FRET} < 0.55$) conformations.

7.5.5 smFRET Temperature Control

For all of the temperature-dependent smFRET experiments, a heated objective collar (Bioptechs Inc.) and Peltier-base stage heater (Instec, Inc.) are used to provide thermal control of the sample with temperature gradients < 0.1 °C/cm. The absolute sample temperature is determined from measurements at the focus of the excitation source using a micro-thermocouple. All other experiments are performed at room temperature (20-22 °C).

7.5.6 smFRET Buffer Conditions

Experiments are performed in a standard fluorescence-imaging buffer (50 mM HEPES, 25 mM KOH, 10 mM NaOH, 95 mM KCl, 2 mM TROLOX, pH 7.7), which consists of the well characterized protocatechuic acid/protocatechuate-3,4-dioxygenase oxygen scavenging system (100 nM PCD and 5 mM PCA)(56). For all experiments, the molar concentrations of each of the buffer components are held constant by accounting for changes in solution volume and density due to the added solute.

References

1. Wynford-Thomas, D.; D. Kipling. The End-Replication Problem, *Nature*, **1997,** *389*, 551-551.

2. Blackburn, E. H. Switching and Signaling at the Telomere, *Cell*, **2001,** *106*, 661-673.

3. Blackburn, E. H. The End of the (DNA) Line, *Nat. Struct. Biol.*, **2000,** *7*, 847-850.

4. Greider, C. W.; E. H. Blackburn. Tracking Telomerase, *Cell*, **2004,** *116*, S83-86.

5. Cech, T. R. Beginning to Understand the End of the Chromosome, *Cell*, **2004,** *116*, 273-279.

6. Hengesbach, M.; B. M. Akiyama; M. D. Stone. Single-Molecule Analysis of Telomerase Structure and Function, *Curr. Opin. Chem. Biol.*, **2011,** *15*, 845-852.

7. Mihalusova, M.; J. Y. Wu; X. Zhuang. Functional Importance of Telomerase Pseudoknot Revealed by Single-Molecule Analysis, *Proc. Natl. Acad. Sci. USA*, **2011,** *108*, 20339-20344.

8. Yeoman, J. A.; A. Orte; B. Ashbridge; D. Klenerman; S. Balasubramanian. RNA Conformation in Catalytically Active Human Telomerase, *J. Am. Chem. Soc.*, **2010,** *132*, 2852-2853.

9. Wu, J. Y.; M. D. Stone; X. Zhuang. A Single-Molecule Assay for Telomerase Structure-Function Analysis, *Nucleic Acids Res.*, **2010,** *38*, e16.

10. Gavory, G.; M. F. Symmons; Y. Krishnan Ghosh; D. Klenerman; S. Balasubramanian. Structural Analysis of the Catalytic Core of Human Telomerase RNA by FRET and Molecular Modeling, *Biochemistry*, **2006,** *45*, 13304-13311.

11. Collins, K. The Biogenesis and Regulation of Telomerase Holoenzymes, *Nat. Rev. Mol. Cell. Biol.*, **2006,** *7*, 484-494.

12. Chen, J. L.; C. W. Greider. Telomerase RNA Structure and Function: Implications for Dyskeratosis Congenita, *Trends Biochem. Sci.*, **2004,** *29*, 183-192.

13. Chen, J. L.; M. A. Blasco; C. W. Greider. Secondary Structure of Vertebrate Telomerase RNA, *Cell*, **2000,** *100*, 503-514.

14. Gilley, D.; E. H. Blackburn. The Telomerase RNA Pseudoknot is Critical for the Stable Assembly of a Catalytically Active Ribonucleoprotein, *Proc. Natl. Acad. Sci. USA*, **1999,** *96*, 6621-6625.

15. Tzfati, Y.; Z. Knight; J. Roy; E. H. Blackburn. A Novel Pseudoknot Element is Essential for the Action of a Yeast Telomerase, *Genes Dev.*, **2003,** *17*, 1779-1788.

16. Reipa, V.; G. Niaura; D. H. Atha. Conformational Analysis of the Telomerase RNA Pseudoknot Hairpin by Raman Spectroscopy, *RNA*, **2007,** *13*, 108-115.

17. Moriarty, T. J.; D. T. Marie-Egyptienne; C. Autexier. Functional Organization of Repeat Addition Processivity and DNA Synthesis Determinants in the Human Telomerase Multimer, *Mol. Cell. Biol.*, **2004,** *24*, 3720-3733.

18. Autexier, C.; R. Pruzan; W. D. Funk; C. W. Greider. Reconstitution of Human Telomerase Activity and Identification of a Minimal Functional Region of the Human Telomerase RNA, *Embo. J.*, **1996,** *15*, 5928-5935.

19. Bachand, F.; I. Triki; C. Autexier. Human Telomerase RNA-Protein Interactions, *Nucleic Acids Res.*, **2001,** *29*, 3385-3393.

20. Kim, N. K.; Q. Zhang; J. Zhou; C. A. Theimer; R. D. Peterson; J. Feigon. Solution Structure and Dynamics of the Wild-Type Pseudoknot of Human Telomerase RNA, *J. Mol. Biol.*, **2008,** *384*, 1249-1261.

21. Comolli, L. R.; I. Smirnov; L. Xu; E. H. Blackburn; T. L. James. A Molecular Switch Underlies a Human Telomerase Disease, *Proc. Natl. Acad. Sci. USA*, **2002,** *99*, 16998-17003.

22. Theimer, C. A.; C. A. Blois; J. Feigon. Structure of the Human Telomerase RNA Pseudoknot Reveals Conserved Tertiary Interactions Essential for Function, *Mol. Cell.*, **2005,** *17*, 671-682.

23. Theimer, C. A.; L. D. Finger; L. Trantirek; J. Feigon. Mutations Linked to Dyskeratosis Congenita Cause Changes in the Structural Equilibrium in Telomerase RNA, *Proc. Natl. Acad. Sci. USA*, **2003,** *100*, 449-454.

24. Theimer, C. A.; L. D. Finger; J. Feigon. YNMG Tetraloop Formation by a Dyskeratosis Congenita Mutation in Human Telomerase RNA, *RNA*, **2003,** *9*, 1446-1455.

25. Chen, G.; J. D. Wen; I. Tinoco, Jr. Single-Molecule Mechanical Unfolding and Folding of a Pseudoknot in Human Telomerase RNA, *RNA*, **2007,** *13*, 2175-2188.

26. Hengesbach, M.; N. K. Kim; J. Feigon; M. D. Stone. Single-Molecule FRET Reveals the Folding Dynamics of the Human Telomerase RNA Pseudoknot Domain, *Angew. Chem. Int. Ed. Engl.*, **2012,** *51*, 5876-5879.

27. Cao, S.; S. J. Chen. Biphasic Folding Kinetics of RNA Pseudoknots and Telomerase RNA Activity, *J. Mol. Biol.*, **2007,** *367*, 909-924.

28. Cao, S.; S. J. Chen. Predicting RNA Pseudoknot Folding Thermodynamics, *Nucleic Acids Res.*, **2006,** *34*, 2634-2652.

29. Li, P. T.; J. Vieregg; I. Tinoco, Jr. How RNA Unfolds and Refolds, *Annu. Rev. Biochem.*, **2008,** *77*, 77-100.

30. Bokinsky, G.; X. Zhuang. Single-Molecule RNA Folding, *Acc. Chem. Res.*, **2005,** *38*, 566-573.

31. Roy, R.; S. Hohng; T. Ha. A Practical Guide to Single-Molecule FRET, *Nat. Methods*, **2008,** *5*, 507-516.

32. Zhao, R.; D. Rueda. RNA Folding Dynamics by Single-Molecule Fluorescence Resonance Energy Transfer, *Methods*, **2009,** *49*, 112-117.

33. Aleman, E. A.; R. Lamichhane; D. Rueda. Exploring RNA Folding One Molecule at a Time, *Curr. Opin. Chem. Biol.*, **2008,** *12*, 647-654.

34. Holmstrom, E. D.; J. L. Fiore; D. J. Nesbitt. Thermodynamic Origins of Monovalent Facilitated RNA Folding, *Biochemistry*, **2012,** *51*, 3732-3743.

35. Fiore, J. L.; E. D. Holmstrom; D. J. Nesbitt. Entropic Origin of Mg^{2+}-Facilitated RNA Folding, *Proc. Natl. Acad. Sci. USA*, **2012,** *109*, 2902-2907.

36. Bartley, L. E.; X. W. Zhuang; R. Das; S. Chu; D. Herschlag. Exploration of the Transition State for Tertiary Structure Formation Between an RNA Helix and a Large Structured RNA, *J. Mol. Biol.*, **2003,** *328*, 1011–1026.

37. Fiore, J. L.; B. Kraemer; F. Koberling; R. Erdmann; D. J. Nesbitt. Enthalpy-Driven RNA Folding: Single-Molecule Thermodynamics of Tetraloop–Receptor Tertiary Interaction, *Biochemistry*, **2009,** *48*, 2550–2558.

38. Shelton, V. M.; T. R. Sosnick; T. Pan. Applicability of Urea in the Thermodynamic Analysis of Secondary and Tertiary RNA Folding, *Biochemistry*, **1999,** *38*, 16831-16839.

39. Lambert, D.; D. E. Draper. Effects of Osmolytes on RNA Secondary and Tertiary Structure Stabilities and RNA-Mg^{2+} Interactions, *J. Mol. Biol.*, **2007,** *370*, 993-1005.

40. Fersht, A. R.; A. Matouschek; L. Serrano. The Folding of an Enzyme .1. Theory of Protein Engineering Analysis of Stability and Pathway of Protein Folding, *J. Mol. Biol.*, **1992,** *224*, 771-782.

41. Priyakumar, U. D.; C. Hyeon; D. Thirumalai; A. D. MacKerell. Urea Destabilizes RNA by Forming Stacking Interactions and Multiple Hydrogen Bonds with Nucleic Acid Bases, *J. Am. Chem. Soc.*, **2009,** *131*, 17759-17761.

42. Lambert, D.; D. E. Draper. Denaturation of RNA secondary and tertiary structure by urea: simple unfolded state models and free energy parameters account for measured m-values, *Biochemistry*, **2012,** *51*, 9014-9026.

43. Williams, S.; T. P. Causgrove; R. Gilmanshin; K. S. Fang; R. H. Callender; W. H. Woodruff; R. B. Dyer. Fast Events in Protein Folding: Helix Melting and Formation in a Small Peptide, *Biochemistry*, **1996,** *35*, 691-697.

44. Yingling, Y. G.; B. A. Shapiro. The Impact of Dyskeratosis Congenita Mutations on the Structure and Dynamics of the Human Telomerase RNA Pseudoknot Domain, *J. Biomol. Struct. Dyn.*, **2007,** *24*, 303-319.

45. Akiyama, B. M.; M. D. Stone. Assembly of Complex RNAs by Splinted Ligation, *Methods Enzymol.*, **2009,** *469*, 27-46.

46. Moore, M. J.; C. C. Query. Joining of RNAs by Splinted Ligation, *Method Enzymol.*, **2000,** *317*, 109-123.

47. Stark, M. R.; J. A. Pleiss; M. Deras; S. A. Scaringe; S. D. Rader. An RNA Ligase-Mediated Method for the Efficient Creation of Large, Synthetic RNAs, *RNA*, **2006,** *12*, 2014-2019.

48. Moore, M. J., Query, C.C. Uses of Site-Specifically Modified RNAs Constructed by RNA Ligation, In *RNA:Protein Interactions: A Practical Approach* (Smith, C. W. J., Ed.), pp 75-140, Oxford University Press Inc., New York.1998

49. Chen, J. L.; C. W. Greider. Functional Analysis of the Pseudoknot Structure in Human Telomerase RNA, *Proc. Natl. Acad. Sci. USA*, **2005,** *102*, 8080-8085; discussion 8077-8089.

50. Lemay, J. F.; J. C. Penedo; R. Tremblay; D. M. Lilley; D. A. Lafontaine. Folding of the Adenine Riboswitch, *Chem. Biol.*, **2006,** *13*, 857-868.

51. Lee, N. K.; A. N. Kapanidis; Y. Wang; X. Michalet; J. Mukhopadhyay; R. H. Ebright; S. Weiss. Accurate FRET Measurements within Single Diffusing Biomolecules using Alternating-Laser Excitation, *Biophys. J.*, **2005,** *88*, 2939-2953.

52. Kapanidis, A. N.; N. K. Lee; T. A. Laurence; S. Doose; E. Margeat; S. Weiss. Fluorescence-Aided Molecule Sorting: Analysis of Structure and Interactions by Alternating-Laser Excitation of Single Molecules, *Proc. Natl. Acad. Sci. USA*, **2004,** *101*, 8936–8941.

53. Kapanidis, A. N.; T. A. Laurence; N. K. Lee; E. Margeat; X. X. Kong; S. Weiss. Alternating-Laser Excitation of Single Molecules, *Acc. Chem. Res.*, **2005,** *38*, 523-533.

54. Orte, A.; R. Clarke; S. Balasubramanian; D. Klenerman. Determination of the Fraction and Stoichiometry of Femtomolar Levels of Biomolecular Complexes in an Excess of Monomer using Single-M olecule, Two-Color Coincidence Detection, *Anal. Chem.*, **2006,** *78*, 7707-7715.

55. Fiore, J. L.; J. H. Hodak; O. Piestert; C. D. Downey; D. J. Nesbitt. Monovalent and Divalent Promoted GAAA-Tetraloop–Receptor Tertiary Interactions from Freely Diffusing Single-Molecule Studies, *Biophys. J.*, **2008,** *95*, 3892-3905.

56. Aitken, C. E.; R. A. Marshall; J. D. Puglisi. An Oxygen Scavenging System for Improvement of Dye Stability in Single-Molecule Fluorescence Experiments, *Biophys. J.*, **2008,** *94*, 1826-1835.

Chapter 8

Vitamin B_{12}-facilitates formation of a regulatory RNA kissing loop[*]

8.1 Introduction

Riboswitches are noncoding structural elements in the leader sequence of certain bacterial messenger RNAs that regulate downstream gene expression in a ligand-dependent fashion(1). The first experimentally verified riboswitch was found in mRNAs that code for the expression of a cobalamin (vitamin B_{12}) transport protein (i.e., *btuB* in *E. coli*)(2,3). These structural elements function to maintain intracellular concentrations of their cognate ligand (i.e., cobalamin), which is a critical cofactor for methyltransferase and isomerase reactions involved in S-adenosylmethionine and succinyl-CoA biosynthesis, respectively(4).The cobalamin clan of riboswitches (Rfam: CL00101) is one of the most abundant and ubiquitous *cis*-acting mRNA regulatory elements throughout the bacterial domain of life(5). The importance of these RNAs and their associated effector molecule is further highlighted by the fact that only certain species of Archaea and Bacteria can biosynthesize cobalamin(6,7), and yet it is essential to many organisms, most notably humans(8).

Generally, all riboswitches consist of two interacting domains that, together, result in biological functionality. Specifically, ligand binding in the receptor (or aptamer) domain promotes a conformational change in the regulatory domain (or expression platform), which modulates the production of a downstream gene(9,10). Single-molecule fluorescence resonance energy transfer (smFRET) is ideally suited(11) and frequently used to observe these ligand-

---

[*] To be submitted

induced conformational transitions(12-17). However, many of these investigations are unable to monitor conformational transitions associated with the regulatory domain, and, until now, none of them have been able to unambiguously link: (*i*) ligand binding to (*ii*) conformational transitions within a structural switch. Here we use these smFRET techniques to independently and simultaneously observe these two processes.

A recent study reported the first x-ray crystal structure of an entirely biologically functional cobalamin riboswitch containing both the receptor and regulatory domains(18). This crystallographic model revealed that the recognition and regulatory domains communicate via a tertiary interaction in order to confer biological functionality. Additionally, cell-based experiments conducted on these RNAs demonstrate that this tertiary interaction modulates gene expression in a vitamin B_{12}-dependent fashion(18). Specifically, hydroxocobalamin, a variant of vitamin B_{12}, was shown to facilitate formation of a kissing loop (KL) interaction, resulting in sequestration of the ribosome binding site (RBS). Although these structural and cell-based experiments have unveiled information about the mechanism of action associated with this riboswitch, many detailed questions regarding both ligand binding kinetics and conformational dynamics remain unanswered.

To this end, a combination of fluorescence techniques—smFRET and cell-based fluorescent-reporter assays—has been used to offer the first, to our knowledge, detailed mechanistic account of a biologically functional riboswitch based on a collection of both cellular and smFRET data. The primary sequence (GenBank accession: AACY021350931.1/557-456) of the *env8* hydroxocobalamin (*env8*HyCbl, Figure 8.1a) riboswitch used throughout these experiments comes from a comparative genomics analysis of structured noncoding RNAs(19). It is member of the *AdoCbl-variant* family (Rfam: RF01689), which is one of three members within the larger cobalamin riboswitch clan (Rfam: CL00101)(20). Previous ligand binding experiments have revealed that *env8*HyCbl selectively binds vitamin B_{12} cofactors with smaller β-axial ligands (e.g., hydroxo- or methylcobalamin) as opposed to the bulkier adenosylcobalamin cofactor(18). Synthetic modifications to this RNA (Figure 8.1a) allow smFRET-based experiments to monitor, in real-time and under equilibrium, the docking/undocking of the L5-L13 regulatory KL in the *presence* or *absence* of ligand (Figure 8.1b).

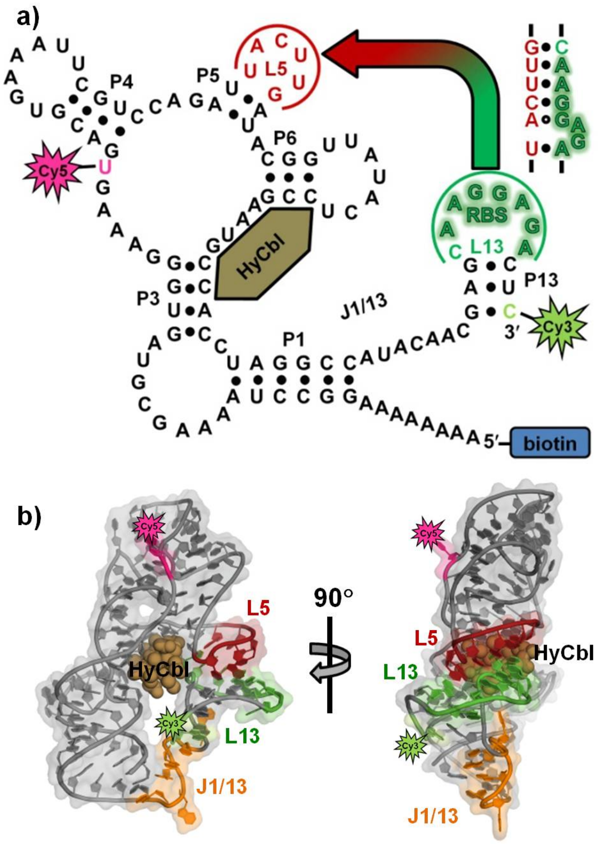

Figure 8.1. Schematic representation of the **a)** secondary and **b)** tertiary structure of the *env8HyCbl* riboswitch, complete with the Cy3 (green star), Cy5 (red star), and biotin (blue rectangle) synthetic moieties. The loops, L5 (red) and L13 (green) form a regulatory RNA kissing-loop (KL), which contains the purine-rich ribosome binding site (shadowed green nucleotides). Binding of hydroxocobalamin (bronze spheres, HyCbl) facilitates formation of the KL, which decreases the distance between the Cy3 (donor) and Cy5 (acceptor) fluorophores resulting in more efficient energy transfer (E_{FRET}).

Simultaneously, hydroxocobalamin-dependent quenching(21) of Cy3 is used as an orthogonal experimental observable to monitor the kinetics of ligand binding independently of conformation. The results of these smFRET experiments provide substantial support for a four-state kinetic model that highlights several key biological features associated with this regulatory switch (Figure 8.2): (*i*) KL docking/undocking occurs in the *absence* of ligand and is dependent on Mg^{2+}, (*ii*) ligand binding only occurs when the KL is *undocked* and (*iii*) KL docking/undocking also occurs in the *presence* of ligand and is dependent on Mg^{2+}.

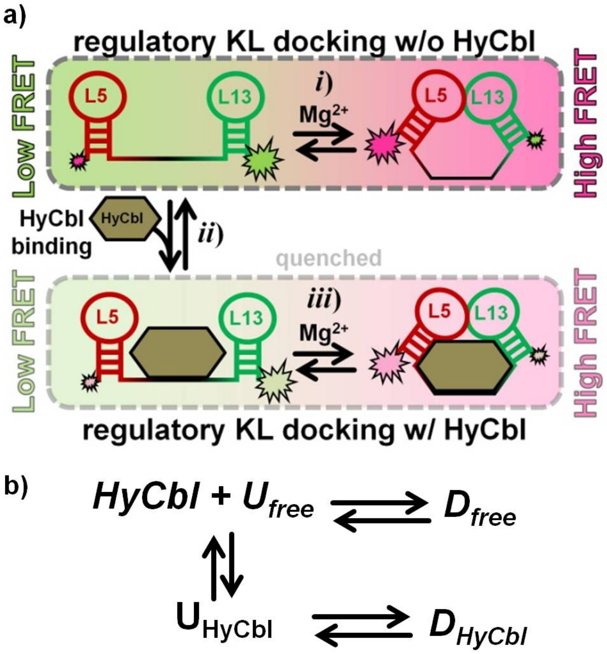

Figure 8.2 Four-state kinetic model for the *env8HyCbl* riboswitch represented **a)** graphically and **b)** symbolically. The four macroscopic conformations are linked by three coupled equilibria: (*i*) KL docking in the absence of ligand, (*ii*) ligand binding in the undocked conformation, and (*iii*) KL docking in the presence of ligand. Formation of the KL decreases the inter-dye distance, resulting in more efficient fluorescence resonance energy transfer (E_{FRET}). Ligand binding quenches Cy3, which decreases the total fluorescence of Cy3 and Cy5 and can be monitored independent of KL docking/undocking.

Additionally, the single-molecule results reveal that, in the presence of Mg^{2+}, ligand binding preferentially stabilizes the *docked* conformation. Finally, results from cell-based reporter assays are used to relate these biophysical findings with the cellular function of this RNA. The highly correlated experimental observations reveals that formation of the regulatory switch (i.e., L5-L13 KL) is responsible for repression of gene expression, regardless of whether or not the ligand is bound to the RNA. As a whole, these findings expose a great deal of information about the dynamical relationship between structure and function in cobalamin riboswitches, which can be applied to various other functional RNAs.

8.2 Results

Both freely diffusing and surface-immobilized experiments (See Experimental Methods) have been used to characterize the conformational transitions associated with the regulatory KL of the *env*8HyCbl riboswitch. Briefly, freely diffusing smFRET experiments make use of the extremely small volume associated with the diffraction-limited focus of a high numerical aperture objective. At low concentrations of Cy3-Cy5 labeled RNA (≈ 100 pM), this volume is void of fluorophores ≈ 98% of the time. Occasionally, an individual molecule will stochastically diffuse through this volume, resulting in a burst of fluorescence limited in duration by the diffusion constant of the RNA (≈ 1 ms). The efficiency of fluorescence resonance energy transfer (E_{FRET}) can be calculated for thousands of fluorescent bursts and compiled into a histogram to describe the probability of observing any given E_{FRET} value, which is related to the conformation of the RNA.

Alternatively, individual Cy3-Cy5 labeled RNAs can be immobilized to a microscope coverslip using biotin-streptavidin chemistry, which prevents the molecule from freely diffusing in solution. The diffraction-limited focus of the confocal fluorescence microscope can be used to continuously excite the fluorophores and subsequently detect fluorescence. The collected signal is used to determine the E_{FRET} of a single RNA as a function of time, where changes in E_{FRET} result from discrete conformations transitions.

The two single-molecule fluorescence experiments described above are used to rigorously characterize the *in vitro* behavior of the env8HyCbl riboswitch. Complementary cell-based fluorescence reporter assays are used to compare and contrast the *in vitro* and cellular behavior of the RNA. Specifically, these reporter assays are designed to monitor the regulation of green fluorescent protein (GFP) expression provided by the *env*8HyCbl riboswitch.

8.2.1 KL docking equilibrium in the absence of ligand

As a first step, freely diffusing smFRET experiments have been used to explore the equilibrium behavior of the L5-L13 kissing loop (KL) interaction from the *env8*HyCbl riboswitch in solutions free of ligand. Under standard buffer conditions (see Experimental Methods), the distribution of E_{FRET} values associated with thousands of individual fluorescently labeled RNA constructs reveals (Figure 8.3a) that the riboswitch resides entirely in a single low $E_{FRET} = 0.15(3)$ population. However, addition of $MgCl_2$ is sufficient to promote KL docking (Figure 8.3a), as indicated by the Mg^{2+}-dependent increase in the relative probability of observing molecules in a second, higher $E_{FRET} = 0.58(3)$ population. This high E_{FRET} value corresponds to an inter-dye distance of ≈ 50(3) Å and, given the experimental uncertainty in the measurement, is consistent with the ≈ 47 Å prediction based on the recent crystal structure(18). Accordingly, we attribute this high E_{FRET} value to molecules residing in the docked KL conformation (D_{free}), with the low E_{FRET} value corresponding to the undocked species (U_{free}), where the subscript "free" denotes that the ligand is not bound the riboswitch (Figure 8.2b). The necessity of Mg^{2+} for the formation of this interaction is supported by the x-ray crystal structure (PDB: 4FRN), which depicts divalent cations near the L5 and L13 loops(18). This is a notable feature among other KL x-ray crystal structures(22,23) and likely reflects the importance of Mg^{2+} in the formation of these types of tertiary interactions.

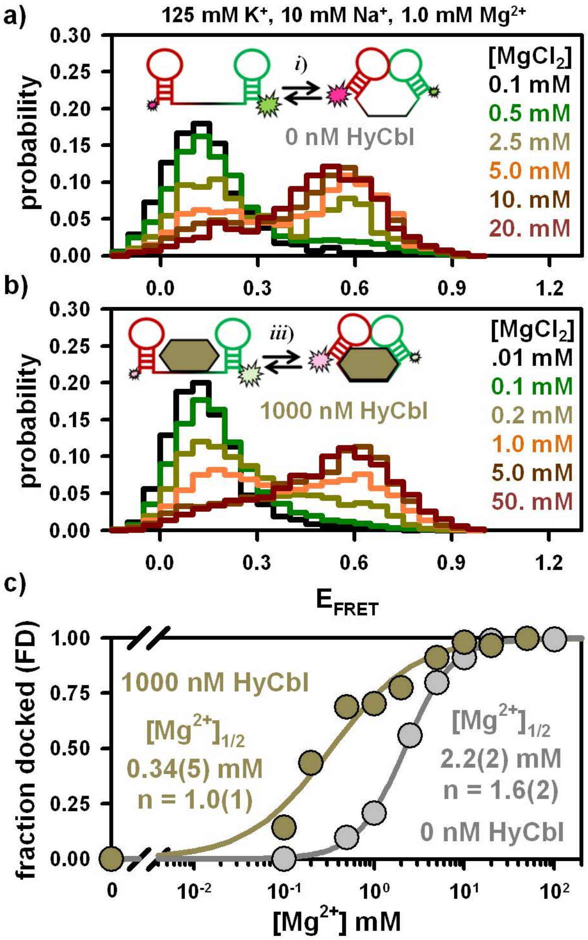

Figure 8.3 Freely diffusing smFRET experiments depict the Mg^{2+}-dependence of the KL docking equilibrium in the **a)** *absence* and **b)** *presence* of 1000 nM HyCbl. **c)** The presence of HyCbl (bronze circles) decreases the concentration of divalent cations (i.e., $[Mg^{2+}]_{½}$) required for *FD* = 0.5.

The residual probability associated with observing the low E_{FRET} population at high $[Mg^{2+}]$ results from molecules that are unable to form the L5-L13 KL interaction (≈ 15 %), as determined in the surface immobilized experiments described later (Section 8.2.5). The normalized probability of observing the two E_{FRET} distributions, when corrected for a 15 % nonresponsive population, can be used to characterize the equilibrium behavior of the riboswitch. Specifically, the fractional occupancy of molecules in the docked or undocked conformation can be calculated using Eq. 8.1a and 1b, respectively.

$$FD_{free} = \frac{P(D_{free})}{P(D_{free}) + P(U_{free})} \quad \text{(Eq. 8.1a)}$$

$$FU_{free} = \frac{P(U_{free})}{P(D_{free}) + P(U_{free})} \quad \text{(Eq. 8.1b)}$$

The parameters $P(D_{free})$ and $P(U_{free})$ describe the probability of observing the docked and undocked conformations, respectively. Again, the subscript "free" is used to indicate that the riboswitches are not bound to ligands. The Mg^{2+} concentration required to achieve $FD = 0.5$ (i.e., $[Mg^{2+}]_{½}$) is obtained by fitting the data to a standard Hill-type binding model. For data collected in the *absence* of HyCbl, such an analysis results in a $[Mg^{2+}]_{½} = 2.2(2)$ mM (Figure 8.3c), which is nearly twice normal physiological concentrations of free Mg^{2+}(24). Although the regulatory KL can form in the *absence* of HyCbl, the FD_{free} is only ≈ 0.22 in solutions that appropriately mimic the ionic environment associated with the inside of a cell (e.g., 1 mM Mg^{2+}, 125 mM K^{+}, 10 mM Na^{+}), suggesting that *undocked* conformation is more stable under these conditions.

To confirm that the high E_{FRET} population results from formation of the L5-L13 regulatory switch, a second, doubly labeled RNA construct has also been studied. This construct, referred to as the L5-mutant *env8*HyCbl riboswitch (Supplemental Figure S8.1), contains a dinucleotide substitution at positions 48 and 49 in L5 (underlined nucleotides, 5′-UAC<u>UU</u>G-′3 → 5′-UAC<u>AA</u>G-′3). The UU to AA mutation prevents formation of two Watson-Crick base pairs that are otherwise present in the wild-type construct and preferentially destabilizes the *docked* conformation of the KL. As expected, this smFRET construct remains in the undocked (low E_{FRET}) conformation even in solutions containing 30 mM $MgCl_2$ (Supplemental Figure S8.1), thus confirming that the donor and acceptor fluorophores accurately report on the formation of this regulatory KL interaction.

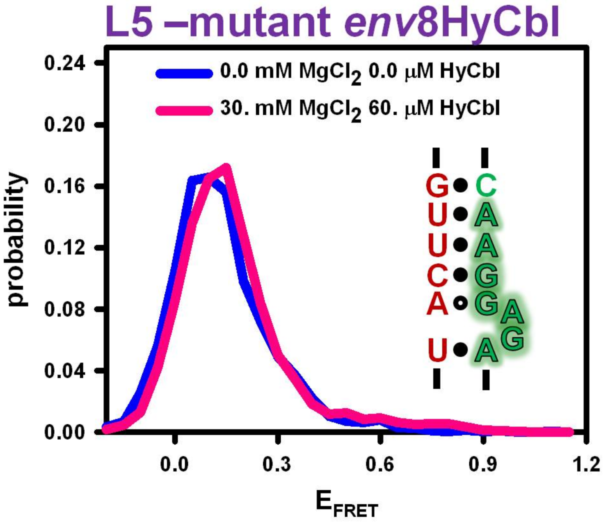

Supplemental Figure S8.1. Results of freely diffusing experiments conducted on the L5-mutant *env8*HyCbl construct. The L5-mutation (inset, underlined nucleotides) inhibits formation of the KL interaction, which prevents occlusion of the ribosome binding site (inset, shadowed nucleotides).

8.2.2 KL docking equilibrium in the presence of ligand

Analogous freely diffusing smFRET experiments have been conducted in the *presence* of ligand in order to interrogate the equilibrium behavior of this interaction in solutions where the HyCbl concentration is ≈ 50 times larger than a previously reported(18) binding affinity of 19(4) nM. Without any Mg^{2+} in solution, fluorescent molecules reside entirely in a single low E_{FRET} = 0.12(3) population (Figure 8.3b) that is experimentally indistinguishable from the low E_{FRET} = 0.15(3) population observed in the *absence* of ligand (Figure 8.3a). As was the case before, Mg^{2+} is still required for the formation of the KL interactions, even under saturating concentrations of HyCbl. Specifically, addition of $MgCl_2$ into solutions containing 1000 nM HyCbl increases the probability of observing a second, higher E_{FRET} = 0.54(4) population (Figure 8.3b) that is also experimentally indistinguishable from the high E_{FRET} = 0.58(3) population noted previously in the *absence* of ligand (Figure 8.3a).

Under these saturating HyCbl conditions, presumably every functional riboswitch is bound to a ligand. Therefore, the above observations support the existence of L5-L13 KL equilibrium associated with the docked (D_{HyCbl}) and undocked (U_{HyCbl}) conformations of the RNA, where the "*HyCbl*" subscript denotes the presence of a bound ligand (Figure 8.2b). Notably, the *presence* of a bound ligand reduces $[Mg^{2+}]_{½}$ by nearly an order of magnitude (Figure 8.3c), which indicates that under physiological free salt conditions (i.e., 1 mM Mg^{2+}, 125 mM K^+, 10 mM Na^+) these ligand bound riboswitches reside predominantly in the docked conformation ($FD_{HyCbl} \approx 0.75$). In conjunction with the results of previous experiments performed in the *absence* of ligand, it is immediately obvious that HyCbl binding increases the stability of the docked conformation in solutions containing Mg^{2+}(e.g., at 1 mM Mg^{2+} $FD_{free} \approx 0.22 < FD_{HyCbl} \approx 0.75$). Moreover, the increased occupancy of the docked conformation, where the L5-L13 KL is form, clearly demonstrates that ligand binding directly modulates the availability of the ribosome binding site nucleotides in L13 of this regulatory switch.

8.2.3 Ligand binding properties

To directly explore the ligand-binding process, we exploit a unique photophysical property of hydroxocobalamin (HyCbl). Specifically, the absorbance spectra of vitamin B_{12} cofactors, including HyCbl, overlap with the fluorescence spectra of yellow-green fluorescent dyes like Cy3, which allows this cofactor to effectively compete with the Cy5 for energy transfer. Because HyCbl is a non-fluorescent acceptor, energy transfer to it results in quenched fluorescence(21). We can utilize this quenching phenomenon to monitor the ligand binding kinetics of the *env8*HyCbl riboswitch via time-dependent ensemble fluorometry. When HyCbl is dissociated from the RNA, the average intermolecular distance between it (acceptor) and Cy3 (donor) is large enough to neglect the effects of this quenching energy transfer process (Figure

8.4a). However, upon ligand binding, the intermolecular distance between the two is reduced to ≈ 23 Å, allowing for predominant energy transfer from the excited donor molecule (Cy3) to the non-fluorescent acceptor (HyCbl).

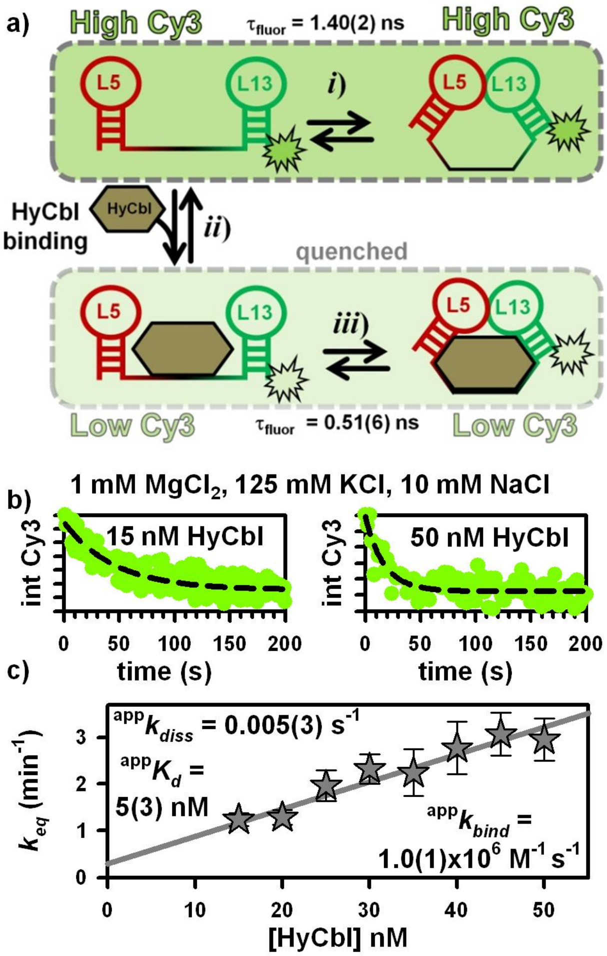

Figure 8.4 Time-dependent ensemble fluorometry. **a)** HyCbl binding quenches the fluorescence of Cy3 (see also Supplementary Figure S8.2). **b)** Elevated concentrations of ligand increases the rate constant for establishing equilibrium. **c)** A linear-fit to the [HyCbl]-dependence of this rate constant is used to measure the apparent ligand binding (${}^{\text{app}}k_{bind}$) and dissociation (${}^{\text{app}}k_{diss}$) rate constants.

Thus, energy transfer to HyCbl results in an additional non-radiative (k_{nrad}) component of the Cy3 fluorescence lifetime ($\tau_{\text{fluor}} = 1/\ (k_{rad} + k_{nrad})$), which leads to a decreased quantum yield (Q.Y. = k_{rad} / ($k_{rad} + k_{nrad}$)). As an attempt to quantify this ligand-dependent quenching, we have measured the fluorescence decay profiles of individual Cy3-only *env8*HyCbl RNAs in the *presence* and *absence* of 1000 nM HyCbl (Supplemental Figure S8.2) using the time-correlated single-photon counting capabilities associated with the experimental apparatus (see Experimental Methods).

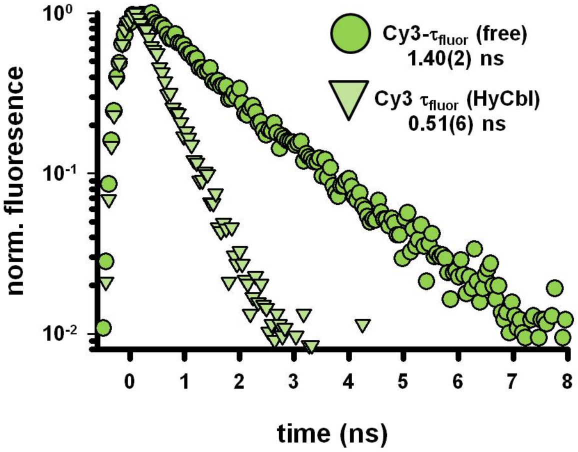

Supplemental Figure S8.2 The fluorescence lifetime (τ_{fluor}) of Cy 3 as determined from surface-immobilized riboswitches bound to (light green triangles) or free of (dark green circles) hydroxocobalamin (HyCbl).

These lifetime measurements (i.e., Cy3-τ_{fluor}(*free*) = 1.40(2) ns and Cy3-τ_{fluor}(*HyCbl*) = 0.51(6) ns) effectively demonstrate the non-radiative quenching phenomenon associated with energy transfer from Cy3 to HyCbl. It is important to stress that the presence of *bound* ligand introduced a non-radiative decay process from the excited state that competes *equally* with *both* radiative emission from the excited donor (i.e., Cy3 fluorescence) and energy transfer from the excited donor to the acceptor (Cy5 fluorescence). Provided that there is sufficient signal-to-noise, this will not alter the observed E_{FRET} values associated with the docked and undocked populations, as is demonstrated above (Section 8.2.2).

Time-dependent ensemble fluorescence experiments are used to monitor the HyCbl-induced reduction in fluorescence intensity of RNA constructs labeled with Cy3 after addition of excess ligand ([HyCbl]/[RNA] > 10). The temporal decay of fluorescence intensity (Figure 8.4b) maps out the rate constant responsible for establishing a binding equilibrium (k_{eq}). For a standard bimolecular process, this rate constant (k_{eq}) can simply be described as a function of ligand concentration using the ligand-binding (k_{bind}) and dissociation (k_{diss}) rate constants (Eq. 8.2).

$$k_{eq} = k_{diss} + [ligand]k_{bind} \tag{Eq. 8.2}$$

However, in the present system, the rate constants only represent apparent parameters because the ligand binding equilibrium is directly coupled to the two KL docking equilibria (Figure 8.2). These two docking equilibria determine the fraction of undocked molecules that can either bind to (FU_{free}) or dissociate from HyCbl (FU_{HyCbl}). The ligand dependence of $^{app}k_{eq}$ is evident in Figure 8.4c and well described by a straight line. The slope of such a linear fit reveals that $^{app}k_{bind}$ = 1.0(1)×10^{6} M^{-1} s^{-1}, where as the intercept shows that $^{app}k_{diss}$ = 0.005(3) s^{-1}. The ratio of these two values describes the apparent HyCbl dissociation equilibrium constant ($^{app}K_d$ = 5(3) nM). These apparent kinetic parameters can be decoupled from the two KL docking equilibria by making a well-justified assumption, which is experimentally validated later in surface-immobilized kinetic studies of the KL docking equilibria (Section 8.2.5 and 8.2.6). Provided the docking kinetics associated with the KL equilibria are much faster than the kinetics of the ligand binding process, the apparent rate constants equal the true k_{bind} and k_{diss} values scaled by the fractional populations of the binding competent (FU_{free}) and dissociation competent (FU_{HyCbl}) species, respectively (see Eq. 8.3a,b).

$$k_{bind}(FU_{free}) = {}^{app}k_{bind} \tag{Eq. 8.3a}$$

$$k_{diss}(FU_{HyCbl}) = {}^{app}k_{diss} \tag{Eq. 8.3b}$$

The values of $FU_{free} \approx 0.78$ and $FU_{HyCbl} \approx 0.25$ are obtained from the freely diffusing data depicted in Figure 8.3c at1 mM MgCl$_2$. These values are used to calculate the true rate and equilibrium constants—denoted by a lack of the superscript “app”—that describe ligand binding by the *env8*HyCbl riboswitch at 1 mM $MgCl_2$ ($k_{bind} = 1.3(2)\times10^6$ M^{-1} s^{-1}, $k_{diss} = 0.02(1)$ s^{-1}, and $K_{d,} = 15(8)$ nM).

8.2.4 CBL-dependence of the KL docking equilibrium

The data sets described in the three previous sections (8.2.1-8.2.3) quantitatively characterize all of the equilibrium constants required to predict the steady-state fractional occupancy of the docked conformation as a function of [HyCbl] at any given [$MgCl_2$]. These predictions are valid only if the true HyCbl dissociation constant (K_d) is not directly influenced by $MgCl_2$. As an aside, many nucleic acid-ligand interactions are known to be highly sensitive to Mg^{2+}; however, the ligand binding process for the *env8*HyCbl riboswitch only seems to be indirectly influenced by Mg^{2+} via the two KL docking equilibria, as described in the following section.

To experimentally test the steady-state model predictions, single-molecule freely diffusing FRET methods are used to determine the fractional occupancy of the docked conformation (*FD*) as HyCbl is titrated into solutions at five different fixed $MgCl_2$ concentrations (0.0, 0.5, 1.0, 2.5, 20. mM). In solutions lacking Mg^{2+}, the addition of ligand is *unable* to promote formation of the docked conformation (Figure 8.5a), as Mg^{2+} is required for the formation of the regulatory KL interaction between L5 and L13. At intermediate concentrations of $MgCl_2$ (e.g., 0.5, 1.0, and 2.5 mM), titration of HyCbl into solution *does* facilitate formation of the docked conformation (Figure 8.5b). This observation is certainly consistent with the four-state model (Figure 8.2), wherein *bound* HyCbl, increases the stability of the regulatory KL interaction (i.e., $FD_{free} < FD_{HyCbl}$). Titration of HyCbl into solutions with saturating concentrations of Mg^{2+} (e.g., 20 mM >> $[Mg^{2+}]_{½}$) reveals that ligand is unable to significantly increase the *FD* (Figure 8.5c), which nicely demonstrates that Mg^{2+} alone is sufficient to promote complete formation of the regulatory interaction responsible for sequestering the ribosome binding site.

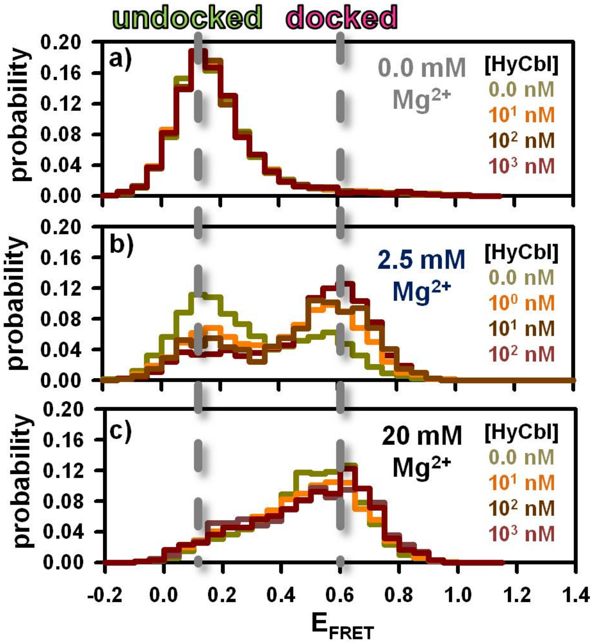

Figure 8.5 Freely diffusing single-molecule burst titrations of hydroxocobalamin (HyCbl) at various concentrations of $MgCl_2$. **a)** At 0 mM Mg^{2+}, addition of ligand *does not* significantly influence distribution of FRET values associated with the L5-L13 regulatory switch. **b)** At intermediate concentrations of Mg^{2+}(e.g., 0.5, 1.0, and 2.5 mM), addition of HyCbl *does* significantly alter the FRET distributions. **c)** 20 mM Mg^{2+} is sufficient to completely form the L5-L13 KL interaction, irrespective of [HyCbl].

Figure 8.6 compares the results of the single-molecule experiments with the model predictions (colored circles and dashed lines, respectively). This comparison demonstrates the remarkable quantitative accuracy of the four state kinetic model (Figure 8.2) used to describe the conformational transitions associated with this biologically functional riboswitch. Most importantly, this astonishing predictive power is a testament to the validity of the kinetic model, including the Mg^{2+} independence of true ligand binding process (K_d).

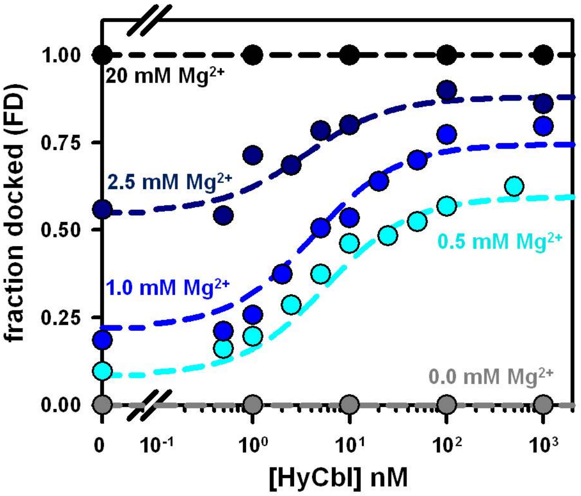

Figure 8.6. Experimental validation of the four-state kinetic model for the *env8*HyCbl riboswitch. The experimentally determined fractional occupancy of the docked conformation (FD, colored circles) is well described by the steady-state solution (dotted line) to the four-state model (Figure 8.2) over a wide range of Mg^{2+} and HyCbl concentrations.

8.2.5 KL docking kinetics in the absence of ligand

To exploit the capabilities of our single-molecule microscopy apparatus for probing kinetics, fluorescence trajectories of individual surface-immobilized molecules have been recorded to observe the KL docking dynamics in real time (Figure 8.7a-c). In the *absence* of HyCbl (Figure 8.7a), single RNAs display strongly anti-correlated fluctuations in donor and acceptor fluorescence, resulting from rapid transitions between the two well-separated FRET states. These FRET values are in excellent agreement with those measured in the freely diffusing experiments, which supports the conclusion that these time trajectories depict single-molecules transitioning between the docked (D_{free}) and undocked (U_{free}) conformations associated with the L5-L13 KL interaction. Kinetic analysis of the surface-immobilized data yields hundreds of individual dwell times that are compiled together and fit to single-exponential decays in order to yield the rate constants associated with docking and undocking. These rate constants reveal that, in ligand free solutions at 1 mM Mg^{2+}, $k_{dock,free} = 1.2(3)\ s^{-1}$ and is slower than $k_{undock,free} = 6(2) s^{-1}$, resulting in $FD_{free} = 0.17(7)$. A titration with respect to Mg^{2+}, analogous to the ones from the freely diffusing smFRET experiments, reveals that increasing divalent cation concentration accelerates the docking and slows the undocking rate constants, respectively.

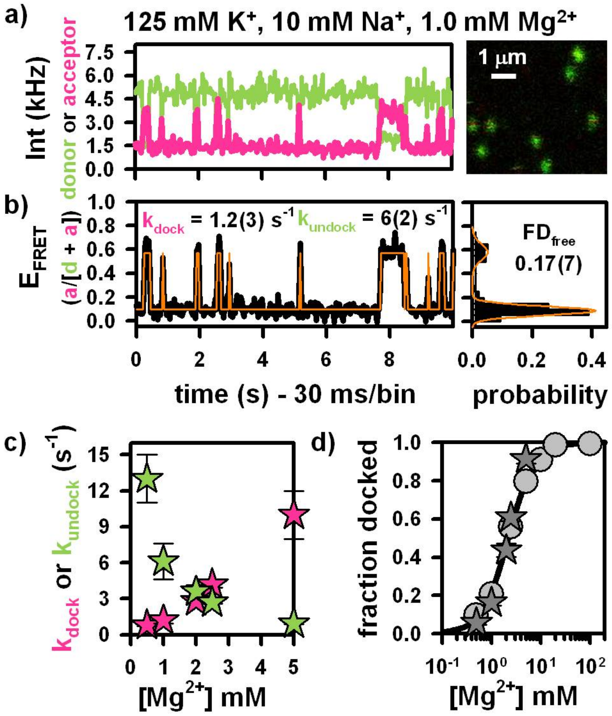

Figure 8.7. Kissing-loop docking kinetics in the absence of bound ligand. Representative **a)** fluorescence and **b)** FRET time-trace from a surface immobilized *env8*HyCbl riboswitch. **c)** Rate constants are determined using both a dwell time analysis and a 2-state Bayesian maximum-likelihood model (orange line). **d)** Kinetic parameters are used to calculate the fractional occupancy of the docked conformation in the absence of HyCbl (FD_{free}), which reveals that the surface immobilized results are in accordance with the freely diffusing experiments.

Both of which contribute nearly equally to Mg^{2+}-dependent formation of the regulatory KL (Figure 8.7c). As alluded to above, the fact that individual surface-immobilized molecules dock completely ($FD_{free} \approx 1.0$) at high [$MgCl_2$] confirms that the residual probability (≈ 15%) for observing the low E_{FRET} population results from inactive molecules that cannot form the L5-L13 interaction. It is important to emphasize that the results for both freely diffusing and surface immobilized studies are in complete agreement as indicated by the circles and stars in Figure

8.7d, respectively. Such a plot convincingly demonstrates that surface immobilization does not influence the biophysical behavior of this RNA.

8.2.6 KL docking kinetics in the presence of ligand

To complete the single-molecule kinetic characterization of this riboswitch, fluorescence time-trajectories of individual surface-immobilized molecules are recorded in the solutions containing 2.5 nM HyCbl and 1 mM Mg^{2+} (Figure 8.8). These results further support the proposed kinetic model (Figure 8.2) for ligand-facilitated formation of the regulatory switch. Specifically, the time-trajectories in the presence of HyCbl display distinct regions with vastly different fluorescence intensities. Some regions exhibit normal fluorescence signals for both the donor and the acceptor fluorophores, which are well resolved and anti-correlated (Figure 8.8b). In the other, intervening regions, the total fluorescence signal is significantly quenched (Figure 8.8c). The rate constants associated with the anti-correlated fluorescence fluctuations in the normal regions mimic those from molecules studied in the absence of hydroxocobalamin (Figure 8.8b vs. 8.7b), as would be expected when the ligand is not bound to the RNA. Conversely, the quenched regions result from ligand binding events that localize HyCbl near Cy3, which introduces additional nonradiative relaxation pathways. Despite the substantially reduced signal in these regions, subtle fluctuations in acceptor intensity that exceed background noise are clearly observable and can be attributed to docking and undocking of the KL interaction during the long ligand-bound episodes. As an attempt to quantitatively measure the docked and undocked dwell times in the ligand-bound state, a Bayesian maximum-likelihood model(25) is used to analyze the two-state fluctuations evident in the quenched regions of the fluorescence trajectories (Figure 8.8c). The results of such an analysis reveal that, when the ligand is bound to the *env8*HyCbl riboswitch in solution containing 1 mM $MgCl_2$, the docking rate only decreases two fold ($k_{dock,HyCbl}$ = 0.64(9) vs. $k_{dock,free}$ = 1.2(3) s^{-1}), but that the undocking rate is much more sensitive and decreases significantly by a ≈ 23-fold ($k_{undock,HyCbl}$ = 0.26(8) vs. $k_{undock,free}$ = 6(2)s^{-1}).

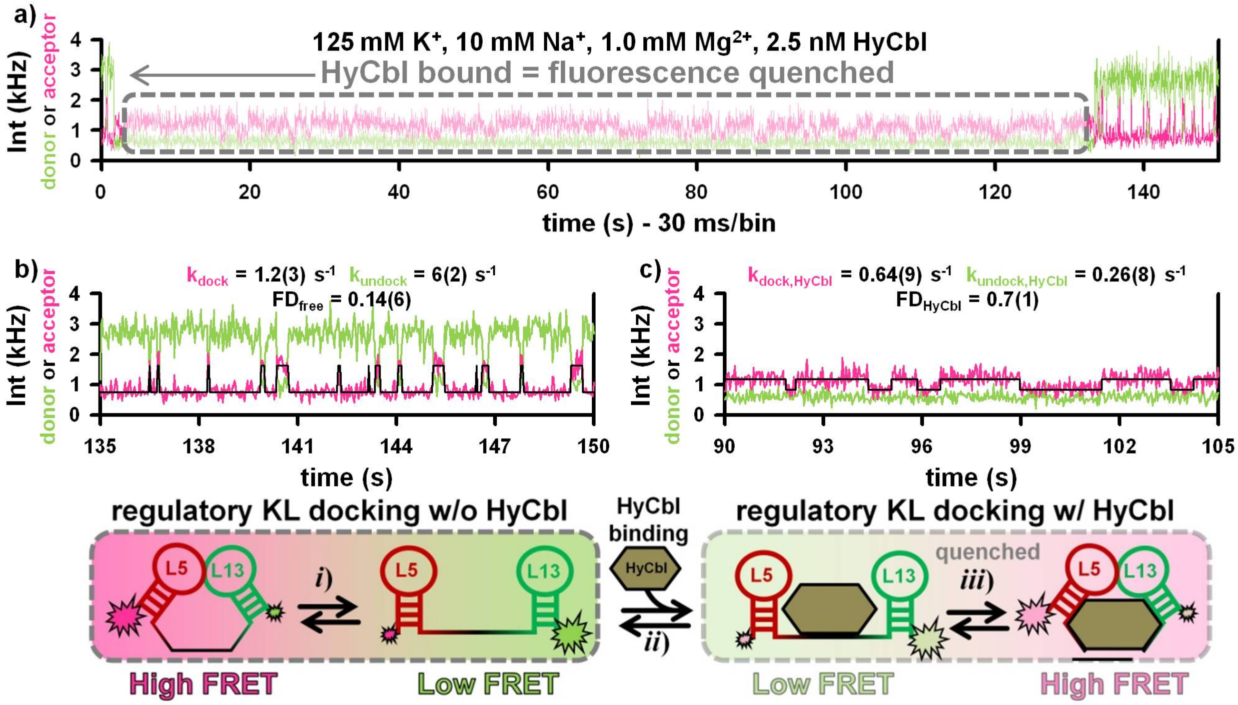

Figure 8.8 Surface immobilized KL docking kinetics in the presence of hydroxocobalamin (HyCbl). **a)** Representative fluorescence trajectory from a surface immobilized molecule in the presence of 2.5 nM HyCbl. While in the undocked conformation, ligand binding (arrow) significantly diminishes the fluorescence intensity, which returns to normal after dissociation. **b)** When the ligand is not bound, the docking kinetics of the regulatory KL are experimentally indistinguishable from those in the absence of any HyCbl (Figure 8.7b). **c)** When the ligand is bound, a maximum-likelihood 2-state model (black line) is used to quantify the dwell times associated with the subtle fluctuations in acceptor fluorescence resulting from KL docking and undocking. A comparison between the two KL docking equilibria reveals that HyCbl binding significantly decreases the undocking rate constant (k_{undock}).

The HyCbl-induced change to the KL undocking kinetics give rise to substantially more favorable formation of the L5-L13 regulatory switch (FD_{free} = 0.17(7) vs. FD_{HyCbl} = 0.7(1)), as also observed in the original freely diffusing experiments (FD_{free} ≈ 0.22 vs. FD_{HyCbl} ≈ 0.75).

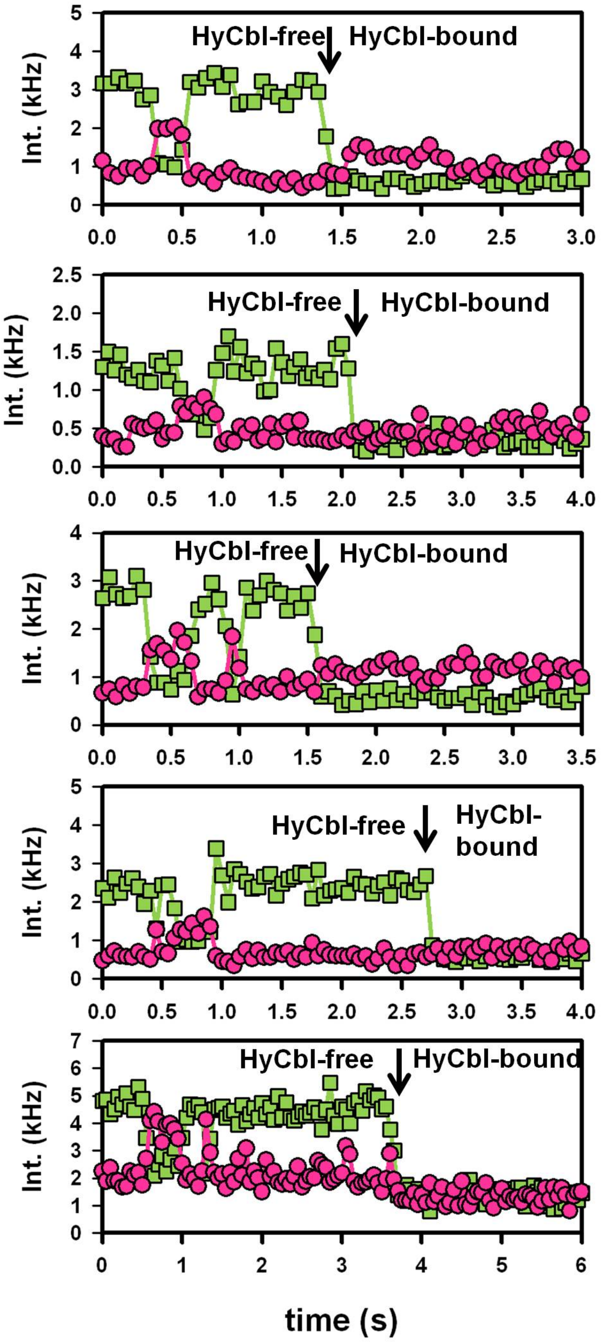

Supplemental Figure S8.3. Representative surface immobilized trajectories revealing the HyCbl-induced decrease in fluorescence intensity of both Cy3 (green squares) and Cy5 (pink circles). Inspection of trajectories reveals that HyCbl binding events (black arrows) can only occur when the RNA is in the *undocked* (low E_{FRET}) conformation. This is consistent with the assumptions of our 4-state kinetic model, whereby formation of the L5-L13 KL interactions prevents HyCbl binding/dissociation events. Only trajectories that exhibit clean fluctuations in acceptor fluorescence after a decrease in total fluorescence are considered for analysis. This constraint excludes molecules that have undergone other photophysical processes resulting in a decrease in fluorescence (e.g., blinking or bleaching).

Further inspection of the fluorescence trajectories reveals that: (*i*) HyCbl can only bind and quench fluorescence when the RNA is in the undocked (low E_{FRET}) conformation (Supplemental Figure S8.3) and (*ii*) ligand-bound dwell times can be longer than a hundred seconds (Figure 8.8a). These bound-state lifetimes are consistent with those predicted from the ensemble time-dependent fluorescence experiments (Figure 8.4c), which yields ${}^{app}\tau_{HyCbl} = (1/{}^{app}k_{off}) = 200(120)$ s. Lastly, the time-traces of surface immobilized molecules clearly verify the previous assumption that the KL kinetics, both in the presence and absence of ligand, are much faster than those associated with establishing a ligand binding equilibrium. In total, the collection of results from the above fluorescence biophysical studies provides unambiguous support for the proposed four-state kinetic model (Figure 8.2) associated with the regulatory conformational transition of the *env8*HyCbl riboswitch.

8.2.7 Relevance of kissing loop formation with respect to regulation of gene expression

To relate the biophysical behavior of this functional riboswitch with its biological function, cell-based gene expression experiments (Figure 8.9) have been performed in an *E.coli* strain lacking cobalamin adenosyl transferase (Δ*btuR)*, thereby preventing the subsequent conversion of hydroxocobalamin to adenosylcobalamin. In these experiments, cells were transformed with vectors containing either the wild type or mutant riboswitches located upstream of a GFPuv reporter gene—termed WT *env8*HyCbl+GFPuv or L5-mutant *env8*HyCbl+GFPuv, respectively—and cultured in liquid media with or without 5000 nM HyCbl. The L5-mutant *env8*HyCbl+GFPuv vector contains a riboswitch with the exact same dinucleotide substitution used in the smFRET experiments (Supplemental Figure S8.1) and is predicted to be incapable of regulating gene expression. In growth media lacking HyCbl, cells transformed with WT *env8*HyCbl+GFPuv have normalized fluorescence values (see Experimental Methods) lower than cells transformed with the L5-mutant *env8*HyCbl+GFPuv plasmid (grey bars, Figure 8.9b). This nicely correlates with the biophysical observation that the WT *env8*HyCbl smFRET construct is mostly undocked ($FU_{free} \approx 0.78$) at 1 mM Mg^{2+}, whereas the L5-mutant is completely undocked ($FU_{free} \approx 1.0$). Additionally, when cultured in media containing 5000 nM HyCbl, only cells harboring WT *env8*HyCbl+GFPuv show a substantial ligand-dependent reduction in GFPuv expression (bronze bars, Figure 8.9b), which is well correlated with the $FU_{HyCbl} = 0.3(1)$ observed in the smFRET experiments.

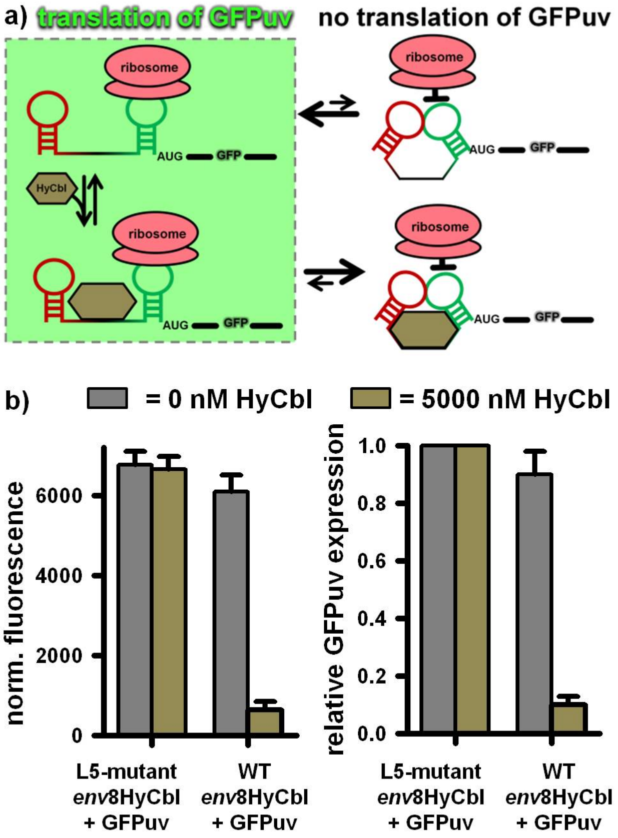

Figure 8.9 Cell-based regulation of gene expression via the *env8*HyCbl riboswitch. **a)** Schematic diagram relating the four-state kinetic model to the regulation of gene expression *in vivo*. **b)** Histograms comparing the normalized fluorescence and relative GFPuv expression of cell cultures grown in the presence (bronze bars) or absence (grey bars) of 5000 nM HyCbl.

The high degree of correlation between the *in vitro* and *in vivo* experiments strongly suggests that: (*i*) the fractional occupancy of the *undocked* conformation dictates the maximum level of gene expression, regardless of whether or not ligand is bound and (*ii*) formation of the *docked* conformation, resulting from a long-range KL interaction between L5 and L13, sequesters the ribosome binding site within L13 and prevents initiation of translation.

8.3 Discussion

Ligand-induced conformational transitions are central to the function of riboswitches. A significant body of structural work has revealed the numerous ways in which riboswitches can specifically interact with their cognate ligands. However, much less is known about how molecular recognition in the receptor domains translates into the regulatory domain's ability to alter gene expression. The results of these single-molecule experiments mechanistically link: (*i*) conformational transitions facilitated by ligand binding to (*ii*) regulation of gene expression in a fully functional riboswitch containing both of these domains. Specifically, the fluorescently labeled RNA constructs examined in this work provide information about the equilibrium and kinetic behavior of a regulatory kissing loop (KL) interaction. Furthermore, the novel use of hydroxocobalamin-induced fluorescence quenching as an orthogonal experimental observable offers additional insights into the ligand binding process. Together, these results highlight several key findings about the functional mechanism of gene expression for the *env*8HyCbl riboswitch. The following is a discussion of these observations and their relevance to other areas of RNA biology.

8.3.1 Kissing Loop docking dynamics

Both the freely diffusing and surface immobilized experiments clearly identify the L5-L13 KL interaction as the structural motif that directly regulates biological function (i.e., gene expression). Additionally, this motif is also responsible for organizing the RNA's global conformation. Many other functional nucleic acids make use of similar types of tertiary interactions to accomplish these same tasks. For example, KL are important for organizing the three dimensional (3D) structure of self-cleaving ribozymes(26,27) and regulate control a variety of biological processes(28), such as dimerization of retroviral genomes(22) and plasmid replication(29,30). One characteristic of both intra- and inter-molecular KL interactions is the formation of canonical Watson-Crick base pairs between the two interacting loops. In addition to 5 complementary base pairs, the L5-L13 interaction contains a G-A mismatch adjacent to a dinucleotide (AG) bulge. Presumably, these structural defects serve to destabilize this interaction. As a result, the KL will only be stably formed in the presence of HyCbl, thereby conferring a ligand-dependent occlusion of the ribosome binding site. This clearly demonstrates how nucleotide sequence can be used to tune the stability of a RNA kissing-loop. Other examples exist where localization of Mg^{2+} modulates the stability of these types of interactions, as is the case with intermolecular HIV (human immunodeficiency virus) genome dimerization (22). In the *env*8HyCbl riboswitch, divalent cations are essential for KL formation and likely play a similar role. Indeed, the x-ray crystal structure of this RNA depicts substantial electron density associated with Ba^{2+}(the more strongly x-ray scattering mimetic of Mg^{2+}) near the interacting loops(18). While divalent cations and nucleotide sequence represent two effective ways to adjust the stability of RNA KLs, there is also another ways to accomplish such a task.

8.3.2 KL docking in the *presence* of a macromolecular stabilizing agent

In addition to distinctly identifying the existence of a KL docking equilibrium in the absence of ligand, the above experimental results reveal that KL docking and undocking also occurs when HyCbl is bound. Specifically, the presence of a *bound* ligand alters the energetics of this process to substantially favor the docked conformation. This is yet another example of how KL stability can be tuned for a particular biological function. Careful inspection of the HyCbl-bound crystal structure reveals that most of the intermolecular contacts are van der Waals interactions governed by shape complementarity(18). These interactions significantly stabilize the docked conformation, as evidenced by the ≈ 23-fold slower undocking rate constant when the ligand is bound to the RNA. This is an excellent demonstration of how a specific macromolecular cosolute can stabilize the formation of a KL interaction directly responsible for a specific biological function.

As a matter of fact, a similar mechanism is employed in the *Rop*-RNA I-RNA II plasmid replication system(30). Specifically, the *Rop* protein acts as a molecular scaffold that stabilizes the intermolecular KL interaction between the loops of RNA I and RNA II (31) and regulates formation of RNA primers required for DNA plasmid replication. In this system, the presence of *Rop* substantially reduces the rate at which RNA I dissociates from the ternary complex(32). Interestingly, the six acetamide functional groups in the corrin ring of HyCbl chemically recapitulate the amino acid side chains of glutamine and asparagine. One can speculate that the protein-like chemical functionality of HyCbl allows this cofactor to imitate the stabilizing properties of *Rop*. Moreover, *Rop* presents eight of these amino acid residues to the interface between the protein and the kissing loops of RNA I and II*(30,33)*. Certainly, the resounding functional similarity between these two biological systems demonstrates how the formation of a KL interaction can be facilitated by a macromolecular binding partner (e.g., protein or ligand) in order to regulate a biologically relevant process (e.g., plasmid replication or gene expression).

8.3.3 Ligand Recognition

A long-standing question in nucleic acid recognition of small molecule ligands is whether: (*i*) an induced-fit or (*ii*) a conformational-capture model most appropriately describes these aptamer-substrate interactions. The induced-fit model demands that ligand binding occurs in open (e.g., undocked) conformations of the aptamer, which then induces a structural transition that encapsulates the bound molecule(10). This is in contrast to the conformational-capture model, whereby ligand recognition occurs in transient, highly organized folded structures, similarly resulting in stabilization of the bound (e.g., docked) conformation(16). For the *env*8HyCbl riboswitch, the experimental validation of the four-state model (Figure 8.6) and the surface-immobilized time-traces in the presence of HyCbl (Figure 8.8a, Supplemental Figure S8.3) strongly suggest that ligand binding (i.e., quenching) occurs only in the undocked conformation. This notion is further supported by existing structural data(18), which reveals that the *env8*HyCbl riboswitch conceals a majority (≈ 60%) of the solvent accessible surface area of the ligand when the KL interaction is formed. Therefore, the approximately spherical HyCbl ligand would not be able to enter, or exit, the binding pocket when the L5-L13 interaction is formed. Additionally, isothermal titration calorimetry experiments demonstrate that riboswitches lacking L13 can still effectively bind HyCbl, implying that ligand binding does readily occur when the RNA is in the undocked conformation (18). Together, these observations support an induced-fit ligand-recognition model for this riboswitch, which bolsters the notion that this behavior is commonly associated with many small-molecule binding RNAs(34-36).

Additionally, the ligand binding kinetics experiments reveal that the bimolecular ${}^{app}k_{bind}$ is fast ($\geq 10^6$ $M^{-1}s^{-1}$), relative to many other RNA-ligand interactions(37). However, the relatively slow (≤ 0.01 s^{-1}) ${}^{app}k_{diss}$ mandates that, at HyCbl concentrations near ${}^{app}K_d$, the time-scale associated with ligand binding (i.e., $[^{app}k_{on} \times {}^{app}K_d]^{-1} \approx 200$ s) is much longer than that required to establish the two KL docking equilibria (i.e., $[k_{dock,free} + k_{undock,free}]^{-1} \approx 1$ s and $[k_{dock,HyCbl} + k_{undock,HyCbl}]^{-1} \approx 0.1$ s). Therefore, when the HyCbl concentration is less than ≈ 1 μM (i.e., where there time-scale associated with these processes are similar, $[^{app}k_{bind} \times 1\ \mu\text{M}]^{-1} \approx [k_{dock,free} + k_{undock,free}]^{-1}$), this uniquely identifies ligand binding as the rate limiting biophysical process in the four-state kinetic model (Figure 8.2). This conclusion raises a significant question with regard to genetic regulation: does the riboswitch-containing mRNA have enough time, after being transcribed, to bind the ligand before being degraded in the cell? It is certainly worth noting that, at HyCbl concentrations near $^{app}K_d$, the time-scale associated with ligand binding (i.e.,$[^{app}k_{on} \times {}^{app}K_d]^{-1} \approx 200$ s) is comparable to that of mRNA decay (≈ 300 s)(38). This would seem to suggest that gene expression is somewhat temporally restricted. However, more rigorous and quantitative studies of mRNA translation and decay will be required to conclusively determine the kinetic vs. thermodynamic nature of genetic regulation for the *env8*HyCbl riboswitch(37).

8.3.4 Mechanism of regulation for the *env*8 hydroxocobalamin riboswitch

The following quantitative comparison of the *in vitro* and *in vivo* results provides a substantial amount of information linking the physical mechanism of the *env*8HyCbl riboswitch to the biologically relevant ligand-dependent modulation of gene expression. The L5-mutant *env8*HyCbl+GFPuv transformed cells are shown to be insensitive to HyCbl (Figure 8.9b) and are used to define the maximum amount of gene expression resulting from completely undocked RNAs. The normalized fluorescence (See Experimental Methods) associated with maximal gene expression is used to calculate the relative gene expression associated with the WT *env8*HyCbl riboswitch in the *presence* or *absence* of 5000 nM ligand. This quantitation of the cell-based experiments reveals that, in the *absence* of HyCbl, the *env8*HyCbl riboswitch encoded upstream of a GFPuv fluorescence reporter results in a relative gene expression value of 0.90(8). This *in vivo* value is nearly experimentally indistinguishable from the 1 mM Mg^{2+} *in vitro* values of FU_{free} = 0.83(7) and $FU_{free} \approx 0.78$ for surface-immobilized and freely diffusing smFRET experiments, respectively. Such quantitative agreement indicates that the amount of gene expressions is highly correlated with the FU_{free}. Furthermore, the WT *env8*HyCbl results in a relative gene expression value of 0.10(3) in the *presence* of 5000 nM HyCbl. Again, this *in vivo* value is similar to the 1 mM Mg^{2+} *in vitro* values of FU_{HyCbl} = 0.3(1) and $FU_{HyCbl} \approx 0.25$ determined via surface-immobilized and freely diffusing smFRET experiments, respectively. Together, the *in vitro* and *in vivo* experiments unambiguously demonstrate that the fractional occupancy of the undocked conformation at 1mM Mg^{2+} is highly correlated with the relative amount of GFPuv expression and that the L5-L13 KL interactions is the physical switch associated with this regulatory element.

8.4 Conclusions

This work represents the first quantitative single-molecule investigations of a fully functional riboswitch, complete with complementary cell-based assays. The results of these experiments clearly identify the conformational mechanism responsible for regulation of gene expression by the *env*8HyCbl riboswitch. Specifically, ligand binding occurs when the L5-L13 kissing loop is absent and alters the energetics associated with this regulatory interaction, resulting in preferential stabilization of the docked state. In this docked conformation, the ribosome binding site (RBS) within L13 makes canonical Watson-Crick base pairing interactions with L5. These base pairs conceal this region of the mRNA from the cellular machinery responsible for translation initiation, thus repressing expression of the downstream gene. Time-resolved ligand-binding experiments indicate that although this process is fast relative to other riboswitches, it is still much slower than the time-scale for equilibration of KL docking. The high degree of correlation between cell-based GFPuv reporter assays and biophysical fluorescence experiments further supports the notion that formation of the KL interaction is directly responsible for repression of gene expression and identifies this region of the RNA as the physical regulatory switch. This KL interaction shares a number of biochemical features with other functional nucleic acids. Together these similarities highlight the importance of nucleotide sequence, divalent cations, and macromolecular binding partners in tuning the stability of this structural motif. One interesting direction would be to more rigorously explore the importance of the structural defects within the KL and their ability to confer ligand-facilitated docking. Lastly, and perhaps most importantly, this works presents a thorough and robust characterization of a ligand-facilitated conformational transition that serves as a point-of-comparison for other such studies of similar RNAs.

8.5 Experimental Methods

8.5.1 Fluorescent Construct Design

All of the *env*8 riboswitch constructs used this in work are based on a sequence originally identified from comparative metagenomic analyses of functional non-coding RNAs(19). The various constructs designed for single-molecule fluorescence resonance energy transfer (smFRET) experiments are prepared via non-splinted ligation(39) of two custom synthetically modified RNA oligonucleotides (Integrated DNA Technologies). The wild-type *env*8 smFRET construct is assembled from the following two RNAs: WT strand 1; (5′-biotin-AAA AAA AAG GCC UAA AAG CGU AGU GGG AAA G[dT*]G ACG UGA AAU UCG UCC AGA UUA C-3′) and WT strand 2; (5′-phosphate-UUG AUA CGG UUA UAC UCC GAA UGC CAC CUA

GGC CAU ACA ACG AGC AAG GAG ACU C-Cy3-3′). According to the x-ray crystal structure of *env*8, nucleotide U24 is completely solvent exposed and lacks intramolecular contacts with other functional groups of the RNA(18). By way of additional confirmation, SHAPE chemical probing experiments reveal this nucleotide to be hyper-reactive, as is often the case with highly solvent exposed nucleotides. In conjunction with the x-ray crystal structure, this conclusion suggests that this position is well suited for synthetic modification, which will negligibly impact the conformational dynamics. To this end, nucleotide U24 is replaced by an amino-modified nucleotide (dT*), which is subsequently chemically labeled with an NHS-functionalized Cy5 fluorophore (GE healthcare) following the manufacturer's suggested protocol. Microcentrifuge size-exclusion columns (ThermoScientific) are used to remove the excess unreacted fluorophores from the labeling reaction. The WT strands 1 and 2 are annealed together by slowly cooling from 85 °C to room temperature in buffer (50 mM HEPES, 800 μM hydroxocobalamin (Sigma Aldrich), 100 mM KCl, pH 7.5) prior to enzymatic ligation via T4 RNA ligase I (New England Biolabs). Isolation of full-length doubly labeled RNA construct is achieved through the use of a reverse phase high-performance liquid chromatography (HPLC) column (Agilent).

Preparation of the L5-mutant construct is carried out using the same procedures expect that L5-mutant strand 2 (5′-phosphate-$\underline{\text{AA}}$G AUA CGG UUA UAC UCC GAA UGC CAC CUA GGC CAU ACA ACG AGC AAG GAG ACU C-Cy3-3′) is used instead of WT strand 2, with the underlined nucleotides corresponding to the desired mutations. Synthesis of the Cy3-only *env*8 construct used in the ensemble fluorometry experiments is performed using *in vitro* transcription by T7 RNA polymerase, as described previously(18). The resulting transcripts are exposed to $NaIO_4$ and $NaBH_3CN$ for selective oxidation of the 3′-ribose(40) and reacted with hydrazidefunctionalized Cy3 to covalently attach the fluorophore to this position. Removal of excess dye and HPLC purification is performed, as described above, in order to isolate full-length fluorescently labeled RNA constructs.

8.5.2 Freely-Diffusing smFRET

Freely-diffusing smFRET experiments are performed on an home-build inverted confocal fluorescence microscope, described previously(17), with a 1.2 N.A. water objective (Olympus Corporation) in epifluorescence configuration to both focus the excitation light and collect the emitted fluorescence. When the concentration of fluorescently labeled RNA is sufficiently low (≈ 125 pM), individual molecules will transiently diffuse into the overlapping foci of two (532 nm,Time-Bandwidth products and 635 nm, PicoQuant GmbH) alternating laser excitation(41) (ALEX) sources with ≈ 100 μW average power. This yields a short (< 1 ms) burst of fluorescence photons dictated by the time the RNA spends within the excitation and detection volume. The FRET efficiency (E_{FRET}) resulting from 532 nm excitation is calculated for each fluorescent burst, where the use of ALEX techniques ensures that only dually labeled, non-photophysically damaged constructs are considered for analysis. All experiments are performed at ambient temperatures (20-22 °C) in standard buffer (50 mM HEPES, 25 mM KOH, 10 mM NaOH, 100 mM KCl, 2 mM TROLOX, 100 nM PCD and 5 mM PCA, pH 7.7) consisting of the well-characterized enzymatic oxygen scavenging system, PCA/PCD(42), and various concentrations of $MgCl_2$ and hydroxocobalamin (HyCbl).

8.5.3 Ensemble Fluorometry

HyCbl-dependent Cy3 quenching ensemble experiments are performed on a fluorimeter (Jobin Yvon) with ≈ 500 pM fluorescent RNA in the standard buffer containing 1mM $MgCl_2$ and 10-50 nM hydroxocobalamin. The excitation and emission filters are set to 532 ± 1 and 570 ± 7 nm, respectively, with each data point representing one second of integrated fluorescence. The narrow, off-peak excitation filter ensures that photobleaching of Cy3 represents a negligible contribution to the time-dependent reduction in the fluorescence intensity.

8.5.4 Surface-Immobilized smFRET

Surface-immobilzed smFRET experiments are performed on the same inverted confocal fluorescence microscope used for the freely-diffusing experiments. Immobilization is accomplished using biotin-streptavidin chemistry, resulting in a surface coverage of < 1 molecule per μm^2. Average laser powers are ≈ 2 µW in order to reduce the effects of photobleaching and prolong the observation of surface immobilized molecules. Fluorescence trajectories are constructed from 30 ms time bins of detected photons. Docking and undocking rate constants are determined using either a previously described thresholding routine(43) or a Bayesian maximum likelihood model(25). The two analyses result in rate constants that are experimentally indistinguishable (when applied to the same data set).

8.5.5 *in vivo* Regulation of GFP Expression

Riboswitch constructs were amplified via recombinant overlapping PCR and cloned into a pBR327 derivative between NsiI and HindIII restriction sites. For the cell-based assays, plasmids are transformed into *E.coli* Keio strain Δ*btuR* (Keio collection(44) JW1262). The cells are plated onto LB agar plates supplemented with 100 µg/mL ampicillin, and incubated at 37°C for 14-16 hours to facilitate colony formation. Three colonies are picked for each construct and grown to saturation in a rich, chemically, defined medium (CSB media: NaH2PO4 (4.6 mg/mL), K2HPO4 (11.7 mg/mL), and $(NH4)_2SO_4$ (2.0 mg/mL), D-glucose (0.6%), sodium citrate (5 mM), and $MgSO_4$ (492 µM), $FeCl_3{\cdot}6H_2O$ (109 µM), $ZnCl_2{\cdot}4H_2O$ (28.3 µM), $CoCl_2{\cdot}6H_2O$ (24.8 µM), Na_2MoO_4 (13.8 µM), $CaCl_2{\cdot}2H_2O$ (20.1 µM), $CuCl_2$ (21.9 µM), $MnCl_2$ (23.4 µM), and H_3BO_3

(23.9 μM)) supplemented with 100 μg/mL ampicillin to maintain plasmid selection. In order to measure cellular fluorescence resulting from GFPuv expression, 5 μL of saturated overnight culture has been added to 5 mL of CSB medium supplemented with 100 μg/mL ampicillin and 5 μM hydoxocobalamin, and grown to mid-log phase via incubation at 37°C in a rotating drum. For fluorescence measurements, 300 μL of cells from each biological replicate are added to the wells of a Greiner 96 well, half-area microplate. GFPuv expression is monitored at an excitation wavelength of 395 nm and a 510 nm emission wavelength using a Tecan Infinite M200 PRO plate-reader. All data shown are the average fluorescence values of three biological replicates measured in triplicate and normalized to cell density as determined by the OD_{600} for each individual well. Normalized fluorescence values for each construct are background corrected via subtraction of cell-density normalized fluorescence from a pBR327 empty vector control.

8.6 References

1. Tucker, B. J.; R. R. Breaker. Riboswitches as versatile gene control elements, *Curr. Opin. Struct. Biol.*, **2005,** *15*, 342-348.

2. Nahvi, A.; N. Sudarsan; M. S. Ebert; X. Zou; K. L. Brown; R. R. Breaker. Genetic control by a metabolite binding mRNA, *Chem. Biol.*, **2002,** *9*, 1043.

3. Nou, X.; R. J. Kadner. Adenosylcobalamin inhibits ribosome binding to btuB RNA, *Proc. Natl. Acad. Sci. USA*, **2000,** *97*, 7190-7195.

4. Banerjee, R.; S. W. Ragsdale. The many faces of vitamin B12: catalysis by cobalamin-dependent enzymes, *Annu. Rev. Biochem.*, **2003,** *72*, 209-247.

5. Nahvi, A.; J. E. Barrick; R. R. Breaker. Coenzyme B12 riboswitches are widespread genetic control elements in prokaryotes, *Nucleic Acids Res.*, **2004,** *32*, 143-150.

6. Rodionov, D. A.; A. G. Vitreschak; A. A. Mironov; M. S. Gelfand. Comparative genomics of the vitamin B12 metabolism and regulation in prokaryotes, *J. Biol. Chem.*, **2003,** *278*, 41148-41159.

7. Martens, J. H.; H. Barg; M. J. Warren; D. Jahn. Microbial production of vitamin B12, *Appl. Microbiol. Biotechnol.*, **2002,** *58*, 275-285.

8. Roth, J. R.; J. G. Lawrence; T. A. Bobik. Cobalamin (coenzyme B12): synthesis and biological significance, *Annu. Rev. Microbiol.*, **1996,** *50*, 137-181.

9. Breaker, R. R. Riboswitches and the RNA world, *Cold Spring Harb. Perspect. Biol.*, **2012,** *4*.

10. Garst, A. D.; A. L. Edwards; R. T. Batey. Riboswitches: structures and mechanisms, *Cold Spring Harb. Perspect. Biol.*, **2011,** *3*.

11. Roy, R.; S. Hohng; T. Ha. A Practical Guide to Single-Molecule FRET, *Nat. Methods*, **2008,** *5*, 507-516.

12. Lemay, J. F.; J. C. Penedo; R. Tremblay; D. M. Lilley; D. A. Lafontaine. Folding of the Adenine Riboswitch, *Chem. Biol.*, **2006,** *13*, 857-868.

13. Suddala, K. C.; A. J. Rinaldi; J. Feng; A. M. Mustoe; C. D. Eichhorn; J. A. Liberman; J. E. Wedekind; H. M. Al-Hashimi; C. L. Brooks, 3rd; N. G. Walter. Single transcriptional and translational preQ1 riboswitches adopt similar pre-folded ensembles that follow distinct folding pathways into the same ligand-bound structure, *Nucleic Acids Res.*, **2013,** *41*, 10462-10475.

14. Souliere, M. F.; R. B. Altman; V. Schwarz; A. Haller; S. C. Blanchard; R. Micura. Tuning a riboswitch response through structural extension of a pseudoknot, *Proc. Natl. Acad. Sci. USA*, **2013,** *110*, E3256-3264.

15. Haller, A.; R. B. Altman; M. F. Souliere; S. C. Blanchard; R. Micura. Folding and ligand recognition of the TPP riboswitch aptamer at single-molecule resolution, *Proc. Natl. Acad. Sci. USA*, **2013,** *110*, 4188-4193.

16. Haller, A.; U. Rieder; M. Aigner; S. C. Blanchard; R. Micura. Conformational capture of the SAM-II riboswitch, *Nat. Chem. Biol.*, **2011,** *7*, 393-400.

17. Fiegland, L. R.; A. D. Garst; R. T. Batey; D. J. Nesbitt. Single-molecule studies of the lysine riboswitch reveal effector-dependent conformational dynamics of the aptamer domain, *Biochemistry*, **2012,** *51*, 9223-9233.

18. Johnson, J. E., Jr.; F. E. Reyes; J. T. Polaski; R. T. Batey. B12 cofactors directly stabilize an mRNA regulatory switch, *Nature*, **2012,** *492*, 133-137.

19. Weinberg, Z.; J. X. Wang; J. Bogue; J. Yang; K. Corbino; R. H. Moy; R. R. Breaker. Comparative genomics reveals 104 candidate structured RNAs from bacteria, archaea, and their metagenomes, *Genome Biol.*, **2010,** *11*, R31.

20. Griffiths-Jones, S.; A. Bateman; M. Marshall; A. Khanna; S. R. Eddy. Rfam: an RNA family database, *Nucleic Acids Res.*, **2003,** *31*, 439-441.

21. Xu, H.; Y. Li; C. Liu; Q. Wu; Y. Zhao; L. Lu; H. Tang. Fluorescence resonance energy transfer between acridine orange and rhodamine 6G and its analytical application for vitamin B12 with flow-injection laser-induced fluorescence detection, *Talanta*, **2008,** *77*, 176-181.

22. Ennifar, E.; P. Walter; B. Ehresmann; C. Ehresmann; P. Dumas. Crystal structures of coaxially stacked kissing complexes of the HIV-1 RNA dimerization initiation site, *Nat. Struct. Biol.*, **2001,** *8*, 1064-1068.

23. Horiya, S.; X. Li; G. Kawai; R. Saito; A. Katoh; K. Kobayashi; K. Harada. RNA LEGO: magnesium-dependent formation of specific RNA assemblies through kissing interactions, *Chem. Biol.*, **2003,** *10*, 645-654.

24. Tyrrell, J.; J. L. McGinnis; K. M. Weeks; G. J. Pielak. The cellular environment stabilizes adenine riboswitch RNA structure, *Biochemistry*, **2013,** *52*, 8777-8785.

25. Bronson, J. E.; J. Fei; J. M. Hofman; R. L. Gonzalez, Jr.; C. H. Wiggins. Learning rates and states from biophysical time series: a Bayesian approach to model selection and single-molecule FRET data, *Biophys. J.*, **2009,** *97*, 3196-3205.

26. Andersen, A. A.; R. A. Collins. Intramolecular secondary structure rearrangement by the kissing interaction of the Neurospora VS ribozyme, *Proc. Natl. Acad. Sci. USA*, **2001,** *98*, 7730-7735.

27. Toor, N.; K. S. Keating; O. Fedorova; K. Rajashankar; J. Wang; A. M. Pyle. Tertiary architecture of the Oceanobacillus iheyensis group II intron, *RNA*, **2010,** *16*, 57-69.

28. Brunel, C.; R. Marquet; P. Romby; C. Ehresmann. RNA loop-loop interactions as dynamic functional motifs, *Biochimie*, **2002,** *84*, 925-944.

29. Wagner, E. G.; S. Brantl. Kissing and RNA stability in antisense control of plasmid replication, *Trends Biochem. Sci.*, **1998,** *23*, 451-454.

30. Eguchi, Y.; J. Tomizawa. Complex formed by complementary RNA stem-loops and its stabilization by a protein: function of CoIE1 Rom protein, *Cell*, **1990,** *60*, 199-209.

31. Helmer-Citterich, M.; M. M. Anceschi; D. W. Banner; G. Cesareni. Control of ColE1 replication: low affinity specific binding of Rop (Rom) to RNAI and RNAII, *Embo. J.*, **1988,** *7*, 557-566.

32. Di Primo, C. Real time analysis of the RNAI-RNAII-Rop complex by surface plasmon resonance: from a decaying surface to a standard kinetic analysis, *J. Mol. Recognit.*, **2008,** *21*, 37-45.

33. Banner, D. W.; M. Kokkinidis; D. Tsernoglou. Structure of the ColE1 rop protein at 1.7 A resolution, *J. Mol. Biol.*, **1987,** *196*, 657-675.

34. Williamson, J. R. Induced fit in RNA-protein recognition, *Nat. Struct. Biol.*, **2000,** *7*, 834-837.

35. Noeske, J.; J. Buck; B. Furtig; H. R. Nasiri; H. Schwalbe; J. Wohnert. Interplay of 'induced fit' and preorganization in the ligand induced folding of the aptamer domain of the guanine binding riboswitch, *Nucleic Acids Res.*, **2007,** *35*, 572-583.

36. Serganov, A.; Y. R. Yuan; O. Pikovskaya; A. Polonskaia; L. Malinina; A. T. Phan; C. Hobartner; R. Micura; R. R. Breaker; D. J. Patel. Structural basis for discriminative regulation of gene expression by adenine- and guanine-sensing mRNAs, *Chem. Biol.*, **2004,** *11*, 1729-1741.

37. Zhang, J.; M. W. Lau; A. R. Ferre-D'Amare. Ribozymes and riboswitches: modulation of RNA function by small molecules, *Biochemistry*, **2010,** *49*, 9123-9131.

38. Bernstein, J. A.; A. B. Khodursky; P. H. Lin; S. Lin-Chao; S. N. Cohen. Global analysis of mRNA decay and abundance in Escherichia coli at single-gene resolution using two-color fluorescent DNA microarrays, *Proc. Natl. Acad. Sci USA*, **2002,** *99*, 9697-9702.

39. Moore, M. J., Query, C.C. Uses of Site-Specifically Modified RNAs Constructed by RNA Ligation, In *RNA:Protein Interactions: A Practical Approach* (Smith, C. W. J., Ed.), pp 75-140, Oxford University Press Inc., New York.1998

40. Proudnikov, D.; A. Mirzabekov. Chemical methods of DNA and RNA fluorescent labeling, *Nucleic Acids Res.*, **1996,** *24*, 4535-4542.

41. Kapanidis, A. N.; T. A. Laurence; N. K. Lee; E. Margeat; X. Kong; S. Weiss. Alternating-laser excitation of single molecules, *Acc. Chem. Res.*, **2005,** *38*, 523-533.

42. Aitken, C. E.; R. A. Marshall; J. D. Puglisi. An Oxygen Scavenging System for Improvement of Dye Stability in Single-Molecule Fluorescence Experiments, *Biophys. J.*, **2008,** *94*, 1826-1835.

43. Hodak, J. H.; C. D. Downey; J. L. Fiore; A. Pardi; D. J. Nesbitt. Docking kinetics and equilibrium of a GAAA tetraloop-receptor motif probed by single-molecule FRET, *Proc. Natl. Acad. Sci. USA*, **2005,** *102*, 10505–10510.

44. Baba, T.; T. Ara; M. Hasegawa; Y. Takai; Y. Okumura; M. Baba; K. A. Datsenko; M. Tomita; B. L. Wanner; H. Mori. Construction of Escherichia coli K-12 in-frame, single-gene knockout mutants: the Keio collection, *Mol. Syst. Biol.*, **2006,** *2*, 2006 0008.

Bibliography

Chapter 1:
Introduction

1. Dahm, R. Discovering DNA: Friedrich Miescher and the early years of nucleic acid research, *Hum. Genet.*, **2008,** *122*, 565-581.

2. Voet, D.; J. G. Voet (2011) *Biochemistry*, 4th ed., John Wiley & Sons, Hoboken, NJ.

3. Crick, F. Central dogma of molecular biology, *Nature*, **1970,** *227*, 561-563.

4. Silverman, S. K. (2006) *Nucleic acid switches and sensors*, Landes Bioscience/Eurekah.com and Springer Science+Business Media, Georgetown, TX and New York, NY.

5. Watson, J. D.; F. H. Crick. Molecular structure of nucleic acids: a structure for deoxyribose nucleic acid, *Nature*, **1953,** *171*, 737-738.

6. Carvalho, J. C. Derivation of the mass of the observable universe, *Int. J. Theor. Phys.*, **1995,** *34*, 2507-2509.

7. Holmstrom, E. D.; N. F. Dupuis; D. J. Nesbitt. Pulsed IR heating studies of single-molecule DNA duplex dissociation kinetics and thermodynamics, *Biophys. J.*, **2014,** *106*, 220-231.

8. Dupuis, N. F.; E. D. Holmstrom; D. J. Nesbitt. Single-Molecule Kinetics Reveal Cation-Promoted DNA Duplex Formation Through Ordering of Single-Stranded Helices, *Biophys. J.*, **2013,** *105*, 756-766.

9. Hodak, J. H.; C. D. Downey; J. L. Fiore; A. Pardi; D. J. Nesbitt. Docking kinetics and equilibrium of a GAAA tetraloop-receptor motif probed by single-molecule FRET, *Proc. Natl. Acad. Sci. USA*, **2005,** *102*, 10505–10510.

10. Holmstrom, E. D.; D. J. Nesbitt. Single Molecule FRET Studies of the Human Telomerase RNA Pseudoknot: Temperature/Urea Dependent Folding Kinetics and Thermodynamics, *J. Phys. Chem. B.*, **2014**.

11. Fiore, J. L.; E. D. Holmstrom; L. R. Fiegland; J. H. Hodak; D. J. Nesbitt. The Role of Counterion Valence and Size in GAAA Tetraloop-Receptor Docking/Undocking Kinetics, *J. Mol. Biol.*, **2012**.

12. Draper, D. E.; D. Grilley; A. M. Soto. Ions and RNA folding, *Annu. Rev. Biophys. Biomolec. Struct.*, **2005,** *34*, 221–243.

13. Leipply, D.; D. Lambert; D. E. Draper. Ion-RNA interactions: Thermodynamic analysis of the effects of mono- and divalent ions on RNA conformational equilibria, *Methods Enzymol.*, **2009,** *469*, 433-463.

14. Holmstrom, E. D.; J. L. Fiore; D. J. Nesbitt. Thermodynamic origins of monovalent facilitated RNA folding, *Biochemistry*, **2012,** *51*, 3732-3743.

15. Shelton, V. M.; T. R. Sosnick; T. Pan. Applicability of Urea in the Thermodynamic Analysis of Secondary and Tertiary RNA Folding, *Biochemistry*, **1999,** *38*, 16831-16839.

16. Lambert, D.; D. E. Draper. Effects of Osmolytes on RNA Secondary and Tertiary Structure Stabilities and RNA-Mg^{2+} Interactions, *J. Mol. Biol.*, **2007,** *370*, 993-1005.

17. Lambert, D.; D. E. Draper. Denaturation of RNA secondary and tertiary structure by urea: simple unfolded state models and free energy parameters account for measured m-values, *Biochemistry*, **2012,** *51*, 9014-9026.

18. Priyakumar, U. D.; C. Hyeon; D. Thirumalai; A. D. MacKerell. Urea Destabilizes RNA by Forming Stacking Interactions and Multiple Hydrogen Bonds with Nucleic Acid Bases, *J. Am. Chem. Soc.*, **2009,** *131*, 17759-17761.

19. Lambert, D.; D. Leipply; D. E. Draper. The osmolyte TMAO stabilizes native RNA tertiary structures in the absence of Mg^{2+}: Evidence for a large barrier to folding from phosphate dehydration, *J. Mol. Biol.*, **2010,** *404*, 138-157.

20. Breaker, R. R. Riboswitches and the RNA world, *Cold Spring Harb. Perspect. Biol.*, **2012,** *4*.

21. Garst, A. D.; A. L. Edwards; R. T. Batey. Riboswitches: structures and mechanisms, *Cold Spring Harb. Perspect. Biol.*, **2011,** *3*.

22. Kador, L.; D. E. Horne; W. E. Moerner. Optical-Detection and Probing of Single Dopant Molecules of Pentacene in a P-Terphenyl Host Crystal by Means of Absorption-Spectroscopy, *J. Phys. Chem.*, **1990,** *94*, 1237-1248.

23. Moerner, W. E.; L. Kador. Optical-Detection and Spectroscopy of Single Molecules in a Solid, *Phys. Rev. Lett.*, **1989,** *62*, 2535-2538.

24. Orrit, M.; J. Bernard. Single pentacene molecules detected by fluorescence excitation in a p-terphenyl crystal, *Phys. Rev. Lett.*, **1990,** *65*, 2716-2719.

25. Joo, C.; H. Balci; Y. Ishitsuka; C. Buranachai; T. Ha. Advances in single-molecule fluorescence methods for molecular biology, *Annu. Rev. Biochem.*, **2008,** *77*, 51-76.

26. Roy, R.; S. Hohng; T. Ha. A Practical Guide to Single-Molecule FRET, *Nat. Methods*, **2008,** *5*, 507-516.

27. Zhao, R.; D. Rueda. RNA folding dynamics by single-molecule fluorescence resonance energy transfer, *Methods*, **2009,** *49*, 112-117.

28. Förster, T. Zwischenmolekulare Energiewanderung und Fluoreszenz, **1948,** *437*, 55-75.

29. Einstein, A. Strahlungs-Emission und -Absorption nach der Quantentheorie, *Deutch. Phys. Ges.*, **1916,** *18*, 318-323.

30. Schuler, B.; E. A. Lipman; P. J. Steinbach; M. Kumke; W. A. Eaton. Polyproline and the "spectroscopic ruler" revisited with single-molecule fluorescence, *Proc. Natl. Acad. Sci. USA*, **2005,** *102*, 2754-2759.

31. Akiyama, B. M.; M. D. Stone. Assembly of Complex RNAs by Splinted Ligation, *Methods Enzymol.*, **2009,** *469*, 27-46.

32. Fiore, J. L.; E. D. Holmstrom; D. J. Nesbitt. Entropic Origin of Mg^{2+}-Facilitated RNA Folding, *Proc. Natl. Acad. Sci. USA*, **2012,** *109*, 2902-2907.

33. Fiore, J. L.; B. Kraemer; F. Koberling; R. Erdmann; D. J. Nesbitt. Enthalpy-Driven RNA Folding: Single-Molecule Thermodynamics of Tetraloop–Receptor Tertiary Interaction, *Biochemistry*, **2009,** *48*, 2550–2558.

34. Holmstrom, E. D.; D. J. Nesbitt. Real-time infrared overtone laser control of temperature in picoliter H_2O samples: "Nanobathtubs" for single-molecule microscopy, *J. Phys. Chem. Lett.*, **2010,** *1*, 2264–2268.

Chapter 2:
Experimental Methods

1. Einstein, A. Strahlungs-Emission und -Absorption nach der Quantentheorie, *Deutch. Phys. Ges.*, **1916,** *18*, 318-323.

2. van der Meer, B. W.; D. M. van der Meer; S. S. Vogel. Optimizing the Orientation Factor Kappa-Squared for More Accurate FRET Measurements, In *FRET – Förster Resonance Energy Transfer*, pp 63-104, Wiley-VCH Verlag GmbH & Co. KGaA.2013

3. Fiore, J. L. (2012) Single-Molecule Kinetic and Thermodynamic Studies of Cation-Facilitated RNA Folding: Isolated Tertiary Interactions, In *Chemical Physics*, University of Colorado, Boulder.

4. Baker, T. A. (2012) Confocal Microscopy Studies of Fluorescence Blinking of Semiconductor Quantum Dots, Metal Nanoparticle Photogeneration, and Multiphoton Photoemission from Thin Metal Films and Metal Nanoparticles, In *Chemistry*, University of Colorado, Boulder.

5. Kapanidis, A. N.; T. A. Laurence; N. K. Lee; E. Margeat; X. Kong; S. Weiss. Alternating-laser excitation of single molecules, *Acc. Chem. Res.*, **2005,** *38*, 523-533.

6. Kapanidis, A. N.; N. K. Lee; T. A. Laurence; S. Doose; E. Margeat; S. Weiss. Fluorescence-aided molecule sorting: Analysis of structure and interactions by alternating-laser excitation of single molecules, *Proc. Natl. Acad. Sci. USA*, **2004,** *101*, 8936-8941.

7. Lee, N. K.; A. N. Kapanidis; H. R. Koh; Y. Korlann; S. O. Ho; Y. Kim; N. Gassman; S. K. Kim; S. Weiss. Three-color alternating-laser excitation of single molecules: Monitoring multiple interactions and distances, *Biophys. J.*, **2007,** *92*, 303–312.

8. Lee, N. K.; A. N. Kapanidis; Y. Wang; X. Michalet; J. Mukhopadhyay; R. H. Ebright; S. Weiss. Accurate FRET Measurements within Single Diffusing Biomolecules using Alternating-Laser Excitation, *Biophys. J.*, **2005,** *88*, 2939-2953.

9. Forconi, M.; D. Herschlag. Metal ion-based RNA cleavage as a structural probe, *Methods Enzymol.*, **2009,** *468*, 91-106.

10. Lonnberg, T.; M. Luomala. Intracomplex general acid/base catalyzed cleavage of RNA phosphodiester bonds: the leaving group effect, *Org. Biomol. Chem.*, **2012,** *10*, 6785-6791.

11. Rasnik, I.; S. A. McKinney; T. Ha. Nonblinking and long-lasting single-molecule fluorescence imaging, *Nat. Methods*, **2006,** *3*, 891-893.

12. Aitken, C. E.; R. A. Marshall; J. D. Puglisi. An Oxygen Scavenging System for Improvement of Dye Stability in Single-Molecule Fluorescence Experiments, *Biophys. J.*, **2008,** *94*, 1826-1835.

13. Ruttinger, S.; V. Buschmann; B. Kramer; R. Erdmann; R. Macdonald; F. Koberling. Comparison and accuracy of methods to determine the confocal volume for quantitative fluorescence correlation spectroscopy, *J. Microsc. Oxford*, **2008,** *232*, 343-352.

14. Joo, C.; H. Balci; Y. Ishitsuka; C. Buranachai; T. Ha. Advances in single-molecule fluorescence methods for molecular biology, *Annu. Rev. Biochem.*, **2008,** *77*, 51-76.

15. Torella, J. P.; S. J. Holden; Y. Santoso; J. Hohlbein; A. N. Kapanidis. Identifying molecular dynamics in single-molecule FRET experiments with burst variance analysis, *Biophys. J.*, **2011,** *100*, 1568-1577.

16. Fiore, J. L.; J. H. Hodak; O. Piestert; C. D. Downey; D. J. Nesbitt. Monovalent and Divalent Promoted GAAA-Tetraloop–Receptor Tertiary Interactions from Freely Diffusing Single-Molecule Studies, *Biophys. J.*, **2008,** *95*, 3892-3905.

Chapter 3:

Real-Time IR Overtone Laser Control of Temperature in Picoliter H_2O Samples: “Nano-Bathtubs” for Single Molecule Microscopy”

1. Li, S.; K. Zhang; J. M. Yang; L. W. Lin; H. Yang. Single quantum dots as local temperature markers, *Nano Lett*, **2007,** *7*, 3102–3105.

2. Valerini, D.; A. Creti; M. Lomascolo; L. Manna; R. Cingolani; M. Anni. Temperature dependence of the photoluminescence properties of colloidal CdSe/ZnS core/shell quantum dots embedded in a polystyrene matrix, *Phys. Rev. B*, **2005,** *71*, 235409.

3. Bartley, L. E.; X. W. Zhuang; R. Das; S. Chu; D. Herschlag. Exploration of the Transition State for Tertiary Structure Formation Between an RNA Helix and a Large Structured RNA, *J. Mol. Biol.*, **2003,** *328*, 1011–1026.

4. Hohng, S.; T. J. Wilson; E. Tan; R. M. Clegg; D. M. J. Lilley; T. J. Ha. Conformational flexibility of four-way junctions in RNA, *J. Mol. Biol.*, **2004,** *336*, 69–79.

5. Kato, H.; T. Nishizaka; T. Iga; K. Kinosita, Jr.; S. Ishiwata. Imaging of thermal activation of actomyosin motors, *Proc. Natl. Acad. Sci. USA*, **1999,** *96*, 9602–9606.

6. de Mello, A. J.; M. Habgood; N. L. Lancaster; T. Welton; R. C. R. Wootton. Precise temperature control in microfluidic devices using Joule heating of ionic liquids, *Lab on a Chip*, **2004,** *4*, 417-419.

7. Hu, G. Q.; Q. Xiang; R. Fu; B. Xu; R. Venditti; D. Q. Li. Electrokinetically controlled real-time polymerase chain reaction in microchannel using Joule heating effect, *Anal. Chim. Acta*, **2006,** *557*, 146–151.

8. Zhao, Q. L.; Q. A. Huang; Y. C. Lin. Design and numerical analysis of a joule-heating-induced continuous-flow polymerase chain reaction microchip, *J. Micro-Nanolithogr. MEMs and MOEMs*, **2009,** *8*, 021101.

9. Braun, D.; A. Libchaber. Trapping of DNA by thermophoretic depletion and convection, *Phys. Rev. Lett.*, **2002,** *89*, 188103.

10. Ebbinghaus, S.; A. Dhar; D. McDonald; M. Gruebele. Protein folding stability and dynamics imaged in a living cell, *Nat. Methods*, **2010,** *7*, 319-323.

11. Schoen, I.; H. Krammer; D. Braun. Hybridization kinetics is different inside cells, *Proc. Natl. Acad. Sci. USA.*, **2009,** *106*, 21649-21654.

12. Zhao, R.; E. Alemán; D. Rueda. Laser Assisted Single-molecule Refolding, *Biophys. J.*, **2009,** *96*, Biophys. Soc. proceedings 9a.

13. Slyadnev, M. N.; Y. Tanaka; M. Tokeshi; T. Kitamori. Photothermal temperature control of a chemical reaction on a microchip using an infrared diode laser, *Anal. Chem.*, **2001,** *73*, 4037–4044.

14. Mao, H. B.; J. R. Arias-Gonzalez; S. B. Smith; I. Tinoco; C. Bustamante. Temperature control methods in a laser tweezers system, *Biophys. J.*, **2005,** *89*, 1308–1316.

15. Peterman, E. J. G.; F. Gittes; C. F. Schmidt. Laser-induced heating in optical traps, *Biophys. J.*, **2003,** *84*, 1308–1316.

16. Fiore, J. L.; B. Kraemer; F. Koberling; R. Erdmann; D. J. Nesbitt. Enthalpy-Driven RNA Folding: Single-Molecule Thermodynamics of Tetraloop–Receptor Tertiary Interaction, *Biochemistry*, **2009,** *48*, 2550–2558.

17. Wieliczka, D. M.; S. S. Weng; M. R. Querry. Wedge shaped cell for highly absorbent liquids: Infrared optical constants of water, *Appl. Opt.*, **1989,** *28*, 1714–1719.

18. Karstens, T.; K. Kobs. Rhodamine B and rhodamine 101 as reference substances for fluorescence quantum yield measurements, *J. Phys. Chem.*, **1980,** *84*, 1871–1872.

19. Muller, C. B.; K. Weiss; A. Loman; J. Enderlein; W. Richtering. Remote temperature measurements in femto-liter volumes using dual-focus-Fluorescence Correlation Spectroscopy, *Lab on a Chip*, **2009,** *9*, 1248-1253.

20. Robinson, T.; Y. Schaerli; R. Wootton; F. Hollfelder; C. Dunsby; G. Baldwin; M. Neil; P. French; A. Demello. Removal of background signals from fluorescence thermometry measurements in PDMS microchannels using fluorescence lifetime imaging, *Lab on a Chip*, **2009,** *9*, 3437–3441.

21. Ross, D.; M. Gaitan; L. E. Locascio. Temperature measurement in microfluidic systems using a temperature-dependent fluorescent dye, *Anal. Chem.*, **2001,** *73*, 4117–4123.

22. Arbeloa, F. L.; T. L. Arbeloa; M. J. T. Estevez; I. L. Arbeloa. Photophysics of Rhodamines - Molecular-Structure and Solvent Effects, *J. Phys. Chem.*, **1991,** *95*, 2203–2208.

23. Casey, K. G.; E. L. Quitevis. Effect of solvent polarity on nonradiative processes in xanthene dyes: Rhodamine B in normal alcohols, *J. Phys. Chem.*, **1988,** *92*, 6590.

24. Downey, C. D.; J. L. Fiore; C. D. Stoddard; J. H. Hodak; D. J. Nesbitt; A. Pardi. Metal ion dependence, thermodynamics, and kinetics for intramolecular docking of a GAAA tetraloop and receptor connected by a flexible linker, *Biochemistry*, **2006,** *45*, 3664–3673.

Chapter 4:
Pulsed Infrared-Heating Studies of Single Molecule DNA Duplex Dissociation Kinetics and Thermodynamics

1. Joo, C.; H. Balci; Y. Ishitsuka; C. Buranachai; T. Ha. Advances in single-molecule fluorescence methods for molecular biology, *Annu. Rev. Biochem.*, **2008,** *77*, 51-76.

2. Roy, R.; S. Hohng; T. Ha. A Practical Guide to Single-Molecule FRET, *Nat. Methods*, **2008,** *5*, 507-516.

3. Zhao, R.; D. Rueda. RNA folding dynamics by single-molecule fluorescence resonance energy transfer, *Methods*, **2009,** *49*, 112-117.

4. Holmstrom, E. D.; J. L. Fiore; D. J. Nesbitt. Thermodynamic origins of monovalent facilitated RNA folding, *Biochemistry*, **2012,** *51*, 3732-3743.

5. Tarsa, P. B.; R. R. Brau; M. Barch; J. M. Ferrer; Y. Freyzon; P. Matsudaira; M. J. Lang. Detecting force-induced molecular transitions with fluorescence resonant energy transfer, *Angew. Chem. Int. Ed.*, **2007,** *46*, 1999-2001.

6. Shroff, H.; B. M. Reinhard; M. Siu; H. Agarwal; A. Spakowitz; J. Liphardt. Biocompatible force sensor with optical readout and dimensions of 6 nm(3), *Nano Lett.*, **2005,** *5*, 1509-1514.

7. Fiore, J. L.; B. Kraemer; F. Koberling; R. Erdmann; D. J. Nesbitt. Enthalpy-Driven RNA Folding: Single-Molecule Thermodynamics of Tetraloop–Receptor Tertiary Interaction, *Biochemistry*, **2009,** *48*, 2550–2558.

8. Graneli, A.; C. C. Yeykal; R. B. Robertson; E. C. Greene. Long-distance lateral diffusion of human Rad51 on double-stranded DNA, *Proc. Natl. Acad. Sci. USA*, **2006,** *103*, 1221-1226.

9. Fiore, J. L.; E. D. Holmstrom; D. J. Nesbitt. Entropic Origin of Mg^{2+}-Facilitated RNA Folding, *Proc. Natl. Acad. Sci. USA*, **2012,** *109*, 2902-2907.

10. Zhao, R.; M. Marshall; E. A. Aleman; R. Lamichhane; A. Feig; D. Rueda. Laser-assisted single-molecule refolding (LASR), *Biophys. J.*, **2010,** *99*, 1925-1931.

11. Gross, P.; G. Farge; E. J. G. Peterman; G. J. L. Wuite. Combining optical tweezers, single-molecule fluorescence microscopy, and microfluidics for studies of DNA-protein interactions, *Method Enzymol.*, **2010,** *475*, 427-453.

12. Holmstrom, E. D.; D. J. Nesbitt. Real-time infrared overtone laser control of temperature in picoliter H_2O samples: "Nanobathtubs" for single-molecule microscopy, *J. Phys. Chem. Lett.*, **2010,** *1*, 2264–2268.

13. Braun, D.; A. Libchaber. Trapping of DNA by thermophoretic depletion and convection, *Phys. Rev. Lett.*, **2002,** *89*, 188103.

14. Slyadnev, M. N.; Y. Tanaka; M. Tokeshi; T. Kitamori. Photothermal temperature control of a chemical reaction on a microchip using an infrared diode laser, *Anal. Chem.*, **2001,** *73*, 4037–4044.

15. Mao, H. B.; J. R. Arias-Gonzalez; S. B. Smith; I. Tinoco; C. Bustamante. Temperature control methods in a laser tweezers system, *Biophys. J.*, **2005,** *89*, 1308–1316.

16. Peterman, E. J. G.; F. Gittes; C. F. Schmidt. Laser-induced heating in optical traps, *Biophys. J.*, **2003,** *84*, 1308–1316.

17. Zondervan, R.; F. Kulzer; H. van der Meer; J. A. Disselhorst; M. Orrit. Laser-driven microsecond temperature cycles analyzed by fluorescence polarization microscopy, *Biophys. J.*, **2006,** *90*, 2958-2969.

18. Yuan, H.; T. Xia; B. Schuler; M. Orrit. Temperature-cycle single-molecule FRET microscopy on polyprolines, *Phys. Chem. Chem. Phys.*, **2011,** *13*, 1762-1769.

19. Wieliczka, D. M.; S. S. Weng; M. R. Querry. Wedge shaped cell for highly absorbent liquids: Infrared optical constants of water, *Appl. Opt.*, **1989,** *28*, 1714–1719.

20. Hung, M. S.; O. Kurosawa; M. Washizu. Single DNA molecule denaturation using laser-induced heating, *Mol. Cell. Probes*, **2012,** *26*, 107-112.

21. Holmberg, A.; A. Blomstergren; O. Nord; M. Lukacs; J. Lundeberg; M. Uhlen. The biotin-streptavidin interaction can be reversibly broken using water at elevated temperatures, *Electrophoresis*, **2005,** *26*, 501-510.

22. Sanborn, M. E.; B. K. Connolly; K. Gurunathan; M. Levitus. Fluorescence properties and photophysics of the sulfoindocyanine Cy3 linked covalently to DNA, *J. Phys. Chem. B.*, **2007,** *111*, 11064-11074.

23. Marras, S. A. Selection of fluorophore and quencher pairs for fluorescent nucleic acid hybridization probes, *Methods Mol. Biol.*, **2006,** *335*, 3-16.

24. Hyre, D. E.; I. Le Trong; E. A. Merritt; J. F. Eccleston; N. M. Green; R. E. Stenkamp; P. S. Stayton. Cooperative hydrogen bond interactions in the streptavidin-biotin system, *Protein Sci.*, **2006,** *15*, 459-467.

25. Selvin, P. R.; T. Ha, (Eds.) (2008) *Single-molecule Techniques: A Laboratory Manual*, Cold Spring Harbor Laboratory Press, Cold Spring Harbor, NY.

26. Lamichhane, R.; A. Solem; W. Black; D. Rueda. Single-molecule FRET of protein-nucleic acid and protein-protein complexes: Surface passivation and immobilization, *Methods*, **2010,** *52*, 192-200.

27. Akabayov, B.; A. Henn; G. Nautrup-Pedersen; M. Elbaum; I. Sagi. (2002) Immobilization of RNA: application to single molecule spectroscopy, In *Molecular, Cellular and Tissue Engineering, 2002. Proc. IEEE-EMBS Special Topic Conference*, pp 71-72.

28. Janissen, R.; L. Oberbarnscheidt; F. Oesterhelt. Optimized straight forward procedure for covalent surface immobilization of different biomolecules for single molecule applications, *Colloid. Surface B.*, **2009,** *71*, 200-207.

29. Aleman, E. A.; H. S. Pedini; D. Rueda. Covalent-bond-based immobilization approaches for single-molecule fluorescence, *ChemBioChem*, **2009,** *10*, 2862-2866.

30. Schwartz, J. J.; S. Stavrakis; S. R. Quake. Colloidal lenses allow high-temperature single-molecule imaging and improve fluorophore photostability, *Nat. Nanotechnol.*, **2010,** *5*, 127-132.

31. Altman, R. B.; D. S. Terry; Z. Zhou; Q. Zheng; P. Geggier; R. A. Kolster; Y. Zhao; J. A. Javitch; J. D. Warren; S. C. Blanchard. Cyanine fluorophore derivatives with enhanced photostability, *Nat. Methods*, **2012,** *9*, 68-71.

32. Chen, Y. Y.; A. W. Wood. Application of a temperature-dependent fluorescent dye (Rhodamine B) to the measurement of radiofrequency radiation-induced temperature changes in biological samples, *Bioelectromagnetics*, **2009,** *30*, 583-590.

33. Karstens, T.; K. Kobs. Rhodamine B and rhodamine 101 as reference substances for fluorescence quantum yield measurements, *J. Phys. Chem.*, **1980,** *84*, 1871–1872.

34. Casey, K. G.; E. L. Quitevis. Effect of solvent polarity on nonradiative processes in xanthene dyes: Rhodamine B in normal alcohols, *J. Phys. Chem.*, **1988,** *92*, 6590.

35. Maus, M.; M. Cotlet; J. Hofkens; T. Gensch; F. C. De Schryver; J. Schaffer; C. A. M. Seidel. An experimental comparison of the maximum likelihood estimation and nonlinear least squares fluorescence lifetime analysis of single molecules, *Anal. Chem.*, **2001,** *73*, 2078-2086.

36. Nesbitt, D. J.; N. F. Dupuis; E. D. Holstrom. Single Molecule Studies of Streptavidin-Biotin Dissociation at Elevated Temperatures, *Biophys. J.*, **2012,** *102*, 270a.

37. Lucius, A. L.; N. K. Maluf; C. J. Fischer; T. M. Lohman. General methods for analysis of sequential "n-step" kinetic mechanisms: application to single turnover kinetics of helicase-catalyzed DNA unwinding, *Biophys. J.*, **2003,** *85*, 2224-2239.

38. Park, J.; S. Myong; A. Niedziela-Majka; K. S. Lee; J. Yu; T. M. Lohman; T. Ha. PCRA helicase dismantles RecA filaments by reeling in DNA in uniform steps, *Cell*, **2010,** *142*, 544-555.

39. Ragunathan, K.; C. Joo; T. Ha. Real-time observation of strand exchange reaction with high spatiotemporal resolution, *Structure*, **2011,** *19*, 1064-1073.

40. Watson, J. D.; F. H. C. Crick. Molecular structure of nucleic acids - a structure for deoxyribose nucleic acid, *Nature*, **1953,** *171*, 737-738.

41. Porschke, D.; O. C. Uhlenbeck; F. H. Martin. Thermodynamics and kinetics of helix-coil transition of oligomers containing GC base pairs, *Biopolymers*, **1973,** *12*, 1313-1335.

42. Dewey, T. G.; D. H. Turner. Laser temperature jump study of solvent effects on poly(adenylic acid) stacking, *Biochemistry*, **1980,** *19*, 1681-1685.

43. Freier, S. M.; K. O. Hill; T. G. Dewey; L. A. Marky; K. J. Breslauer; D. H. Turner. Solvent Effects on the Kinetics and Thermodynamics of Stacking in Poly(Cytidylic Acid), *Biochemistry*, **1981,** *20*, 1419-1426.

44. Dewey, T. G.; D. H. Turner. Laser temperature-jump study of stacking in adenylic acid polymers, *Biochemistry*, **1979,** *18*, 5757-5762.

45. Ikuta, S.; K. Takagi; R. B. Wallace; K. Itakura. Dissociation kinetics of 19 base paired oligonucleotide-DNA duplexes containing different single mismatched base pairs, *Nucleic Acids Res.*, **1987,** *15*, 797-811.

46. Sauer-Budge, A. F.; J. A. Nyamwanda; D. K. Lubensky; D. Branton. Unzipping kinetics of double-stranded DNA in a nanopore, *Phys. Rev. Lett.*, **2003,** *90*, 238101.

47. Liphardt, J.; B. Onoa; S. B. Smith; I. Tinoco, Jr.; C. Bustamante. Reversible unfolding of single RNA molecules by mechanical force, *Science*, **2001,** *292*, 733-737.

48. Biancaniello, P. L.; A. J. Kim; J. C. Crocker. Long-time stretched exponential kinetics in single DNA duplex dissociation, *Biophys. J.*, **2008,** *94*, 891-896.

49. Gunnarsson, A.; P. Jonsson; V. P. Zhdanov; F. Hook. Kinetic and thermodynamic characterization of single-mismatch discrimination using single-molecule imaging, *Nucleic Acids Res.*, **2009,** *37*, e99.

50. Tawa, K.; W. Knoll. Mismatching base-pair dependence of the kinetics of DNA-DNA hybridization studied by surface plasmon fluorescence spectroscopy, *Nucleic Acids Res.*, **2004,** *32*, 2372-2377.

51. Sinden, R. R. (1994) *DNA Structure and Function*, Academic Press, San Diego, CA.

52. Yakovchuk, P.; E. Protozanova; M. D. Frank-Kamenetskii. Base-stacking and base-pairing contributions into thermal stability of the DNA double helix, *Nucleic Acids Res.*, **2006,** *34*, 564-574.

53. Porschke, D. A direct measurement of the unzippering rate of a nucleic acid double helix, *Biophys. Chem.*, **1974,** *2*, 97-101.

54. Nikolova, E. N.; H. M. Al-Hashimi. Preparation, resonance assignment, and preliminary dynamics characterization of residue specific 13C/15N-labeled elongated DNA for the study of sequence-directed dynamics by NMR, *J. Biomol. NMR*, **2009,** *45*, 9-16.

55. Porschke, D. Model calculations on the kinetics of oligonucleotide double helix coil transitions. Evidence for a fast chain sliding reaction, *Biophys. Chem.*, **1974,** *2*, 83-96.

56. Dupuis, N. F.; E. D. Holmstrom; D. J. Nesbitt. Single-Molecule Kinetics Reveal Cation-Promoted DNA Duplex Formation Through Ordering of Single-Stranded Helices, *Biophys. J.*, **2013,** *105*, 756-766.

57. SantaLucia, J. A unified view of polymer, dumbbell, and oligonucleotide DNA nearest-neighbor thermodynamics, *Proc. Natl. Acad. Sci. USA*, **1998,** *95*, 1460-1465.

58. Hodak, J. H.; C. D. Downey; J. L. Fiore; A. Pardi; D. J. Nesbitt. Docking kinetics and equilibrium of a GAAA tetraloop-receptor motif probed by single-molecule FRET, *Proc. Natl. Acad. Sci. USA*, **2005,** *102*, 10505–10510.

59. Aitken, C. E.; R. A. Marshall; J. D. Puglisi. An Oxygen Scavenging System for Improvement of Dye Stability in Single-Molecule Fluorescence Experiments, *Biophys. J.*, **2008,** *94*, 1826-1835.

60. Kapanidis, A. N.; T. A. Laurence; N. K. Lee; E. Margeat; X. Kong; S. Weiss. Alternating-laser excitation of single molecules, *Acc. Chem. Res.*, **2005,** *38*, 523-533.

61. Lee, N. K.; A. N. Kapanidis; Y. Wang; X. Michalet; J. Mukhopadhyay; R. H. Ebright; S. Weiss. Accurate FRET Measurements within Single Diffusing Biomolecules using Alternating-Laser Excitation, *Biophys. J.*, **2005,** *88*, 2939-2953.

Chapter 5:
Thermodynamic Origins of Monovalent-Facilitated RNA Folding

1. Mattick, J. S.; I. V. Makunin. Non-coding RNA, *Hum. Mol. Genet.*, **2006,** *15*, R17-R29.

2. Butcher, S. E.; A. M. Pyle. The molecular interactions that stabilize RNA tertiary structure: RNA motifs, patterns, and networks, *Acc. Chem. Res.*, **2011,** *44*, 1302-1311.

3. Ditzler, M. A.; D. Rueda; J. J. Mo; K. Hakansson; N. G. Walter. A rugged free energy landscape separates multiple functional RNA folds throughout denaturation, *Nucl. Acids Res.*, **2008,** *36*, 7088-7099.

4. Steiner, M.; D. Rueda; R. K. O. Sigel. Ca^{2+} induces the formation of two distinct subpopulations of group II intron molecules, *Angew. Chem. Int. Ed. Engl.* , **2009,** *48*, 9739-9742.

5. Xie, Z.; N. Srividya; T. R. Sosnick; T. Pan; N. F. Scherer. Single-molecule studies highlight conformational heterogeneity in the early folding steps of a large ribozyme, *Proc. Natl. Acad. Sci. USA*, **2004,** *101*, 534-539.

6. Zhuang, X. W.; H. Kim; M. J. B. Pereira; H. P. Babcock; N. G. Walter; S. Chu. Correlating structural dynamics and function in single ribozyme molecules, *Science*, **2002,** *296*, 1473–1476.

7. Record, M. T.; W. T. Zhang; C. F. Anderson. Analysis of effects of salts and uncharged solutes on protein and nucleic acid equilibria and processes: A practical guide to recognizing and interpreting polyelectrolyte effects, Hofmeister effects, and osmotic effects of salts, *Adv. Protein. Chem.*, **1998,** *51*, 281-353.

8. Privalov, P. L.; O. B. Ptitsyn; Birshtei.Tm. Determination of stability of DNA double helix in an aqueous medium, *Biopolymers*, **1969,** *8*, 559-571.

9. Manning, G. S. Application of polyelectrolyte limiting laws to helix-coil transition of DNA .1. Excess univalent cations, *Biopolymers*, **1972,** *11*, 937-947.

10. Downey, C. D.; J. L. Fiore; C. D. Stoddard; J. H. Hodak; D. J. Nesbitt; A. Pardi. Metal ion dependence, thermodynamics, and kinetics for intramolecular docking of a GAAA tetraloop and receptor connected by a flexible linker, *Biochemistry*, **2006,** *45*, 3664–3673.

11. Heilman-Miller, S. L.; J. Pan; D. Thirumalai; S. A. Woodson. Role of counterion condensation in folding of the Tetrahymena ribozyme II. Counterion-dependence of folding kinetics, *J. Mol. Biol.*, **2001,** *309*, 57–68.

12. Heilman-Miller, S. L.; D. Thirumalai; S. A. Woodson. Role of counterion condensation in folding of the Tetrahymena ribozyme. I. Equilibrium stabilization by cations, *J. Mol. Biol.*, **2001,** *306*, 1157–1166.

13. Nixon, P. L.; D. P. Giedroc. Energetics of a strongly pH dependent RNA tertiary structure in a frameshifting pseudoknot, *J. Mol. Biol.*, **2000,** *296*, 659–671.

14. Takamoto, K.; Q. He; S. Morris; M. R. Chance; M. Brenowitz. Monovalent cations mediate formation of native tertiary structure of the Tetrahymena thermophila ribozyme, *Nat. Struct. Biol.*, **2002,** *9*, 928-933.

15. Uchida, T.; K. Takamoto; Q. He; M. R. Chance; M. Brenowitz. Multiple monovalent ion-dependent pathways for the folding of the L-21 Tetrahymena thermophila ribozyme, *J. Mol. Biol.*, **2003,** *328*, 463-478.

16. Ke, A.; F. Ding; J. D. Batchelor; J. A. Doudna. Structural roles of monovalent cations in the HDV ribozyme, *Structure*, **2007,** *15*, 281-287.

17. Jiang, Y. F.; M. Xiao; P. Yin; Y. Zhang. Monovalent cations use multiple mechanisms to resolve ribozyme misfolding, *RNA*, **2006,** *12*, 561-566.

18. Lambert, D.; D. Leipply; R. Shiman; D. E. Draper. The influence of monovalent cation size on the stability of RNA tertiary structures, *J. Mol. Biol.*, **2009,** *390*, 791-804.

19. Shiman, R.; D. E. Draper. Stabilization of RNA tertiary structure by monovalent cations, *J. Mol. Biol.*, **2000,** *302*, 79–91.

20. Uchida, T.; Q. He; C. Y. Ralston; M. Brenowitz; M. R. Chance. Linkage of monovalent and divalent ion binding in the folding of the P4-P6 domain of the Tetrahymena ribozyme, *Biochemistry*, **2002,** *41*, 5799-5806.

21. Basu, S.; R. P. Rambo; J. Strauss-Soukup; J. H. Cate; A. R. Ferre-D'Amare; S. A. Strobel; J. A. Doudna. A specific monovalent metal ion integral to the AA platform of the RNA tetraloop receptor, *Nat. Struct. Biol.*, **1998,** *5*, 986–992.

22. Wang, Y. X.; M. Lu; D. E. Draper. Specific ammonium ion requirement for functional ribosomal-RNA tertiary structure, *Biochemistry*, **1993,** *32*, 12279-12282.

23. Draper, D. E. RNA folding: Thermodynamic and molecular descriptions of the roles of ions, *Biophys. J.*, **2008,** *95*, 5489-5495.

24. Anderson, C. F.; M. T. Record. Salt nucleic-acid interactions, *Annu. Rev. Phys. Chem.*, **1995,** *46*, 657–700.

25. Tinoco, I.; C. Bustamante. How RNA folds, *J. Mol. Biol.*, **1999,** *293*, 271–281.

26. Sosnick, T. R.; T. Pan. RNA folding: Models and perspectives, *Curr. Opin. Struct. Biol.*, **2003,** *13*, 309–316.

27. Woese, C. R.; S. Winker; R. R. Gutell. Architecture of ribosomal-RNA: "Constraints on the sequence of Tetraloops", *Proc. Natl. Acad. Sci. USA*, **1990,** *87*, 8467-8471.

28. Hodak, J. H.; C. D. Downey; J. L. Fiore; A. Pardi; D. J. Nesbitt. Docking kinetics and equilibrium of a GAAA tetraloop-receptor motif probed by single-molecule FRET, *Proc. Natl. Acad. Sci. USA*, **2005,** *102*, 10505–10510.

29. Cate, J. H.; A. R. Gooding; E. Podell; K. H. Zhou; B. L. Golden; C. E. Kundrot; T. R. Cech; J. A. Doudna. Crystal structure of a group I ribozyme domain: Principles of RNA packing, *Science*, **1996,** *273*, 1678–1685.

30. Batey, R. T.; R. P. Rambo; J. A. Doudna. Tertiary motifs in RNA structure and folding, *Angew. Chem. Int. Ed.*, **1999,** *38*, 2327–2343.

31. Costa, M.; F. Michel. Frequent use of the same tertiary motif by self-folding RNAs, *Embo. J.*, **1995,** *14*, 1276–1285.

32. Vander Meulen, K. A.; J. H. Davis; T. R. Foster; T. Record; S. E. Butcher. Thermodynamics and folding pathway of tetraloop receptor-mediated RNA helical packing, *J. Mol. Biol.*, **2008,** *384*, 702-717.

33. Young, B. T.; S. K. Silverman. The GAAA tetraloop-receptor interaction contributes differentially to folding thermodynamics and kinetics for the P4-P6 RNA domain, *Biochemistry*, **2002,** *41*, 12271–12276.

34. Sattin, B. D.; W. Zhao; K. Travers; S. Chut; D. Herschlag. Direct measurement of tertiary contact cooperativity in RNA folding, *J. Am. Chem. Soc.*, **2008,** *130*, 6085–6087.

35. Fiore, J. L.; J. H. Hodak; O. Piestert; C. D. Downey; D. J. Nesbitt. Monovalent and Divalent Promoted GAAA-Tetraloop–Receptor Tertiary Interactions from Freely Diffusing Single-Molecule Studies, *Biophys. J.*, **2008,** *95*, 3892-3905.

36. Fiore, J. L.; B. Kraemer; F. Koberling; R. Erdmann; D. J. Nesbitt. Enthalpy-Driven RNA Folding: Single-Molecule Thermodynamics of Tetraloop–Receptor Tertiary Interaction, *Biochemistry*, **2009,** *48*, 2550–2558.

37. Butcher, S. E.; T. Dieckmann; J. Feigon. Solution structure of a GAAA tetraloop receptor RNA, *Embo. J.*, **1997,** *16*, 7490–7499.

38. Davis, J. H.; M. Tonelli; L. G. Scott; L. Jaeger; J. R. Williamson; S. E. Butcher. RNA helical packing in solution: NMR structure of a 30 kDa GAAA tetraloop-receptor complex *J. Mol. Biol.*, **2005,** *351*, 371–382.

39. Heus, H. A.; A. Pardi. Structural features that give rise to the unusual stability of RNA hairpins containing GNRA loops, *Science*, **1991,** *253*, 191-194.

40. Jucker, F. M.; H. A. Heus; P. F. Yip; E. H. M. Moors; A. Pardi. A network of heterogeneous hydrogen bonds in GNRA tetraloops, *J. Mol. Biol.*, **1996,** *264*, 968-980.

41. Aleman, E. A.; R. Lamichhane; D. Rueda. Exploring RNA Folding One Molecule at a Time, *Curr. Opin. Chem. Biol.*, **2008,** *12*, 647-654.

42. Bokinsky, G.; X. W. Zhuang. Single-molecule RNA folding, *Acc. Chem. Res.*, **2005,** *38*, 566–573.

43. Blanco, M.; N. G. Walter. Analysis of complex single-molecule FRET time trajectories, *Methods Enzymol.*, **2010,** *472*, 153-178.

44. Bartley, L. E.; X. W. Zhuang; R. Das; S. Chu; D. Herschlag. Exploration of the Transition State for Tertiary Structure Formation Between an RNA Helix and a Large Structured RNA, *J. Mol. Biol.*, **2003,** *328*, 1011–1026.

45. Zhou, Y. J.; X. W. Zhuang. Robust reconstruction of the rate constant distribution using the phase function method, *Biophys. J.*, **2006,** *91*, 4045-4053.

46. Leipply, D.; D. Lambert; D. E. Draper. Ion-RNA interactions: Thermodynamic analysis of the effects of mono- and divalent ions on RNA conformational equilibria, *Methods Enzymol.*, **2009,** *469*, 433-463.

47. Bokinsky, G.; D. Rueda; V. K. Misra; M. M. Rhodes; A. Gordus; H. P. Babcock; N. G. Walter; X. W. Zhuang. Single-molecule transition-state analysis of RNA folding, *Proc. Natl. Acad. Sci. USA*, **2003,** *100*, 9302–9307.

48. Fiore, J. L.; E. D. Holmstrom; D. J. Nesbitt. An Entropic origin of Mg^{2+}-Facilitated RNA Folding, *Proc. Natl. Acad. Sci. USA*, **2011**, (Accepted).

49. Hanggi, P.; P. Talkner; M. Borkovec. Reaction-rate theory - 50 years after Kramers, *Rev. Mod. Phys.*, **1990,** *62*, 251-341.

50. Vander Meulen, K. A.; S. E. Butcher. Characterization of the kinetic and thermodynamic landscape of RNA folding using a novel application of isothermal titration calorimetry, **2011,** *DOI:10.1093/nar/gkr894*.

51. Davis, J. H.; T. R. Foster; M. Tonelli; S. E. Butcher. Role of metal ions in the tetraloop-receptor complex as analyzed by NMR, *RNA*, **2007,** *13*, 76-86.

52. Buchmueller, K. L.; A. E. Webb; D. A. Richardson; K. M. Weeks. A collapsed non-native RNA folding state, *Nat. Struct. Biol.*, **2000,** *7*, 362-366.

53. Swisher, J. F.; L. H. J. Su; M. Brenowitz; V. E. Anderson; A. M. Pyle. Productive folding to the native state by a group II intron ribozyme, *J. Mol. Biol.*, **2002,** *315*, 297-310.

54. Silverman, S. K.; T. R. Cech. An early transition state for folding of the P4-P6 RNA domain, *RNA*, **2001,** *7*, 161–166.

55. Pljevaljcic, G.; D. Klostermeier; D. P. Millar. The tertiary structure of the hairpin ribozyme is formed through a slow conformational search, *Biochemistry*, **2005,** *44*, 4870-4876.

56. Szewczak, A. A.; E. R. Podell; P. C. Bevilacqua; T. R. Cech. Thermodynamic stability of the P4-P6 domain RNA tertiary structure measured by temperature gradient gel electrophoresis, *Biochemistry*, **1998,** *37*, 11162–11170.

57. Vander Meulen, K. A.; S. E. Butcher. Characterization of the kinetic and thermodynamic landscape of RNA folding using a novel application of isothermal titration calorimetry, *Nucl. Acids Res.*, **2012,** *40*, 2140-2151.

58. Holbrook, J. A.; M. W. Capp; R. M. Saecker; M. T. Record. Enthalpy and heat capacity changes for formation of an oligomeric DNA duplex: Interpretation in terms of coupled processes of formation and association of single-stranded helices, *Biochemistry*, **1999,** *38*, 8409-8422.

59. Takach, J. C.; P. J. Mikulecky; A. L. Feig. Salt-dependent heat capacity changes for RNA duplex formation, *J. Am. Chem. Soc.*, **2004,** *126*, 6530-6531.

60. Qin, P. Z.; J. Feigon; W. L. Hubbell. Site-directed spin labeling studies reveal solution conformational changes in a GAAA tetraloop receptor upon Mg^{2+}-dependent docking of a GAAA tetraloop, *J. Mol. Biol.*, **2005,** *351*, 1-8.

61. Lambert, D.; D. Leipply; D. E. Draper. The osmolyte TMAO stabilizes native RNA tertiary structures in the absence of Mg^{2+}: Evidence for a large barrier to folding from phosphate dehydration, *J. Mol. Biol.*, **2010,** *404*, 138-157.

62. Breslauer, K. J.; J. M. Sturtevant. Calorimetric investigation of single stranded base stacking in ribo-oligonucleotide-A7, *Biophys. Chem.*, **1977,** *7*, 205-209.

63. Seol, Y.; G. M. Skinner; K. Visscher. Elastic properties of a single-stranded charged homopolymeric ribonucleotide, *Phys. Rev. Lett.*, **2004,** *93*, 118102.

64. Michelson, A. M.; C. Monny. Polynucleotides .8. Base stacking in polyuridylic acid, *Proc. Natl. Acad. Sci. U.S.A.*, **1966,** *56*, 1528-1534.

65. Fiore, J. L.; E. D. Holmstrom; L. R. Feigland; J. H. Hodak; D. J. Nesbitt. The Role of Counterion Valence and Size in the GAAA Tetraloop-Receptor Docking/Undocking Kinetics, **2011**, (In preperation).

66. Holmstrom, E. D.; D. J. Nesbitt. Real-time infrared overtone laser control of temperature in picoliter H_2O samples: "Nanobathtubs" for single-molecule microscopy, *J. Phys. Chem. Lett.*, **2010,** *1*, 2264–2268.

Chapter 6:
Kinetic and Thermodynamic Origins of Osmolyte-Influenced Nucleic Acid Folding

1. Draper, D. E. A guide to ions and RNA structure, *RNA*, **2004,** *10*, 335-343.

2. Klein, D. J.; P. B. Moore; T. A. Steitz. The contribution of metal ions to the structural stability of the large ribosomal subunit, *RNA*, **2004,** *10*, 1366-1379.

3. Kurz, M. Compatible solute influence on nucleic acids: many questions but few answers, *Saline Systems*, **2008,** *4*, 6.

4. Yancey, P. H.; M. E. Clark; S. C. Hand; R. D. Bowlus; G. N. Somero. Living with water stress: evolution of osmolyte systems, *Science*, **1982,** *217*, 1214-1222.

5. Record, M. T., Jr.; E. S. Courtenay; D. S. Cayley; H. J. Guttman. Responses of E. coli to osmotic stress: large changes in amounts of cytoplasmic solutes and water, *Trends Biochem. Sci.*, **1998,** *23*, 143-148.

6. Yancey, P. H.; G. N. Somero. Counteraction of urea destabilization of protein structure by methylamine osmoregulatory compounds of elasmobranch fishes, *Biochem. J.*, **1979,** *183*, 317-323.

7. Record, M. T., Jr.; E. S. Courtenay; S. Cayley; H. J. Guttman. Biophysical compensation mechanisms buffering E. coli protein-nucleic acid interactions against changing environments, *Trends Biochem. Sci.*, **1998,** *23*, 190-194.

8. Liu, Y.; D. W. Bolen. The peptide backbone plays a dominant role in protein stabilization by naturally occurring osmolytes, *Biochemistry*, **1995,** *34*, 12884-12891.

9. Timasheff, S. N. Control of protein stability and reactions by weakly interacting cosolvents: the simplicity of the complicated, *Adv. Protein Chem.*, **1998,** *51*, 355-432.

10. Courtenay, E. S.; M. W. Capp; R. M. Saecker; M. T. Record, Jr. Thermodynamic analysis of interactions between denaturants and protein surface exposed on unfolding: interpretation of urea and guanidinium chloride m-values and their correlation with changes in accessible surface area (ASA) using preferential interaction coefficients and the local-bulk domain model, *Proteins*, **2000,** *4*, 72-85.

11. Courtenay, E. S.; M. W. Capp; C. F. Anderson; M. T. Record, Jr. Vapor pressure osmometry studies of osmolyte-protein interactions: implications for the action of osmoprotectants in vivo and for the interpretation of "osmotic stress" experiments in vitro, *Biochemistry*, **2000,** *39*, 4455-4471.

12. Lambert, D.; D. E. Draper. Effects of Osmolytes on RNA Secondary and Tertiary Structure Stabilities and RNA-Mg^{2+} Interactions, *J. Mol. Biol.*, **2007,** *370*, 993-1005.

13. Lambert, D.; D. Leipply; D. E. Draper. The osmolyte TMAO stabilizes native RNA tertiary structures in the absence of Mg^{2+}: Evidence for a large barrier to folding from phosphate dehydration, *J. Mol. Biol.*, **2010,** *404*, 138-157.

14. Lambert, D.; D. E. Draper. Denaturation of RNA secondary and tertiary structure by urea: simple unfolded state models and free energy parameters account for measured m-values, *Biochemistry*, **2012,** *51*, 9014-9026.

15. Spink, C. H.; N. Garbett; J. B. Chaires. Enthalpies of DNA melting in the presence of osmolytes, *Biophys. Chem.*, **2007,** *126*, 176-185.

16. Hong, J.; M. W. Capp; C. F. Anderson; R. M. Saecker; D. J. Felitsky; M. W. Anderson; M. T. Record, Jr. Preferential interactions of glycine betaine and of urea with DNA: implications for DNA hydration and for effects of these solutes on DNA stability, *Biochemistry*, **2004,** *43*, 14744-14758.

17. Felitsky, D. J.; J. G. Cannon; M. W. Capp; J. Hong; A. W. Van Wynsberghe; C. F. Anderson; M. T. Record, Jr. The exclusion of glycine betaine from anionic biopolymer surface: why glycine betaine is an effective osmoprotectant but also a compatible solute, *Biochemistry*, **2004,** *43*, 14732-14743.

18. Bennion, B. J.; V. Daggett. The molecular basis for the chemical denaturation of proteins by urea, *Proc. Natl. Acad. Sc.i USA*, **2003,** *100*, 5142-5147.

19. Greene, R. F., Jr.; C. N. Pace. Urea and guanidine hydrochloride denaturation of ribonuclease, lysozyme, alpha-chymotrypsin, and beta-lactoglobulin, *J. Biol. Chem.*, **1974,** *249*, 5388-5393.

20. Tanford, C. Isothermal Unfolding of Globular Proteins in Aqueous Urea Solutions, *J. Am. Chem. Soc.*, **1964,** *86*, 2050-&.

21. Shelton, V. M.; T. R. Sosnick; T. Pan. Applicability of Urea in the Thermodynamic Analysis of Secondary and Tertiary RNA Folding, *Biochemistry*, **1999,** *38*, 16831-16839.

22. Canchi, D. R.; A. E. Garcia. Cosolvent Effects on Protein Stability, *Annu. Rev. Phys. Chem.*, **2013**.

23. Schwinefus, J. J.; M. J. Kuprian; J. W. Lamppa; W. E. Merker; K. N. Dorn; G. W. Muth. Human telomerase RNA pseudoknot and hairpin thermal stability with glycine betaine

and urea: Preferential interactions with RNA secondary and tertiary structures, *Biochemistry*, **2007,** *46*, 9068-9079.

24. Cho, S. S.; G. Reddy; J. E. Straub; D. Thirumalai. Entropic Stabilization of Proteins by TMAO, *J. Phys. Chem. B*, **2011,** *115*, 13401-13407.

25. Wang, A. J.; D. W. Bolen. A naturally occurring protective system in urea-rich cells: Mechanism of osmolyte protection of proteins against urea denaturation, *Biochemistry*, **1997,** *36*, 9101-9108.

26. Pincus, D. L.; C. Hyeon; D. Thirumalai. Effects of trimethylamine N-oxide (TMAO) and crowding agents on the stability of RNA hairpins, *J. Am. Chem. Soc.*, **2008,** *130*, 7364-7372.

27. Priyakumar, U. D.; C. Hyeon; D. Thirumalai; A. D. MacKerell. Urea Destabilizes RNA by Forming Stacking Interactions and Multiple Hydrogen Bonds with Nucleic Acid Bases, *J. Am. Chem. Soc.*, **2009,** *131*, 17759-17761.

28. Tinoco, I.; R. L. Gonzalez. Biological mechanisms, one molecule at a time, *Gene Dev.*, **2011,** *25*, 1205-1231.

29. Roy, R.; S. Hohng; T. Ha. A practical guide to single-molecule FRET, *Nat. Methods*, **2008,** *5*, 507-516.

30. Li, P. T.; J. Vieregg; I. Tinoco, Jr. How RNA Unfolds and Refolds, *Annu. Rev. Biochem.*, **2008,** *77*, 77-100.

31. Bokinsky, G.; X. Zhuang. Single-Molecule RNA Folding, *Acc. Chem. Res.*, **2005,** *38*, 566-573.

32. Aleman, E. A.; R. Lamichhane; D. Rueda. Exploring RNA folding one molecule at a time, *Curr. Opin. Chem. Biol.* **2008,** *12*, 647-654.

33. Dupuis, N. F.; E. D. Holmstrom; D. J. Nesbitt. Single-Molecule Kinetics Reveal Cation-Promoted DNA Duplex Formation Through Ordering of Single-Stranded Helices, *Biophys. J.*, **2013,** *105*, 756-766.

34. Downey, C. D.; J. L. Fiore; C. D. Stoddard; J. H. Hodak; D. J. Nesbitt; A. Pardi. Metal ion dependence, thermodynamics, and kinetics for intramolecular docking of a GAAA tetraloop and receptor connected by a flexible linker, *Biochemistry*, **2006,** *45*, 3664–3673.

35. Fiore, J. L.; J. H. Hodak; O. Piestert; C. D. Downey; D. J. Nesbitt. Monovalent and Divalent Promoted GAAA-Tetraloop–Receptor Tertiary Interactions from Freely Diffusing Single-Molecule Studies, *Biophys. J.*, **2008,** *95*, 3892-3905.

36. Fiore, J. L.; E. D. Holmstrom; L. R. Feigland; J. H. Hodak; D. J. Nesbitt. The Role of Counterion Valence and Size in the GAAA Tetraloop-Receptor Docking/Undocking Kinetics, **2012**, *J. Mol. Biol.,* **2012,** 423, 198-216.

37. Fiore, J. L.; E. D. Holmstrom; D. J. Nesbitt. Entropic origin of Mg2+-facilitated RNA folding, *Proc. Natl. Acad. Sci. USA*, **2012,** *109*, 2902-2907.

38. Fiore, J. L.; B. Kraemer; F. Koberling; R. Erdmann; D. J. Nesbitt. Enthalpy-Driven RNA Folding: Single-Molecule Thermodynamics of Tetraloop–Receptor Tertiary Interaction, *Biochemistry*, **2009,** *48*, 2550–2558.

39. Hodak, J. H.; C. D. Downey; J. L. Fiore; A. Pardi; D. J. Nesbitt. Docking kinetics and equilibrium of a GAAA tetraloop-receptor motif probed by single-molecule FRET, *Proc. Natl. Acad. Sci. USA*, **2005,** *102*, 10505–10510.

40. Holmstrom, E. D.; J. L. Fiore; D. J. Nesbitt. Thermodynamic Origins of Monovalent Facilitated RNA Folding, *Biochemistry*, **2012,** *51*, 3732-3743.

41. Blanco, M.; N. G. Walter. Analysis of complex single-molecule FRET time trajectories, *Methods Enzymol.*, **2010,** *472*, 153-178.

42. Bartley, L. E.; X. W. Zhuang; R. Das; S. Chu; D. Herschlag. Exploration of the Transition State for Tertiary Structure Formation Between an RNA Helix and a Large Structured RNA, *J. Mol. Biol.*, **2003,** *328*, 1011–1026.

43. Zhou, Y. J.; X. W. Zhuang. Robust reconstruction of the rate constant distribution using the phase function method, *Biophys. J.*, **2006,** *91*, 4045-4053.

44. Sclavi, B.; S. Woodson; M. Sullivan; M. R. Chance; M. Brenowitz. Time-resolved synchrotron X-ray "footprinting", a new approach to the study of nucleic acid structure and function: application to protein-DNA interactions and RNA folding, *J. Mol. Biol.*, **1997,** *266*, 144-159.

45. Pan, J.; D. Thirumalai; S. A. Woodson. Folding of RNA involves parallel pathways, *J. Mol. Biol.*, **1997,** *273*, 7-13.

46. Pace, C. N. The stability of globular proteins, *CRC Crit. Rev. Biochem.*, **1975,** *3*, 1-43.

47. Myers, J. K.; C. N. Pace; J. M. Scholtz. Denaturant m values and heat capacity changes: relation to changes in accessible surface areas of protein unfolding, *Protein Sci.*, **1995,** *4*, 2138-2148.

48. Fiore, J. L.; E. D. Holmstrom; D. J. Nesbitt. Entropic Origin of Mg^{2+}-Facilitated RNA Folding, *Proc. Natl. Acad. Sci. USA*, **2012,** *109*, 2902-2907.

49. Holmstrom, E. D.; D. J. Nesbitt. Single-molecule fluorescence resonance energy transfer studies of the human telomerase RNA pseudoknot: temperature-/urea-dependent folding kinetics and thermodynamics, *J. Phys. Chem. B*, **2014,** *118*, 3853-3863.

50. Dalgarno, P. A.; J. Bordello; R. Morris; P. St-Pierre; A. Dube; I. D. Samuel; D. A. Lafontaine; J. C. Penedo. Single-molecule chemical denaturation of riboswitches, *Nucleic Acids Res.*, **2013,** *41*, 4253-4265.

51. Dupuis, N. F.; E. D. Holmstrom; D. J. Nesbitt. Molecular-crowding effects on single-molecule RNA folding/unfolding thermodynamics and kinetics, *Proc. Natl. Acad. Sci. USA,* **2013**. (in Press)

52. Cornish-Bowden, A. Enthalpy-entropy compensation: a phantom phenomenon, *J. Biosci.*, **2002,** *27*, 121-126.

53. Burg, M. B. Coordinate regulation of organic osmolytes in renal cells, *Kidney Int.*, **1996,** *49*, 1684-1685.

54. Aitken, C. E.; R. A. Marshall; J. D. Puglisi. An Oxygen Scavenging System for Improvement of Dye Stability in Single-Molecule Fluorescence Experiments, *Biophys. J.*, **2008,** *94*, 1826-1835.

Chapter 7:
Single Molecule FRET Studies of the Human Telomerase RNA Pseudoknot: Temperature/Urea Dependent Folding Kinetics and Thermodynamics

1. Wynford-Thomas, D.; D. Kipling. The End-Replication Problem, *Nature*, **1997,** *389*, 551-551.

2. Blackburn, E. H. Switching and Signaling at the Telomere, *Cell*, **2001,** *106*, 661-673.

3. Blackburn, E. H. The End of the (DNA) Line, *Nat. Struct. Biol.*, **2000,** *7*, 847-850.

4. Greider, C. W.; E. H. Blackburn. Tracking Telomerase, *Cell*, **2004,** *116*, S83-86.

5. Cech, T. R. Beginning to Understand the End of the Chromosome, *Cell*, **2004,** *116*, 273-279.

6. Hengesbach, M.; B. M. Akiyama; M. D. Stone. Single-Molecule Analysis of Telomerase Structure and Function, *Curr. Opin. Chem. Biol.*, **2011,** *15*, 845-852.

7. Mihalusova, M.; J. Y. Wu; X. Zhuang. Functional Importance of Telomerase Pseudoknot Revealed by Single-Molecule Analysis, *Proc. Natl. Acad. Sci. USA*, **2011,** *108*, 20339-20344.

8. Yeoman, J. A.; A. Orte; B. Ashbridge; D. Klenerman; S. Balasubramanian. RNA Conformation in Catalytically Active Human Telomerase, *J. Am. Chem. Soc.*, **2010,** *132*, 2852-2853.

9. Wu, J. Y.; M. D. Stone; X. Zhuang. A Single-Molecule Assay for Telomerase Structure-Function Analysis, *Nucleic Acids Res.*, **2010,** *38*, e16.

10. Gavory, G.; M. F. Symmons; Y. Krishnan Ghosh; D. Klenerman; S. Balasubramanian. Structural Analysis of the Catalytic Core of Human Telomerase RNA by FRET and Molecular Modeling, *Biochemistry*, **2006,** *45*, 13304-13311.

11. Collins, K. The Biogenesis and Regulation of Telomerase Holoenzymes, *Nat. Rev. Mol. Cell. Biol.*, **2006,** *7*, 484-494.

12. Chen, J. L.; C. W. Greider. Telomerase RNA Structure and Function: Implications for Dyskeratosis Congenita, *Trends Biochem. Sci.*, **2004,** *29*, 183-192.

13. Chen, J. L.; M. A. Blasco; C. W. Greider. Secondary Structure of Vertebrate Telomerase RNA, *Cell*, **2000,** *100*, 503-514.

14. Gilley, D.; E. H. Blackburn. The Telomerase RNA Pseudoknot is Critical for the Stable Assembly of a Catalytically Active Ribonucleoprotein, *Proc. Natl. Acad. Sci. USA*, **1999,** *96*, 6621-6625.

15. Tzfati, Y.; Z. Knight; J. Roy; E. H. Blackburn. A Novel Pseudoknot Element is Essential for the Action of a Yeast Telomerase, *Genes Dev.*, **2003,** *17*, 1779-1788.

16. Reipa, V.; G. Niaura; D. H. Atha. Conformational Analysis of the Telomerase RNA Pseudoknot Hairpin by Raman Spectroscopy, *RNA*, **2007,** *13*, 108-115.

17. Moriarty, T. J.; D. T. Marie-Egyptienne; C. Autexier. Functional Organization of Repeat Addition Processivity and DNA Synthesis Determinants in the Human Telomerase Multimer, *Mol. Cell. Biol.*, **2004,** *24*, 3720-3733.

18. Autexier, C.; R. Pruzan; W. D. Funk; C. W. Greider. Reconstitution of Human Telomerase Activity and Identification of a Minimal Functional Region of the Human Telomerase RNA, *Embo. J.*, **1996,** *15*, 5928-5935.

19. Bachand, F.; I. Triki; C. Autexier. Human Telomerase RNA-Protein Interactions, *Nucleic Acids Res.*, **2001,** *29*, 3385-3393.

20. Kim, N. K.; Q. Zhang; J. Zhou; C. A. Theimer; R. D. Peterson; J. Feigon. Solution Structure and Dynamics of the Wild-Type Pseudoknot of Human Telomerase RNA, *J. Mol. Biol.*, **2008,** *384*, 1249-1261.

21. Comolli, L. R.; I. Smirnov; L. Xu; E. H. Blackburn; T. L. James. A Molecular Switch Underlies a Human Telomerase Disease, *Proc. Natl. Acad. Sci. USA*, **2002,** *99*, 16998-17003.

22. Theimer, C. A.; C. A. Blois; J. Feigon. Structure of the Human Telomerase RNA Pseudoknot Reveals Conserved Tertiary Interactions Essential for Function, *Mol. Cell.*, **2005,** *17*, 671-682.

23. Theimer, C. A.; L. D. Finger; L. Trantirek; J. Feigon. Mutations Linked to Dyskeratosis Congenita Cause Changes in the Structural Equilibrium in Telomerase RNA, *Proc. Natl. Acad. Sci. USA*, **2003,** *100*, 449-454.

24. Theimer, C. A.; L. D. Finger; J. Feigon. YNMG Tetraloop Formation by a Dyskeratosis Congenita Mutation in Human Telomerase RNA, *RNA*, **2003,** *9*, 1446-1455.

25. Chen, G.; J. D. Wen; I. Tinoco, Jr. Single-Molecule Mechanical Unfolding and Folding of a Pseudoknot in Human Telomerase RNA, *RNA*, **2007,** *13*, 2175-2188.

26. Hengesbach, M.; N. K. Kim; J. Feigon; M. D. Stone. Single-Molecule FRET Reveals the Folding Dynamics of the Human Telomerase RNA Pseudoknot Domain, *Angew. Chem. Int. Ed. Engl.*, **2012,** *51*, 5876-5879.

27. Cao, S.; S. J. Chen. Biphasic Folding Kinetics of RNA Pseudoknots and Telomerase RNA Activity, *J. Mol. Biol.*, **2007,** *367*, 909-924.

28. Cao, S.; S. J. Chen. Predicting RNA Pseudoknot Folding Thermodynamics, *Nucleic Acids Res.*, **2006,** *34*, 2634-2652.

29. Li, P. T.; J. Vieregg; I. Tinoco, Jr. How RNA Unfolds and Refolds, *Annu. Rev. Biochem.*, **2008,** *77*, 77-100.

30. Bokinsky, G.; X. Zhuang. Single-Molecule RNA Folding, *Acc. Chem. Res.*, **2005,** *38*, 566-573.

31. Roy, R.; S. Hohng; T. Ha. A Practical Guide to Single-Molecule FRET, *Nat. Methods*, **2008,** *5*, 507-516.

32. Zhao, R.; D. Rueda. RNA Folding Dynamics by Single-Molecule Fluorescence Resonance Energy Transfer, *Methods*, **2009,** *49*, 112-117.

33. Aleman, E. A.; R. Lamichhane; D. Rueda. Exploring RNA Folding One Molecule at a Time, *Curr. Opin. Chem. Biol.*, **2008,** *12*, 647-654.

34. Holmstrom, E. D.; J. L. Fiore; D. J. Nesbitt. Thermodynamic Origins of Monovalent Facilitated RNA Folding, *Biochemistry*, **2012,** *51*, 3732-3743.

35. Fiore, J. L.; E. D. Holmstrom; D. J. Nesbitt. Entropic Origin of Mg^{2+}-Facilitated RNA Folding, *Proc. Natl. Acad. Sci. USA*, **2012,** *109*, 2902-2907.

36. Bartley, L. E.; X. W. Zhuang; R. Das; S. Chu; D. Herschlag. Exploration of the Transition State for Tertiary Structure Formation Between an RNA Helix and a Large Structured RNA, *J. Mol. Biol.*, **2003,** *328*, 1011–1026.

37. Fiore, J. L.; B. Kraemer; F. Koberling; R. Erdmann; D. J. Nesbitt. Enthalpy-Driven RNA Folding: Single-Molecule Thermodynamics of Tetraloop–Receptor Tertiary Interaction, *Biochemistry*, **2009,** *48*, 2550–2558.

38. Shelton, V. M.; T. R. Sosnick; T. Pan. Applicability of Urea in the Thermodynamic Analysis of Secondary and Tertiary RNA Folding, *Biochemistry*, **1999,** *38*, 16831-16839.

39. Lambert, D.; D. E. Draper. Effects of Osmolytes on RNA Secondary and Tertiary Structure Stabilities and RNA-Mg^{2+} Interactions, *J. Mol. Biol.*, **2007,** *370*, 993-1005.

40. Fersht, A. R.; A. Matouschek; L. Serrano. The Folding of an Enzyme .1. Theory of Protein Engineering Analysis of Stability and Pathway of Protein Folding, *J. Mol. Biol.*, **1992,** *224*, 771-782.

41. Priyakumar, U. D.; C. Hyeon; D. Thirumalai; A. D. MacKerell. Urea Destabilizes RNA by Forming Stacking Interactions and Multiple Hydrogen Bonds with Nucleic Acid Bases, *J. Am. Chem. Soc.*, **2009,** *131*, 17759-17761.

42. Lambert, D.; D. E. Draper. Denaturation of RNA secondary and tertiary structure by urea: simple unfolded state models and free energy parameters account for measured m-values, *Biochemistry*, **2012,** *51*, 9014-9026.

43. Williams, S.; T. P. Causgrove; R. Gilmanshin; K. S. Fang; R. H. Callender; W. H. Woodruff; R. B. Dyer. Fast Events in Protein Folding: Helix Melting and Formation in a Small Peptide, *Biochemistry*, **1996,** *35*, 691-697.

44. Yingling, Y. G.; B. A. Shapiro. The Impact of Dyskeratosis Congenita Mutations on the Structure and Dynamics of the Human Telomerase RNA Pseudoknot Domain, *J. Biomol. Struct. Dyn.*, **2007,** *24*, 303-319.

45. Akiyama, B. M.; M. D. Stone. Assembly of Complex RNAs by Splinted Ligation, *Methods Enzymol.*, **2009,** *469*, 27-46.

46. Moore, M. J.; C. C. Query. Joining of RNAs by Splinted Ligation, *Method Enzymol.*, **2000,** *317*, 109-123.

47. Stark, M. R.; J. A. Pleiss; M. Deras; S. A. Scaringe; S. D. Rader. An RNA Ligase-Mediated Method for the Efficient Creation of Large, Synthetic RNAs, *RNA*, **2006,** *12*, 2014-2019.

48. Moore, M. J., Query, C.C. Uses of Site-Specifically Modified RNAs Constructed by RNA Ligation, In *RNA:Protein Interactions: A Practical Approach* (Smith, C. W. J., Ed.), pp 75-140, Oxford University Press Inc., New York.1998

49. Chen, J. L.; C. W. Greider. Functional Analysis of the Pseudoknot Structure in Human Telomerase RNA, *Proc. Natl. Acad. Sci. USA*, **2005,** *102*, 8080-8085; discussion 8077-8089.

50. Lemay, J. F.; J. C. Penedo; R. Tremblay; D. M. Lilley; D. A. Lafontaine. Folding of the Adenine Riboswitch, *Chem. Biol.*, **2006,** *13*, 857-868.

51. Lee, N. K.; A. N. Kapanidis; Y. Wang; X. Michalet; J. Mukhopadhyay; R. H. Ebright; S. Weiss. Accurate FRET Measurements within Single Diffusing Biomolecules using Alternating-Laser Excitation, *Biophys. J.*, **2005,** *88*, 2939-2953.

52. Kapanidis, A. N.; N. K. Lee; T. A. Laurence; S. Doose; E. Margeat; S. Weiss. Fluorescence-Aided Molecule Sorting: Analysis of Structure and Interactions by

Alternating-Laser Excitation of Single Molecules, *Proc. Natl. Acad. Sci. USA*, **2004,** *101*, 8936–8941.

53. Kapanidis, A. N.; T. A. Laurence; N. K. Lee; E. Margeat; X. X. Kong; S. Weiss. Alternating-Laser Excitation of Single Molecules, *Acc. Chem. Res.*, **2005,** *38*, 523-533.

54. Orte, A.; R. Clarke; S. Balasubramanian; D. Klenerman. Determination of the Fraction and Stoichiometry of Femtomolar Levels of Biomolecular Complexes in an Excess of Monomer using Single-M olecule, Two-Color Coincidence Detection, *Anal. Chem.*, **2006,** *78*, 7707-7715.

55. Fiore, J. L.; J. H. Hodak; O. Piestert; C. D. Downey; D. J. Nesbitt. Monovalent and Divalent Promoted GAAA-Tetraloop–Receptor Tertiary Interactions from Freely Diffusing Single-Molecule Studies, *Biophys. J.*, **2008,** *95*, 3892-3905.

56. Aitken, C. E.; R. A. Marshall; J. D. Puglisi. An Oxygen Scavenging System for Improvement of Dye Stability in Single-Molecule Fluorescence Experiments, *Biophys. J.*, **2008,** *94*, 1826-1835.

Chapter 8:
Vitamin B_{12}-facilitates formation of a regulatory RNA kissing loop

1. Tucker, B. J.; R. R. Breaker. Riboswitches as versatile gene control elements, *Curr. Opin. Struct. Biol.*, **2005,** *15*, 342-348.

2. Nahvi, A.; N. Sudarsan; M. S. Ebert; X. Zou; K. L. Brown; R. R. Breaker. Genetic control by a metabolite binding mRNA, *Chem. Biol.*, **2002,** *9*, 1043.

3. Nou, X.; R. J. Kadner. Adenosylcobalamin inhibits ribosome binding to btuB RNA, *Proc. Natl. Acad. Sci. USA*, **2000,** *97*, 7190-7195.

4. Banerjee, R.; S. W. Ragsdale. The many faces of vitamin B12: catalysis by cobalamin-dependent enzymes, *Annu. Rev. Biochem.*, **2003,** *72*, 209-247.

5. Nahvi, A.; J. E. Barrick; R. R. Breaker. Coenzyme B12 riboswitches are widespread genetic control elements in prokaryotes, *Nucleic Acids Res.*, **2004,** *32*, 143-150.

6. Rodionov, D. A.; A. G. Vitreschak; A. A. Mironov; M. S. Gelfand. Comparative genomics of the vitamin B12 metabolism and regulation in prokaryotes, *J. Biol. Chem.*, **2003,** *278*, 41148-41159.

7. Martens, J. H.; H. Barg; M. J. Warren; D. Jahn. Microbial production of vitamin B12, *Appl. Microbiol. Biotechnol.*, **2002,** *58*, 275-285.

8. Roth, J. R.; J. G. Lawrence; T. A. Bobik. Cobalamin (coenzyme B12): synthesis and biological significance, *Annu. Rev. Microbiol.*, **1996,** *50*, 137-181.

9. Breaker, R. R. Riboswitches and the RNA world, *Cold Spring Harb. Perspect. Biol.*, **2012,** *4*.

10. Garst, A. D.; A. L. Edwards; R. T. Batey. Riboswitches: structures and mechanisms, *Cold Spring Harb. Perspect. Biol.*, **2011,** *3*.

11. Roy, R.; S. Hohng; T. Ha. A Practical Guide to Single-Molecule FRET, *Nat. Methods*, **2008,** *5*, 507-516.

12. Lemay, J. F.; J. C. Penedo; R. Tremblay; D. M. Lilley; D. A. Lafontaine. Folding of the Adenine Riboswitch, *Chem. Biol.*, **2006,** *13*, 857-868.

13. Suddala, K. C.; A. J. Rinaldi; J. Feng; A. M. Mustoe; C. D. Eichhorn; J. A. Liberman; J. E. Wedekind; H. M. Al-Hashimi; C. L. Brooks, 3rd; N. G. Walter. Single transcriptional and translational preQ1 riboswitches adopt similar pre-folded ensembles that follow distinct folding pathways into the same ligand-bound structure, *Nucleic Acids Res.*, **2013,** *41*, 10462-10475.

14. Souliere, M. F.; R. B. Altman; V. Schwarz; A. Haller; S. C. Blanchard; R. Micura. Tuning a riboswitch response through structural extension of a pseudoknot, *Proc. Natl. Acad. Sci. USA*, **2013,** *110*, E3256-3264.

15. Haller, A.; R. B. Altman; M. F. Souliere; S. C. Blanchard; R. Micura. Folding and ligand recognition of the TPP riboswitch aptamer at single-molecule resolution, *Proc. Natl. Acad. Sci. USA*, **2013,** *110*, 4188-4193.

16. Haller, A.; U. Rieder; M. Aigner; S. C. Blanchard; R. Micura. Conformational capture of the SAM-II riboswitch, *Nat. Chem. Biol.*, **2011,** *7*, 393-400.

17. Fiegland, L. R.; A. D. Garst; R. T. Batey; D. J. Nesbitt. Single-molecule studies of the lysine riboswitch reveal effector-dependent conformational dynamics of the aptamer domain, *Biochemistry*, **2012,** *51*, 9223-9233.

18. Johnson, J. E., Jr.; F. E. Reyes; J. T. Polaski; R. T. Batey. B12 cofactors directly stabilize an mRNA regulatory switch, *Nature*, **2012,** *492*, 133-137.

19. Weinberg, Z.; J. X. Wang; J. Bogue; J. Yang; K. Corbino; R. H. Moy; R. R. Breaker. Comparative genomics reveals 104 candidate structured RNAs from bacteria, archaea, and their metagenomes, *Genome Biol.*, **2010,** *11*, R31.

20. Griffiths-Jones, S.; A. Bateman; M. Marshall; A. Khanna; S. R. Eddy. Rfam: an RNA family database, *Nucleic Acids Res.*, **2003,** *31*, 439-441.

21. Xu, H.; Y. Li; C. Liu; Q. Wu; Y. Zhao; L. Lu; H. Tang. Fluorescence resonance energy transfer between acridine orange and rhodamine 6G and its analytical application for vitamin B12 with flow-injection laser-induced fluorescence detection, *Talanta*, **2008,** *77*, 176-181.

22. Ennifar, E.; P. Walter; B. Ehresmann; C. Ehresmann; P. Dumas. Crystal structures of coaxially stacked kissing complexes of the HIV-1 RNA dimerization initiation site, *Nat. Struct. Biol.*, **2001,** *8*, 1064-1068.

23. Horiya, S.; X. Li; G. Kawai; R. Saito; A. Katoh; K. Kobayashi; K. Harada. RNA LEGO: magnesium-dependent formation of specific RNA assemblies through kissing interactions, *Chem. Biol.*, **2003,** *10*, 645-654.

24. Tyrrell, J.; J. L. McGinnis; K. M. Weeks; G. J. Pielak. The cellular environment stabilizes adenine riboswitch RNA structure, *Biochemistry*, **2013,** *52*, 8777-8785.

25. Bronson, J. E.; J. Fei; J. M. Hofman; R. L. Gonzalez, Jr.; C. H. Wiggins. Learning rates and states from biophysical time series: a Bayesian approach to model selection and single-molecule FRET data, *Biophys. J.*, **2009,** *97*, 3196-3205.

26. Andersen, A. A.; R. A. Collins. Intramolecular secondary structure rearrangement by the kissing interaction of the Neurospora VS ribozyme, *Proc. Natl. Acad. Sci. USA*, **2001,** *98*, 7730-7735.

27. Toor, N.; K. S. Keating; O. Fedorova; K. Rajashankar; J. Wang; A. M. Pyle. Tertiary architecture of the Oceanobacillus iheyensis group II intron, *RNA*, **2010,** *16*, 57-69.

28. Brunel, C.; R. Marquet; P. Romby; C. Ehresmann. RNA loop-loop interactions as dynamic functional motifs, *Biochimie*, **2002,** *84*, 925-944.

29. Wagner, E. G.; S. Brantl. Kissing and RNA stability in antisense control of plasmid replication, *Trends Biochem. Sci.*, **1998,** *23*, 451-454.

30. Eguchi, Y.; J. Tomizawa. Complex formed by complementary RNA stem-loops and its stabilization by a protein: function of CoIE1 Rom protein, *Cell*, **1990,** *60*, 199-209.

31. Helmer-Citterich, M.; M. M. Anceschi; D. W. Banner; G. Cesareni. Control of ColE1 replication: low affinity specific binding of Rop (Rom) to RNAI and RNAII, *Embo. J.*, **1988,** *7*, 557-566.

32. Di Primo, C. Real time analysis of the RNAI-RNAII-Rop complex by surface plasmon resonance: from a decaying surface to a standard kinetic analysis, *J. Mol. Recognit.*, **2008,** *21*, 37-45.

33. Banner, D. W.; M. Kokkinidis; D. Tsernoglou. Structure of the ColE1 rop protein at 1.7 A resolution, *J. Mol. Biol.*, **1987,** *196*, 657-675.

34. Williamson, J. R. Induced fit in RNA-protein recognition, *Nat. Struct. Biol.*, **2000,** *7*, 834-837.

35. Noeske, J.; J. Buck; B. Furtig; H. R. Nasiri; H. Schwalbe; J. Wohnert. Interplay of 'induced fit' and preorganization in the ligand induced folding of the aptamer domain of the guanine binding riboswitch, *Nucleic Acids Res.*, **2007,** *35*, 572-583.

36. Serganov, A.; Y. R. Yuan; O. Pikovskaya; A. Polonskaia; L. Malinina; A. T. Phan; C. Hobartner; R. Micura; R. R. Breaker; D. J. Patel. Structural basis for discriminative regulation of gene expression by adenine- and guanine-sensing mRNAs, *Chem. Biol.*, **2004,** *11*, 1729-1741.

37. Zhang, J.; M. W. Lau; A. R. Ferre-D'Amare. Ribozymes and riboswitches: modulation of RNA function by small molecules, *Biochemistry*, **2010,** *49*, 9123-9131.

38. Bernstein, J. A.; A. B. Khodursky; P. H. Lin; S. Lin-Chao; S. N. Cohen. Global analysis of mRNA decay and abundance in Escherichia coli at single-gene resolution using two-color fluorescent DNA microarrays, *Proc. Natl. Acad. Sci USA*, **2002,** *99*, 9697-9702.

39. Moore, M. J., Query, C.C. Uses of Site-Specifically Modified RNAs Constructed by RNA Ligation, In *RNA:Protein Interactions: A Practical Approach* (Smith, C. W. J., Ed.), pp 75-140, Oxford University Press Inc., New York.1998

40. Proudnikov, D.; A. Mirzabekov. Chemical methods of DNA and RNA fluorescent labeling, *Nucleic Acids Res.*, **1996,** *24*, 4535-4542.

41. Kapanidis, A. N.; T. A. Laurence; N. K. Lee; E. Margeat; X. Kong; S. Weiss. Alternating-laser excitation of single molecules, *Acc. Chem. Res.*, **2005,** *38*, 523-533.

42. Aitken, C. E.; R. A. Marshall; J. D. Puglisi. An Oxygen Scavenging System for Improvement of Dye Stability in Single-Molecule Fluorescence Experiments, *Biophys. J.*, **2008,** *94*, 1826-1835.

43. Hodak, J. H.; C. D. Downey; J. L. Fiore; A. Pardi; D. J. Nesbitt. Docking kinetics and equilibrium of a GAAA tetraloop-receptor motif probed by single-molecule FRET, *Proc. Natl. Acad. Sci. USA*, **2005,** *102*, 10505–10510.

44. Baba, T.; T. Ara; M. Hasegawa; Y. Takai; Y. Okumura; M. Baba; K. A. Datsenko; M. Tomita; B. L. Wanner; H. Mori. Construction of Escherichia coli K-12 in-frame, single-gene knockout mutants: the Keio collection, *Mol. Syst. Biol.*, **2006,** *2*, 2006 0008.